

## Sealing Performance of Fractured Claystone and Clay-Based Materials



Gesellschaft für Anlagen-  
und Reaktorsicherheit  
(GRS) gGmbH

## Sealing Performance of Fractured Claystone and Clay-Based Materials

within the Framework of the  
German Project THM-TON  
and the EC Project DOPAS

Final Report

Chun-Liang Zhang

March 2017

### **Remark:**

This report was prepared under contract No. 02E10377 with the German Federal Ministry for Economic Affairs and Energy (BMWi) and under grant agreement No. 323273 with the European Union's European Atomic Energy Community's (Euratom) Seventh Framework Programme FP7/2007-2011.

The work was conducted by the Gesellschaft für Anlagen- und Reaktorsicherheit (GRS) gGmbH.

The authors are responsible for the content of this report.

**GRS - 451**  
**ISBN 978-3-946607-38-0**

**Keywords**

clay rock, modelling, properties of seal materials, performance of drift seal, sealing concepts, self-sealing of fractured claystone, repository, testing

## Foreword

The geological disposal concepts for radioactive waste are generally based on a multi-barrier system comprising the natural geological formations and engineered barriers. After waste emplacement, disposal cells, access drifts and shafts will be backfilled and sealed with suitable materials to prevent release of radionuclides into the biosphere.

In the framework of the THM-TON project during the last ten years from 2007 to 2016, which was funded by the German Federal Ministry for Economic Affairs and Energy (BMWi) under contract number 02E10377, GRS investigated the thermo-hydro-mechanical properties and responses of clay rocks and clay-based backfill/seal materials. The results obtained during the first time period of 2007 to 2013 are summarized in the GRS report “Thermo-Hydro-Mechanical Processes in the Nearfield around a HLW Repository in Argillaceous Formations” with two volumes:

Volume I - Laboratory Investigations (GRS-312) /ZHA 13a/ and

Volume II - In-situ-Investigations and Interpretative Modelling (GRS-313) /ZHA 14a/.

Following that, GRS participated in the European project with Full-Scale Demonstration of Plugs and Seals (DOPAS) for safe sealing repositories in different geological formations (clay, crystalline and salt). The DOPAS project conducted from September 2012 to August 2016 was co-funded by BMWi and by the European Commission (EC) under grant agreement no. 323273. As a part of the GRS programme within the DOPAS project, self-sealing capability of damaged claystone and sealing properties of clay-based seal materials were experimentally investigated. The experimental results were evaluated concerning the model prediction of the long-term sealing performance of a drift seal system. The investigations focused on the following aspects:

- Examination of self-sealing of fractures in clay rock by measurements of fracture closure, water permeability and gas migration;
- Characterization of crushed claystone-bentonite mixture as seal material in comparison to bentonite and bentonite-sand mixture with respect to relevant sealing properties such as compacted density, mechanical stability, water uptake and retention, swelling capacity, water permeability and gas migration;
- Development of specific constitutive relationships for the seal materials and the clay rock in order to enhance the predictability of numerical models for the long-term sealing performance of seal systems in repositories;

- Model validation by simulating the hydro-mechanical behaviour of the seal materials and the clay rock observed during laboratory experiments;
- Model prediction and analysis of the long-term performance of a reference drift seal constructed using the compacted claystone-bentonite mixture, bentonite and bentonite-sand mixture, respectively.

The important results and conclusions achieved from the GRS research work within the THM-TON and the DOPAS projects are summarized in this report.

## Contents

	<b>Foreword</b> .....	<b>I</b>
<b>1</b>	<b>Introduction</b> .....	<b>1</b>
<b>2</b>	<b>Backfilling and sealing concepts</b> .....	<b>5</b>
2.1	Swiss concept .....	6
2.2	French concept .....	8
2.3	German concept.....	12
<b>3</b>	<b>Sealing behaviour of fractured claystone</b> .....	<b>17</b>
3.1	Characteristics of investigated claystones .....	18
3.2	Fracturing-induced permeability .....	18
3.3	Fracture closure and permeability variation .....	24
3.4	Water conductivity of fractured claystone.....	32
3.5	Gas migration in water-saturated and resealed claystone .....	36
3.6	Conclusions on the sealing of fractured claystone .....	41
<b>4</b>	<b>Sealing properties of clay-based materials</b> .....	<b>43</b>
4.1	Characteristics of investigated seal materials .....	44
4.2	Compressibility and compacted density .....	45
4.2.1	Compaction in normal oedometer .....	46
4.2.2	Compaction in large oedometer .....	49
4.3	Water retention.....	51
4.4	Water saturation.....	58
4.5	Swelling capacity.....	62
4.5.1	Free swelling .....	62
4.5.2	Swelling pressure.....	65
4.5.3	Swelling under loads .....	67
4.6	Water permeability .....	74
4.7	Gas migration.....	75
4.7.1	Gas breakthrough tests under constant volume conditions .....	75

4.7.2	Gas breakthrough tests under constant stress conditions .....	79
4.8	Borehole sealing performance .....	83
4.9	Evaluation of the studied clay-based mixtures as seal material.....	89
<b>5</b>	<b>Modelling of hydro-mechanical processes in a seal system .....</b>	<b>93</b>
5.1	Fundamental theories of coupled THM modelling.....	93
5.1.1	THM coupling phenomena .....	93
5.1.2	Balance equations.....	95
5.2	Modelling of the hydro-mechanical behaviour of seal materials.....	97
5.2.1	Basic properties .....	97
5.2.2	Hydraulic constitutive models.....	98
5.2.3	Mechanic constitutive models .....	106
5.2.4	Simulations of water uptake and swelling pressure evolution .....	111
5.3	Modelling of the hydro-mechanical behaviour of clay rock.....	129
5.3.1	Hydraulic constitutive models.....	129
5.3.2	Mechanical constitutive models .....	134
5.3.3	Simulations of short- and long-term deformation .....	144
5.4	Predictive modelling of the long-term performance of a drift seal .....	152
5.4.1	Numerical model of a drift seal.....	152
5.4.2	Material parameters .....	154
5.4.3	Results and analysis .....	160
5.5	Lessons learnt from the modelling exercises .....	171
5.5.1	Modelling of the HM behaviour of the seal materials .....	171
5.5.2	Modelling of the HM behaviour of the clay rock .....	172
5.5.3	Predictive modelling of a drift seal .....	173
<b>6</b>	<b>Summary and conclusions .....</b>	<b>175</b>
6.1	Self-sealing of fractures in claystone .....	176
6.2	Sealing properties of clay-based materials .....	177
6.3	Modelling of the sealing performance of the clay-based materials .....	179
	<b>Acknowledgements .....</b>	<b>183</b>

<b>References .....</b>	<b>185</b>
<b>List of figures .....</b>	<b>195</b>
<b>List of tables .....</b>	<b>205</b>
<b>Appendix A: Water retention data obtained on the seal materials.....</b>	<b>207</b>
<b>Appendix B: Water saturation data obtained on the seal materials.....</b>	<b>219</b>

# 1 Introduction

Clay formations are world-widely investigated for deep geological disposal of radioactive waste due to their favourable properties such as large homogeneous rock mass, stable geological structure, extremely low hydraulic conductivity, self-sealing potential of fractures and especially high sorption capacity for retardation of radionuclides. In France and Switzerland, for instance, the potential repositories were proposed to be constructed in the highly-consolidated Callovo-Oxfordian and Opalinus argillaceous formations respectively /AND 05/ and /NAG 02/. In Germany, exemplarily for different geological conditions, two generic models were developed based on the known data for the Lower Cretaceous Clay (northern Germany) and the Opalinus Clay (southern Germany) in order to elaborate the methodology of demonstration of the safety of a repository for high-level radioactive waste (HLW) in clay formations according to the German regulations /REI 13/ and /REI 16/.

According to the respective geological conditions and national regulations, disposal concepts were proposed in Switzerland and France /NAG 02/, /AND 05/, whereas in Germany a conceptual design for the two generic model regions was developed /JOB 15a/, /JOB 15b/, /LOM 15/. In order to prove the feasibility of the disposal and backfilling/sealing concepts, comprehensive scientific research and technical development activities have been conducted in Underground Research Laboratories (URL), for instance, at Mont-Terri (MT-URL) in Switzerland and at Bure (MHM-URL) in France.

In accordance with the German R&D programme defined by the German Federal Ministry for Economic Affairs and Energy (BMWi) /BMW 12/, GRS has performed site-independent research work on clay rocks and backfill/seal materials during the last decade. Most of the investigations focused on the Callovo-Oxfordian (COX) and Opalinus (OPA) clay rocks by participation in international research projects conducted at the MHM-URL and MT-URL. In the framework of the present project "THM-TON" during the last ten years from 2007 to 2016, GRS has intensively studied the thermo-hydro-mechanical (THM) properties and responses of the clay rocks and clay-based backfill/seal materials with laboratory investigations, in situ experiments and numerical modelling. Comprehensive results have been obtained. The important findings obtained during the first time period of 2007 to 2013 are summarized in two interim project reports: (I) Laboratory Investigations /ZHA 13a/ and (II) In-situ-Investigations and Interpretative Modelling /ZHA 14a/. After that, GRS participated in the European project with Full-Scale Demonstration

of Plugs and Seals (DOPAS) /DOP 12/ to improve the adequacy, consistency and feasibility of the plugs and seals for safe sealing repositories in different geological formations /HAN 13/ and /HAN 14/. A number of full-scale plug/seal experiments were performed for safe sealing repositories in clay, crystalline and salt rocks:

- Clay rock: Full-Scale Seal (FSS) experiment undertaken by ANDRA in a surface facility in France to test the techniques of seal construction in drifts and intermediate-level waste (ILW) disposal vaults;
- Crystalline rock: Three full-scale experiments aimed at testing plugs in horizontal tunnels, including
  - Dome Plug (DOMPLU) experiment undertaken by SKB and Posiva at the Äspö Hard Rock Laboratory (Äspö HRL) in Sweden;
  - Posiva's Deposition Tunnel Plug (POPLU) experiment undertaken by Posiva, SKB, VTT and BTECH at the ONKALO Underground Rock Characterisation Facility (URCF) in Finland;
  - Experimental Pressure and Sealing Plug (EPSP) experiment undertaken by SÚRAO and the Czech Technical University (CTU) at the Josef underground research centre (URC) in the Czech Republic;
- Salt rock: ELSA experiment undertaken by DBE-TEC together with the Technical University of Freiburg and associated partners to develop shaft sealing concepts in Germany.

In most of the concepts for backfilling and sealing repositories in clay formations, bentonite-based materials are chosen to ensure certain swelling pressures to compress the surrounding damaged rock and to achieve low hydraulic conductivity of the plug/seal systems. As an alternative to the bentonite-based materials, crushed claystone produced by repository excavation was taken into account for backfilling and sealing repositories in clay formations and preliminarily investigated before the DOPAS project /ZHA 10a/13a/. The utilization of the excavated claystone for backfilling and sealing repositories has significant advantages such as chemical-mineralogical compatibility with the host rock, environmental and economical efficiency with no or less occupancy of the ground surface for the excavated claystone and low costs of material preparation and transport. Moreover, the preliminary experiments showed favourable properties of the crushed claystone and its mixture with bentonite with respect to the safe backfilling and sealing repositories /ZHA 10a/13a/14b/14e/.

In order to enhance the confidence in the experimental findings, GRS continued the investigations within the DOPAS project /DOP 12/ with emphasis on the crushed claystone-bentonite mixture in comparison with bentonite and bentonite-sand mixture. Comprehensive experiments were performed to characterise these clay-based materials with respect to the safety relevant properties and behaviour such as density and porosity, mechanical stability, water uptake and retention, swelling capacity, water permeability and gas migration.

As a key component in a plug/seal system, self-sealing potential of the excavation damaged zone (EDZ) surrounding the plugs and seals is a crucial factor governing the sealing performance of the whole seal system. The self-sealing of EDZ was investigated on artificially-cracked claystone samples with various aspects such as fracture closure under mechanical compression, moisture effects on self-sealing of fractures, water permeability and gas migration in resealed fractures.

For prediction and assessment of the sealing performance of a seal system in clay rock, theoretical modelling work was performed with the following objectives:

- validation of the existing constitutive models for description of the hydro-mechanical behaviour of the clay rock and clay-based seal materials;
- development of specific constitutive equations to extend the model capability;
- determination of the model parameters from laboratory experiments;
- modelling of hydro-mechanical phenomena observed in laboratory experiments to examine the model predictability; and
- model prediction and analysis of the long-term sealing performance of compacted claystone-bentonite mixture, bentonite and bentonite-sand mixture for a drift seal under repository relevant conditions.

The research work and results achieved from both the German project THM-TON and the European project DOPAS are presented in this report. Chapter 2 gives a short overview of the backfilling/sealing concepts developed by several countries for repositories in clay formations. The self-sealing behaviour of fractured claystone is highlighted in chapter 3. The sealing properties of the claystone-bentonite and bentonite-sand mixtures are illustrated in chapter 4. The modelling work with the model validation, development and application for the prediction of the long-term performance of a drift seal are revealed in chapter 5. Chapter 6 summarizes main conclusions from the experimental and theoretical studies.



## 2 Backfilling and sealing concepts

The fundamental basis of the geological disposal concepts for radioactive waste is generally a multi-barrier system, which comprises the natural geological formations and engineered barriers (EBS). The EBS represents engineered materials placed within a repository, including the waste form, waste canisters, buffer, backfill, plugs and seals. After emplacement of radioactive waste, the disposal boreholes/drifts, access drifts and shafts must be backfilled and sealed with suitable materials to prevent release of radionuclides into the biosphere. The engineered barriers have to be designed and constructed to assure the stability of the repository and of the thermo-hydro-mechanical-chemical-biological (THMCCB) conditions, and to provide low permeabilities and diffusivities, chemical buffering and long-term retardation of radionuclides /IAE 90/, /IAE 92/ and /OEC 03/.

In deep clay host formations, which are practically impermeable and have sufficiently large dimensions, the engineered barriers will play a central role in the disposal system ensuring the long-term containment and retardation of radioactive waste. According to the characteristics of the clay host rocks at selected potential repository sites, the disposal concepts and the functional requirements on each component of the EBS, basic concepts for backfilling and sealing repositories have been developed in several countries including France, Switzerland, Belgium, and others /WHI 14/. In Germany, a conceptual design with backfilling/sealing concepts was developed for HLW repositories for the two generic model regions in the Lower Cretaceous Clay (northern Germany) and the Opalinus Clay (southern Germany) /JOB 15a/b/, /LOM 15/.

In these concepts, clay-based materials are taken for the backfill and seal. These materials, particularly bentonite-based mixtures, have been widely investigated with respect to the safe sealing properties and responses. Specific techniques for backfilling and sealing the repository facilities have been developed and demonstrated in large/full-scale experiments in the URLs under realistic conditions. The most important results achieved are presented in international conferences and workshops:

- International Conferences on Clays in Natural and Engineered Barriers for Radioactive Waste Confinement, Reims 2002; Tours 2005; Lille 2007; Nantes 2010; Montpellier 2012; Brussels 2015
- ESDRED – International Technical Conference on the Practical Aspects of Deep Geological Disposal of Radioactive Waste, Prague, June 16-18, 2008

- FORGE – International Conference on Gas Generation and Migration, Luxembourg, 2013
- PEBS – International Symposium and Workshop on the Performance of Engineered Barriers, Hannover, 2014
- LUCOEX – International Symposium and Workshop on Full-scale Demonstration Tests in Technology Development of Repositories for Disposal of Radioactive Waste, Oskarshamn, 2015
- DOPAS – International Topical Seminar on Plugging and Sealing, Turku, 2016.

In the following, the backfilling/sealing concepts proposed by Switzerland, France and Germany are briefly overviewed.

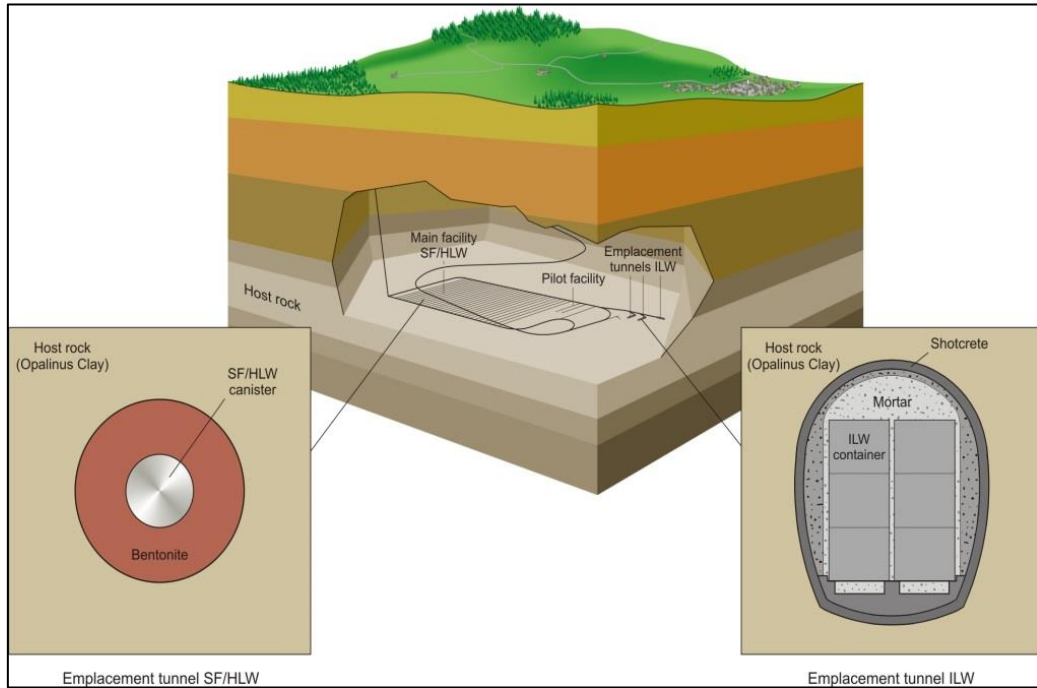
## 2.1 Swiss concept

Fig. 2.1 shows an overview on the Swiss backfilling/sealing concept for spent fuel and high-level radioactive waste (SF/HLW) in the Opalinus Clay at a depth of about 650 m below the surface /NAG 02/, /OEC 04/, /KOH 15/. The argillaceous formation at the potential repository site has a thickness of about 100 m. In order to maximise the length of the radionuclide transport to adjacent formations both above and below the repository, the horizontal disposal in drifts was selected. The waste emplacement drifts and the operation drifts will be excavated in the centre of the formation. SF/HLW will be emplaced in horizontal drifts of 2.8 m inner diameter and 800 m length. The disposal drifts are separated by pillars of 40 m width and oriented in the direction of the maximum principle stress so as to favour the stability. Each canister will be embedded in a suitable buffer material that is made of compacted bentonite blocks for bearing canisters and of granulated bentonite mixture filling the remaining space in the drifts.

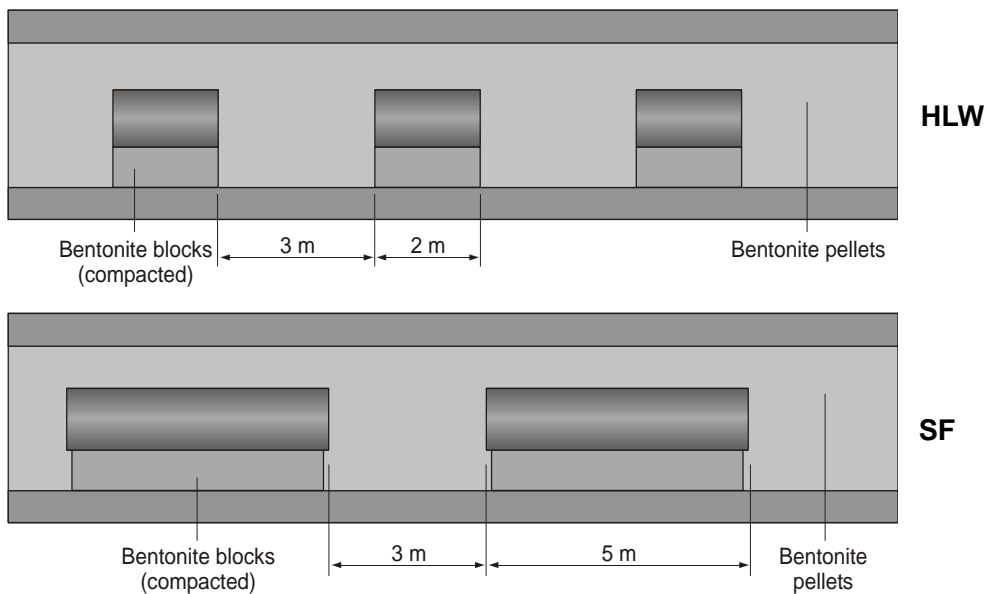
Sufficiently high density is required for the buffer to ensure adequate long-term sealing performance of the bentonite-based material since the density directly influences the other safety relevant attributes such as mechanical stability, swelling pressure, hydraulic conductivity, porosity and suppression of microbial activity. A saturated density of 1.90 g/cm<sup>3</sup> (corresponding to a dry density of 1.45 g/cm<sup>3</sup>) for the bentonite buffer is a desirable target and can be achieved by constructing bentonite blocks of a dry density of 1.80 g/cm<sup>3</sup> on the drift floor and by backfilling bentonite pellets into the remaining space. In the ongoing Full-Scale Emplacement (FE) experiment at the Mont-Terri URL, a higher dry density of 1.5 g/cm<sup>3</sup> for the buffer/backfill was achieved using denser bentonite blocks

with a higher density of 2.0 g/cm<sup>3</sup> and using a prototype backfilling machine for filling bentonite-pellets into the remaining space /KÖH 15/ and /MUL 15/.

Final closure of the repository would involve installation of ~40 m long seals of highly compacted bentonite in the access drifts and backfilling the ramp with a mixture of bentonite and sand.



a) Possible layout of a deep repository



b) SF/HLW drift backfill and seal

**Fig. 2.1** Swiss repository concept for SF and HLW disposal in horizontal drifts in the Opalinus clay formation (a-b) /NAG 02/

## 2.2 French concept

In the French disposal concept, HLW and ILW will be disposed in the Callovo-Oxfordian argillaceous formation at a depth of about 500 m below the surface /AND 05/15/. The repository will be located on a single level in the middle of the formation with a thickness of about 130 m and divided into HLW and ILW disposal areas. Fig. 2.2 shows the concept of the French Deep Geological Repository (Cigéo) /AND 15/.

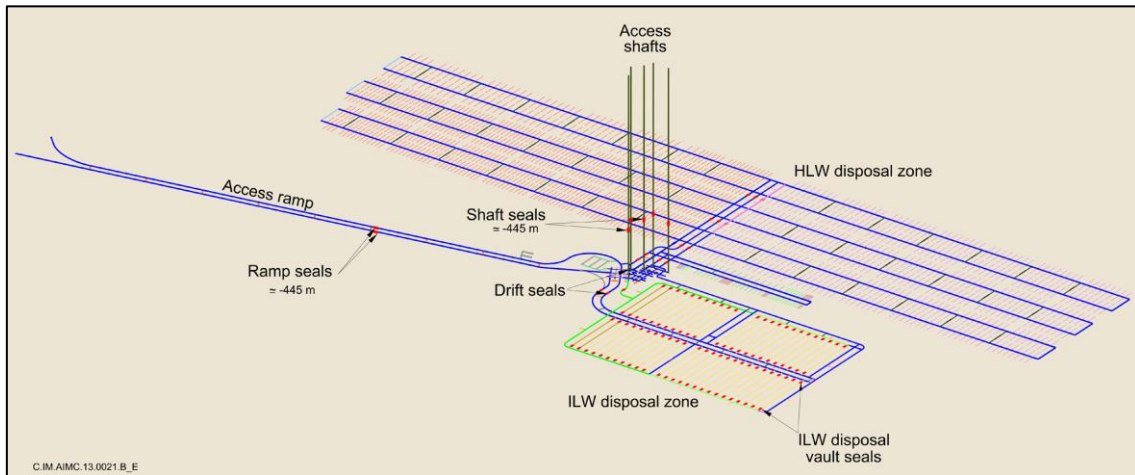


**Fig. 2.2** French repository concept for HLW and ILW disposal in horizontal boreholes and drifts in the Callovo-Oxfordian clay formation /AND 15/

The HLW disposal area includes several hundred disposal boreholes of 70 cm diameter and tens of meters in length. The boreholes are steel-lined to support the surrounding rock and to ensure emplacement and potential retrieval of waste packages. No buffer material is placed in the disposal cells, but grout is injected in the annular gap between the rock wall and the steel liner. Each disposal borehole is sealed with a swelling clay core and with two low-pH concrete containment plugs, one at each end.

The ILW disposal area includes several tens of large-diameter disposal vaults, each about 400-500 m long. Waste containers are emplaced in a concrete disposal container. Vault concrete lining and disposal containers provide a cementitious environment for the waste. The gaps between waste packages and vault lining could be left empty or back-filled with cementitious material or neutral filler.

The remaining openings are backfilled and sealed. The excavated host rock is used to backfill the drifts, shafts and ramps with the concrete lining maintained. In key positions, the shafts, ramps, drifts, and disposal vaults will be sealed (see Fig. 2.2). The conceptual

designs for the seals are quite similar. Fig. 2.3 illustrates an example for a drift seal /FOI 15/. Each seal consists of a swelling clay core and two low-pH concrete containment walls. The swelling core provides the required long-term sealing performance, whereas the containment walls are to confine the core mechanically. Before installation of the swelling core, the concrete linings in the selected positions are fully or partly removed, depending on the mechanical strength of the host rock there. Shaft and ramp seals will be located in the upper part of the Callovo-Oxfordian formation with sufficiently high strength, so that the lining can be fully removed there. For the drift and vault seals in the middle part of the formation with less strength, the lining is allowed to be partly removed. The removal of the lining ensures a good contact and seal between the clay core and the host rock.

Based on the safety functions, requirements on the seals are specified. For instance, a low hydraulic conductivity of  $10^{-11}$  m/s is currently set for the swelling cores in the drift seals, even though the performance assessment modelling has suggested a higher value of  $10^{-9}$  m/s for the seals /WHI 14/. The swelling pressure shall be close to but not exceed the effective mechanical stress of 7 MPa. The length of the seal must be two drift diameters (or 20 m) at least. Bentonite-based materials such as bentonite pellets and bentonite-sand mixture are suggested for the swelling cores. The swelling cores have to be constructed homogeneously and have a good contact with the surrounding rock.

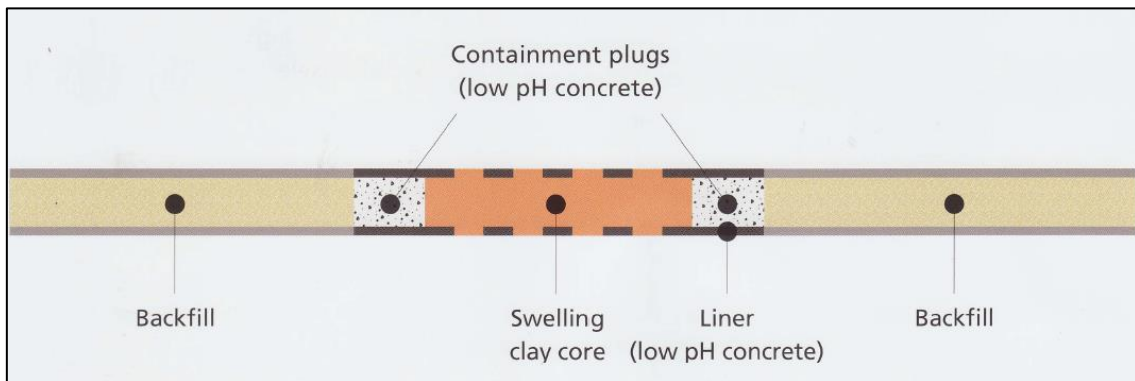


**Fig. 2.3** French reference drift sealing and backfilling concept /FOI 15/

In order to develop confidence in and to demonstrate the feasibility of constructing the full-scale seals, large and full-scale experiments have been undertaken in the MHM-URL and in the surface facilities.

The Full-Scale Seal (FSS) experiment was undertaken by ANDRA in a surface facility to test the techniques of seal construction in drifts and ILW disposal vaults /FOI 15/. The

swelling core was comprised of bentonite pellets and powder in a ratio of 70 % to 30 %. The material was backfilled in a concrete-made drift model of 7.6 m diameter and 36 m length. The feasibility of filling the drift with recesses in the host rock was demonstrated. After emplacement an average dry density of 1.49 g/cm<sup>3</sup> was achieved. Fig. 2.4 shows the layout of the FSS seal as constructed.

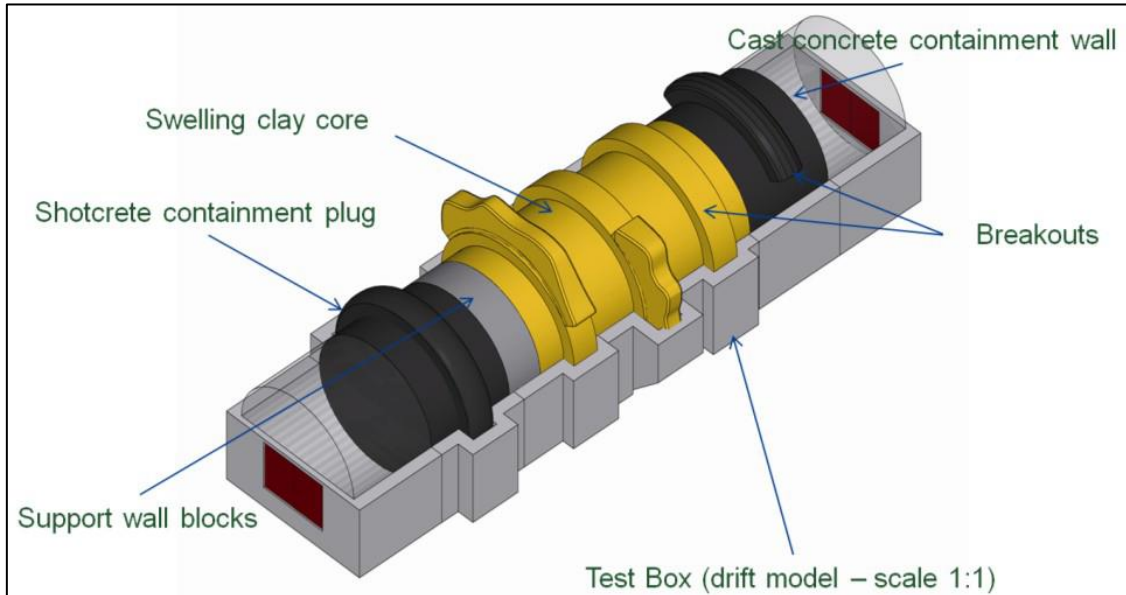


**Fig. 2.4** Longitudinal view of the FSS experiment made by ANDRA /FOI 15/

Another large-scale experiment (NSC) was conducted in the MHM-URL to evaluate the sealing performance of a bentonite-sand mixture for drift sealing /DEL 13/15/. A drift section of 5 m in length and 4.6 m in diameter was sealed using the compacted bentonite-sand blocks (300 x 200 x 100 mm) in a ratio of 60 % to 40 %. The gap between the drift wall and the seal was filled with bentonite pellets. Fig. 2.5 shows the test layout and a picture of the seal construction. An average dry density of the mixed bentonite was estimated by 1.45 g/cm<sup>3</sup> and the swelling pressure in the bentonite-sand seal varied in a range of 2.5 to 3.4 MPa.

In addition, several borehole sealing experiments were also carried out in the MHM-URL using bentonite-pellets of a dry density of 1.45 g/cm<sup>3</sup> and bentonite-sand (70 % / 30 %) mixture of a dry density of 1.60 g/cm<sup>3</sup> /DEL 13/. Relatively high swelling pressures of 4.5 MPa to 6.5 MPa were recorded and a low hydraulic conductivity of about 10<sup>-13</sup> m<sup>2</sup> was estimated.



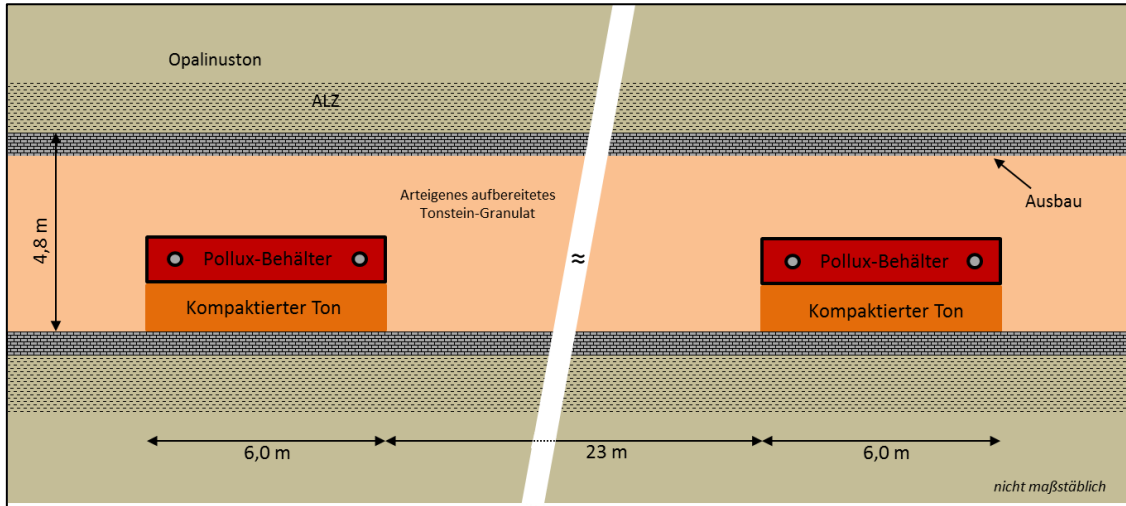
### 2.3 German concept

Within the framework of the German project “ANSICHT”, two generic models with backfilling/sealing concepts were developed for the Lower Cretaceous Clay (northern Germany) and the Opalinus Clay (southern Germany) in order to elaborate the methodology of demonstration of the safety of a HLW repository in clay rock according to the German regulations /REI 13/16, /JOB 15a/b/, /LOM 15/. One key issue of the concepts is to demonstrate the integrity of the geological and engineered barriers for isolating the waste in the host rock mass called “containment rock zone” (CRZ) for a period of 1 million years.

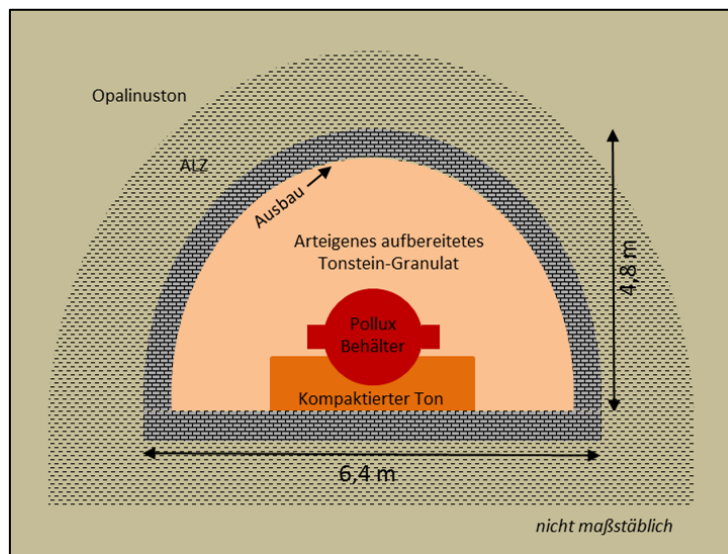
The Opalinus Clay host rock at the model site in the south of Germany has a thickness of 100 to 130 m. The potential repository will be at a depth of about 670 m below the ground surface. Due to the limited thickness of the Opalinus clay the horizontal drift disposal, like in the Swiss concept (Fig. 2.1), is the only suitable option. Fig. 2.6 shows the schematic of the disposal drift with concrete liner, backfill and POLLUX casks. The drifts have an excavated cross section of about 22 - 24 m<sup>2</sup> and a length of 400 m. With regard to temperature limitations in buffer and host rock /JOB 15a/, the distance between neighbouring casks will be of 23 m and the distance between the drifts of 20 m. In the preliminary concept, the casks will be laid down on highly compacted blocks consisting of prepared excavated rock material (Opalinus clay). If necessary, expansive clay minerals will be added to ensure a sufficient swelling pressure development. The remaining spaces in the emplacement drifts will be backfilled using a prepared granulate of the same material. The use of the excavated claystone or claystone-bentonite mixture as buffer material is desired because of its chemical-mineralogical compatibility with the host rock and other advantages.

The large thickness of about 540 m of the Lower Cretaceous Clay host rock in the north of Germany allows HLW disposal in vertical boreholes with sufficient large distances to the above and below adjacent formations leading to a much smaller footprint of the repository. The main level of the potential repository will be at a depth of ca. 770 m below the ground surface. Fig. 2.7 illustrates the principle of the vertical borehole disposal concept. Vertical boreholes will be drilled to a depth of 27 m. Considering possibly high rock stresses, the boreholes are lined with steel tubes to prevent breakout of the borehole walls. Three waste canisters are emplaced in an inner steel tube and separated with dry sand. This inner casing allows the retrieval of the canisters easily, when it is required within 500 years after the disposal. The casing is emplaced on the compacted clay-based

buffer at the bottom. The annular space between the inner and outer liners is backfilled with the compacted clay-based ring blocks. The boreholes are sealed with plugs at the tops. The utilisation of the excavated claystone is desired for the buffers.



a) Vertical section of horizontal HLW disposal drifts



b) Cross section of horizontal HLW disposal drifts

**Fig. 2.6** German concept for HLW disposal in horizontal drifts in Opalinus Clay (a-b) /JOB 15b/

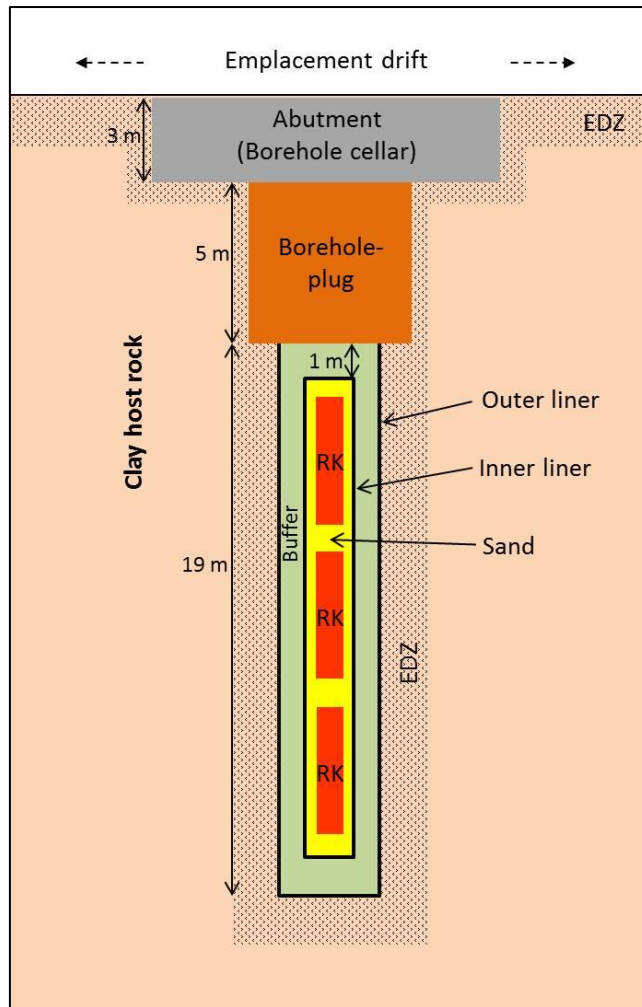


**Fig. 2.7** German concept for HLW disposal in vertical boreholes in Lower Cretaceous Clay /LOB 15/

A similar principle to ANDRA's drift backfill/seal concept (Fig. 2.2) is taken into account in the German concepts for backfilling and sealing drifts. Fig. 2.8 shows an example of the drift plug/seal system proposed for the potential repository in the Lower Cretaceous Clay. Subject to mechanical stability, the liner at the sealing element location will be removed and several slots will be excavated into the rock. Two seal cores will be constructed with compacted clay-based blocks and bentonite pellets filling the remaining space between the drift walls and blocks (cf. Fig. 2.5). The seal cores must have certain swelling capacity to compress and cut off the EDZ. The seal cores are confined by three concrete plugs at each end and in the middle to ensure the mechanical stability. It is also considered to add asphalt/bitumen elements between the seal cores and plugs as immediate active seal elements. The remaining space in the drifts will be backfilled with the excavated claystone, which is expected to take the long-term barrier function.

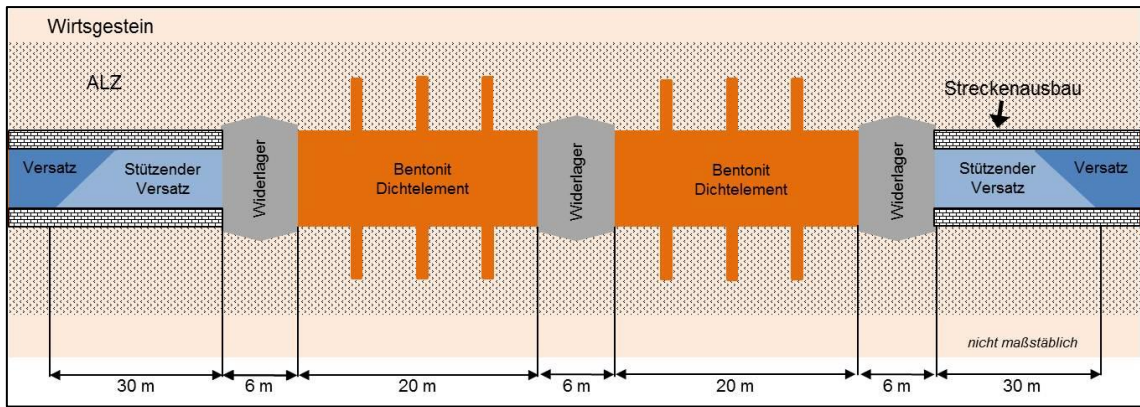


**Fig. 2.8** German drift backfilling and sealing concept /LOB 15/

It is to be pointed out that the EDZ as a crucial component belongs to any plug/seal systems because its hydro-mechanical behaviour determines the sealing performance of the whole systems.

Shaft sealing systems, currently under development in the German ELSA project /HER 15/, will complement the overall sealing system yielding a multi-barrier system considering redundancy and diversity in sealing elements and sealing material.



### 3 Sealing behaviour of fractured claystone

Excavation of a repository leads to a concentration of the deviatoric stress in the surrounding rock and results in micro- and macrocracks in the near-field, which may act as potential pathways for fluid flow and radionuclide migration into the biosphere. As observed in the URLs at Mont-Terri /BOS 04/ and at Bure /ARM 14/, /DEL 15b/, the damaged zone is developed near drift walls and the permeability increases over several orders of magnitude.

However, restoration of the EDZ can be expected due to the convergent compression of the surrounding clay rock, the increasing resistance of the backfill/seal materials, and the swelling of clay minerals into fracture interstices. The closure of the fractures will decrease the hydraulic conductivity, depending on the mineralogical components of the clay rock and the hydro-mechanical conditions. As the EDZ becomes water-saturated, gas migration through the EDZ may need a sufficiently high pressure to overcome the capillary resistance in it.

For assessment of the sealing performance of the plug/seal systems and hence the long-term safety of a repository, the development of the EDZ surrounding the plugs and seals has to be precisely characterized, deeply understood, and reliably predicted. This important issue has been extensively investigated at the GRS laboratory in the frame of the German national and European projects such as the NFPRO /ZHA 08a/, TIMODAZ /ZHA 10a/, THM-TON /ZHA 13a/ and DOPAS /ZHA 14c/d/ projects. Various laboratory experiments were performed on core samples from the Callovo-Oxfordian and the Opalinus claystones in order to investigate the long-term deformation, damage and failure strength, damage-induced permeability, swelling capacity, self-sealing of fractures, water and gas flow in damaged and resealed claystone /ZHA 08/a/b/, /ZHA 09/, /ZHA 10a/b/, /ZHA 11/, /ZHA 13a/b/, /ZHA 14a/b/c/d/, /ZHA 15a/, /ZHA 16/. The main results obtained during this project period (2013 – 2016) were published in several scientific papers:

- A. Deformation of clay rock under THM conditions, *Journal of Geomechanics and Tunneling* (2015) /ZHA 15a/
- B. Stress-strain-permeability behaviour of clay rock during damage and recompaction, *Journal of Rock Mechanics and Geotechnical Engineering* (2016) /ZHA 16/
- C. Sealing of fractures in claystone, *Journal of Rock Mechanics and Geotechnical Engineering* (2013) /ZHA 13b/

- D. Gas migration in damaged and resealed claystone, *Geological Society Special Publication* 415 (2014) /ZHA 14c/
- E. Examination of Effective Stress in Clay Rock, *Journal of Rock Mechanics and Geotechnical Engineering*, 2017 /ZHA 17A/
- F. Thermal Effects on Clay Rocks for Deep Disposal of High-Level Radioactive Waste, *Journal of Rock Mechanics and Geotechnical Engineering* 2017/ZHA 17B/.

This chapter summarises the main experimental findings on the damage-induced permeability and self-sealing of fractures in claystones.

### **3.1 Characteristics of investigated claystones**

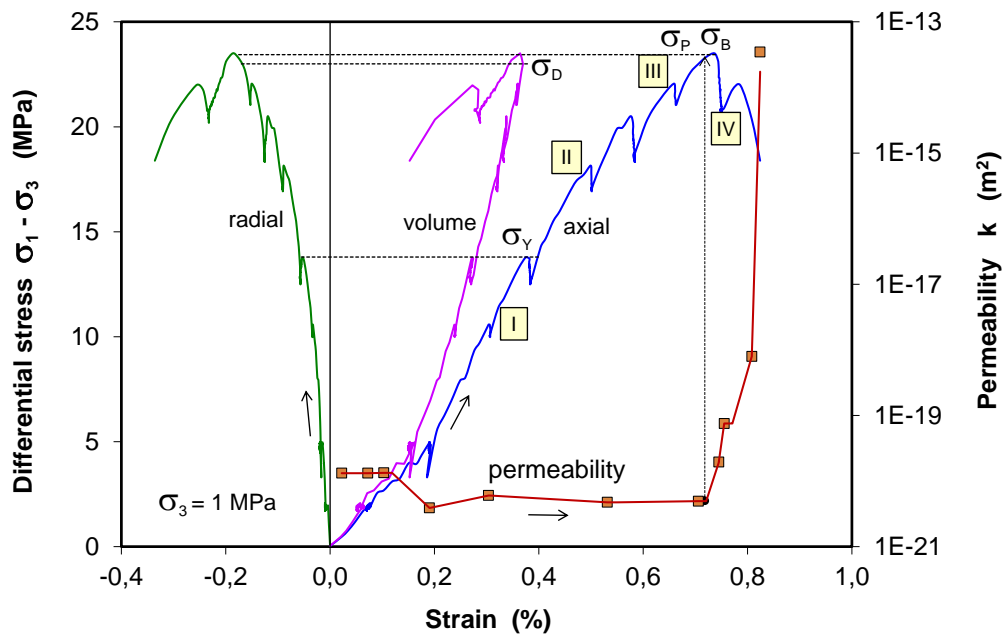
The Callovo-Oxfordian claystone (COX) at the -490m level of the MHM-URL and the Opalinus claystone (OPA) from the shaly facies at the MT-URL have been experimentally investigated at the GRS laboratory. Both COX and OPA argillaceous formations are results of a specific geological history that lasted hundreds of millions of years, beginning with deposition and aggregation of fine-grained particles in sea water, followed by sedimentation and consolidation with a concurrent expelling of porewater, development of diagenetic bonds between mineral particles, and other processes /AND 05/, /NAG 02/, /BOC 10/. They have been highly consolidated to porosities of 14 - 18 %. The pore sizes mainly range from nanometer scale in between the parallel platelets of the clay particles to micro- and mesometer scale between solid particles. The fraction of pores smaller than 20 nm amounts to about 60 - 80 % for the clay rocks. On average, the COX claystone contains 25 - 55 % clay minerals, 20 - 38 % carbonates and 20 - 30 % quartz, while the OPA clay-schist has higher clay contents (58 - 76 %), less carbonates (6 - 24 %) and quartz (5 - 28 %). Because of the relatively high clay components, both the investigated claystones can be referred as clay rich. The claystone matrix contains accessory minerals but mainly clay, which consists of particles with strongly adsorbed interlayer water and adsorbed water at the external surfaces. In large pores is bulk water mobile.

### **3.2 Fracturing-induced permeability**

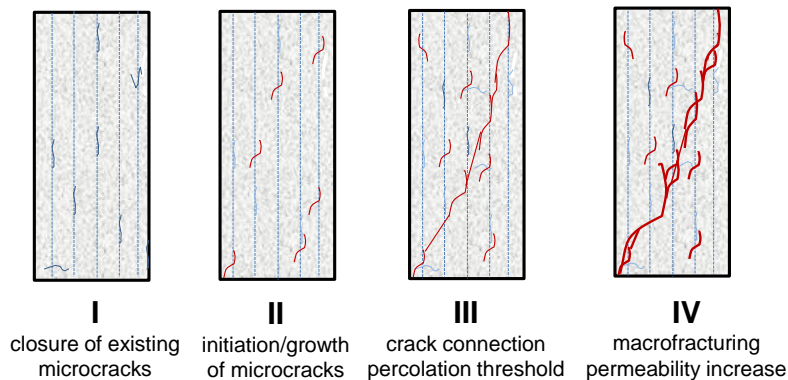
Mechanical damage and induced permeability changes were determined on COX claystone samples under triaxial compression stresses, whereby deformation of the samples,

gas permeability and wave velocity through them were recorded. Details of the tests and results are given in /ZHA 16/.

Fig. 3.1 shows a typical example of the stress-strain-permeability response of the claystone and a conceptual mode of crack evolution during triaxial loading. The establishment of this mode takes into account the micro tomography of localized damage and deformation made on the same claystone during triaxial loading /VIG 11/, and also the typical fracture pattern observed on the samples after testing. The stress-strain-permeability behaviour may be characterized in four sequential stages.



a) Stress-strain-permeability curves

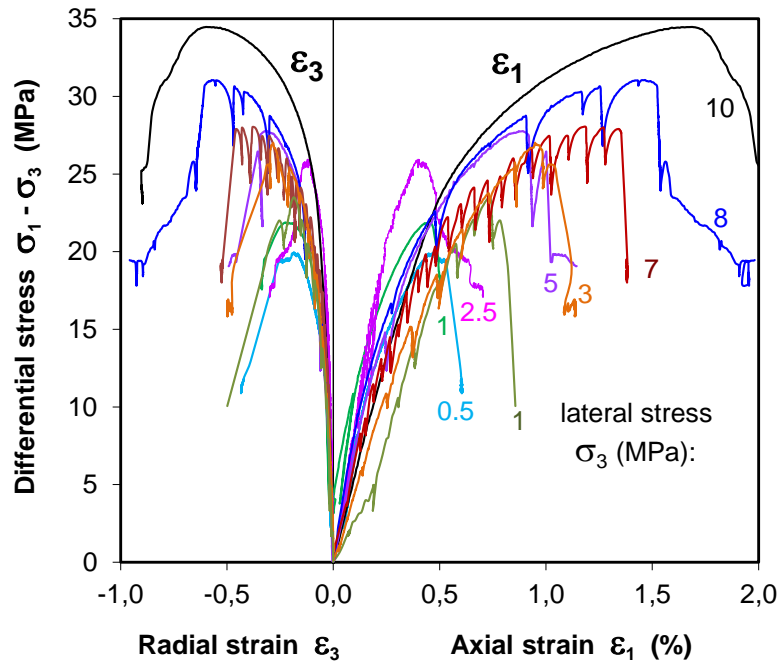


b) Schematic of crack evolution during loading

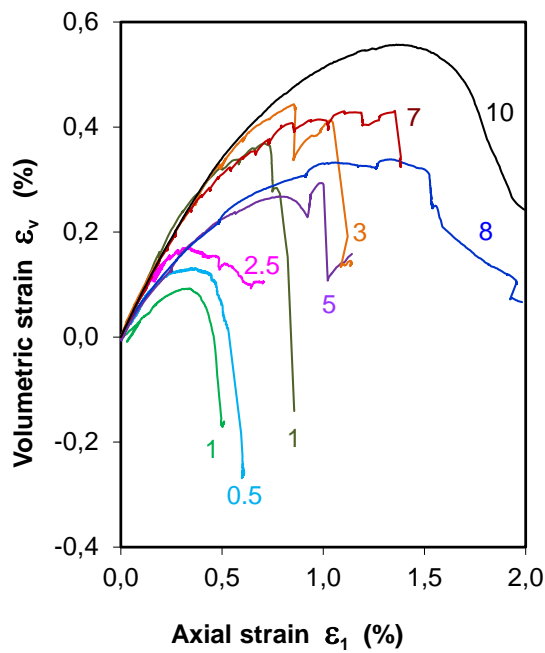
**Fig. 3.1** Stress-strain-permeability behaviour of COX claystone including thresholds of yield  $\sigma_Y$ , dilatancy  $\sigma_D$ , percolation  $\sigma_P$ , and peak failure  $\sigma_B$  (a-b)

- I. The claystone deforms relatively largely in the very beginning of the load due to the closure of the pre-existing microcracks, and then it follows a linear axial compression  $\varepsilon_1$ , radial extension  $\varepsilon_3$  and volumetric compaction  $\varepsilon_v$  until a deviation appears at a differential stress  $\sigma_Y$ . The yield point indicates onset of microcracking, as detected by shear wave velocity on the Opalinus claystone /POP 07/. The yield stress recorded is about 60 % of the peak failure strength  $\sigma_B$ .
- II. Further increasing the stress results in a non-linear plastic hardening process with an overall volume compaction. This implies that the pre-existing and newly-created microcracks mostly keep closed during shearing /VIG 11/. As a result, the initially very low permeability does not change much.
- III. When the deviatoric stress reaches a high value  $\sigma_D$  close to the peak  $\sigma_B$ , the volume compaction changes over to dilatancy due to crack opening. Exceeding the dilatancy threshold, the microcracks grow and propagate much faster with further loading. Just as some of the neighbouring microcracks coalesce to a continuous network through the sample, the permeability begins to rise. The corresponding differential stress  $\sigma_P$  is usually called percolation threshold. It occurs shortly before the peak failure at low lateral stresses  $\sigma_3 \leq 1$  MPa but shortly after the peak at high lateral stresses. So it is reasonable to assume  $\sigma_P \approx \sigma_B$ .
- IV. Beyond the fracture percolation during the post-failure phase at the residual stress, the connection of the cracks results in a spontaneous increase of the permeability, accompanied with very small dilatancy. After the crack connectivity is sufficiently developed, further deformation is mainly dominated by fracture slipping, so that further increase of the fracturing-induced permeability is limited.

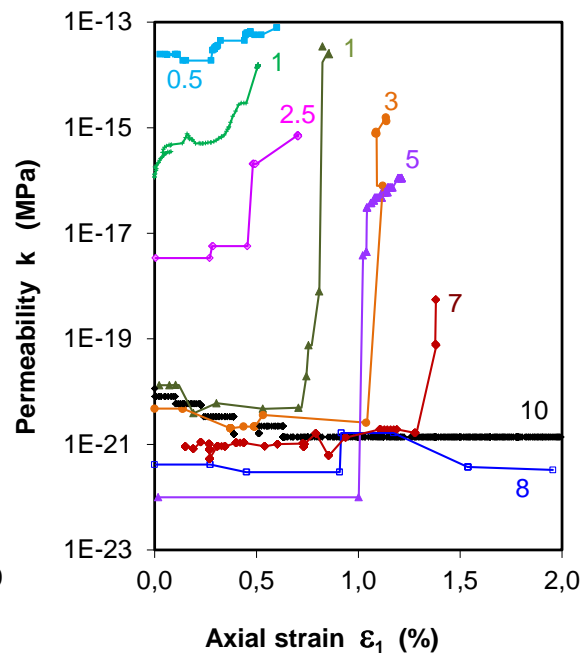
The damage and the resulting permeability change are dependent on the lateral confining stress. As the confining stress is increased, the inner structure of the claystone becomes more compacted and fracturing is inhibited. The deformation becomes progressively from brittle to ductile, as shown in Fig. 3.2. Because high confining stresses suppress the initiation, growth and propagation of cracks, the compaction phase before the onset of dilatancy lasts longer and the fracture percolation occurs later on at high lateral stresses. The increased permeability is also relatively low at high confining stresses. Generally, the critical stresses and strains at yield, dilatancy, percolation, and peak failure increase with increasing lateral confining stress.



a) Axial/radial strains with deviatoric loading



b) Volumetric strain with axial strain



c) Permeability with axial strain

**Fig. 3.2** Dependency of the deformation and permeability of COX claystone on lateral confining stress (a-c)

The critical stresses at yield, dilatancy, percolation, and peak failure increase with increasing confining stress, as shown in Fig. 3.3. The peak failure strength can be described by the Hoek-Brown (HB) and Mohr-Coulomb (MC) criteria

$$\text{HB: } \sigma_B = (m \cdot \sigma_c \cdot \sigma_3 + s\sigma_c^2)^{1/2} \quad (3.1)$$

where the uniaxial compression strength  $\sigma_c = 19 \text{ MPa}$ , the parameter  $m = 4$ , and  $s = 1$  are estimated for the claystone; and

$$\text{MC: } \sigma_B = 2 \cdot c \cdot \tan\left(45^\circ + \frac{\varphi}{2}\right) - \sigma_3 \cdot \left[1 - \tan^2\left(45^\circ + \frac{\varphi}{2}\right)\right] \quad (3.2)$$

where the cohesion  $c = 6 \text{ MPa}$  and the internal friction angle  $\varphi = 26^\circ$  are determined.

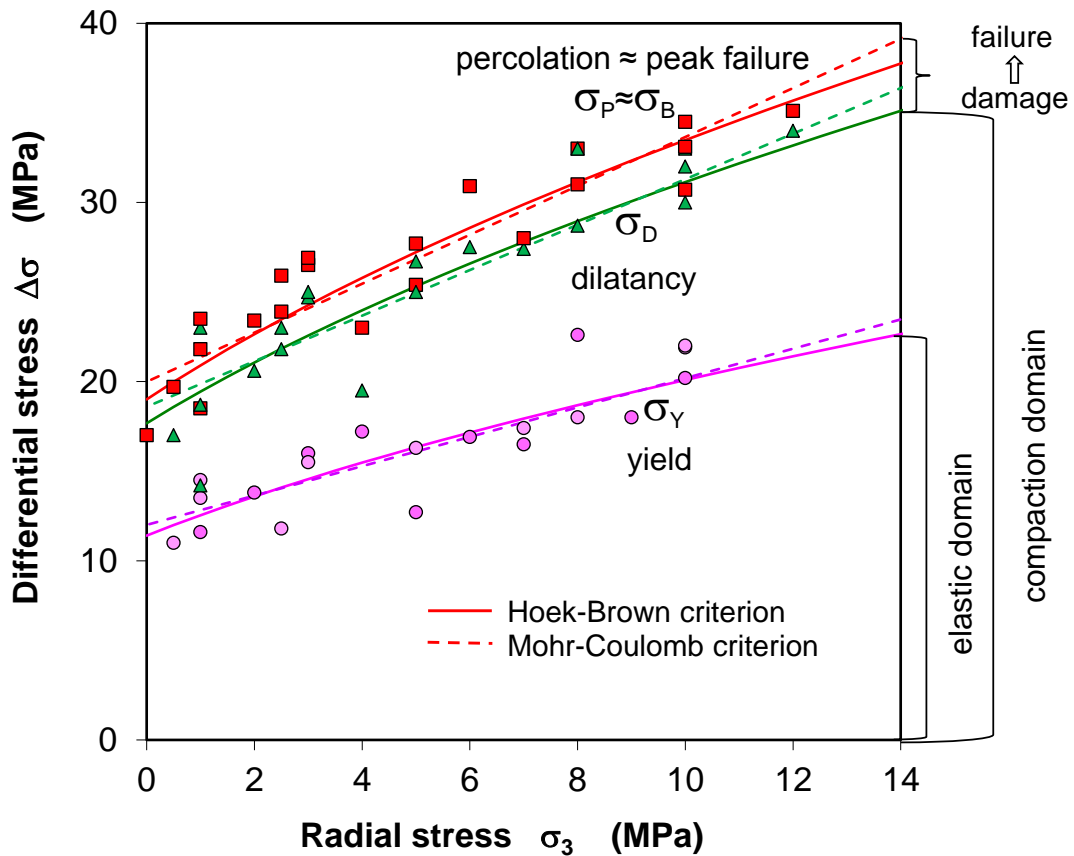


**Fig. 3.3** Stress boundaries of yield, dilatancy, percolation and peak failure of the claystone

It appears that the ratios of the yield and dilatant stresses to the peak strength are more or less constant, being independent of the confining stress. The average values are obtained as  $\sigma_Y/\sigma_B = 0.60$ ,  $\sigma_D/\sigma_B = 0.93$ , and  $\sigma_P \approx \sigma_B$ .

These stress boundary conditions identified are helpful for characterising the state of the rock subjected to any given stress state. For stresses below the yield boundary  $\sigma_Y$ , the rock behaves elastically. Above the yield boundary but below the dilatancy boundary,  $\sigma_Y < (\sigma_1 - \sigma_3) < \sigma_D$ , the overall volume is under compression without damage even though some microcracks may be created. If the dilatancy boundary is violated,  $(\sigma_1 - \sigma_3) \geq \sigma_D$ , the microcracks grow and coalesce with increasing deviatoric stresses. When the stress reaches the percolation and failure boundary,  $(\sigma_1 - \sigma_3) \geq \sigma_P \approx \sigma_B$ , a crack network builds up leading to a spontaneous increase of the permeability and to failure.

The fracturing-induced permeability is contributed by the connectivity and the conductivity of cracks and can be expressed in a general form by  $K_g = K_f \cdot P$ , where  $K_f$  is the ultimate permeability of the fractured rock with perfectly interconnected cracks and  $P$  is the percolation probability defining the fraction of cracks belonging to the conducting part of a network. The ultimate fracture permeability was observed to increase with decreasing the minor principle stress  $\sigma_3$  by  $K_f = K_o \cdot \exp(-\gamma\sigma_3)$ , where  $K_o$  is the permeability at zero minor stress and  $\gamma$  being a parameter characterizing the dilatability of the interconnected cracks. In addition, the percolation probability is assumed to be a function of crack dilatancy:  $P = [1 - \exp(-\Delta\varepsilon_D/\varepsilon_P)]$ , where  $\Delta\varepsilon_D = |\varepsilon_v - \varepsilon_P|$  is the volumetric dilatancy with reference to the volumetric strain  $\varepsilon_P$  at the percolation threshold. At  $\varepsilon_v = \varepsilon_P$ ,  $P = 0$ , the connectivity of the cracks is zero. With increasing dilatancy the cracks tend to a full connection,  $P \rightarrow 1$  as  $\varepsilon_v \rightarrow \infty$ . In fact, a sufficiently high connectivity of the cracks for a high and final permeability can develop at very small dilatancy, for instance,  $\Delta\varepsilon_D < 0.1\%$  as observed on the claystone in the tests. The final expression shows the relationship of fracturing-induced permeability to the minimum principle stress and dilatancy

$$K_g = K_o \exp(-r\sigma_3) \left( 1 - \exp\left(-\frac{\Delta\varepsilon_D}{\varepsilon_P}\right) \right) \quad (3.3)$$

The values of the parameters are estimated to be  $K_o = 3 \cdot 10^{-13} \text{ m}^2$  and  $\gamma = 1.9 \text{ MPa}^{-1}$ .

The model predictions for the permeability evolution at exceeding dilatancy are compared in Fig. 3.4 with the data obtained during fracturing at different lateral stresses. It is

evident that the fracturing-induced permeability with the spontaneous increase due to the formation of a continuous crack network and the subsequent considerable slowdown of this increase with further development of the network can be reasonably described by the model. However, more experiments are needed to confirm the parameters obtained here.

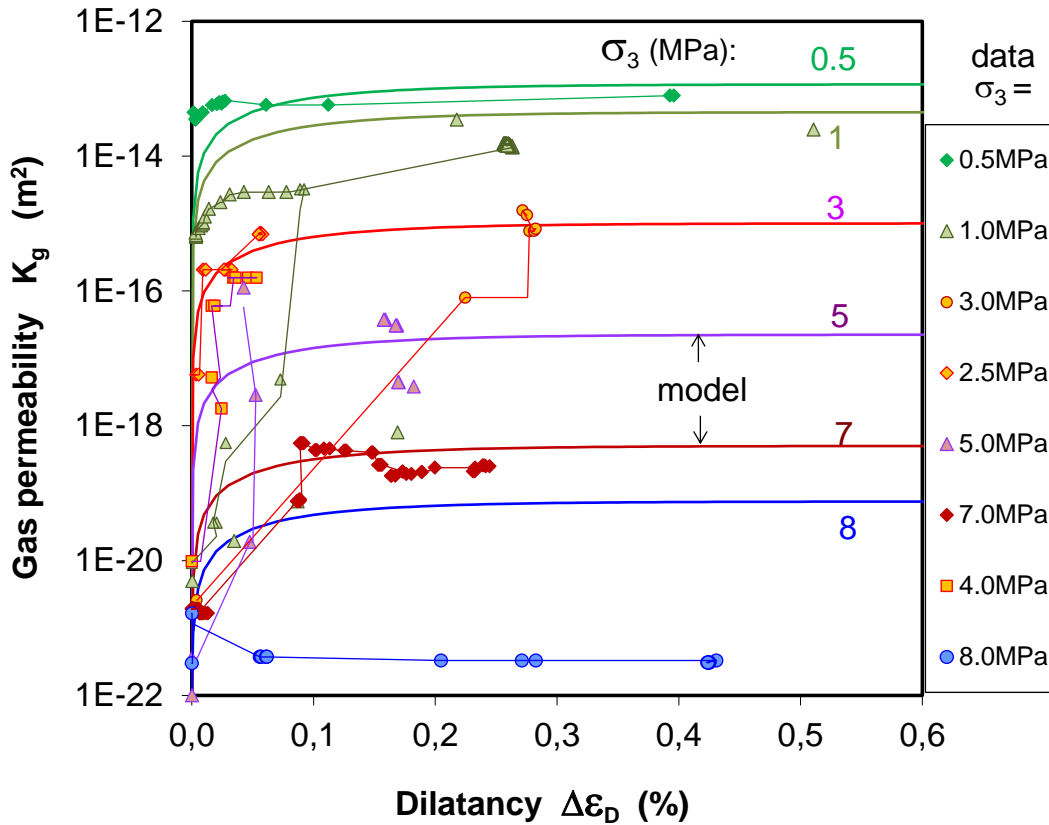
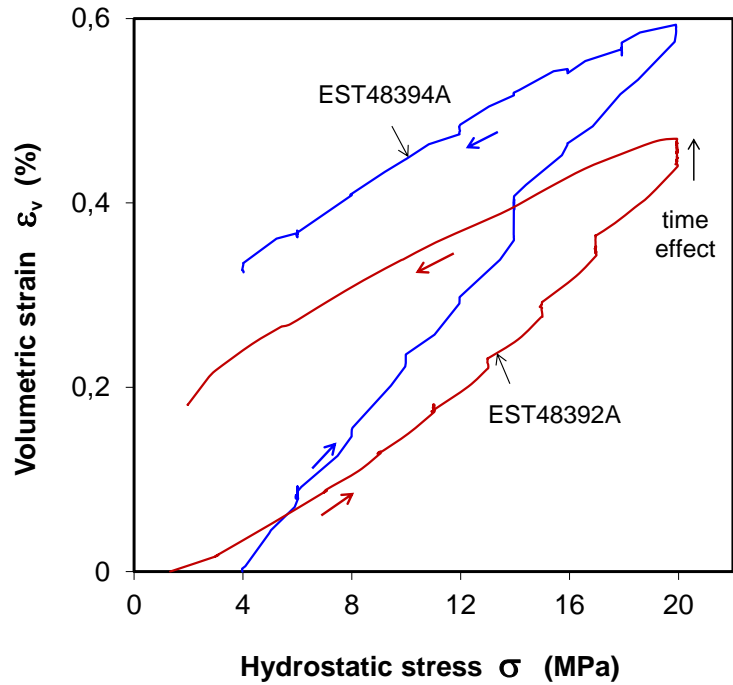


**Fig. 3.4** Prediction of the fracturing-induced permeability in the claystone using the percolation model

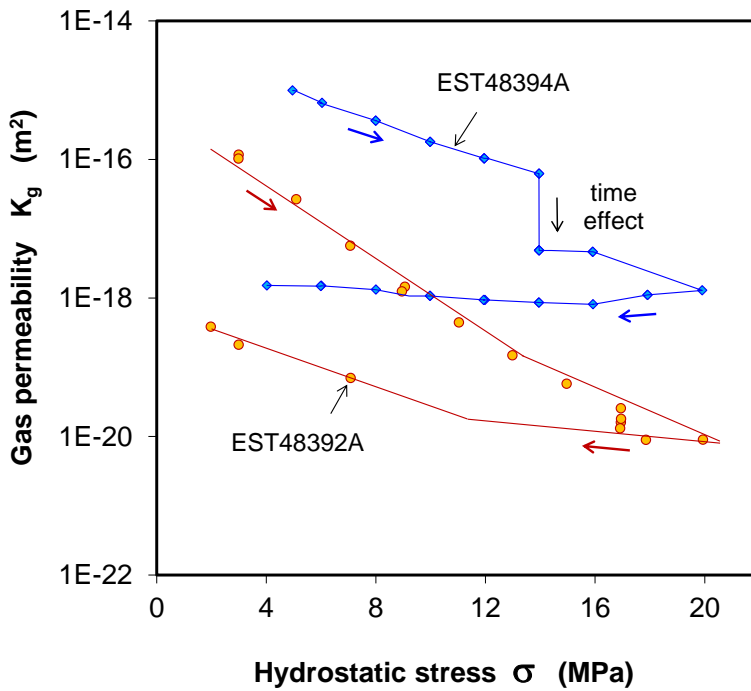
### 3.3 Fracture closure and permeability variation

The compaction behaviour of damaged claystone was investigated under hydrostatic and deviatoric load conditions and at constant water content. Fig. 3.5 shows results of the hydrostatic compaction on two fractured COX samples. It can be seen that a) the increase of hydrostatic stress closes up the fractures and hence decreases the fracture permeability; and b) the subsequent unloading leads to some elastic reopening of the fractures without significant reversibility of the permeability. It suggests that parts of the

fractures have been permanently closed and disconnected from the pathway. The quantitative differences are caused by different factors such as geometry, size, roughness, and connectivity of the cracks.

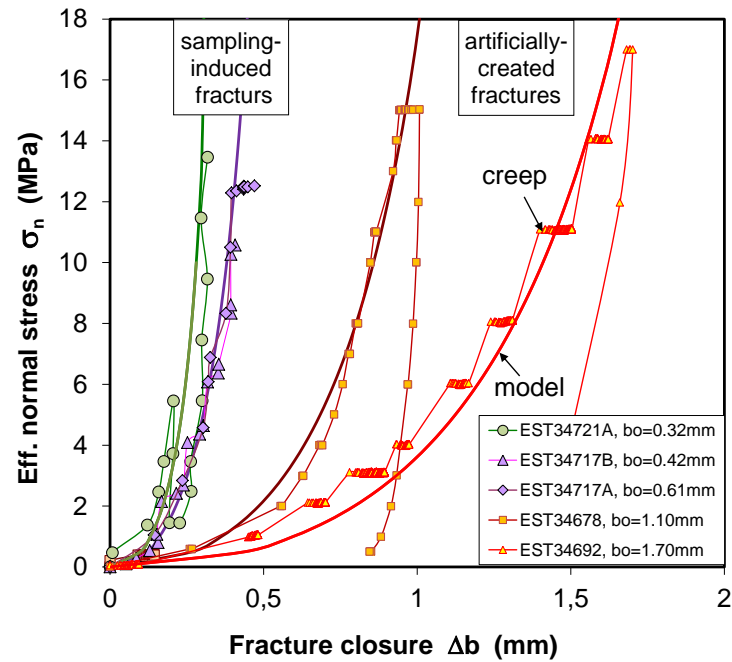


a) Volumetric compaction

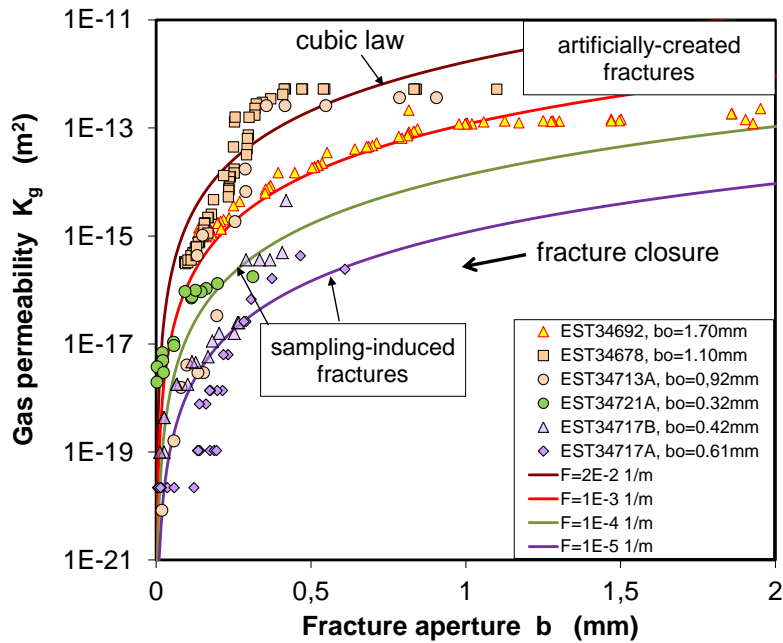


b) Permeability variation

**Fig. 3.5** Volume compaction (a) and permeability changes (b) of fractured COX claystone during hydrostatic loading and unloading



a) Fracture closure under normal stress



b) Fracture permeability-aperture relationship

**Fig. 3.6** Fracture closure as a function of normal stress (a) and permeability reduction with fracture closure (b)

Fig. 3.6 presents the other test examples in terms of fracture closure vs. normal stress and the corresponding permeability reduction. The fracture closure evolves faster at large apertures in the initial loading stage and then closure rate decreases with increasing stiffness at smaller apertures. Corresponding to the fracture closure, the gas permeability decreases significantly by 3 to 5 orders of magnitude, from the initial values of  $10^{-13} \text{ m}^2$  down to  $10^{-16} \text{ m}^2$  at large initial apertures (1.1 - 1.7 mm) and from  $10^{-15} \text{ m}^2$  down to  $10^{-18}$ - $10^{-20} \text{ m}^2$  at small initial apertures (0.3 - 0.6 mm).

The fracture closure can be approximated by an exponential equation of effective normal stress:

$$\Delta b = b_o \left( 1 - \exp(-\alpha \sigma_n^\beta) \right) \quad (3.4)$$

where  $\Delta b$  is the aperture closure,  $b_o$  the initial aperture equivalent to the maximum aperture closure,  $\sigma_n$  the effective normal stress,  $\alpha$  and  $\beta$  are constants. If the stress tends to infinity,  $\sigma_n \rightarrow \infty$ , the fractures will be fully closed,  $\Delta b \rightarrow 0$ . Fitting the data derives a unique set of the parameters  $\alpha = 0.3$  and  $\beta = 0.5$  for the fractured samples.

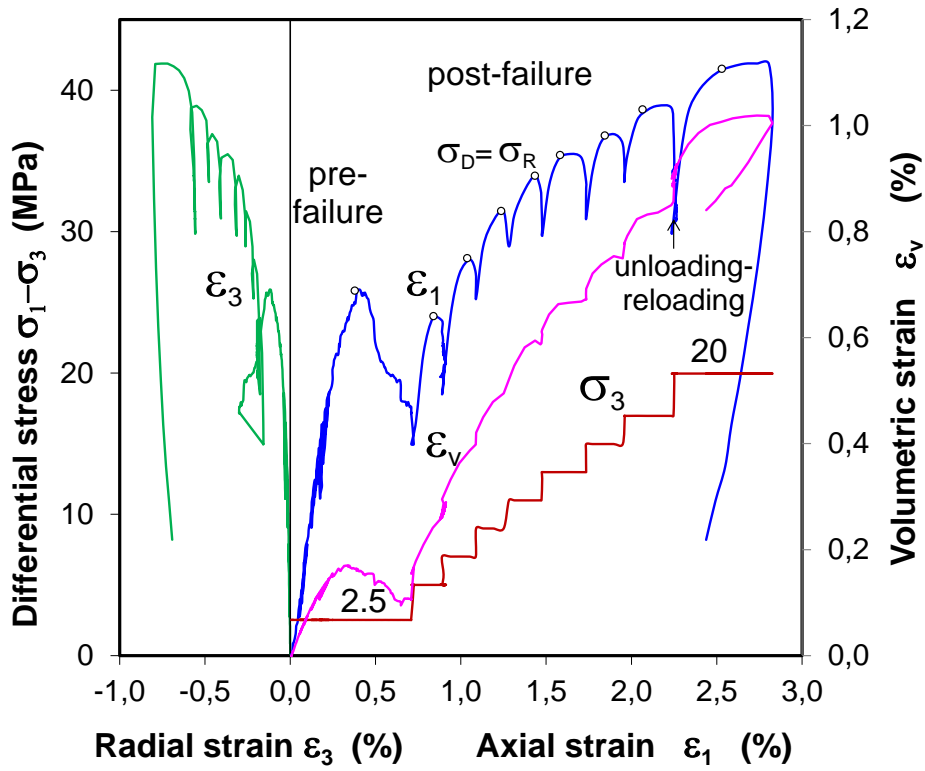
The permeability reduction with fracture closure can be described by the cubic law:

$$K_g = \frac{R}{12s} b^3 = \frac{F}{12} b^3 \quad (3.5)$$

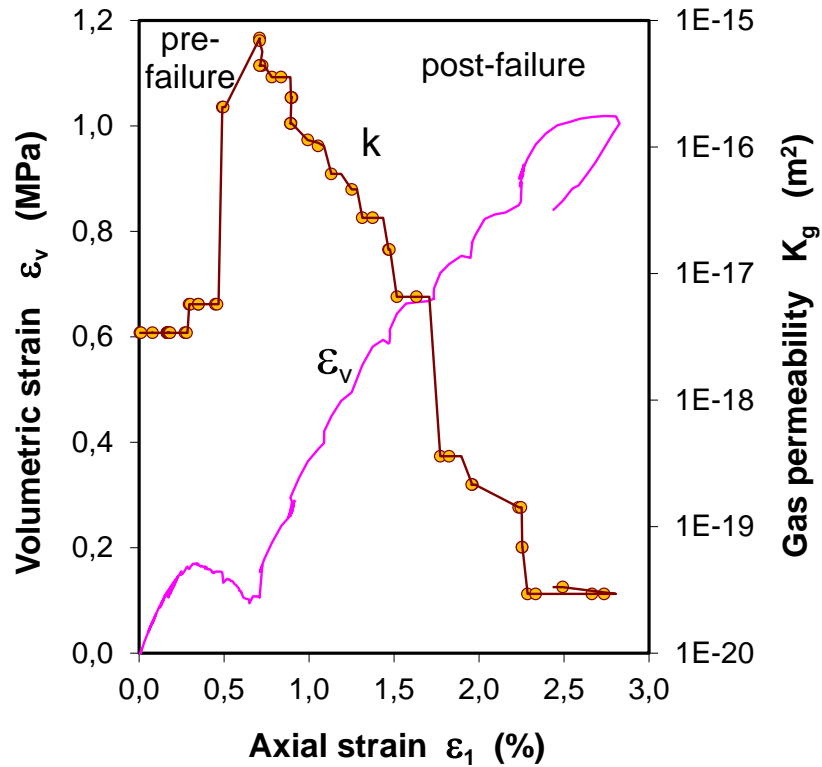
where  $b$  is the average fracture aperture ( $b = b_o - \Delta b$ ),  $s$  is the mean fracture spacing,  $R$  is the roughness factor of the fracture surfaces, and  $F$  is the  $R/s$  represents an integrated character of the set of fractures. As the fracture aperture  $b$  decreases to zero,  $K_g$  tends to zero. Fitting the data yields different  $F$ -values of  $1 \times 10^{-5}$  up to  $2 \times 10^{-2} \text{ m}^{-1}$  due to the different characteristics of the fractures in samples.

Supplementary to the hydrostatic recompaction, effects of deviatoric loading were also examined along multistep paths. Fig. 3.7 shows a typical example of the tests in terms of differential stress vs. axial and radial strain ( $\Delta\sigma - \varepsilon_1$ ;  $\Delta\sigma - \varepsilon_3$ ), and volumetric strain and permeability vs. axial strain ( $\varepsilon_v - \varepsilon_1$ ;  $k - \varepsilon_1$ ). The stress-strain curves show that a) the post-failure behaviour at each elevated lateral stress is quite similar to the behaviour under pre-failure conditions, i.e. non-linear axial compression, radial extension and volume compaction until the onset of dilatancy at  $\sigma_D$ ; b) then the stress does not increase much

because further deformation is dominated by plastic sliding of the fractures; c) the main-  
 taining dilatancy stress  $\sigma_D$  represents the maximum residual stress-bearing capacity  $\sigma_R$   
 of the fractured claystone; d) the residual strength increases with increasing lateral stress  
 $\sigma_3$ .



a) Stress-strain curves



b) Permeability in correlation to volumetric change

**Fig. 3.7** Stress-strain-permeability behaviour of fractured claystone during multistep deviatoric loading (a-b)

The residual strength of the damaged claystone is non-linearly related to the minor principle stress (Fig. 3.8). This can reasonably be described by the Hoek-Brown criterion (Eq. 3.1). Because of the different intensities of damage in the samples, the residual strength varies within a relatively large bandwidth. The boundaries of the scattered data can be defined by the respective parameters:  $\sigma_c = 7$  MPa and  $m = 5$  for the lower boundary;  $\sigma_c = 11$  MPa and  $m = 9$  for the upper one;  $\sigma_c = 9$  MPa and  $m = 7$  for the mean curve; and  $s = 0$  for all of them. The lower boundary shall be applied for the residual strength of the heavily damaged clay rock near drift walls, while the upper one for the less damaged rock mass in the far-field.

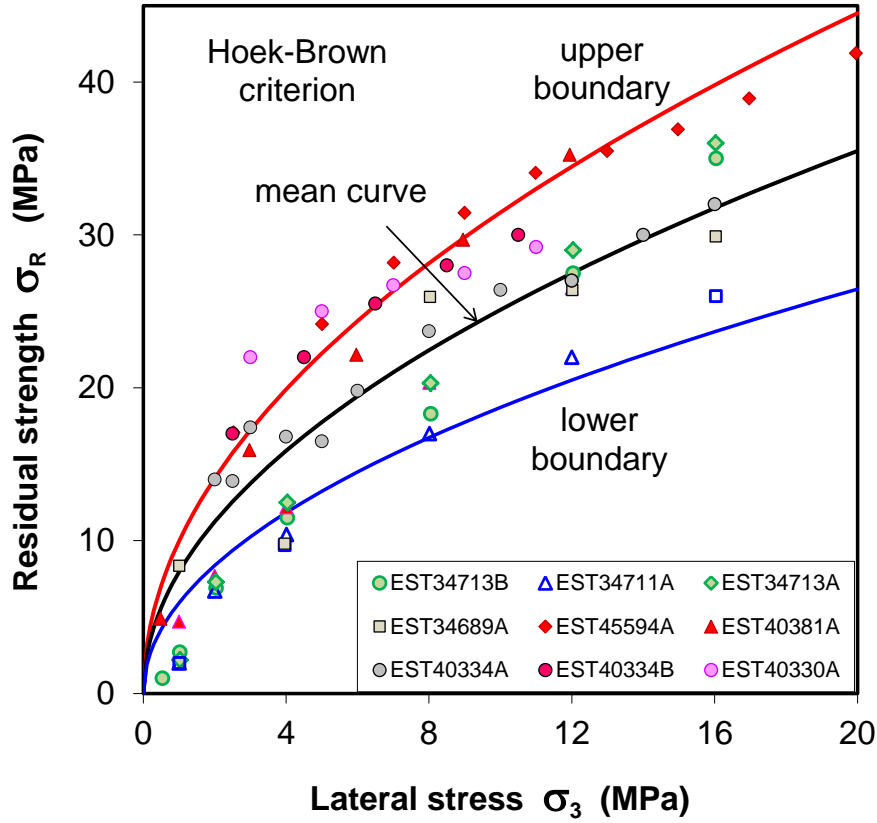


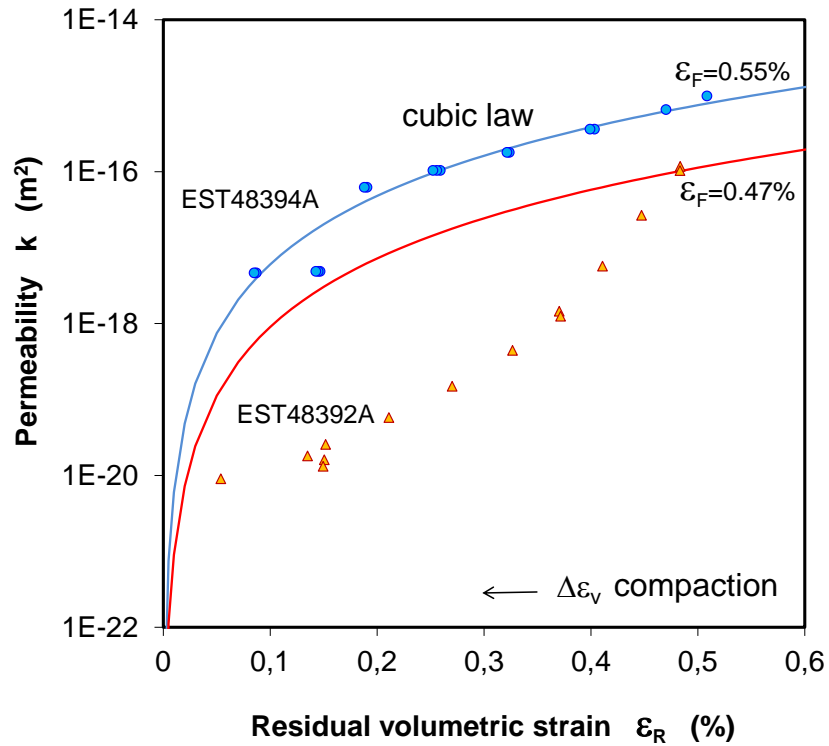
**Fig. 3.8** Residual strength of fractured COX claystone as a function of minor confining stress

In correspondence with the closure of fractures or the volume compaction before onset of dilatancy at each lateral stress, the permeability decreases. Dilation with further deviatoric loading does not raise the permeability significantly. This behaviour is different from the spontaneous permeability increase observed in the intact claystone (cf. Fig. 3.1). The permeability in fractured claystone is largely determined by the amplitude and distribution of the apertures and surface roughness of the interconnected fractures along the flow path. It can also be approximated by the cubic law in terms of permeability  $K_g$  as a function of volumetric strain  $\varepsilon_v$

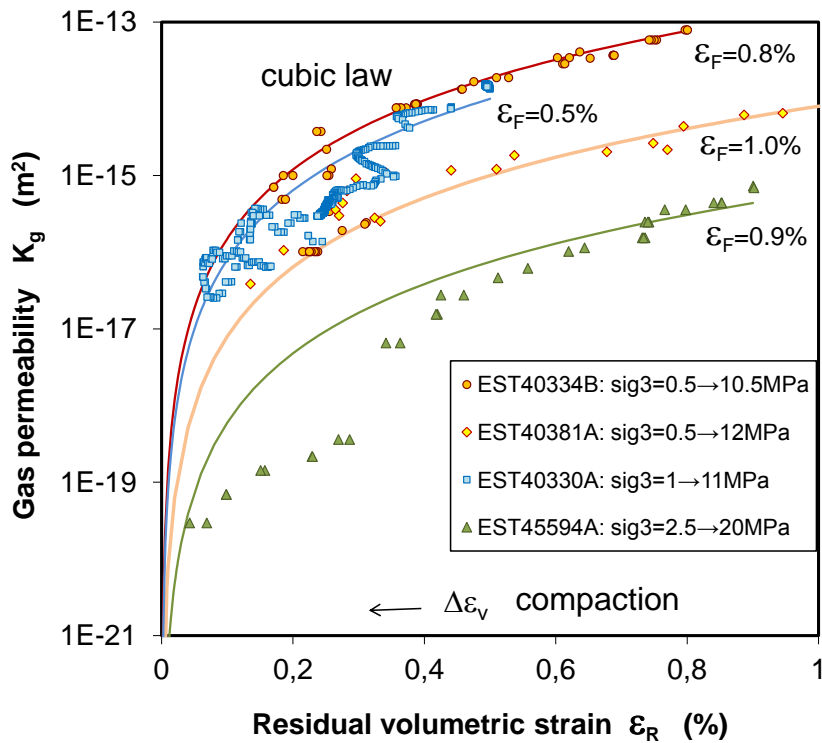
$$K_g = D(\varepsilon_R)^3 = D|\varepsilon_F - \varepsilon_v|^3 \quad (3.6)$$

where  $\varepsilon_F$  is the maximum dilatancy reached after sufficient fracturing,  $\varepsilon_R = |\varepsilon_F - \varepsilon_v|$  represents the residual voids in the fractures, and  $D$  is a parameter characterising the rock state after fracturing,  $D = K_f/(\varepsilon_F)^3$ . As the residual fracture void tends to zero,  $\varepsilon_R \rightarrow 0$ ,

the fracture permeability disappears. Fig. 3.9 shows a comparison of the predicted permeability based on the cubic law and the measured permeability as a function of the residual volumetric strain during the hydrostatic compaction and multistep deviatoric compression. The parameter  $D$  is derived from the measured  $\varepsilon_f$  and  $K_f$  data to lie in a range of  $7 \cdot 10^{-10} \text{ m}^2$  to  $1 \cdot 10^{-7} \text{ m}^2$ . A satisfactory agreement between the model and the data can be stated for the compaction phases during the deviatoric loading.



a) Hydrostatic compaction



b) Deviatoric compression

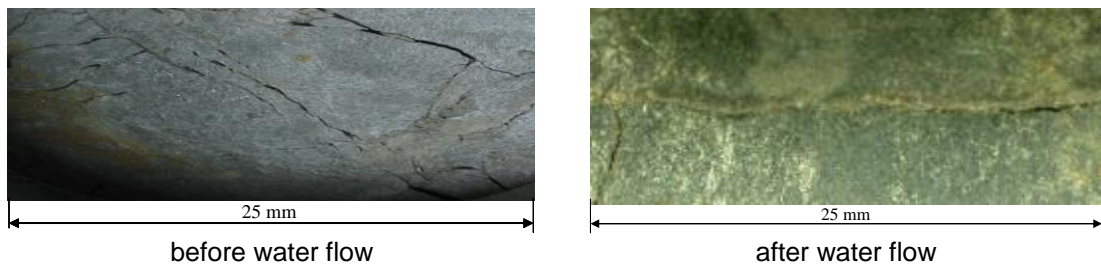
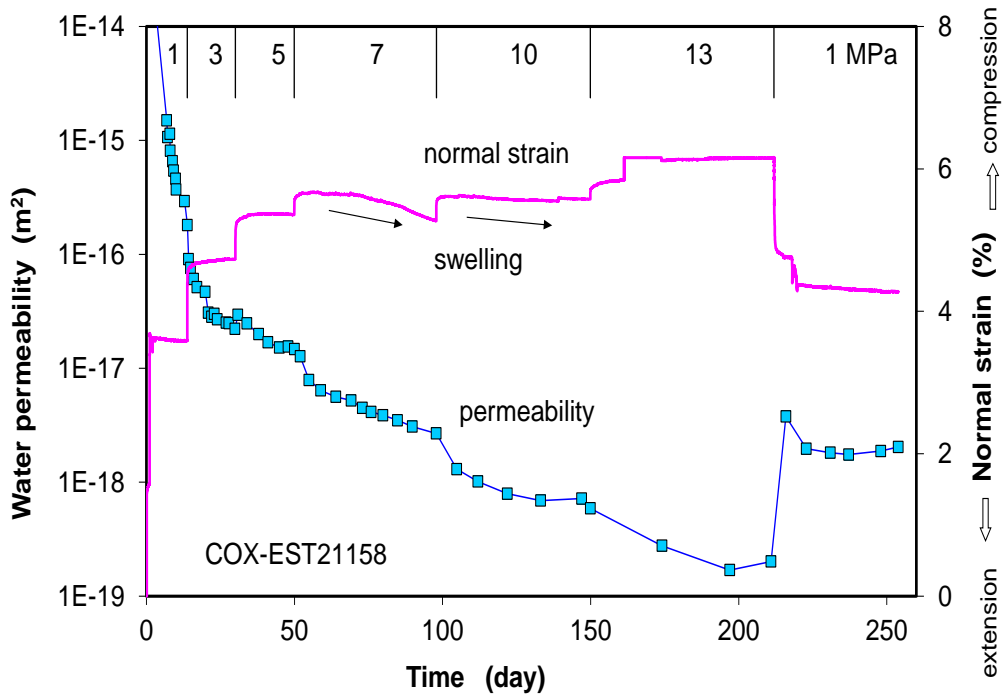
**Fig. 3.9** Variation in permeability of fractured claystone with volume compaction during hydrostatic loading (a) and multistep deviatoric loading (b)

### 3.4 Water conductivity of fractured claystone

As water enters and flows through fractures in claystone, the clay matrix can take up water and expand into the interstices. The water-induced swelling, weakening and slaking of the claystone leads to sealing of the fractures. Consequently, the hydraulic conductivity of the fractured claystone decreases.

Fig. 3.10 illustrates the combined impact of compression and water flow on the sealing of fractures. The recorded radial strain normal to the fracture planes shows that each load increase causes an immediate closure of the fractures. Because of the high swelling capability of the claystone, the fractured claystone expands rather than compacts followed at loads up to 10 MPa. The externally observed expansion indicates high local swelling pressures acting in contacting areas between fracture walls, where the deforming material must expand more into the stress-free fracture voids than elsewhere. Additionally, the clay matrix near the fracture walls contacting with water becomes weakening, slaking and filling the voids. The sealing of the fractures leads to a decrease in

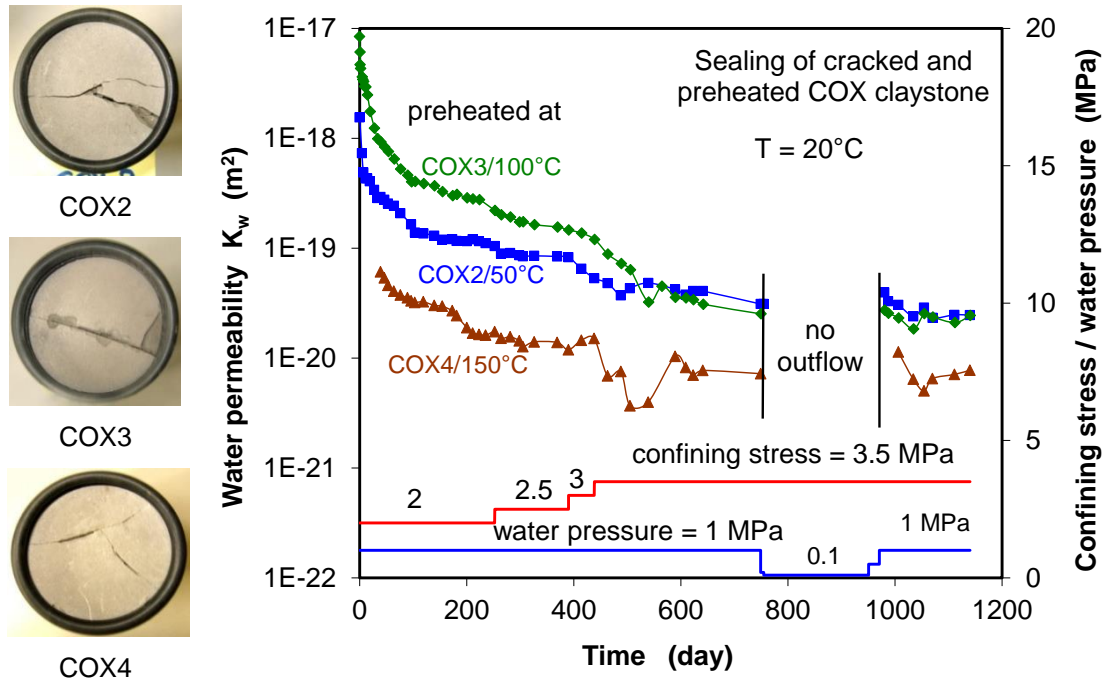
permeability. After stepwise increasing the load to 13 MPa over seven months, a very low water permeability of  $2 \cdot 10^{-19} \text{ m}^2$  was reached, which is close to that of  $10^{-20}$ – $10^{-21} \text{ m}^2$  for the undisturbed claystone. The permanent sealing of fractures by swelling and slaking of clay matrix is clearly visible on the pictures. The fractures with sharp wall edges disappeared due to the water-enhanced weakening effects.



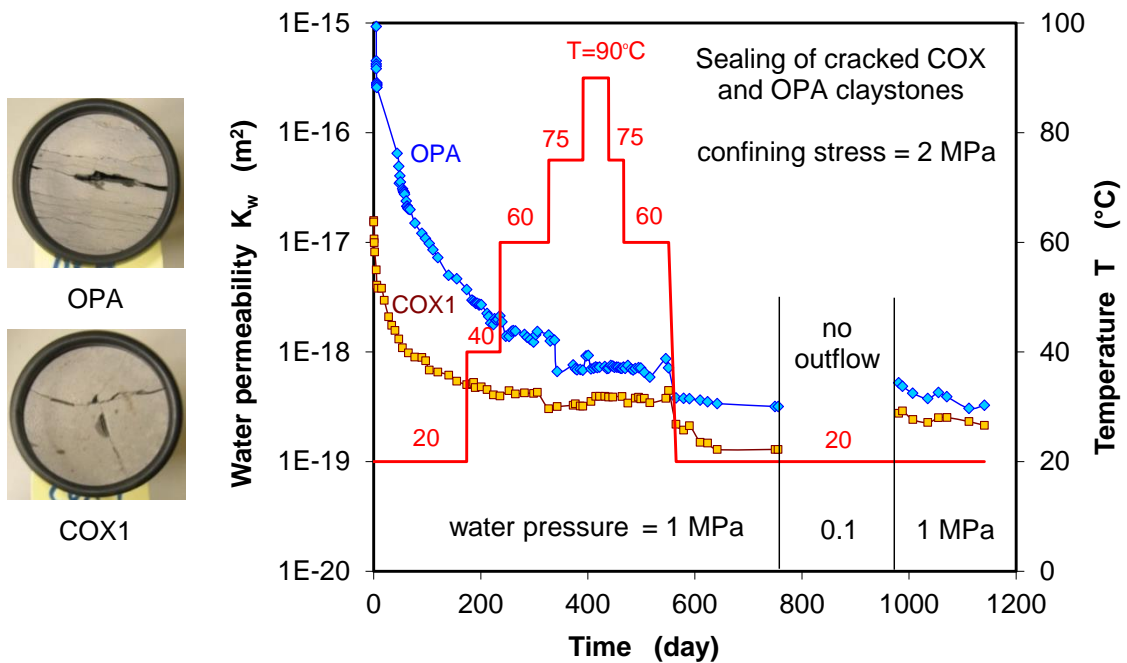
**Fig. 3.10** Sealing of fractures in COX claystone under various confining stresses

Fig. 3.11 shows the long-term evolution of water permeability obtained on fractured COX and OPA claystones under low confining stresses of 2 - 3.5 MPa and temperatures of 20 - 90 °C. They were flowed with synthetic porewater through over more than 3 years. As soon as the water was supplied, the high initial gas permeability of  $3 \cdot 10^{-12} \text{ m}^2$  dropped immediately by five to seven orders of magnitude down to  $10^{-17}$  –  $10^{-19} \text{ m}^2$ , depending on the fracture intensity of each sample. At each load level, the permeability decreased gradually with time. The influence of the confining stress on the permeability variation

was not significant in the testing range. Interesting is that the pre-heating up to 150 °C did not hinder the sealing process of the fractures in the claystone.



a) Evolution of water permeability under increased confining stress



b) Evolution of water permeability during a heating/cooling cycle

**Fig. 3.11** Long-term evolution of water permeability obtained on fractured claystones under confining stresses of 2 to 3.5 MPa and temperatures of 20 °C to 90 °C (a-b)

During the heating/cooling cycle and water flow, the permeability decreased with time down to a very low level of  $10^{-19} \text{ m}^2$ . It is evident that the self-sealing of fractures is not affected by the applied thermal load. The final permeability values after 3 years are very low at  $3 \cdot 10^{-20} - 7 \cdot 10^{-21} \text{ m}^2$ , being the same order of magnitude as that of the intact clay rock.

As observed in the tests, the water permeability decreases with the effective confining stress ( $\sigma_{eff} = \sigma - p_w$ ). The permeability values obtained at the end of each stress stage are summarized in Fig. 3.12 as a function of confining stress. The  $\log(K_w) - \sigma_{eff}$  dataset for each sample can be approximated by an exponential equation

$$K_w = K_{wo} \exp(-\beta \cdot \sigma_{eff}) \quad (3.7)$$

where  $K_{wo}$  is the initial water permeability at zero confining stress  $\sigma_{eff} = 0$  and  $\beta$  is a parameter characterising the compressibility of the water pathways. While  $K_{wo}$ -values are estimated in the range of  $2 \times 10^{-16}$  to  $4 \times 10^{-20} \text{ m}^2$  depending on the fracture features of each sample, a unique  $\beta$ -value of  $0.6 \text{ MPa}^{-1}$  is obtained for all tested samples.

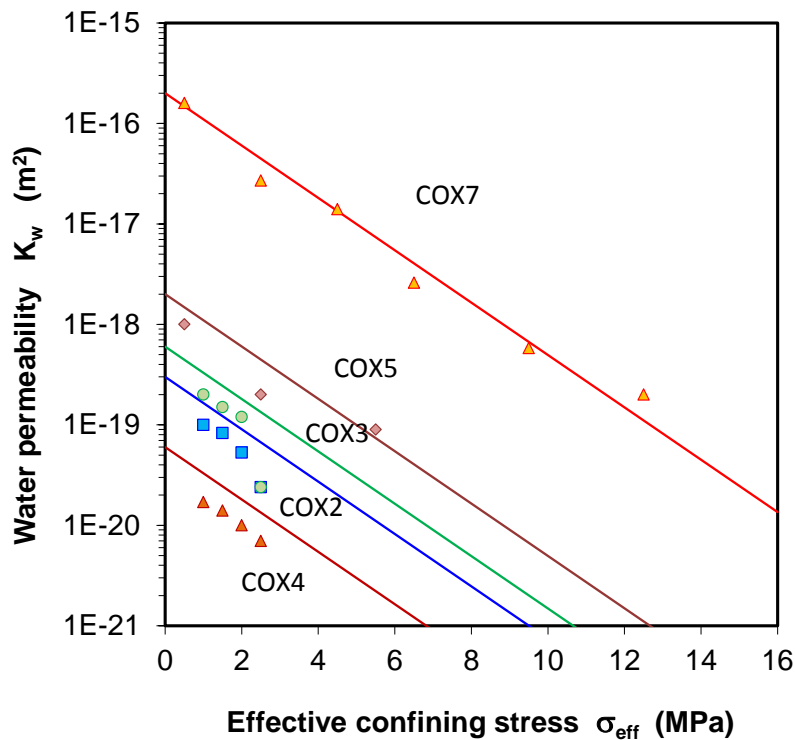


**Fig. 3.12** Dependence of stabilized water permeability of fractured claystone on effective confining stress

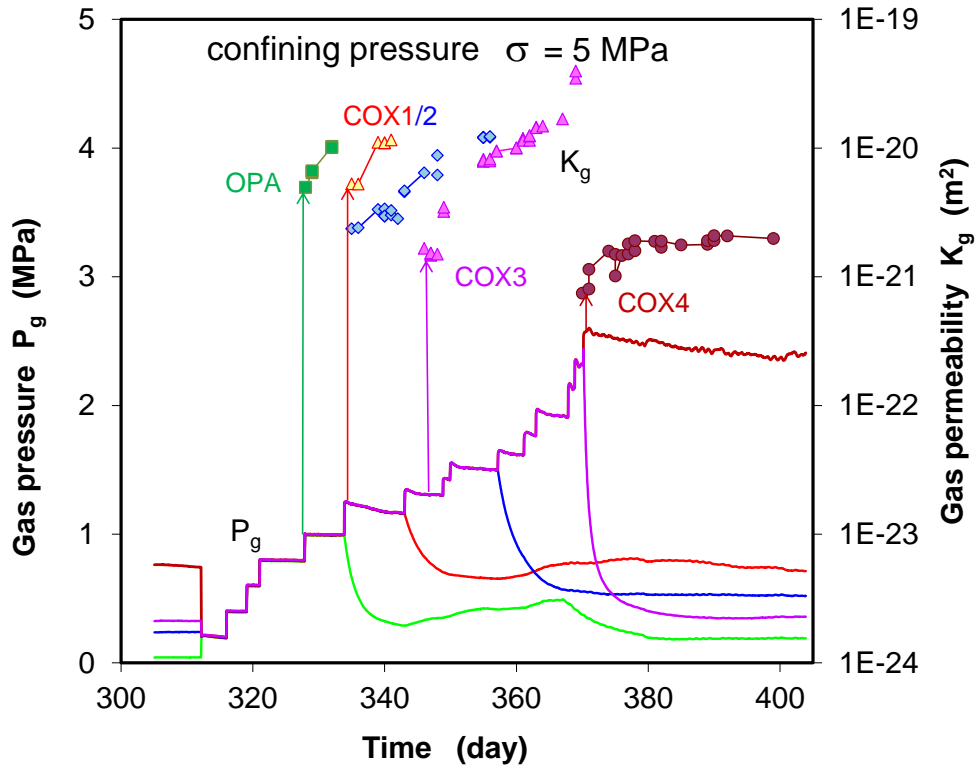
### 3.5 Gas migration in water-saturated and resealed claystone

The highly-consolidated and water-saturated clay rocks are practically impermeable for advective transport of gas under normally-encountered pressure gradients. However, the EDZ may act as conduits for preferential gas flow, depending on the resealed state. Particularly after water saturation, gas entry into the resealed fractures needs driving forces to overcome the capillary thresholds and to generate migration pathways.

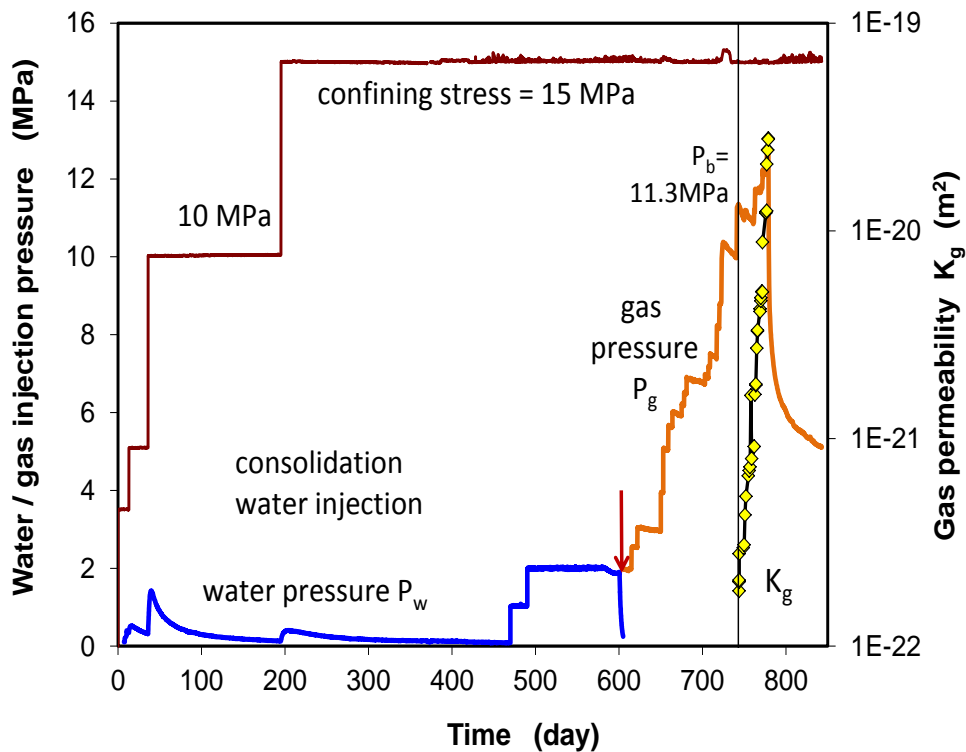
Fig. 3.13 presents the measured gas breakthrough pressures of the highly-resealed COX and OPA samples with very low water permeabilities of  $10^{-19} - 10^{-21} \text{ m}^2$  (cf. Fig. 3.9). It can be seen that gas entry and penetration into the water-saturated and highly-resealed claystones needs high gas pressures to overcome the capillary thresholds, which are determined by the sealing intensity of the fractures under confining stress.

The advective gas flow through resealed claystone is accompanied by micro-fissuring and dilation of the generated fissures. Fig. 3.14 shows an example of the gas pressure impact. During the first stage with stepwise gas pressure increase from 2 to 4 MPa, compressive strains evolved progressively in all directions and no gas outflow was detectable. The subsequent pressure increase to 4.5 MPa inhibited the continuation of the radial compression. Further pressure increase to 5 – 7 MPa led to a slightly gradual dilatancy in radial direction, indicating a progressive gas penetration into some fissures (probably along the resealed fractures). As the gas pressure was increased up to 8.3 MPa, a sudden dilatancy in all directions took place and gas outflow could be detected, suggesting the gas breakthrough.

As shown above, the gas breakthrough pressures observed are below the minor confining stress and thus below the fracturing criterion as shown in Fig. 3.15. This important finding implies that the EDZ, even when highly-resealed, will still have the capacity for gas migration with moderate pressures and thus contribute to avoid high pressure building up, so that the host rock is prevented from gas fracturing.



a) Gas breakthrough pressure and permeability at confining stress of 5 MPa



b) Gas breakthrough pressure and permeability at confining stress of 15 MPa

**Fig. 3.13** Gas breakthrough pressures measured on highly-resealed claystones under different confining stresses (a-b)

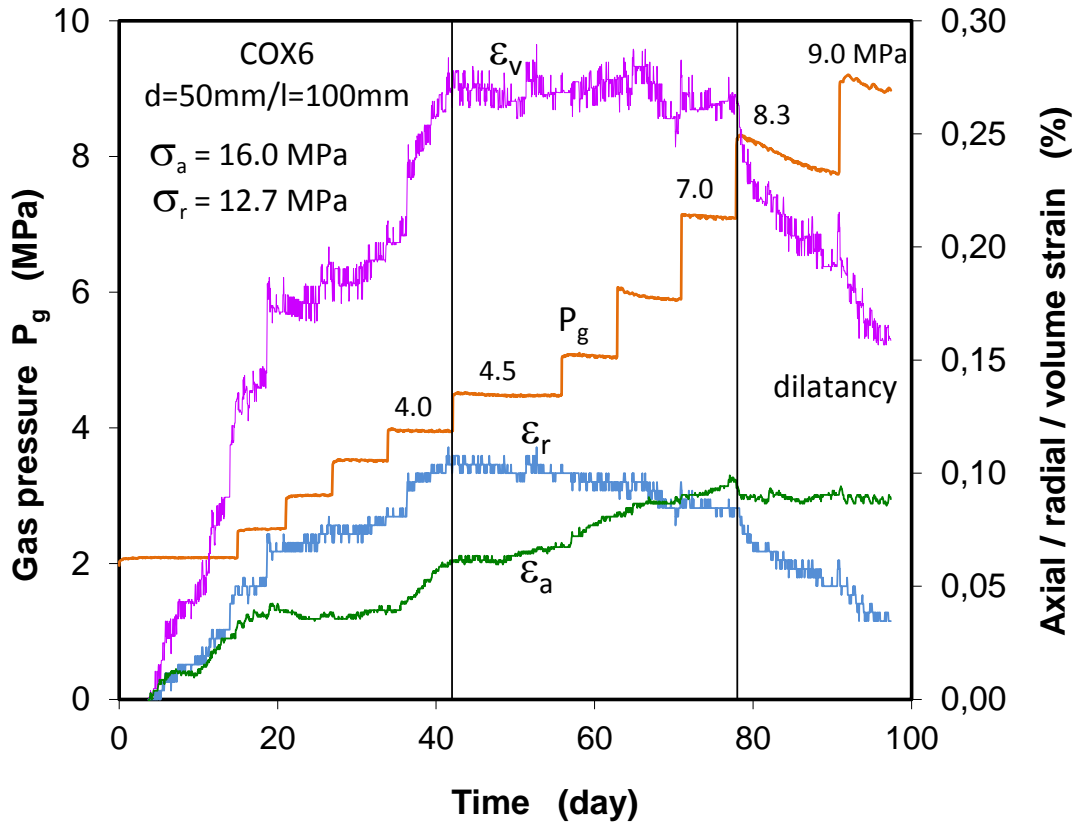


**Fig. 3.14** Gas pressure induced dilatancy in a highly-resealed claystone sample under triaxial compression

The gas breakthrough pressure of water-saturated and resealed claystone can be expressed as function of water permeability and minimum confining stress

$$P_b = B \cdot (K_{wo})^{-1/n} \cdot \exp(-\gamma \sigma_{min}) \quad (3.8)$$

where  $P_b$  is the gas breakthrough pressure,  $K_{wo}$  is the initial water permeability at zero minor principal stress  $\sigma_{min} = 0$ ,  $B$ ,  $n$  and  $\gamma$  are parameters. For the resealed claystone with  $K_{wo} = 5 \times 10^{-19}$  to  $5 \times 10^{-20}$  m<sup>2</sup> and for the intact claystone with  $K_{wo} = 1 \times 10^{-20}$  m<sup>2</sup>, the parameters are estimated to be  $B = 2 \times 10^{-7}$  MPa·m<sup>2/3</sup>,  $n = 3$  and  $\gamma = 0.2$  MPa<sup>-1</sup>. The model prediction provides a reasonable agreement with the data (Fig. 3.15).

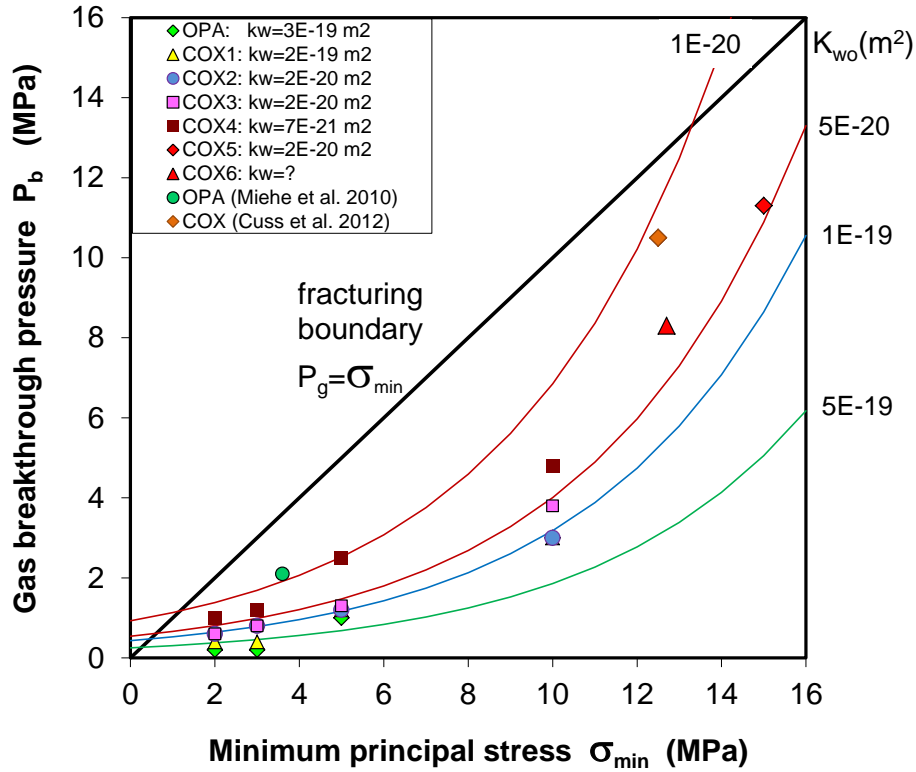


**Fig. 3.15** Gas breakthrough pressure of highly-resealed claystones in comparison with a conservative fracturing criterion without considering tensile strength

Further gas pressure rising can reopen more weakly resealed micro-fissures as well as dilate the gas-occupied pathways. The growth of the micro-fissure networks allows gas to flow easier, so that the effective gas permeability increases as shown in Fig. 3.16. The drastic increase in gas permeability with increasing pressure represents a typical percolation process of crack initiation, growth and coalescence. The permeability increase can be related to the minimum effective confining stress  $\sigma'_{min}$

$$K_g = K_{go} \cdot \exp[-\mu\sigma'_{min}] \quad (3.9)$$

where  $\sigma'_{min} = \sigma_{min} - (P_g + P_o)/2$ ,  $K_{go}$  is the gas permeability at  $\sigma'_{min} = 0$ , and  $\mu$  is a parameter characterising the dilatibility and interconnectivity of the gas pathways. Fitting the data yields varying  $K_{go}$  values of  $1 \times 10^{-10}$  up to  $3 \times 10^{-7}$  m<sup>2</sup> for the studied sample but a unique value of  $\mu = 3.5$  MPa<sup>-1</sup> for all samples except for COX4. Fig. 3.17 compares the model with the data and shows a good agreement between them.

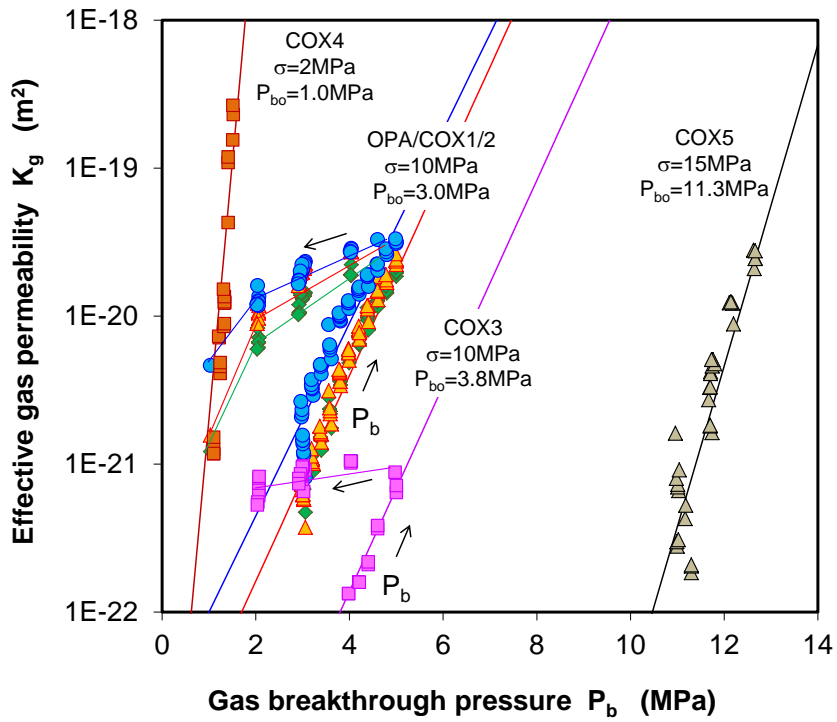


Fig. 3.16 Dependence of gas permeability on gas pressure after breakthrough

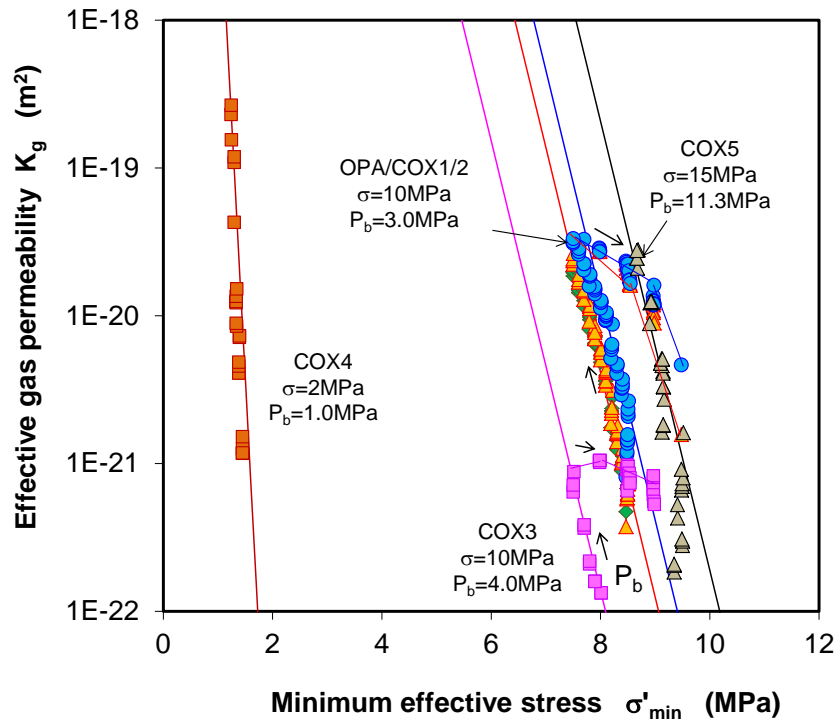


Fig. 3.17 Dependence of gas permeability on effective minimum stress after breakthrough

### 3.6 Conclusions on the sealing of fractured claystone

The studied COX and OPA claystones behave elasto-plastically with an overall volume compaction until the onset of dilatancy at a high stress. Closely as the peak stress is reached, microcracks are created leading to a spontaneous increase in permeability and to failure. The damage and failure are suppressed under high confining stresses. The fracturing-induced permeability increases exponentially with increasing dilatancy and with decreasing minor principal stress. After failure, the claystone still possesses a certain residual strength and the increased permeability does not change much further. When the confining stress normal to the fracture planes increases again, the fractures tend to be closed and the fracture permeability reduces following the cubic law.

As water enters and flows through fractures, the clay matrix can take up a great amount of the water and expand into the interstices. The water-induced swelling, weakening and slaking of the claystone lead to sealing of the fractures. Consequently, the hydraulic conductivity decreases dramatically by several orders of magnitude down to very low levels of  $10^{-19}$  to  $10^{-21}$  m<sup>2</sup> even at low confining stresses of 2 - 4 MPa within short periods of months to years, compared with the long post-closure phase of tens of thousands of years. The very low water permeabilities reached are the same order as that of the intact claystones, indicating that the fractures in the claystones can be completely resealed.

Before water saturation, the fractures act as conduits for preferential gas flow. However, after water saturation, gas entry and penetration into the fractures needs certain driving forces to overcome the capillary thresholds. The gas entry/breakthrough pressure is determined by the sealing intensity of the fractures and the confining stress. It was observed that the gas breakthrough pressures in the water-saturated and highly-resealed claystones are still lower than the confining stresses. It implies that the EDZ, even when highly resealed, will still have the capacity for gas migration at moderate pressures without fracturing the host rock.

Generally speaking, the high sealing capacities of the claystones hinder water transport and thus radionuclides migration through the EDZ, but allow gas flow without over-pressurisation and fracturing the surrounding host rock. These significant advantages guarantee the long-term sealing functions of the plug/seal systems and hence the long-term safety of the repositories in the clay formations.



## 4 Sealing properties of clay-based materials

After backfilling and sealing a repository, the initially unsaturated clay-based backfill/seal materials will take up water from the saturated surrounding rock. The saturation causes swelling of clay minerals, sealing the pores and reducing the hydraulic conductivity of the backfill and seal. Depending on the density and the boundary confinement, swelling pressure will build up with increasing water saturation of the backfill/seal materials. In case of a drift seal that will be constructed after removing the drift support linings, the development of swelling pressure in the seal hinders extension of the surrounding EDZ. On the other side, the seal will be more consolidated under compression of the surrounding rock, which increases the stiffness and backpressure of the seal against the EDZ and hence enhances its sealing function of the seal system. The hydro-mechanical interactions between the seal and the EDZ/rock will continue until equilibrium is reached in the system. Another important issue is that gas generation from corrosion of metallic components may result in high gas pressures in the repository. If the minor principal stress in the surround rock is exceeded, high gas pressures can create fractures in the rock and thus damage the integrity of the geological and engineered barrier system. These dynamic repository conditions must be taken into account for design of seals in boreholes, drifts and shafts. First of all, adequate seal materials are to be identified with respect to the safety relevant properties such as:

- sufficiently high density to ensure the other required attributes;
- certain mechanical stiffness to guarantee the stability of the seal system;
- sufficiently high swelling capacity to seal gaps between the seal and the drift wall and to support the EDZ against further damage propagation and enhance its sealing process;
- sufficiently low hydraulic conductivity to limit or avoid advective water transport and to retard migration of radionuclides;
- low gas entry/breakthrough pressures to allow gas release without damaging the integrity of the geological and engineered barrier system;
- chemical-mineralogical compatibility with the host rock to keep the long-term stability of the seal system;
- adequate thermal conductivity of the seal/buffer close to HLW to transfer heat and thus avoid high temperatures as well as thermal impact on the sealing functions.

In most of the drift and shaft sealing concepts, bentonite and bentonite-sand mixtures are taken into account as seal material and widely investigated during last decades. Moreover, as alternative to the bentonite-based materials, crushed claystone and mixture with bentonite was also investigated by GRS during the last years /ZHA 10a/13a/14c/d/. The preliminary results showed favourable sealing properties and behaviour of the compacted claystone-bentonite mixture. In order to enhance the confidence in its suitability for sealing repositories, further investigations on the claystone-bentonite mixture were continued in the framework of the EC DOPAS project by determination of the above-mentioned sealing properties and by comparison with the bentonite and bentonite-sand mixture.

#### **4.1 Characteristics of investigated seal materials**

Crushed COX claystone produced by the drift excavation in the MHM-URL was used in the experiments. The originally water-saturated claystone with a water content of ~ 7.4 % was somewhat desaturated to a residual water content of about 4.2 % due to exposure to air. Two sets of grain sizes with diameters smaller than 10 mm and 5 mm were selected for testing. The testing materials were prepared by sieving the grains through the corresponding sieves. On an average, the COX claystone contains 25 - 55 % clay minerals, 20 - 38 % carbonates, 20 - 30 % quartz, and small amounts of others /AND 05/.

Expansive Na-bentonite MX80 from Wyoming in the USA was prepared to two grain size distributions of  $d < 0.5$  mm and  $d < 2$  mm. The bentonite contains 75 % montmorillonite, 15 % quartz and 10 % other minerals /KAR 08/. The delivered bentonite was relatively dry with a water content of 9.6 %. The bentonite was mixed with crushed claystone mainly in two ratios of COX/MX80 = 60/40 and 80/20. In comparison, the bentonite-sand mixture with a mixing ratio of MX80/Sand = 70/30, which had been used by ANDRA in the borehole sealing experiment PGZ /DEL 13/, was tested too. Quartz sand with grains smaller than 2 mm was used for the bentonite-sand mixture.

Fig. 4.1 shows the grain size distributions and pictures of the testing materials and mixtures. The dry grain densities of the materials were measured to be  $\rho_s = 2.70$  g/cm<sup>3</sup> for COX claystone,  $\rho_s = 2.78$  g/cm<sup>3</sup> for MX80 bentonite, and  $\rho_s = 2.68$  g/cm<sup>3</sup> for the sand.

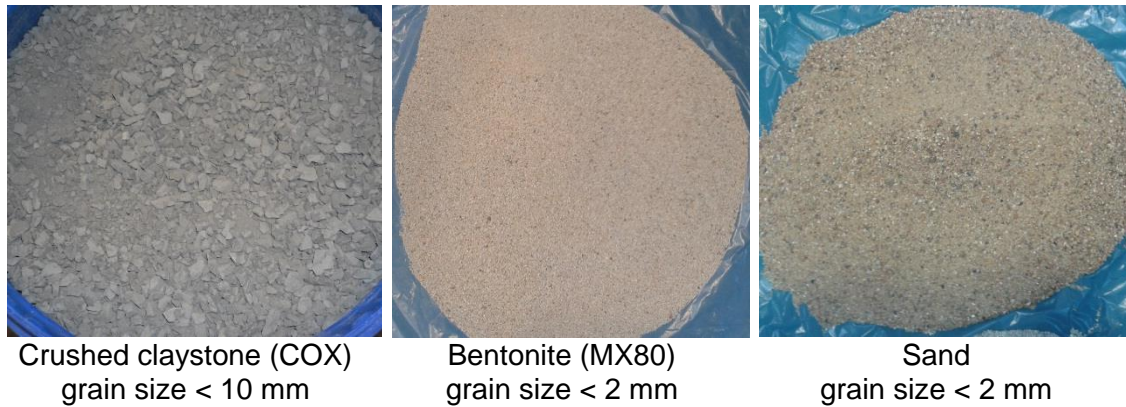
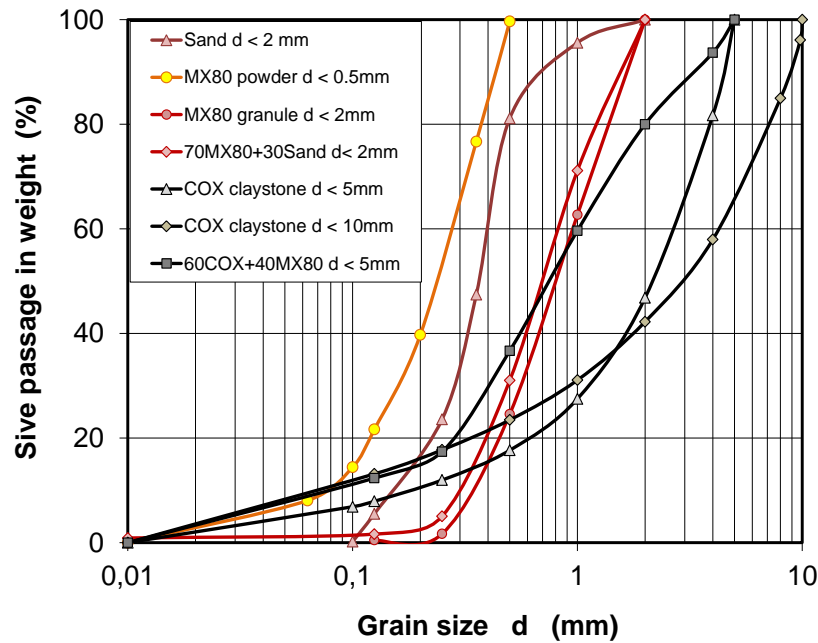


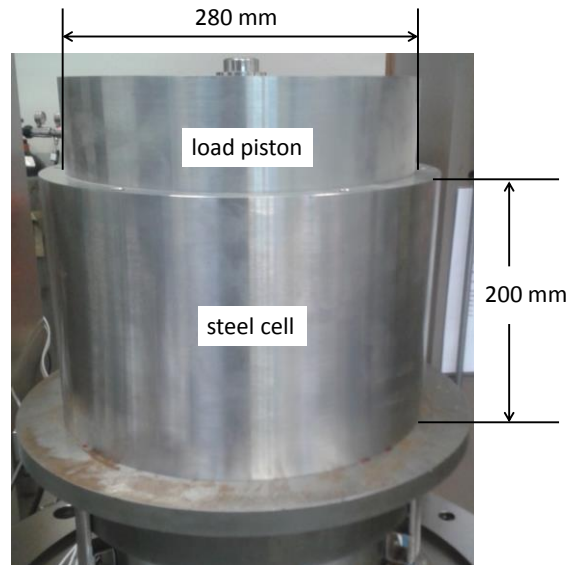
**Fig. 4.1** Grain size distributions of crushed claystone, bentonite, sand and mixtures

#### 4.2 Compressibility and compacted density

Drift seals are mostly designed to consist of compacted blocks of clay-based mixtures and bentonite pellets filling the remaining gaps between the blocks and the drift wall. The blocks must have sufficiently high densities to ensure the requirements on the sealing functions. The seal blocks are manufactured by compressing the loose mixtures in mould to the desired density. The compressibility of a seal mixture is essential for the achievement of the density and the requirement of compression energy. In our laboratory experiments, the claystone-bentonite and bentonite-sand mixtures were compacted in two oedometer cells with different sizes respectively: a normal cell with a diameter of 100 mm and 200 mm height and a large cell with a diameter of 280 mm and 200 mm height, as shown in Fig. 4.2.



a) Normal oedometer  
diameter = 100 mm; height = 200mm



b) Large oedometer  
diameter = 280mm; height = 200mm

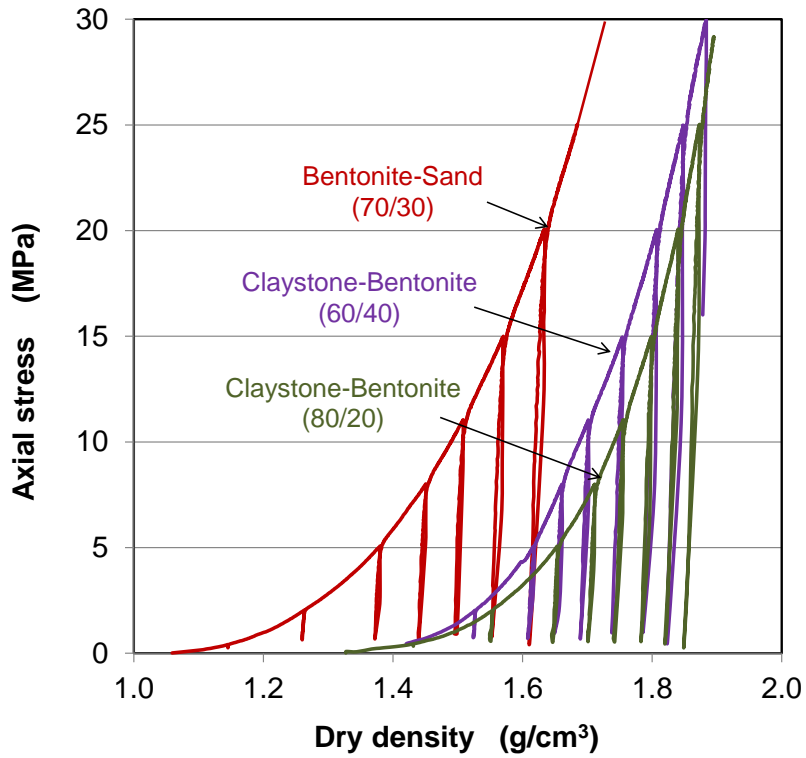
**Fig. 4.2** Normal (a) and large (b) oedometers used for compaction of seal materials

#### 4.2.1 Compaction in normal oedometer

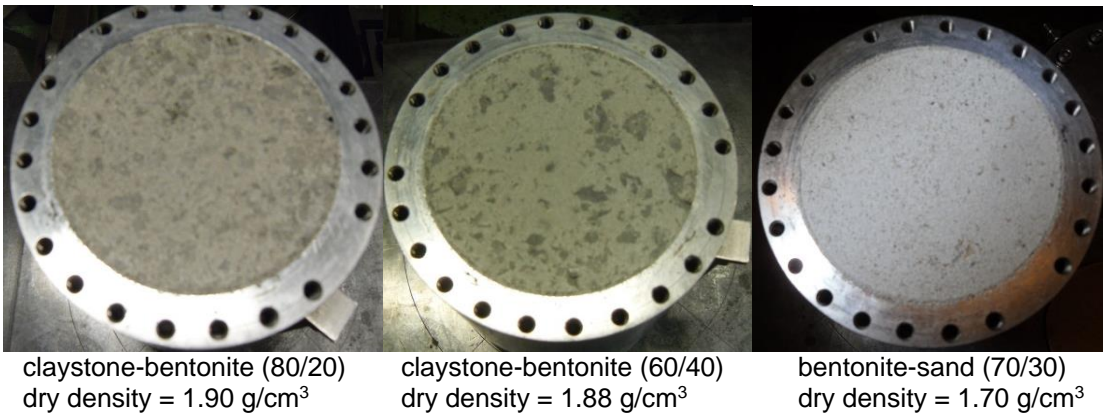
Three mixtures were compacted in the normal oedometer cell up to a maximum axial load of 30 MPa:

1. Bentonite-sand mixture in a ratio of MX80/Sand = 70/30 with grain sizes of  $d < 0.5$  mm for bentonite and  $d < 2$  mm for sand and with a water content  $w = 9.1$  %;
2. Claystone-bentonite mixture in a ratio of COX/MX80 = 80/20 with grain sizes of  $d < 5$  mm for crushed claystone and  $d < 0.5$  mm for bentonite and with a water content  $w = 6.0$  %;
3. Claystone-bentonite mixture in a ratio of COX/MX80 = 60/40 with grain sizes of  $d < 5$  mm for crushed claystone and  $d < 0.5$  mm for bentonite and with a water content  $w = 7.7$  %.

Fig. 4.3 illustrates the axial stress- compacted dry density curves and pictures of the compacted samples.



a) Compaction curves



b) Fotos of compacted samples

**Fig. 4.3** Compacted dry densities of the claystone-bentonite and bentonite-sand mixtures in normal oedometer (a-b)

One can find out from the compaction curves that:

- The initial dry densities of both loose-filled claystone-bentonite samples before loading are higher than that of the loose-filled bentonite-sand mixture, which is probably due to the favourable grain size distributions of both the claystone-bentonite mixtures;

- Consequently, the claystone-bentonite samples become denser at the applied maximal load of 30 MPa to the final dry densities of  $\rho_d = 1.90$  and  $1.88 \text{ g/cm}^3$  for the ratio of COX/MX80 = 80/20 and 60/40 respectively, compared to  $\rho_d = 1.70 \text{ g/cm}^3$  for the bentonite-sand mixture (MX80/Sand = 70/30);
- The coarse particles of the crushed claystone and sand are homogeneously embedded in the fine-grained bentonite.

The mechanical stiffness of the mixtures is determined by the measurement of elastic bulk modulus ( $K = \Delta\sigma / \Delta\varepsilon_v$ ) from each reloading path at different densities. The results obtained for the different mixtures are depicted in Fig. 4.4 as function of dry density. It is obvious that the mechanical stiffness of the materials exponentially increases with increasing density. At a given density, the stiffness of the claystone-bentonite mixtures is higher than that of the bentonite-sand mixture. The low stiffness of the bentonite-sand mixture is probably attributed to the relatively lower density of the bentonite matrix embedding the sand particles and thus the lower inner friction resistance.

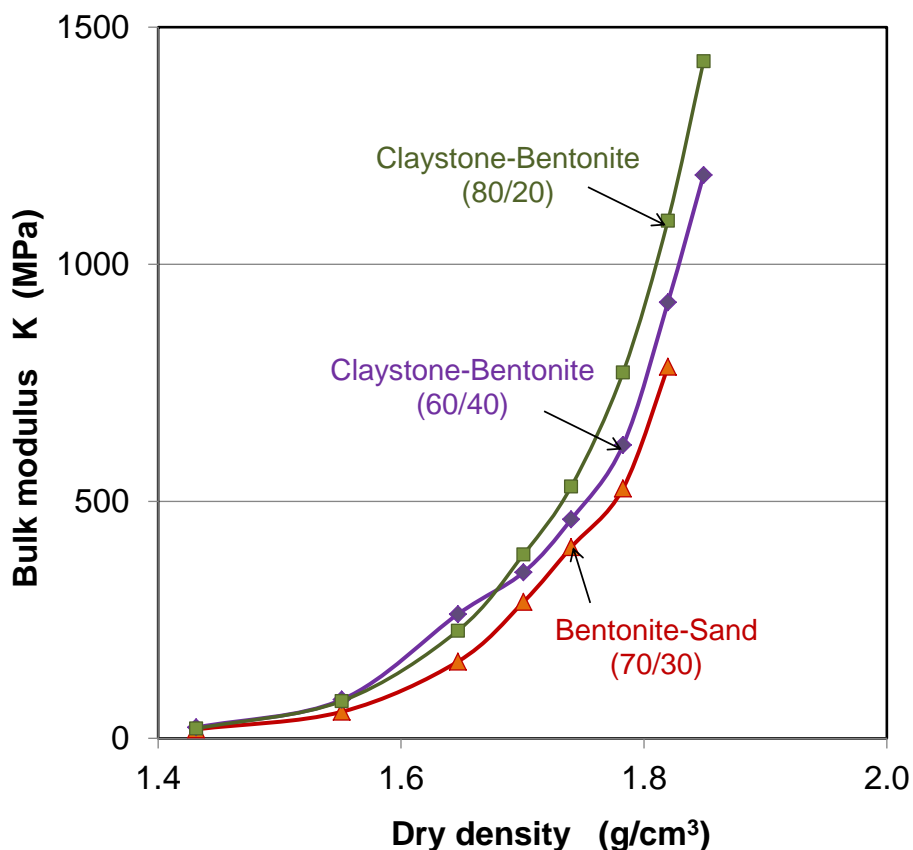


**Fig. 4.4** Elastic bulk modulus of the compacted claystone-bentonite and bentonite-sand mixtures as function of dry density

#### 4.2.2 Compaction in large oedometer

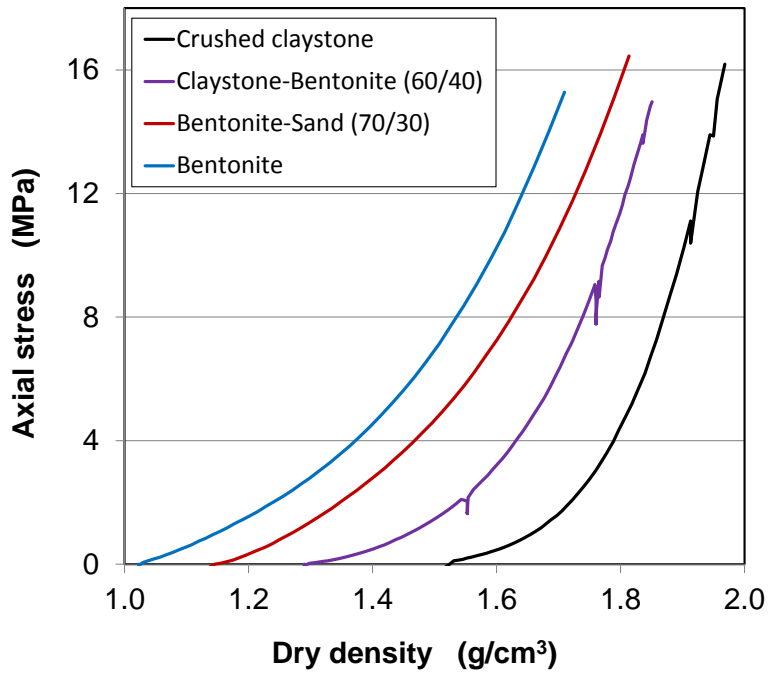
Four mixtures were compacted in the large oedometer cell:

- Crushed claystone with grains of  $d < 10$  mm and water content of  $w = 4.2$  %;
- Bentonite with grains of  $d < 2$  mm and water content of  $w = 13.0$  %;
- Bentonite-sand mixture (70/30) with grains of  $d < 2$  mm and water content of  $w = 9.1$  %.
- Claystone-bentonite mixture (60/40) with grains of  $d < 10$  mm for the crushed claystone and  $d < 2$  mm for the bentonite and with water content of  $w = 7.7$  %.

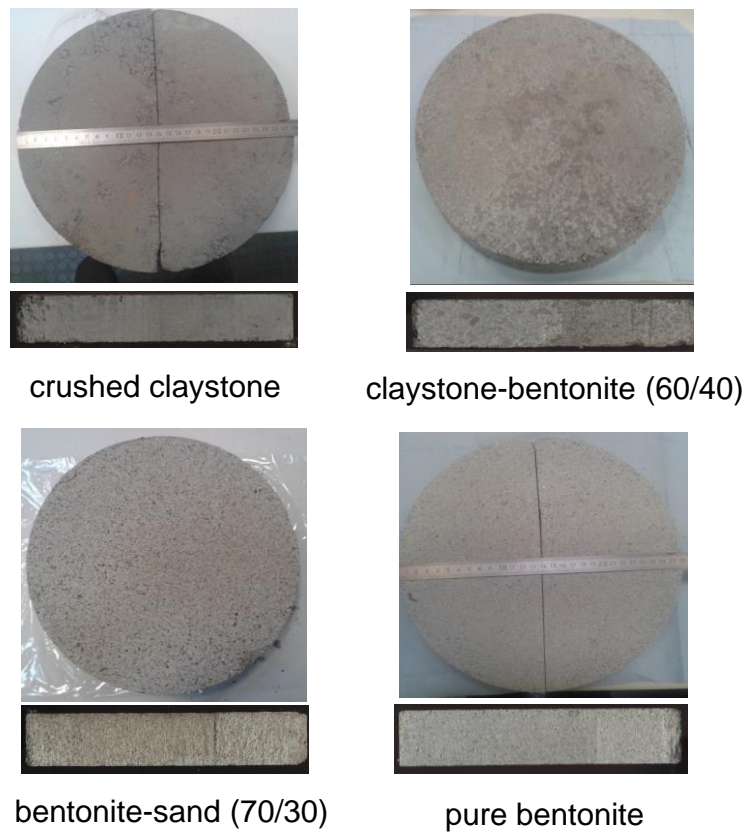
The samples were filled in the cell by hand stamping and compressed by the load piston at a displacement rate of  $7 \cdot 10^{-3}$  mm/s to a maximal stress of about 16 MPa. The compacted dry densities of the samples are depicted in Fig. 4.5 as function of applied axial load. The similar conclusions drawn above from the normal oedometer tests are confirmed by the large oedometer tests, i.e.

- a. The initial dry densities of the installed crushed claystone and the claystone-bentonite mixture are significantly higher than those of the pure bentonite and bentonite-sand mixture due to the different grain size distributions.
- b. The final dry densities of the crushed claystone and claystone-bentonite mixture after compaction at 16 MPa are higher too at  $\rho_d = 1.97$  and  $1.87$  g/cm<sup>3</sup> respectively, whereas the dry densities of the compacted bentonite and bentonite-sand mixture are relatively lower at  $\rho_d = 1.70$  and  $1.80$  g/cm<sup>3</sup> respectively.
- c. The compacted mixtures are visually homogeneously in grain distributions.

Additionally, the repeatability of the test results was examined by compacting 6 samples of the claystone-bentonite-mixture (60/40). The compaction curves are close to each other, as shown in Fig. 4.6. The maximal dry densities achieved lie in a narrow scatter between 1.85 and 1.88 g/cm<sup>3</sup>, even though the initial densities of the samples were relatively different from each other.



a) Compaction curves



b) Fotos of compacted samples

**Fig. 4.5** Dry densities of the compacted crushed claystone, bentonite, claystone-bentonite and bentonite-sand mixtures in large oedometer cell (a-b)

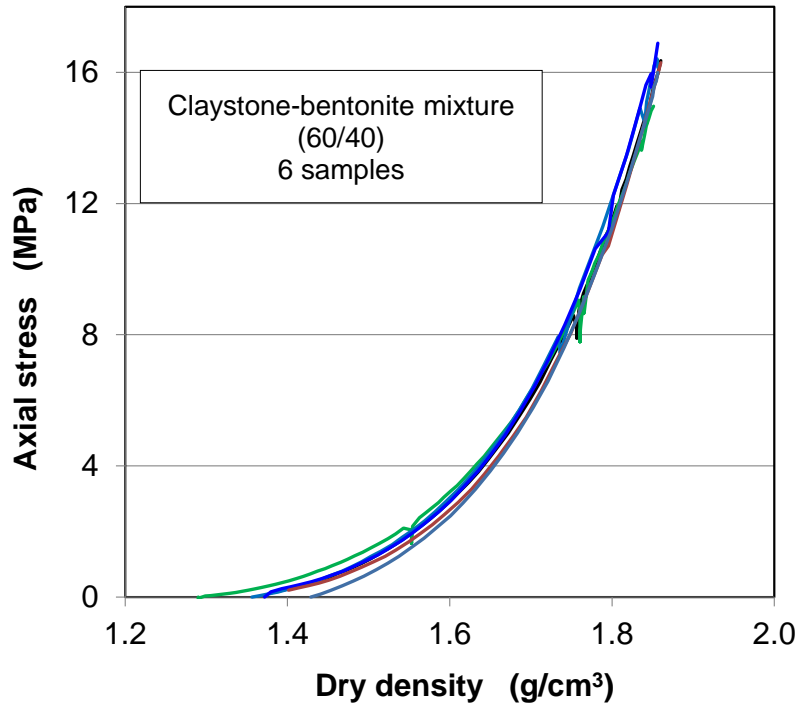


**Fig. 4.6** Compacted dry densities obtained on six samples of the claystone-bentonite mixtures in large oedometer cell

A comparison between the compaction curves obtained from the normal and large oedometer tests indicates significant differences for a same mixture. To achieve a given dry density, a higher load is needed by compaction of the material in the normal cell than in the large cell. This is attributed to the different height/diameter ( $h/d$ ) ratios of the samples,  $h/d = 0.75 - 1.0$  at the normally-sized samples and  $h/d = 0.18 - 0.30$  at the largely-sized samples. The small height/diameter ratios of the samples in the large oedometer cell imply the relatively small friction areas between the sample and cell, thus low friction resistances in the sample/cell interface against the applied load and relatively homogenous distributions of stress in the samples.

### 4.3 Water retention

An initially unsaturated clay-based material will take up water from humid environment. The amount of water uptake is governed by suction in the material. The water content adsorbed in the interlayers and on the external surfaces of clay particles remains constant as equilibrium is reached at a given suction. The relationship between suction and water content or saturation degree is essential for understanding and modelling of the

hydro-mechanical behaviour of the material, which is usually called water retention curve.

The water retention properties of the selected mixtures, including pure MX80 bentonite, bentonite-sand mixture, claystone-bentonite mixture and COX claystone, were determined under various humid and confining conditions. The tests were divided in three groups consisting of the different mixtures, as summarized in Table 4.1.

**Tab. 4.1** Basic properties of the samples prepared from the different clay-based mixtures for determination of the water retention curves

Test group I						
Material property	MX80 bentonite	80 COX+ 20 MX80	60 COX+ 40 MX80	Crushed COX claystone		
Grain size $d_{max}$ (mm)	0.5	5.0	5.0	5.0		
Grain density $\rho_s$ (g/cm <sup>3</sup> )	2.78	2.72	2.73	2.70		
Dry density $\rho_d$ (g/cm <sup>3</sup> )	1.64	1.95	1.88	2.05		
Porosity $\phi$ (%)	41.1	28.2	31.2	24.2		
Water content $w$ (%)	9.67	4.50	5.45	3.0		
Test group	II		III			
Material property	70MX80+ 30Sand	60COX+ 40MX80	MX80 bentonite	60COX+ 40MX80	COX claystone	Crushed claystone
Grain size $d_{max}$ (mm)	2.0	5.0	2.0	5.0		
Grain density $\rho_s$ (g/cm <sup>3</sup> )	2.75	2.73	2.74	2.73	2.70	2.70
Dry density $\rho_d$ (g/cm <sup>3</sup> )	1.72	1.81	1.15	1.89	2,28	2.23
Porosity $\phi$ (%)	37.5	33.5	58.0	30.7	15.5	17.5
Water content $w$ (%)	7.0	5.5	11.0	6.0	5.5	5.5

Group I consisted of the MX80 bentonite powder ( $d < 0.5$  mm), crushed COX aggregate ( $d < 5$  mm), and claystone-bentonite mixture in two ratios of COX/MX80 = 80/20 and 60/40. The materials were compacted in steel cells of 50 mm diameter and 33 mm height up to the maximum load of 30 MPa, at which different dry densities were achieved. Seven

compacted samples from each mixture were unconfined during testing. Fig. 4.7a shows the photos of the samples.

In group II the bentonite-sand (70/30) and claystone-bentonite (60/40) mixtures were compacted in steel cells of 50 mm diameter and 20 mm height to the desired densities. The samples were covered with sintered porous discs, which allow water molecules migrating through. Five compacted samples from each mixture were confined in the cells during testing.

In group III COX claystone cores were prepared to a size of  $d = 50$  mm and  $h = 20$  mm. They were inserted and confined in the steel cells and covered with sintered porous discs. The claystone-bentonite (60/40) mixture was compacted in the steel cells to the desired density. MX80 bentonite powder and COX claystone aggregate were unconfined. Seven samples from each mixture were tested. Fig. 4.7b shows the photos of the samples.

All the samples were placed in desiccators at different relative humidity values of  $RH = 15\%$  to  $100\%$  in group I and  $RH = 30\%$  to  $100\%$  in groups II and III (Fig. 4.7c). The humidity values were adjusted using different salt solutions. The temperature was kept at  $\sim 24$  °C. The relative humidity in each desiccator was continuously recorded by transistor psychrometer sensors, while the water content of each sample was measured at time intervals of weeks and months. Long time periods of several months to a year were needed to reaching equilibrium, particularly at high humidities close to  $100\%$ . With water absorption or desorption, the unconstrained samples in group I deformed with change in water content, which were recorded too. The data obtained on all the samples are presented in Appendix E.

The suction is related to the relative humidity by the psychrometric law /FRE 93/:

$$s = \frac{RT}{v_{wo} \omega_v} \ln \left( \frac{p_{va}}{p_{vp}} \right) = - \frac{RT}{v_{wo} \omega_v} \ln(RH) \quad (4.1)$$

where  $s$  = soil suction (kPa),  $T$  = absolute temperature (K),  $R$  = universal gas constant (8.31432 J/mol K),  $v_{wo}$  = specific volume of water or the inverse of density of water ( $1/\rho_w$ ,  $m^3/kg$ ),  $\rho_w$  = density of water (998  $kg/m^3$  at 20 °C),  $\omega_v$  = molecular mass of water vapour (18.016  $kg/kmol$ ),  $p_v$  = partial pressure of pore-water vapour (kPa),  $p_{vo}$  = saturation

pressure of water vapour over a flat surface of pure water at the same temperature (kPa),  $RH = \text{relative humidity } (p_v / p_{v0} \cdot 100\%)$ .



a) Samples in test group I



b) Samples in test group III: confined in cells and unconfined

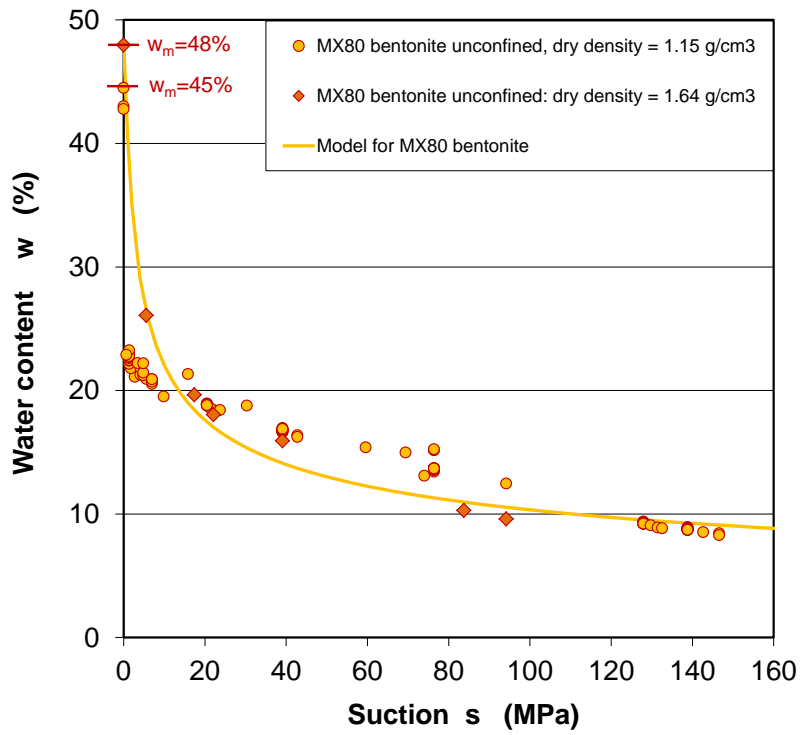


c) Samples in desiccators

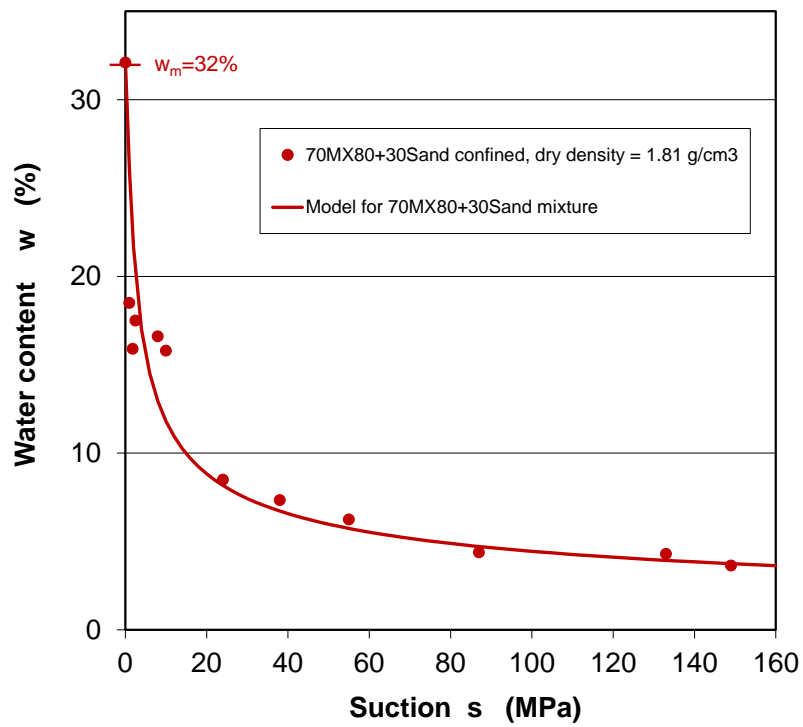
**Fig. 4.7** Measurement of water retention properties of the clay-based materials in desiccators at different air humidities (a-c)

The water contents reached in equilibrium at each humid condition are plotted as a function of suction  $s$  in Fig. 4.8 for each mixture. It can be found out that

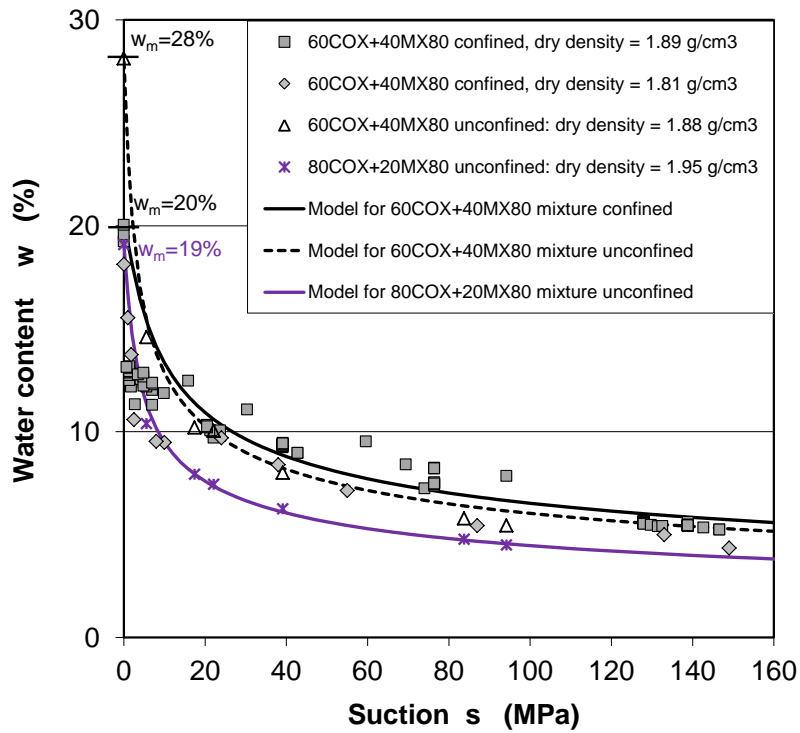
- The water content of each mixture increases gradually with decreasing suction. At zero suction or 100 % humidity, a maximum of water content is reached:  
 $w_m = 45 - 48 \%$  for the pure bentonite;  
 $w_m = 32 \%$  for the 70MX80+30Sand mixture;  
 $w_m = 20 \%$  and  $w_m = 28 \%$  for the 60COX+40MX80 mixture in confined and unconfined conditions respectively;  
 $w_m = 19 \%$  for the unconfined 80COX+20MX80 mixture;  
 $w_m = 8.8 \%$  for the confined claystone and  $w_m = 12 \%$  for the unconfined crushed claystone.
- The  $w - s$  data obtained on the unconfined pure bentonite with the different initial densities are close to each other (Fig. 4.8a). The pure bentonite exhibits the most high water retention capacity.
- With adding sand and claystone, the amount of water uptake decreases (comparing Figs. 4.8a/b/c).
- The water contents measured on the unconfined 60COX+40MX80 mixture (Fig. 4.8c) and the crushed claystone at suctions of higher than 20 MPa are slightly higher than those measured in confined conditions. This cannot be reasonably interpreted yet.



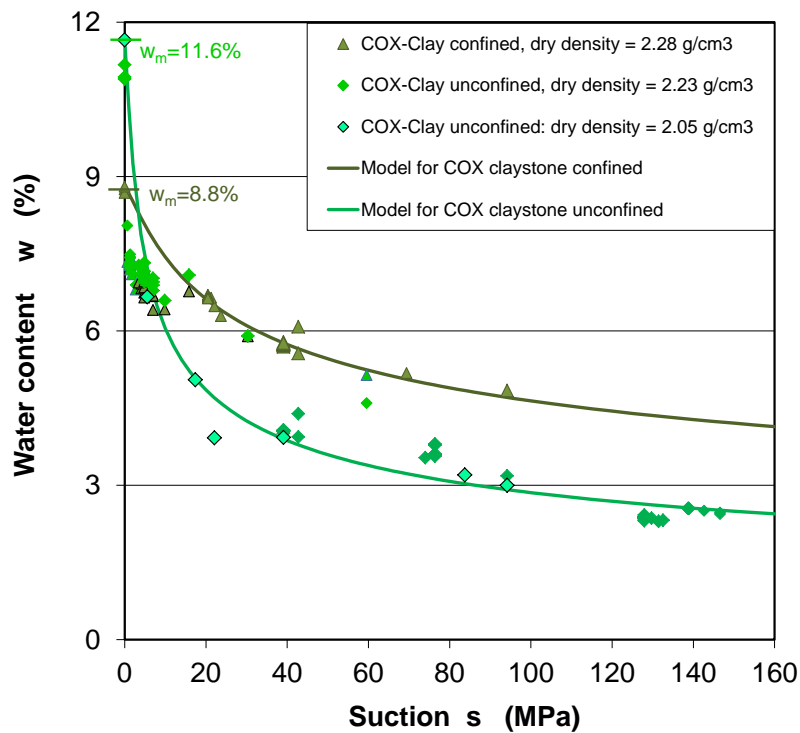
a) Pure bentonite in unconfined condition



b) Compacted bentonite-sand mixture in confined condition



c) Compacted claystone-bentonite mixture in confined and unconfined conditions



d) Intact claystone in confined and crushed claystone in unconfined conditions

**Fig. 4.8** Relationships of water content to suction for the seal materials: bentonite, bentonite-sand mixture, claystone-bentonite mixture, intact and crushed claystone (a-d)

The relationships between water content and suction can be approximated by the van Genuchten model /VAN 80/

$$w = w_m \cdot \left[ 1 + \left( \frac{s}{P_o} \right)^{\frac{1}{1-\beta}} \right]^{-\beta} \quad (4.2)$$

where  $P_o$  and  $\beta$  are the material parameters. The parameter values are estimated by fitting the  $w - s$  data for each mixture and summarized in Table 4.2. A comparison in Figs. 4.8a-d indicates a satisfactory agreement between the model and the data for each mixture.

**Tab. 4.2** Parameters of the water retention curves in expression of water content

Parameter	MX80 bentonite unconfined	70MX80+30Sand confined	80COX+20MX80 unconfined	60COX+40MX80 unconfined	60COX+40MX80 confined	COX claystone	Crushed claystone
$w_m$ (%)	48.0	32.0	19.0	28.0	20.0	8.8	11.6
$P_o$ (MPa)	1.0	1.0	1.3	1.0	3.5	8.0	1.5
$\beta$ (-)	0.25	0.3	0.25	0.25	0.25	0.2	0.25

#### 4.4 Water saturation

For evaluation of the hydration or water saturation process in a seal system, water uptake experiments were performed on the selected mixtures: pure bentonite, bentonite-sand mixture, claystone-bentonite mixture, intact claystone and crushed claystone. The materials were compacted to the desired densities in steel cylinders of 50 mm diameter and 100 mm length. Synthetic COX clay water was supplied to an end face of each sample using a burette at atmospheric pressure. The opposite face was connected to the atmosphere via a porous plate. Amounts of water uptake were recorded with time over 10 to 20 months. Fig. 4.9 shows the test setup. After testing, the samples were cut into slices of ~10 mm thickness to determine the distribution of water content and density. The initial characteristics of the samples and the measured water uptake data are given in Appendix F.

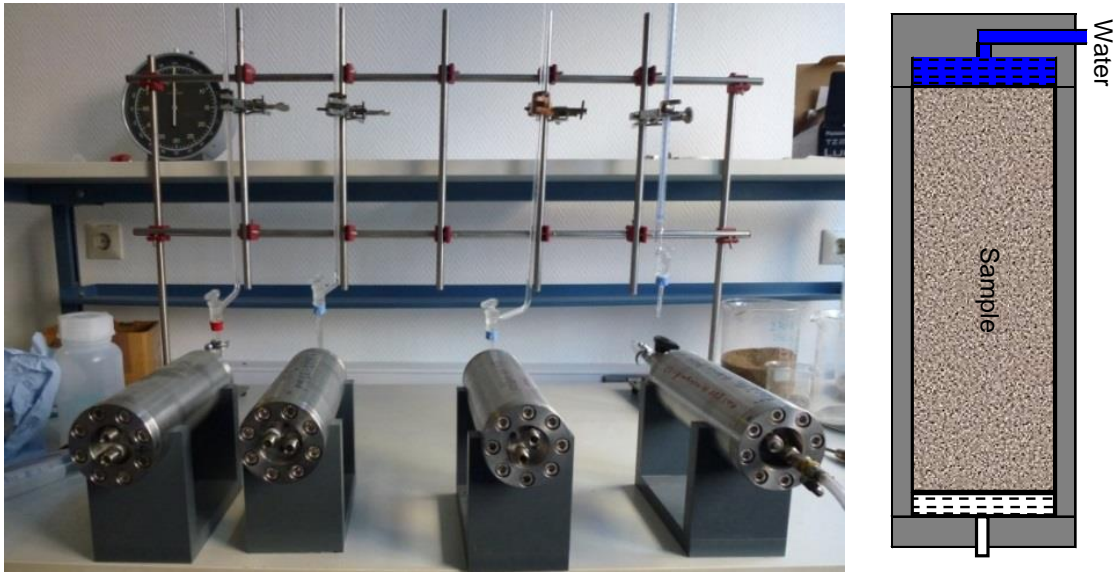


**Fig. 4.9** Setup of water saturation measurements on the compacted seal mixtures in steel cylinders

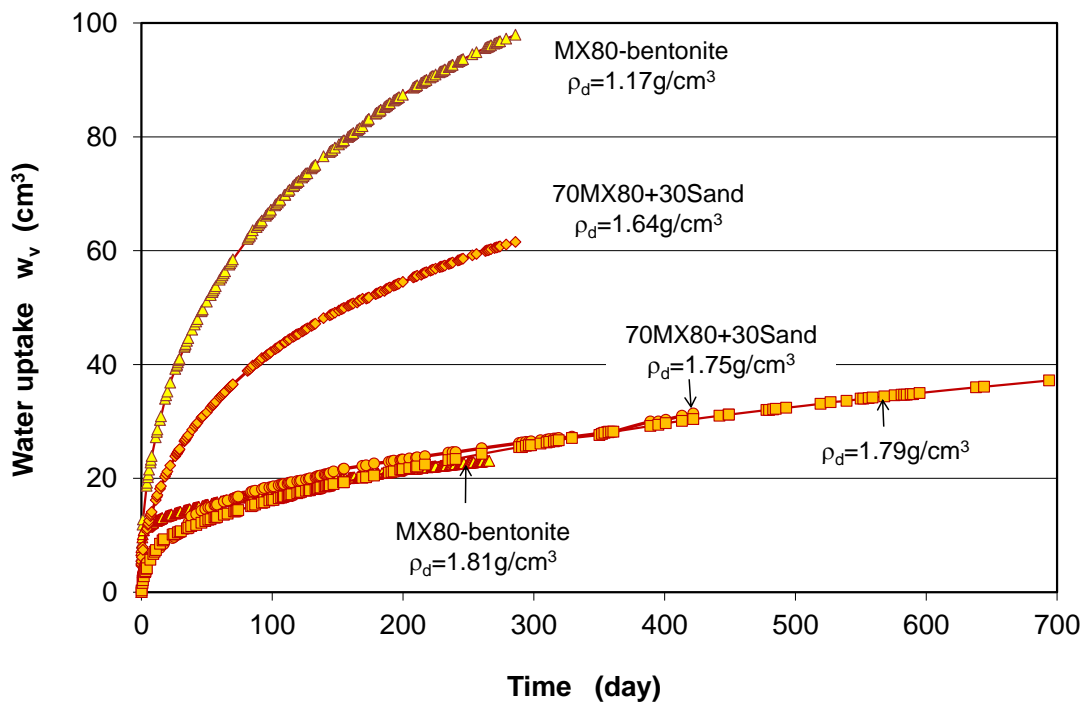
The cumulative amounts of water uptake recorded are plotted in Figs. 4.10a-d for (a) pure MX80 bentonite and bentonite-sand mixture (70MX80+30Sand), (b) claystone-bentonite mixture (COX/MX80 = 80/20; 60/40), (c) intact and crushed COX claystone, and (d) comparison between the bentonite-sand (70/30) and claystone-bentonite (60/40) mixtures, respectively. The results show that:

- a. The amounts of water uptake by the pure bentonite and bentonite-sand mixture are largely determined by the density or porosity, which restricts the volume of water uptake. In large porosities, the water migration is less impeded so that the rate is relatively faster. The distributions of the uptake water were determined by post-measurements of water content after testing over 10 to 23 months, given in App. F. The results show that the water distributions in the compacted bentonite and bentonite-sand mixture were relatively homogeneous along the sample length (except for the water entry part). However, no full saturation was reached at each of the samples over such long time periods of 1 - 2 years.
- b. Similarly, the water uptake of the compacted claystone-bentonite mixture decreases with increasing density. All the compacted claystone-bentonite samples with ratios of COX/MX80 = 80/20 and 60/40 were practically saturated over about 10 months (App. F).
- c. The water uptake of the high dense intact claystone is much slower than that of the compacted aggregate with a relatively low density, even though the initial water contents of both samples were comparable at  $w = 3.7\%$  for the claystone and  $w = 3.0$

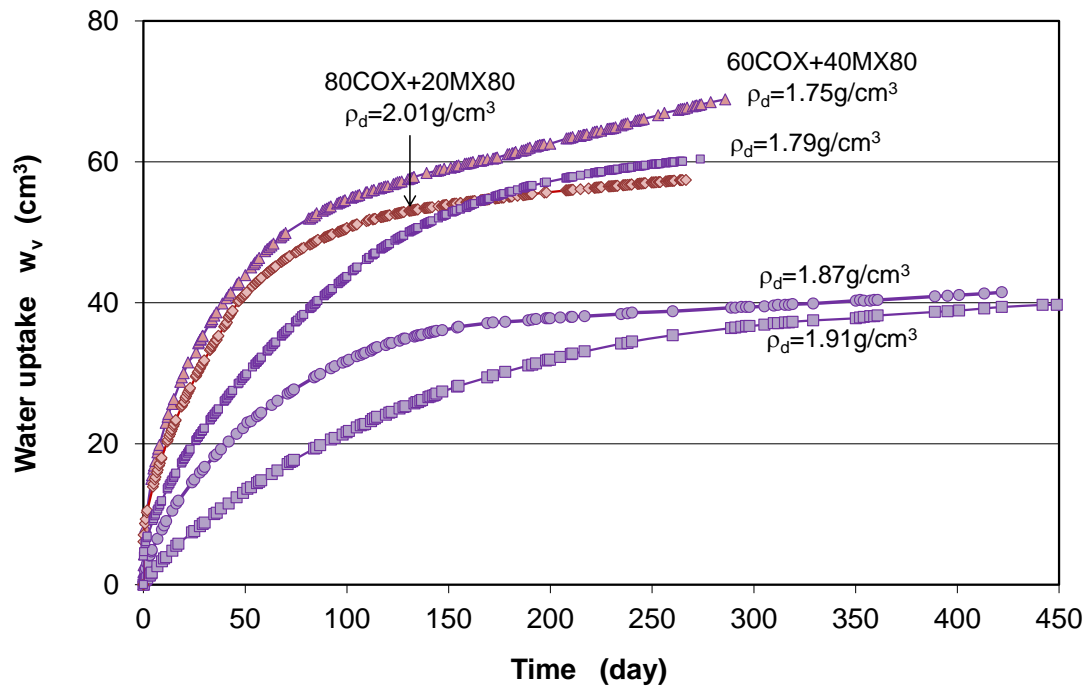
% for the aggregate. The compacted aggregate was practically saturated over 7 months (App. F).

- d. The saturation process of the compacted claystone-bentonite (60/40) mixture is faster than that of the compacted bentonite-sand (70/30) mixture, even though the density of the claystone-bentonite mixture is higher than that of the bentonite-sand mixture. This demonstrates that the water uptake is dominated by the bentonite content.
- e. Due to the high initial suction in a relatively dry state, each sample takes up water faster in the beginning and then the saturation process becomes slower. The retardation of water migration is primarily caused by the adsorption of water molecules on clay particles. As a consequence, the suction gradient in the clay-based materials decreases on the one hand; and on the another hand, the adsorbed water films and also the resulting swelling of the clay minerals reduce the accessible pore space for further water migration.

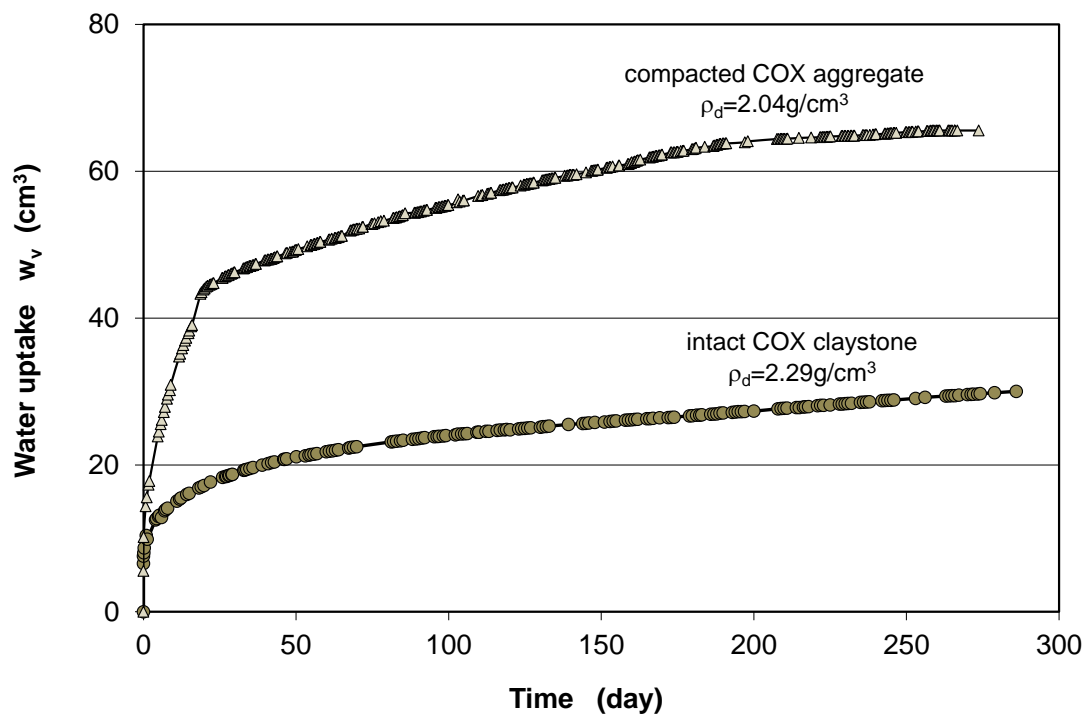
It is noted that most of the water saturation tests are numerically simulated by coupled hydro-mechanical calculations in chapter 5.



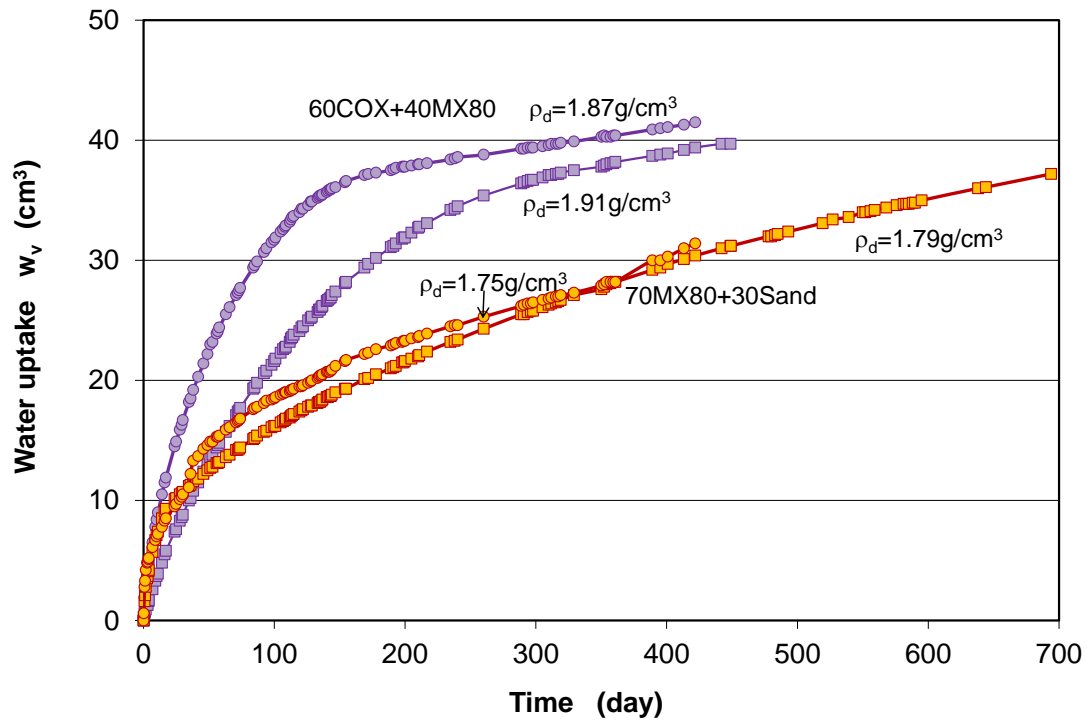
a) Compacted bentonite and bentonite-sand mixture



b) Compacted claystone- bentonite mixture



c) Intact and crushed claystone



d) Comparison between claystone-bentonite and bentonite-sand mixtures

**Fig. 4.10** Evolution of cumulative water uptake of compacted seal materials in contact with synthetic clay water at atmospheric pressure (a-d)

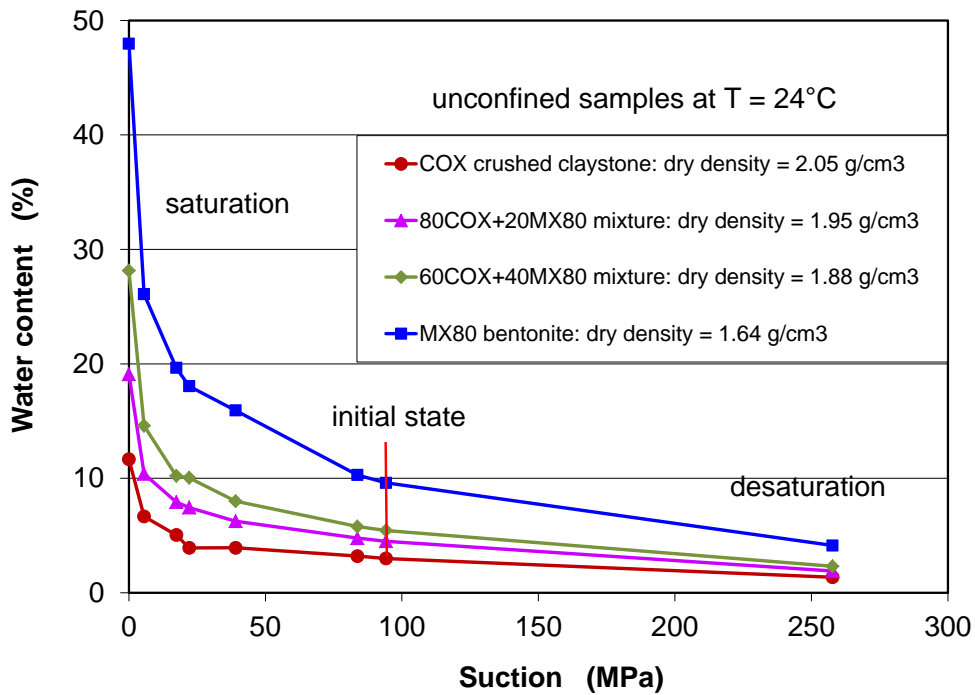
#### 4.5 Swelling capacity

The swelling capacities of the compacted claystone-bentonite and bentonite-sand mixtures were measured by swelling deformation and pressure under various conditions.

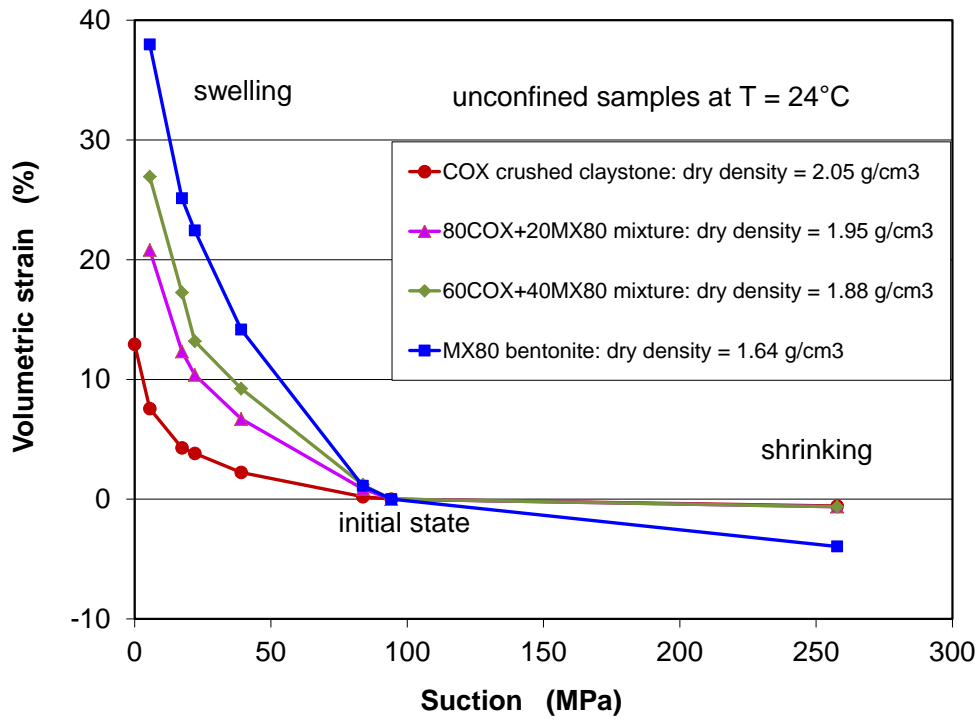
##### 4.5.1 Free swelling

Swelling capacities of the selected mixtures were firstly examined by free swelling deformation of the unconfined samples at different humidities during the water retention tests (group I) in section 4.3. The crushed COX claystone, pure bentonite MX80, claystone-bentonite mixture with ratios of COX/MX80 = 80/20 and 60/40 were compacted to a sample size of 50 mm diameter and 33 mm height with different dry densities of 2.05, 1.64, 1.88 and 1.95 g/cm<sup>3</sup> respectively. The main characteristics of the samples (group I) are given in Table 4.1. The compacted samples were unconfined and placed in desiccators at different relative humidity values of  $RH = 15\%$  to  $100\%$ , corresponding to suctions between 260 and 0.0 MPa. The water content and the free deformation obtained on each sample are illustrated in Fig. 4.11 as function of applied suction. It is obvious that the

water content of each sample increases with decreasing suction. The water content at a given suction increases with increasing bentonite content in the mixture. At high relative humidity values of  $RH = 96-100\%$  or low suctions of  $s = 6 - 0$  MPa, all the mixtures can take up large amounts of water up to 12% for the compacted crushed claystone and 48% for the bentonite. The increase in water content is accompanied by free expansion. The compacted crushed claystone can expand by a volumetric increase up to 12%, while the other mixtures expand even more up to 20-40% due to the more bentonite contents. The volume expansion is almost linearly related with the increased water content, as shown in Fig. 4.12. It is to be pointed out that the free swelling can result in cracks in the compacted mixtures, as shown in Fig. 4.13. The pictures of the samples after free swelling over 6 months at  $RH = 96\%$  show the wetting-induced cracks. Obviously, the cracking intensity (number and size of cracks) increases with increasing bentonite content. Almost no significant cracks appeared in the compacted crushed claystone.



a) Water retention curves



b) Volumetric strain – suction relation

**Fig. 4.11** Water uptake (a) and free swelling (b) measured on the compacted clay-stone-bentonite mixtures at different suctions

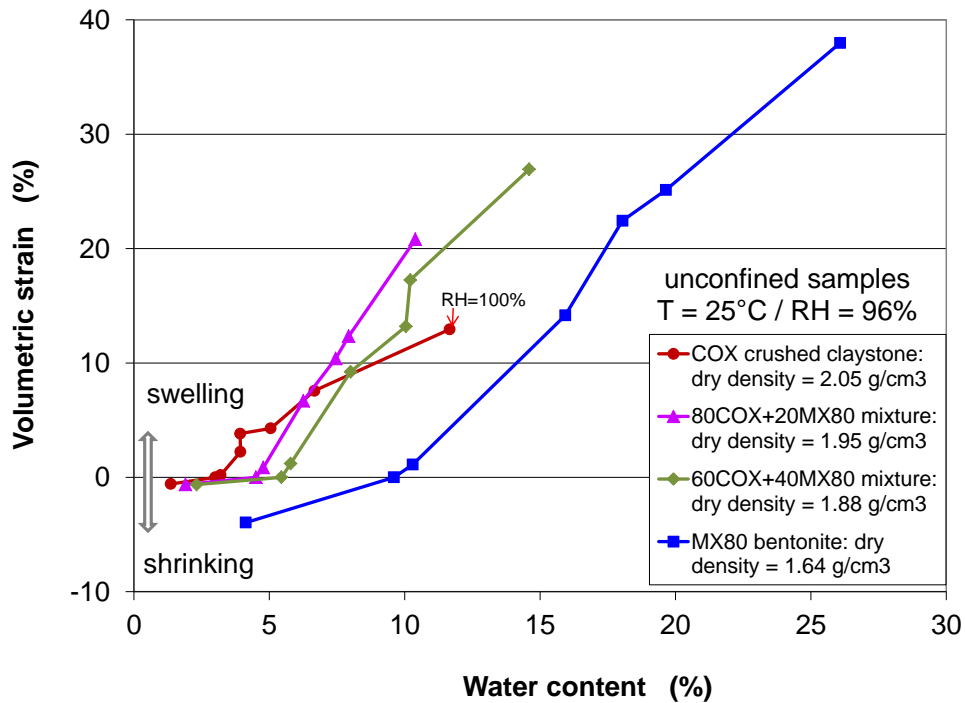


**Fig. 4.12** Free swelling of the compacted seal materials with increasing water content



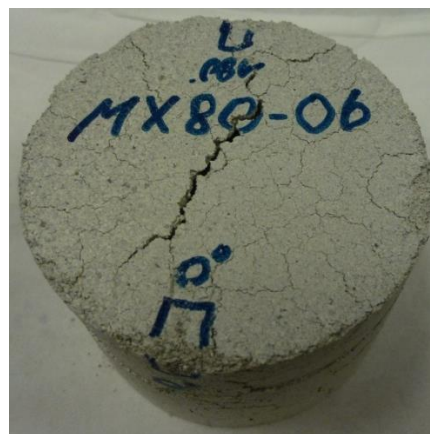
a) Compacted crushed claystone



b) Claystone-bentonite-mixture (80/20)



c) Claystone-bentonite-mixture (60/40)



d) Compacted bentonite

**Fig. 4.13** Pictures of the compacted claystone-bentonite samples after free swelling at a high relative humidity of 96 % over 6 months (a-d)

#### 4.5.2 Swelling pressure

In confined conditions, the swelling of a clay-based material is hindered, so that repulsive force or swelling pressure built up in interlayer water within the sheet structures of clay particles and in interparticle water in the narrow pore space due to physico-chemical interactions of clay minerals with water. So the swelling pressure is another important indicator of the swelling capacity. In this programme, the swelling capacities of the claystone-bentonite (60/40) and bentonite-sand (70/30) mixture were examined by measurement of swelling pressures in two oedometer cells of 50 mm diameter and 30 mm height. Fig. 4.14 shows the test setup. The mixtures were compacted in the cells to dry densities of  $\rho_d = 1.86 \text{ g/cm}^3$  for the claystone-bentonite mixture and  $\rho_d = 1.82 \text{ g/cm}^3$  for the bentonite-sand mixture at axial load of 30 MPa. The synthetic COX clay water was brought

into both samples firstly at the bottom and then at the top under atmosphere pressure. Development of axial swelling pressure was recorded using a pressure sensor installed at the top of the cell between load piston and cap.

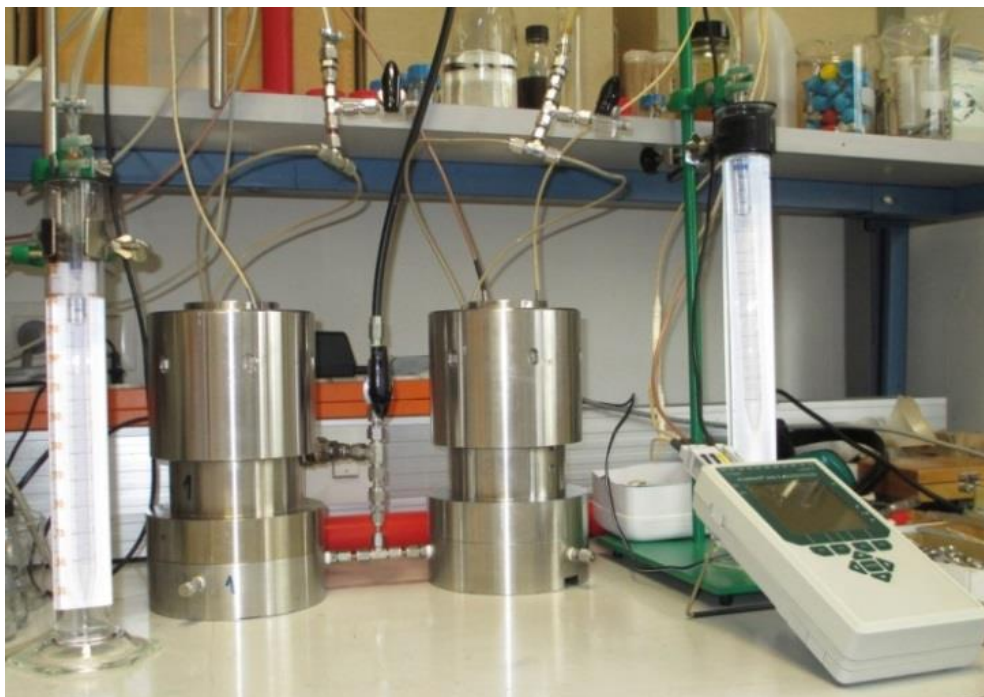
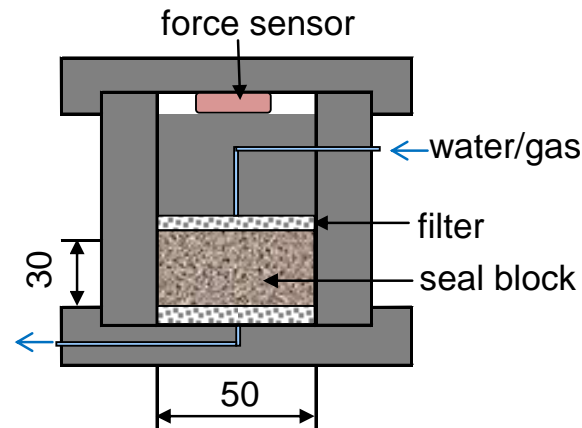


**Fig. 4.14** Test setup for swelling pressure measurements on seal samples

Fig. 4.15 depicts the evolution of measured swelling pressures during the saturation process. The rapid water uptake within the first days led to a dramatic increase in the swelling pressure up to a peak at each of the samples. Following that, the swelling pressure of the bentonite-sand sample (70MX80+30Sand) decreased slowly for several days and then increased again to a value of 5.6 MPa, while the swelling pressure of the claystone-

bentonite sample (60COX+40MX80) increased with some fluctuations to 3.7 MPa. The swelling pressures maintained over time.

In the previous experiments /ZHA 13a/14c/d/, the compacted claystone-bentonite samples with bentonite contents of 40 - 60 % were confined in axial direction and free in radial direction. High swelling pressures up to 6.0 to 9.5 MPa were observed during wetting with vapour. Generally, the swelling pressure increases with increasing bentonite content and density. It is also true for the bentonite-sand (70/30) mixture.

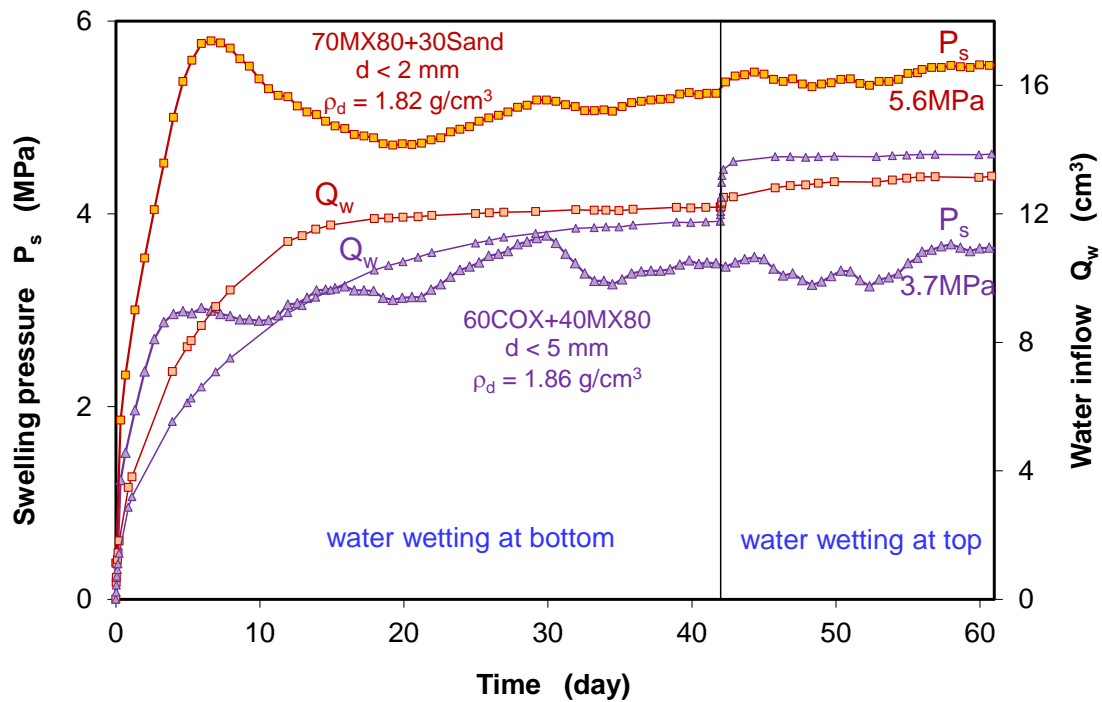


**Fig. 4.15** Development of swelling pressure in the compacted claystone-bentonite and bentonite-sand mixtures during wetting with synthetic clay water

#### 4.5.3 Swelling under loads

The swelling capacities of the selected mixtures were also examined under various load conditions.

##### 4.5.3.1 Oedometer swelling tests

Both claystone-bentonite (60/40) and bentonite-sand (70/30) mixtures were precompact to a dry density of  $\rho_d = 1.85 \text{ g/cm}^3$  for sample 60COX+40MX80 and  $\rho_d = 1.75$

g/cm<sup>3</sup> for 70MX80+30Sand. They were inserted in two oedometer cells of 80 mm diameter and 25 mm height. A constant axial load of 1 MPa was applied to the samples. They were wetted from the bottom with the synthetic COX clay water. Fig. 4.16 demonstrates axial swelling strains of both mixtures. The fast water uptake led to a rapid expansion of each sample in the beginning, and then the water uptake and the swelling became slow and tended to a stable state after about a month. The maximum swelling strains reached to 9.5 % at 60COX+40MX80 and 8.5 % at 70MX80+30Sand respectively. As the load was totally removed, both samples expanded more up to 23 % at 60COX+40MX80 and 17 % at 70MX80+30Sand respectively. This maximum expansion of the compacted claystone-bentonite mixture is comparable to the free swelling recorded during wetting with vapour (cf. Fig. 4.11). Comparing both mixtures, the claystone-bentonite mixture showed higher swelling than the bentonite-sand mixture. This might be attributed to the higher compacted density of the claystone-bentonite mixture.

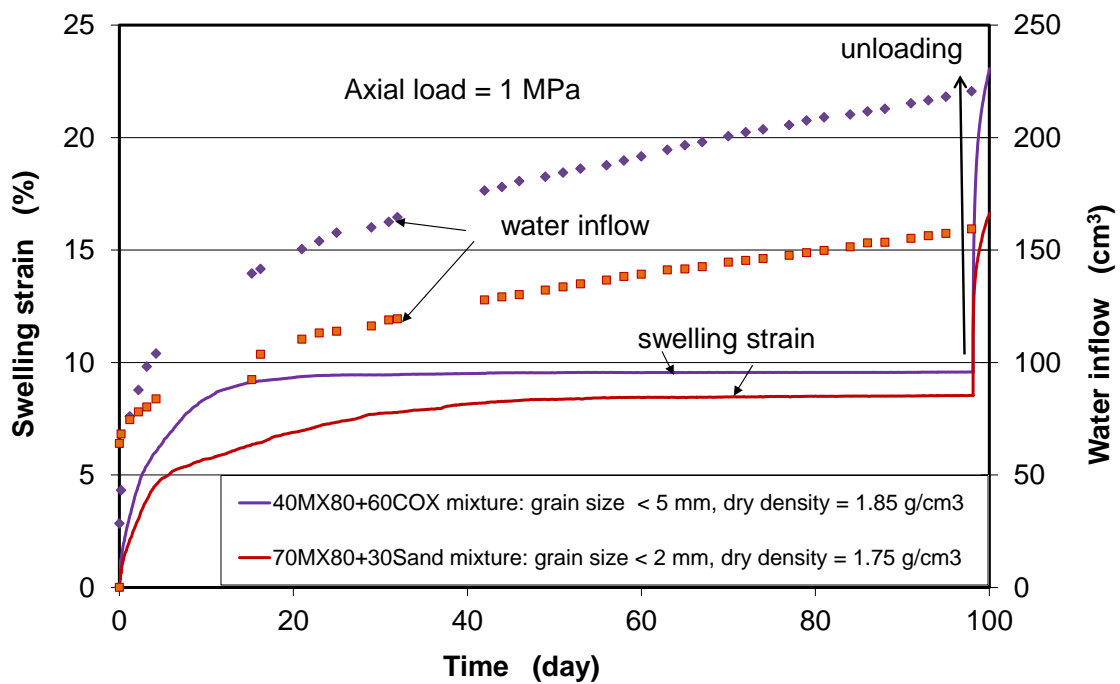


**Fig. 4.16** Uniaxial swelling deformation of the compacted claystone-bentonite and bentonite-sand mixtures in oedometers at axial load of 1 MPa during wetting with synthetic clay water

#### 4.5.3.2 Triaxial swelling tests

##### *Compacted claystone-bentonite mixture*

The swelling capacity of the compacted claystone-bentonite (60/40) mixture was also examined under triaxial stress conditions. The bentonite with grains of  $d < 2$  mm was mixed with the crushed claystone of  $d < 5$  mm. The mixture was precompact to a size of 50 mm diameter and 100 mm length with a dry density of  $\rho_d = 1.92$  g/cm<sup>3</sup>. The compacted sample was then confined in a triaxial cell under a hydrostatic stress of 2 MPa. Fig. 4.17 illustrates the assembly of the sample. The picture shows that the bentonite particles (light grey) were homogeneously distributed in the coarse-grained claystone aggregate (dark grey). The synthetic COX clay water was injected into the sample at pressures of  $p_w = 1.0$  and 1.5 MPa over 5 months.

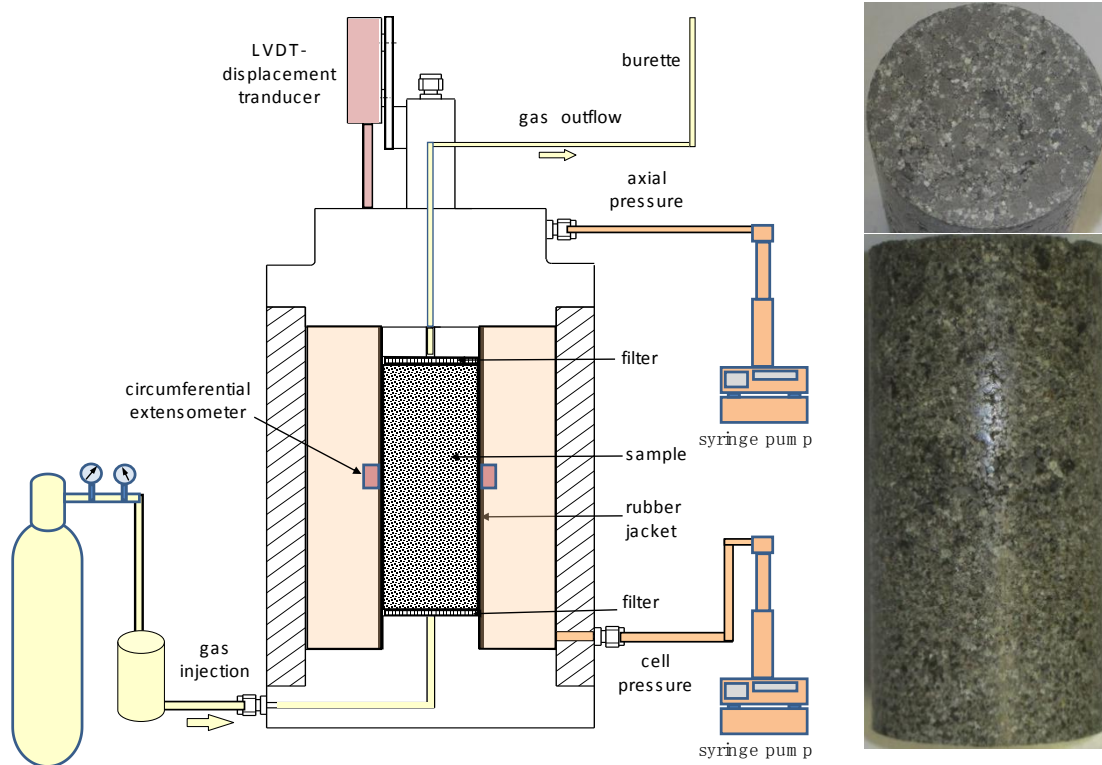


**Fig. 4.17** Schematic of triaxial swelling test on a claystone-bentonite sample

Responses of axial and radial strain to the water injection were recorded and illustrated in Fig. 4.18. At  $p_w = 1.0$  MPa, the sample slightly expanded in the axial direction with time. Before the water flow reached the middle part where the radial strain was measured, a gradual radial compression there was observed over 1.5 months. As the water flow reached this measuring position at the increased water pressure of  $p_w = 1.5$  MPa, radial swelling began and increased by 4 % with water saturation over about 3 months.

After full saturation, the subsequent measurement of water permeability yielded a low value of  $6 \cdot 10^{-20} \text{ m}^2$ . Switching off the water supply, the water pressure decreased gradually with time, but only small strains reversed. The remaining deformation is obviously the final result of the combined impact from the confining stress and the swelling of clay minerals in the mixture.

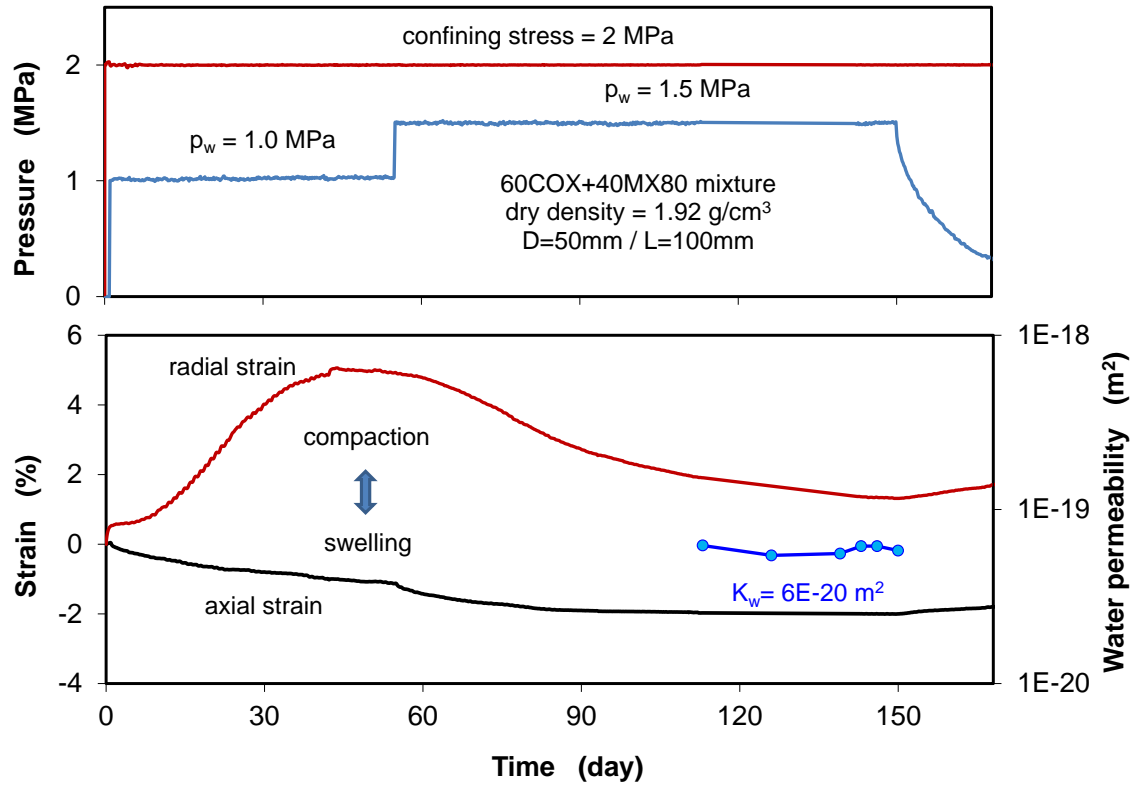


**Fig. 4.18** Triaxial swelling deformation of the compacted claystone-bentonite sample at a confining stress of 2 MPa during water injection at pressures of 1.0 and 1.5 MPa

**Compacted crushed claystone**

In another triaxial test, the crushed claystone was investigated in a large scale sample of 280 mm diameter and 200 mm length. The coarse-grained aggregate with sizes of  $d < 10 \text{ mm}$  was filled in 5 layers of 50 mm height each. Each layer was compacted by hand stamping to an average dry density of  $1.73 \text{ g/cm}^3$ . Fig. 4.19 shows schematically the test layout.

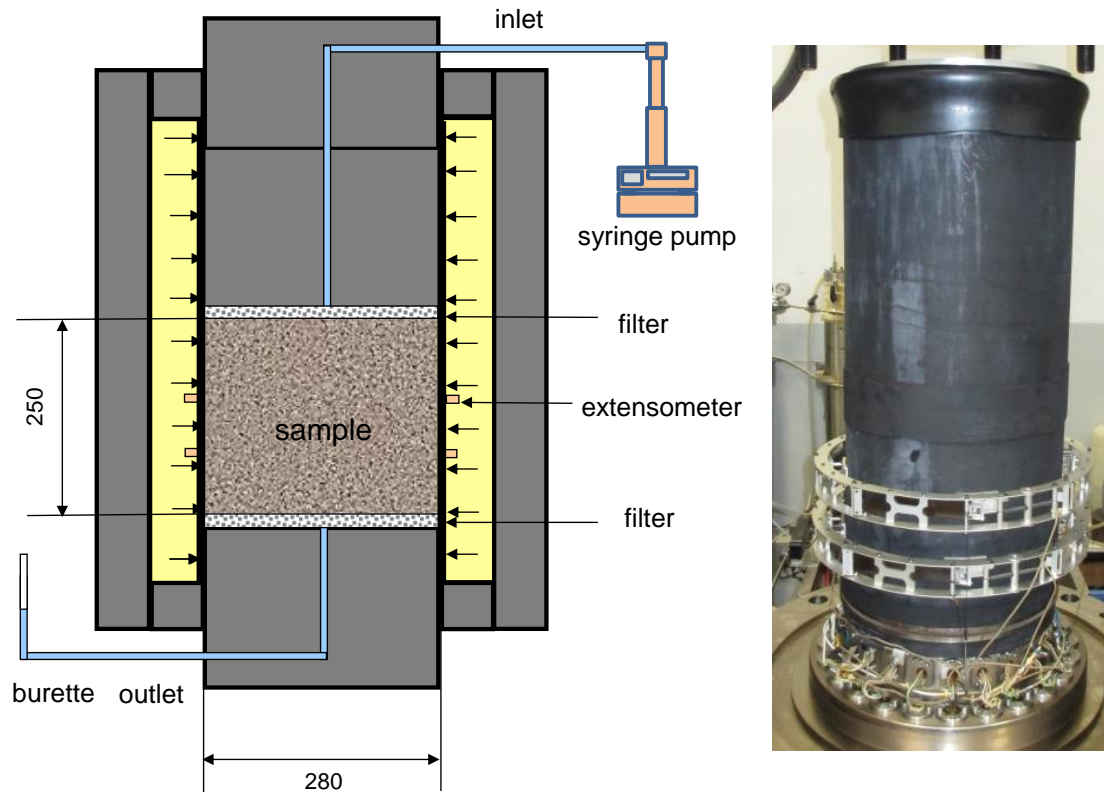


**Fig. 4.19** Schematic of large-scale swelling test on compacted crushed claystone

The sample was firstly compacted to a desired dry density of  $2.0 \text{ g/cm}^3$  at increased axial stress of  $\sigma_1 = 17 \text{ MPa}$  and radial stress of  $\sigma_3 = 15 \text{ MPa}$ . After the precompaction, the stresses were reduced down to  $\sigma_1 = 2.5 \text{ MPa}$  and  $\sigma_3 = 1.8 \text{ MPa}$ , under which the synthetic COX clay water was injected into the sample at a pressure of  $p_w = 1 \text{ MPa}$  and then followed gas testing at elevated pressures  $p_g$ . Fig. 4.20 illustrates the applied conditions of the ambient temperature, axial and radial stresses, water and gas injecting pressures. During the test, axial and radial strain was measured by means of a LVDT deformation transducer and two circumferential extensometers at two positions of  $70 \text{ mm}$  ( $\epsilon_{r-u}$ ) and  $150 \text{ mm}$  ( $\epsilon_{r-m}$ ) from the bottom, respectively. The water in- and outflow were recorded. After full saturation, water permeability was determined. The subsequent gas testing aimed at examining gas breakthrough pressure of the water-saturated sample.

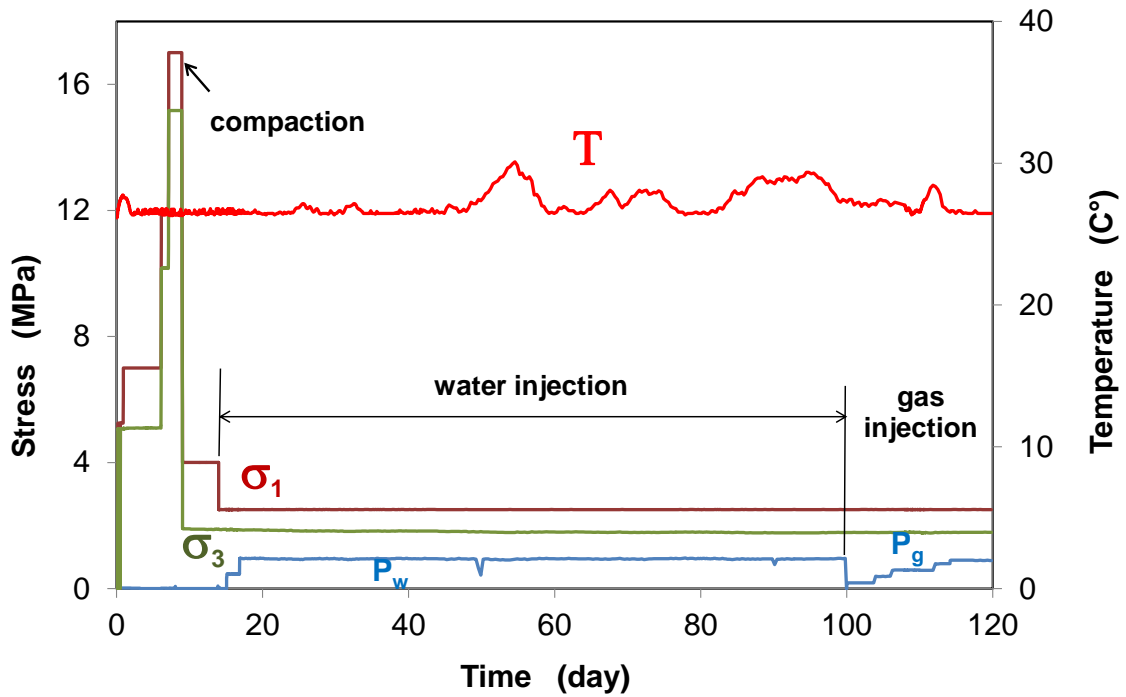
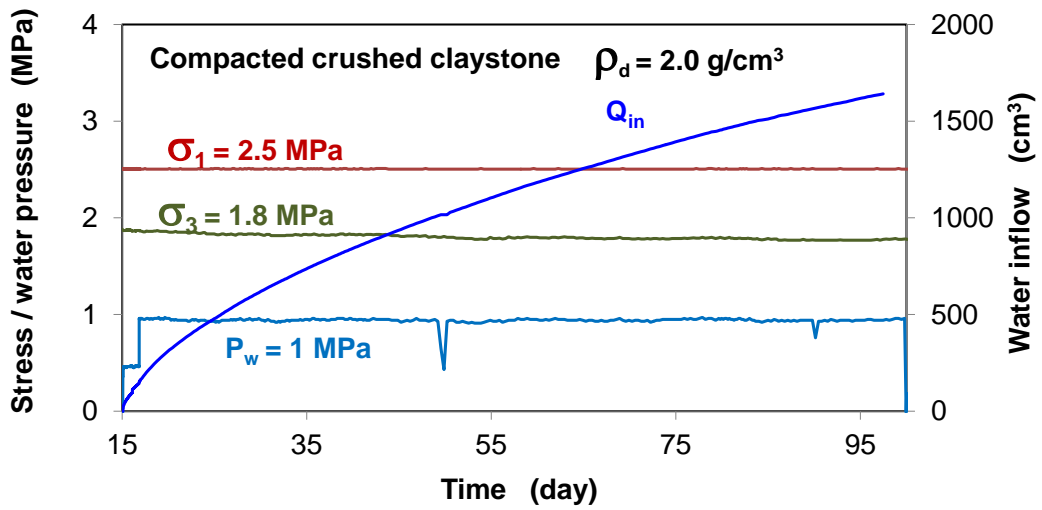
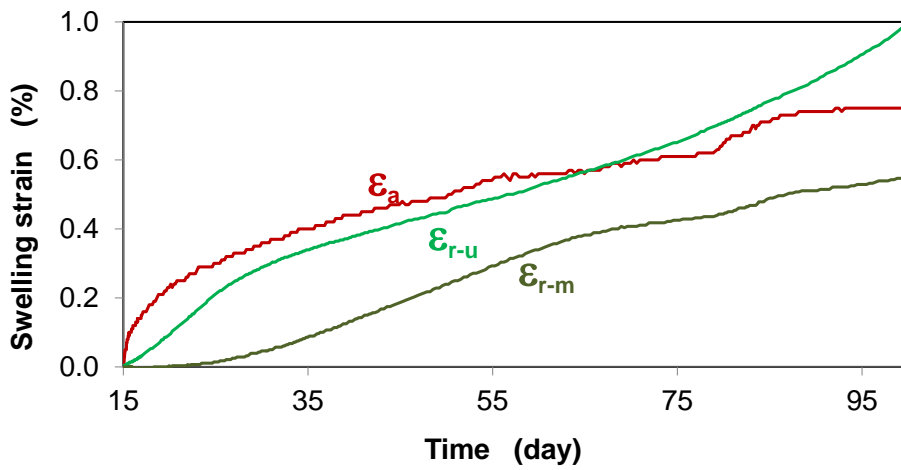


**Fig. 4.20** Testing conditions applied to the compacted crushed claystone

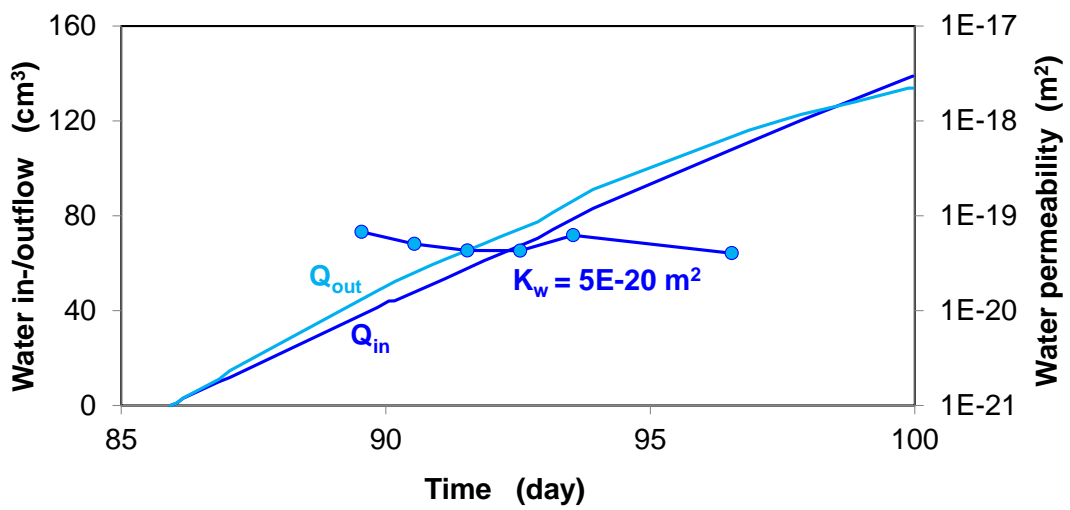
Fig. 4.21 shows results of measured axial and radial strain, water in and outflow during the water injection phase over about three months. The water uptake led to expansion of the compacted crushed claystone in all directions (Fig. 4.21b). The swelling strains reached to 0.5 - 0.6 % in radial direction and 1.0 % in axial direction. The water outflow observed after 2.5 months indicated the sample fully water-saturated (Fig. 4.21c). From the measurement of the water outflow, a water permeability value was derived to  $K_w = 5 \cdot 10^{-20} \text{ m}^2$ .



a) Applied stresses, water pressure and water inflow



b) Responses of strains



c) Water in- and out flow and permeability

Fig. 4.21 Testing conditions applied to the compacted crushed claystone (a-c)

#### 4.6 Water permeability

The main function of seals in a repository is to prevent fluid access into the repository and the release of radionuclides from it. Therefore, low hydraulic conductivities of the seals are required from the beginning over long time periods of hundreds of thousands of years. Water permeabilities of the compacted crushed claystone, claystone-bentonite and bentonite-sand mixtures were determined after water saturation during the swelling experiments mentioned above in section 4.5:

- the compacted claystone sample in the large triaxial cell under the confining stresses of  $\sigma_1 = 2.5$  MPa and  $\sigma_3 = 1.8$  and at a water injecting pressure of  $p_w = 1$  MPa;
- the compacted claystone-bentonite (80/20; 60/40) and bentonite-sand (70/30) samples in the oedometer cells at a water injecting pressure of 0.5 MPa;
- the claystone-bentonite (60/40) sample in the normal triaxial cell under the isostatic stress of  $\sigma_m = 2.0$  MPa and at a water injecting pressure of  $p_w = 1.5$  MPa.

Fig. 4.22 summarizes the measured data for the samples. All the compacted mixtures exhibited very low water permeabilities, being close to that of the intact clay rock ( $K_w < 10^{-20}$  m<sup>2</sup>):

- $K_w = 5 \cdot 10^{-20}$  m<sup>2</sup> for the compacted crushed claystone with grains of  $d < 10$  mm and a dry density  $\rho_d = 2.0$  g/cm<sup>3</sup>;
- $K_w = 2 \cdot 10^{-19}$  for the fine-grained claystone-bentonite sample 80COX+20MX80 ( $d < 0.5$  mm) with a dry density  $\rho_d = 1.86$  g/cm<sup>3</sup> ;
- $K_w = 1 \cdot 10^{-19}$  m<sup>2</sup> for the coarse claystone-bentonite sample 80COX+20MX80 ( $d < 5$  mm) with a dry density  $\rho_d = 1.90$  g/cm<sup>3</sup>;
- $K_w = 3 \cdot 10^{-20}$  m<sup>2</sup> for the fine-grained claystone-bentonite samples 60COX+40MX80 ( $d < 0.5$  mm) with a dry densities  $\rho_d = 1.79$  g/cm<sup>3</sup>;
- $K_w = 1 \cdot 10^{-19} - 6 \cdot 10^{-20}$  m<sup>2</sup> for the coarse claystone-bentonite samples 60COX+40MX80 ( $d < 5$  mm) with dry densities  $\rho_d = 1.86 - 1.92$  g/cm<sup>3</sup>;
- $K_w = 2 \cdot 10^{-20}$  m<sup>2</sup> for the bentonite-sand sample 70MX80+30Sand with grains  $d < 2$  mm and dry density  $\rho_d = 1.82$  g/cm<sup>3</sup>.

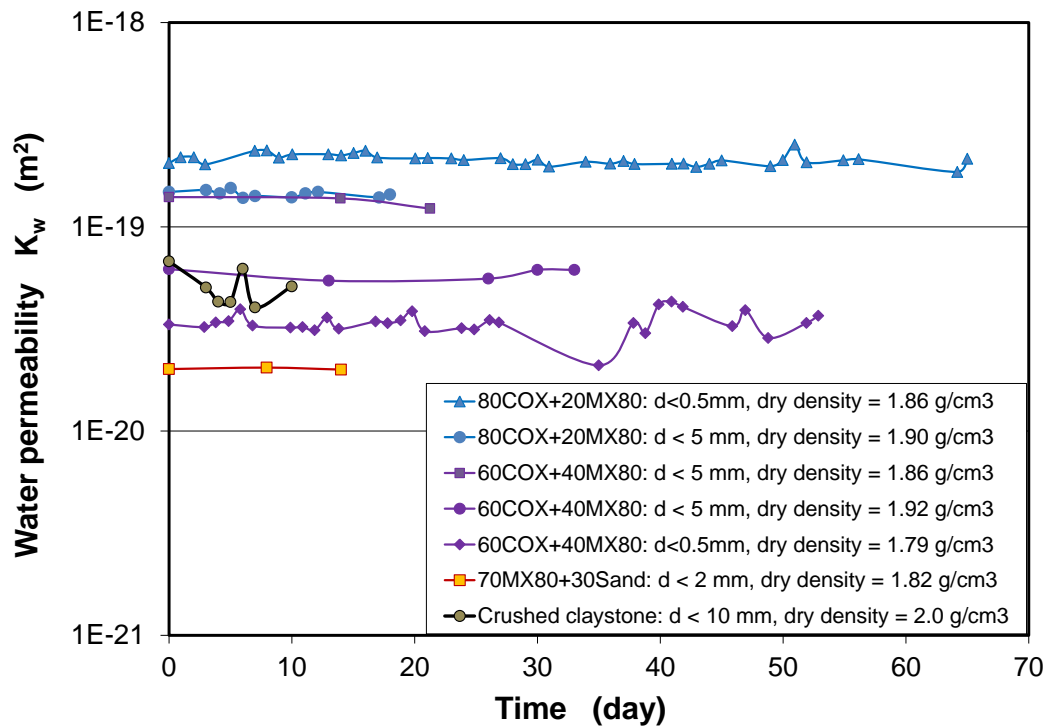


**Fig. 4.22** Water permeabilities of the compacted crushed claystone, claystone-bentonite and bentonite-sand mixtures

#### 4.7 Gas migration

Gases produced within a repository can pass through a seal system before water-saturated. When the seal becomes water-saturated, the gas pathways are sealed. Certainly high pressures are needed to overcome the capillary threshold pressures for gas flow through the water-saturated seal. In clay-based materials, the gas migration behaviour is commonly characterized with the pressure threshold or breakthrough pressure, over which gas can flow through. Low gas breakthrough pressures are desired for the back-fill/seal systems to guarantee the integrity of the geological and engineered barrier system. So the gas breakthrough pressure was taken as an important criterion for the suitability of the selected materials for sealing repository.

##### 4.7.1 Gas breakthrough tests under constant volume conditions

Following the measurements of swelling pressure and water permeability of the compacted claystone-bentonite (80/20; 60/40) and bentonite-sand (70/30) mixtures constrained in oedometer cells (Figs. 4.14 - 15), gas breakthrough testing was carried out by injecting nitrogen gas into the water-saturated samples (D/L = 50mm/30mm). The

upstream gas pressure was stepwise increased with small increments of 0.2 to 0.5 MPa at intervals of several days until gas outflow occurred. The corresponding upstream pressure at the gas outflow is defined as the gas breakthrough pressure ( $P_b$ ). After the breakthrough event, the apparent effective gas permeability ( $K_g$ ) was measured in relation with increased gas pressures. Following that, the inlet was switched off to estimate gas shut-in pressure ( $P_i$ ) after declination of the upstream pressure with time to a lowest constant. The characteristics of the samples are given in Table 4.3.

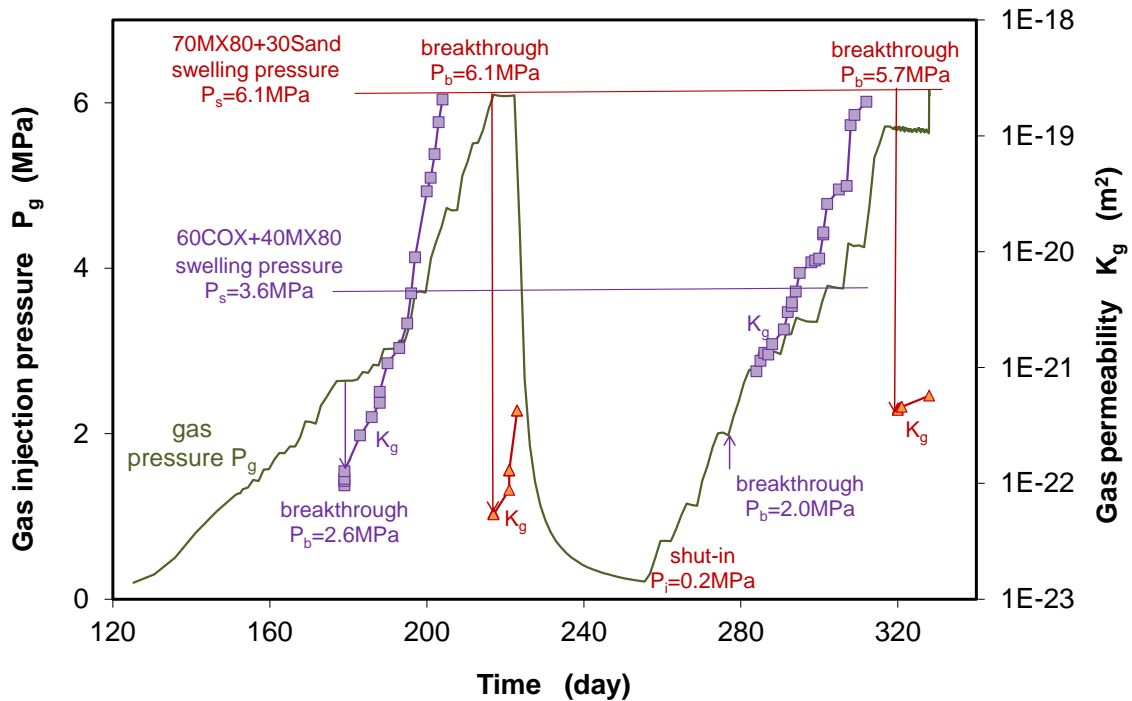
**Tab. 4.3** Characteristics of the water-saturated and compacted claystone-bentonite and bentonite-sand mixtures for gas testing

Material property	70MX80+30Sand	60COX+40MX80	80COX+20MX80
Grain size $d_{max}$ (mm)	2	5	5
Grain density $\rho_s$ (g/cm <sup>3</sup> )	2,75	2,73	2,72
Bulk density $\rho_b$ (g/cm <sup>3</sup> )	2,08	2,06	2,11
Dry density $\rho_d$ (g/cm <sup>3</sup> )	1,82	1,86	1,89
Porosity $\phi$ (%)	34,1	32,8	30,4
Swelling pressure $P_s$ (MPa)	6,1	3,6	2,7
Gas breakthrough pressure $P_b$ (MPa)	6,1	2,6	1,2
Gas shut-in pressure $P_b$ (MPa)	0,2	-	0,3

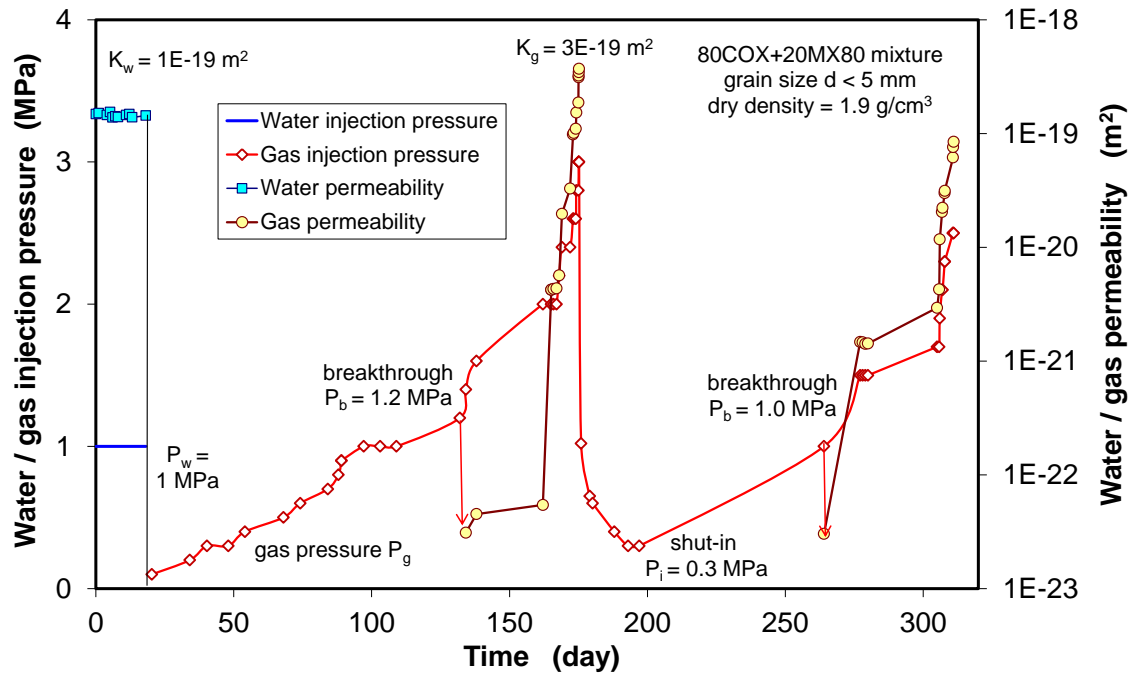
Fig. 4.23 shows results of the gas tests on the water-saturated mixtures under constant volume conditions. The gas breakthrough pressures identified are  $P_b = 2.6$  MPa for 60COX+40MX80 (Fig. 4.23a) and  $P_b = 1.2$  MPa for 80COX+20MX80 (Fig. 4.23b) respectively. The values are lower than their respective swelling pressures of  $P_s = 3.7$  and 2.7 MPa. In contrast, the event of gas breaking through the bentonite-sand mixture (70MX80+30Sand) occurred at a high pressure  $P_b = 6.1$  MPa equal to the external confining stress (Fig. 4.23a). When the gas injection was stopped, the upstream pressure fell quickly and declined with time to a low value of  $P_i \leq 0.3$  MPa at 80COX+20MX80 (Fig. 4.23b) and  $P_i \approx 0.2$  MPa at 70MX80+30Sand (Fig. 4.23a). The shut-in pressure indicates the shut-off of the interconnected gas pathways and therefore is referred to as the minimum capillary displacement pressure and/or as the minimum internal gas pressure capable of maintaining the network. During the shut-in phase, the previously created gas

pathways are going to reseal under effects of clay swelling and compression with reducing the pore pressure. Reopening the pathways again also needs certainly high gas pressures to overcome the rebuilt capillary thresholds, as indicated by the second breakthrough tests.

After breakthrough event, the effective gas permeability increases rapidly with increasing gas pressure, as shown in Fig. 4.24 for both the claystone-bentonite samples. At a given gas pressure, the permeability recorded during the second gas flowing phase is relatively higher than during the first phase. Post-testing measurements showed that all the samples remained almost fully water-saturated. It means that the gas passed only through a very limited pathways and negligible amount of water was displaced out.



a) Claystone-bentonite (60/40) and bentonite-sand (70/30) mixtures



b) Claystone-bentonite (80/20) mixture

**Fig. 4.23** Gas breakthrough pressures and permeability of the compacted claystone-bentonite and bentonite-sand mixtures (a-b)

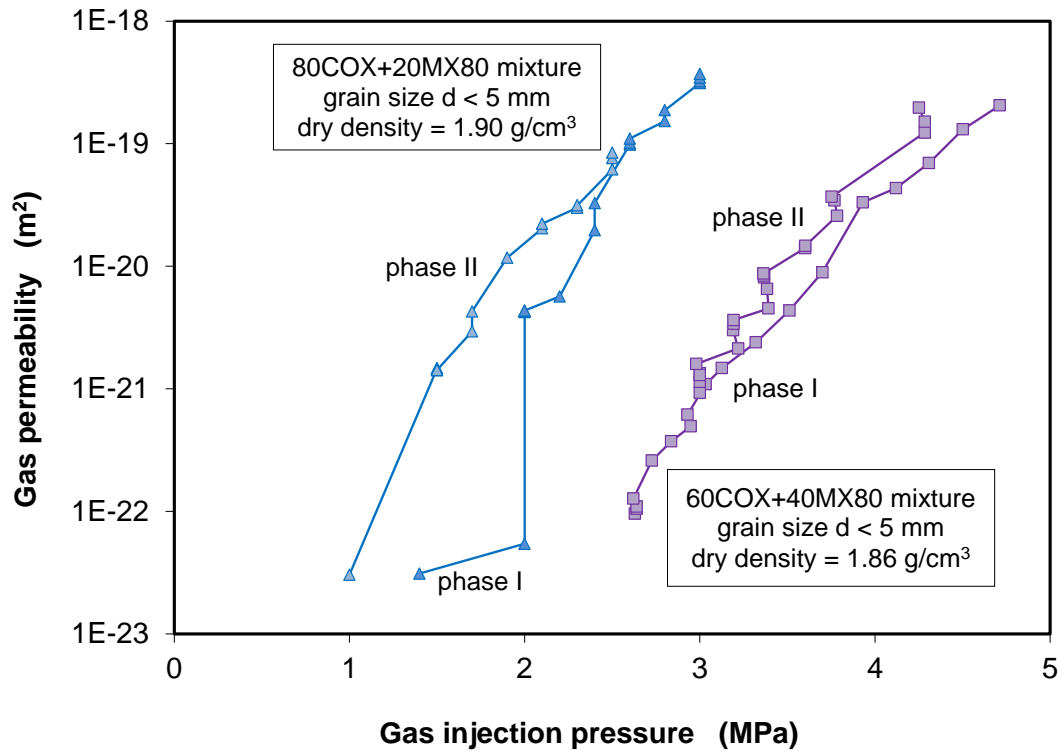


**Fig. 4.24** Gas breakthrough permeability as a function of gas pressure

#### 4.7.2 Gas breakthrough tests under constant stress conditions

In another series of gas tests, the gas flow properties of three other compacted mixtures were simultaneously examined under hydrostatic confining stresses in a pressure vessel:

1. Claystone ( $d < 10$  mm) with a compacted dry density of  $1.93 \text{ g/cm}^3$ ;
2. MX80 bentonite powder ( $d < 0.5$  mm) with a dry density of  $1.76 \text{ g/cm}^3$ ;
3. Bentonite-sand mixture (65/35;  $d < 2$  mm) with a dry density of  $1.90 \text{ g/cm}^3$ .

The samples were prepared by hand stamping the loose mixtures in rubber jackets of 100 mm diameter and 160 mm length, covered by sintered porous discs, and compacted in an oil pressure vessel up to a confining stress of 12 MPa. Fig. 4.25 illustrates schematically the assembly of the samples in the apparatus. Each sample was connected via sintered porous discs to upstream and downstream lines at both end faces. Before gas testing, a water saturation phase had been performed using the synthetic COX clay water for a long duration of 1.5 years. However, only the compacted crushed claystone was fully saturated and a very low water permeability of  $K_w = 2 \cdot 10^{-20} \text{ m}^2$  was determined. Because no water outflow was detected at the other bentonite-based samples, their saturation state could not be estimated.

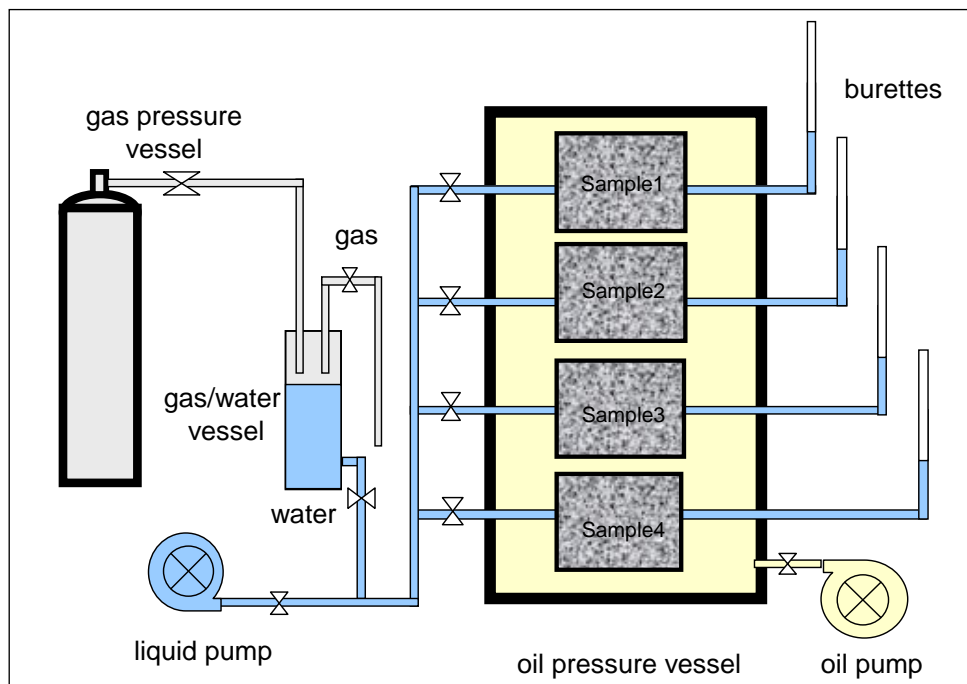


**Fig. 4.25** Schematic illustration of the water and gas flow tests with seal mixtures

The gas injection was performed by stepwise increasing pressure up to the levels of the applied confining stresses of 2 to 8 MPa. Fig. 4.26 depicts the evolution of applied confining stress, gas injection pressure, and gas permeability obtained on the compacted claystone. Whereas the gas breakthrough pressures observed at the compacted crushed claystone are still below the confining stresses, both the compacted bentonite-based samples maintained gas tight at pressures close to the confining stresses. This finding is consistent with the common observations made on the compacted bentonite and bentonite-sand mixture /BIR 13/ /SHA 15/, i.e. gas intrusion only occurs when the pressure of the external gas phase equals or exceeds the confining pressure (equivalent to the swelling pressure) of the bentonite.

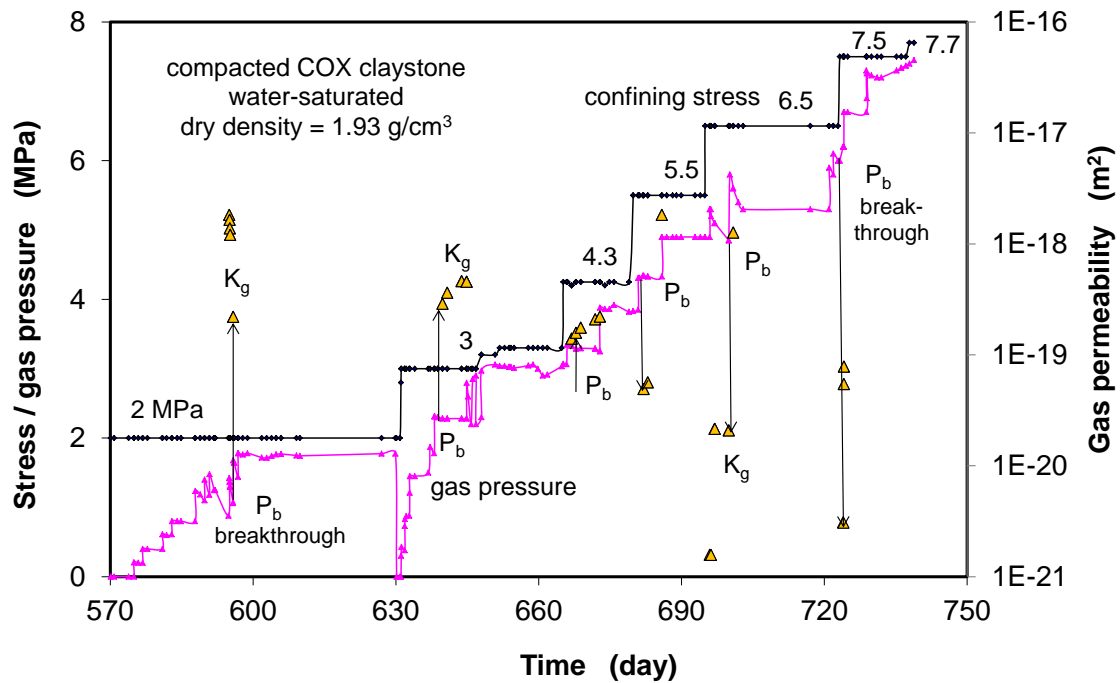


**Fig. 4.26** Gas breakthrough pressures and permeabilities obtained on the compacted and water-saturated claystone aggregate at different confining stresses

For the compacted crushed claystone, the gas breakthrough pressures recorded are directly related to the confining stress. Fig. 4.27 illustrates the relationships of gas breakthrough pressure and permeability with confining stress for the material. Whereas the gas breakthrough pressure increases linearly with confining stress, the gas permeability decreases exponentially. The fitting curves can be presented by

$$P_b = \alpha\sigma - b \quad (4.3)$$

where the parameters  $a = 1$  and  $b = 1.3$  MPa are determined by fitting the data.

The relationship of gas permeability to the confining stress can be expressed by

$$K_g = K_o \exp(-\sigma) \quad (4.4)$$

where the factor  $K_o = 8 \cdot 10^{-18} \text{ m}^2$  determined is the gas permeability at zero confining stress ( $\sigma = 0$ ).

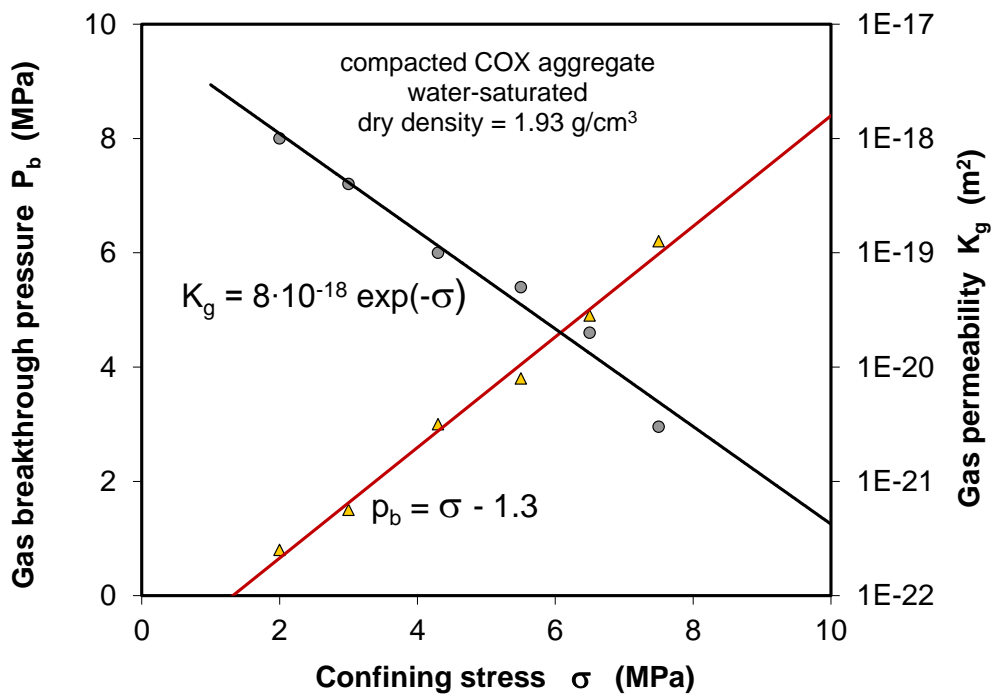


**Fig. 4.27** Gas breakthrough pressure and permeability as function of confining stress

An additional gas test was carried out on the 60COX+80MX80 sample with a dry density of  $1.91 \text{ g/cm}^3$  at confining stress of 2 MPa. The sample ( $D/L = 50\text{mm}/100\text{mm}$ ) had been fully saturated during the measurement of water permeability (Fig. 4.18). Fig. 4.28 shows that the gas pressure was stepwise increased from 0.3 to 1.8 MPa, during which no clear breakthrough event could be observed. Switching off the inlet, however, the gas pressure declined gradually with time down to 1.3 MPa at 6 months. It implies that the sample was not gas tight at pressures of higher than 1.3 MPa.

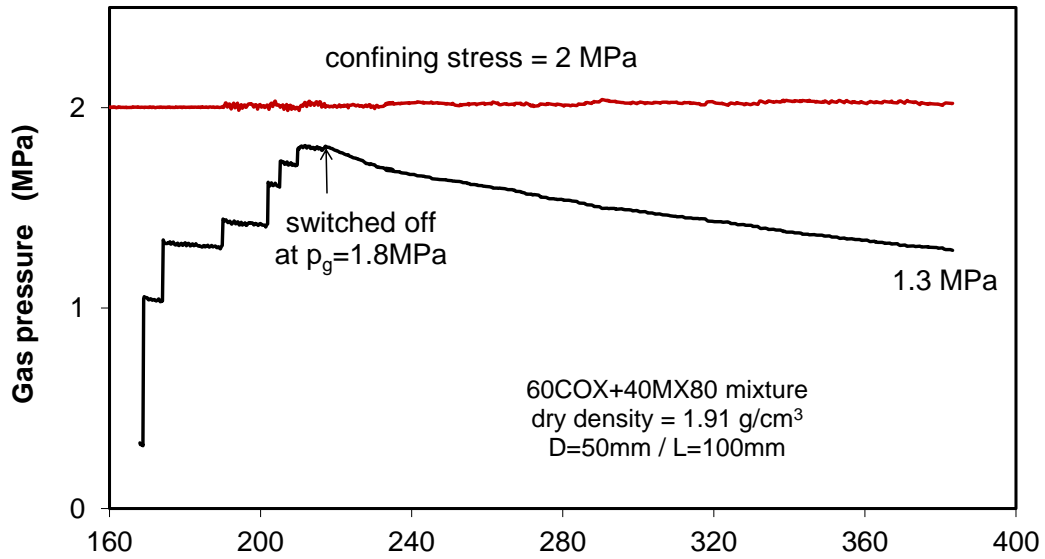


**Fig. 4.28** Evolution of gas injection pressure after switching off the inlet to the water-saturated claystone-bentonite mixture

Following the measurement of water permeability of the compacted claystone aggregate in the large-scale experiment (Fig. 4.21), nitrogen gas was injected by stepwise increasing pressure, as shown in Fig. 4.29. At a low injection pressure of 0.2 MPa, gas outflow was observed, indicating a low gas breakthrough pressure.

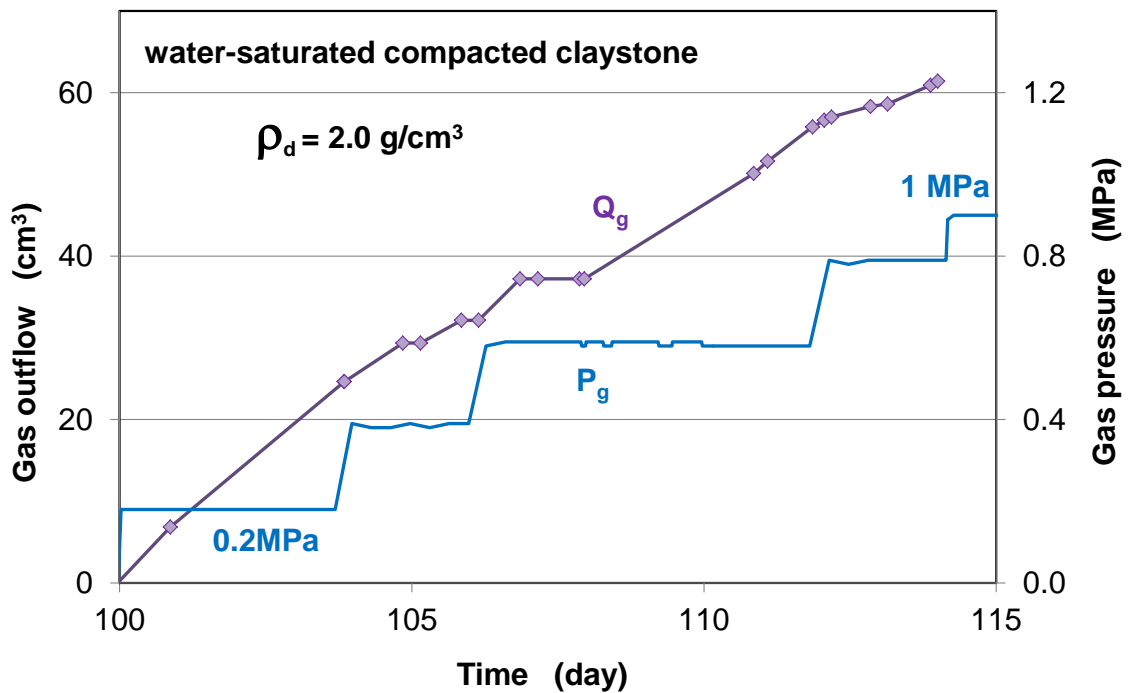


**Fig. 4.29** Gas flow through the water-saturated and compacted claystone aggregate

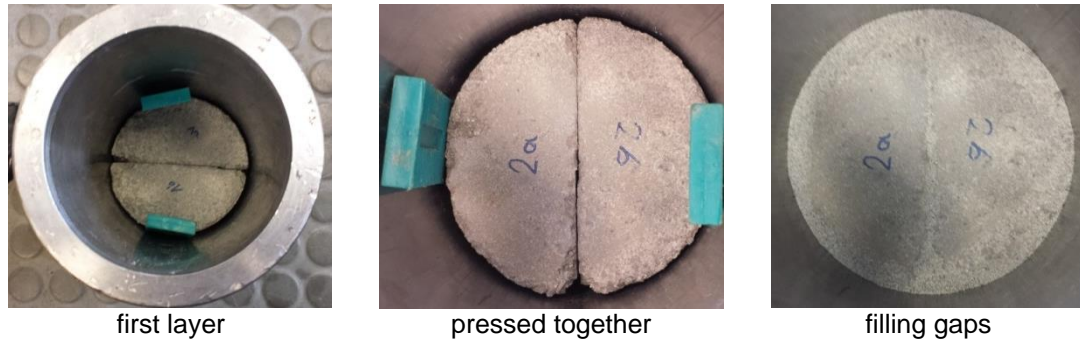
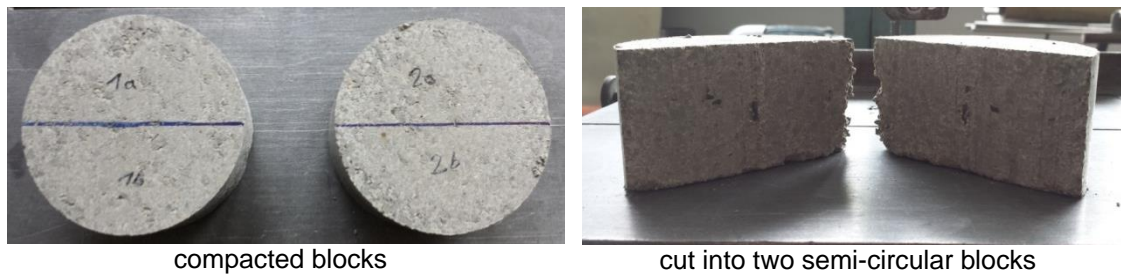
#### 4.8 Borehole sealing performance

As a technical concept (chapter 2), the seals in drifts are constructed with compacted blocks of clay-based mixtures between concrete plugs. Gaps between blocks and drift walls are filled with bentonite pellets. In order to examine sealing effects of the investigated materials, small-scale borehole sealing tests were conducted on the compacted claystone-bentonite (60COX+40MX80) and bentonite-sand (70MX80+30Sand) mixtures in steel cylinders. The mixtures were prepared to cylindrical blocks of 95 mm diameter and 50 mm height:

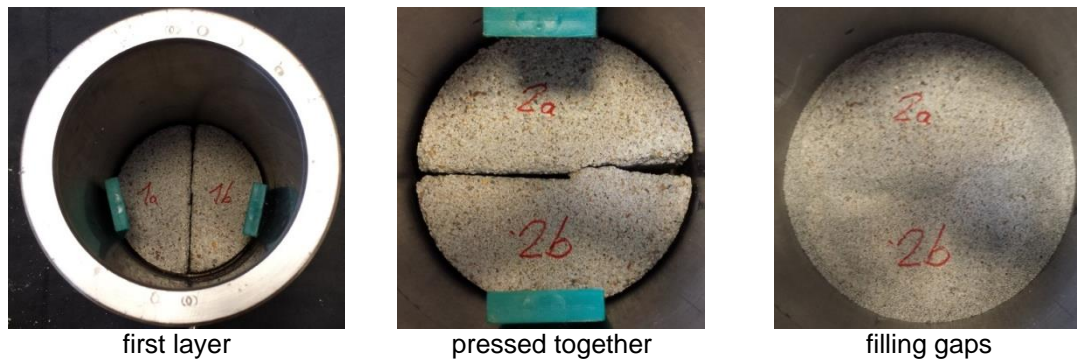
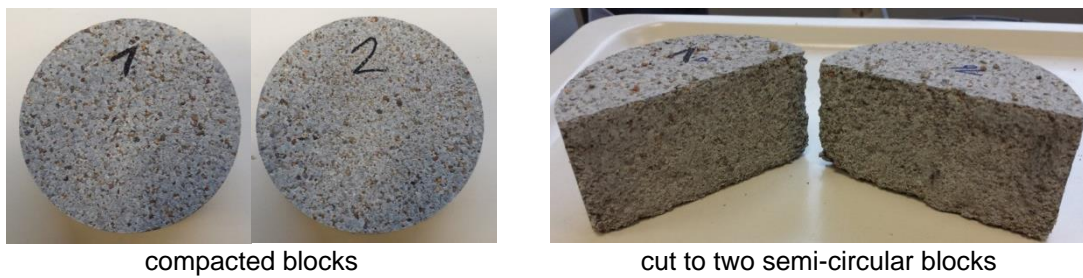
- Claystone-bentonite blocks: mixed with crushed claystone of  $d < 5$  mm and MX80 bentonite powder of  $d < 0.5$  mm in a ratio of COX/MX80 = 60/40 and compacted to an average dry density of  $1.88 \text{ g/cm}^3$  and water content of 7.0 %;
- Bentonite-sand blocks: mixed with MX80 bentonite of  $d < 0.5$  mm and quartz sand of  $d < 2$  mm in a ratio of MX80/Sand = 70/30 and compacted to an average dry density of  $1.82 \text{ g/cm}^3$  and water content of 10.7 %.

Fig. 4.30 shows photos of the installation of the blocks in the steel cylinders. The blocks were cut along the length cross the central axis into semi-circular blocks and then installed in two layers into steel cylinders of 100 mm diameter and 100 mm length. The total gap of 5 mm width between the cell wall and the blocks was filled with the bentonite powder and stamped by hand to a dry density of  $1.20 \text{ g/cm}^3$ . Both ends of each sample were covered with sintered porous discs allowing water and gas flow. A pressure sensor was installed at the top of the cell between piston and cap to monitor evolution of swelling pressure during water saturation. The testing setup is shown in Fig. 4.31. The relevant in situ conditions in a drift seal system were identically applied to both samples:

1. Water saturation by introduction of the synthetic COX clay water to the seal bottom at atmospheric pressure, whereby swelling pressures in the seals were recorded;
2. Increasing water injection pressure to simulate high pore pressures and pressure gradients developed in the drift seals, whereby water permeabilities of the seals were measured;
3. Gas injection to simulate gas generation in a repository, whereby gas flow behaviour of the seals was examined by measuring gas breakthrough pressures and flow rate.

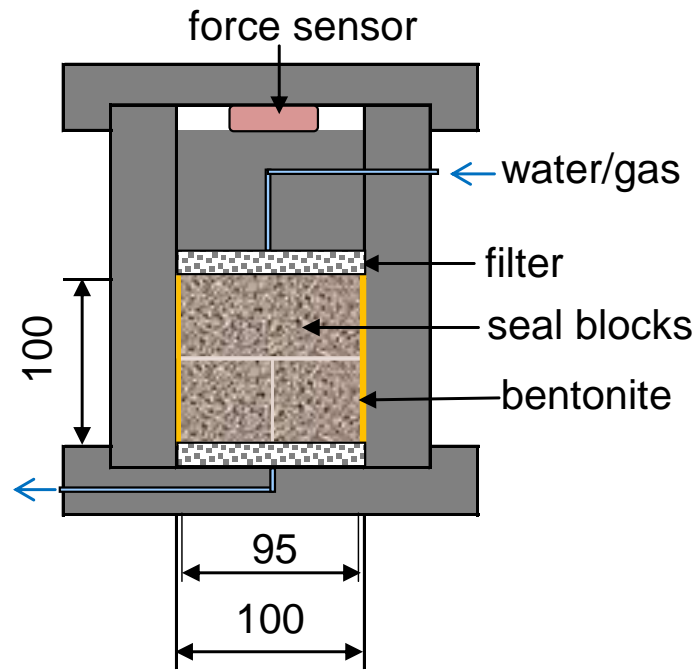


a) Installation of 60COX+40MX80 semi-circular blocks in a steel cylinder



b) Installation of 70MX80+30Sand semi-circular blocks in a steel cylinder

**Fig. 4.30** Installation of small-scale borehole sealing tests in steel cylinders with compacted blocks of the claystone-bentonite and bentonite-sand mixtures and bentonite powder filling the gaps



a) Assemble of compacted blocks in a cell



b) Setup of borehole sealing tests

**Fig. 4.31** Setup of the small-scale borehole sealing tests in steel cylinders with compacted blocks of claystone-bentonite and bentonite-sand mixtures (a-b)

### Water saturation and induced swelling pressure

Fig. 4.32 plots the evolution of water uptake and swelling pressure of both seals during the first water saturation phase over 8 months. Whereas the water uptake increased gradually with time, the resulting swelling pressure built up quickly within the first one to two months up to 2.1 MPa at seal 60COX+40MX80 and 2.5 MPa at seal 70MX80+30Sand. After the peak, the swelling pressures of both seals declined gradually to a same value of about 2.0 MPa. Comparing with the swelling pressures developed in the compacted blocks from both mixtures in Fig. 4.15, one can find out that

- the development of swelling pressure is qualitatively not differing from the individual compacted blocks and the seals consisting of the blocks and bentonite powder;
- the magnitude of swelling pressure is relatively lower in each assembled seal than that of the compacted blocks because the density of the bentonite powder filled in the gap is much low, leading to a small swelling pressure.

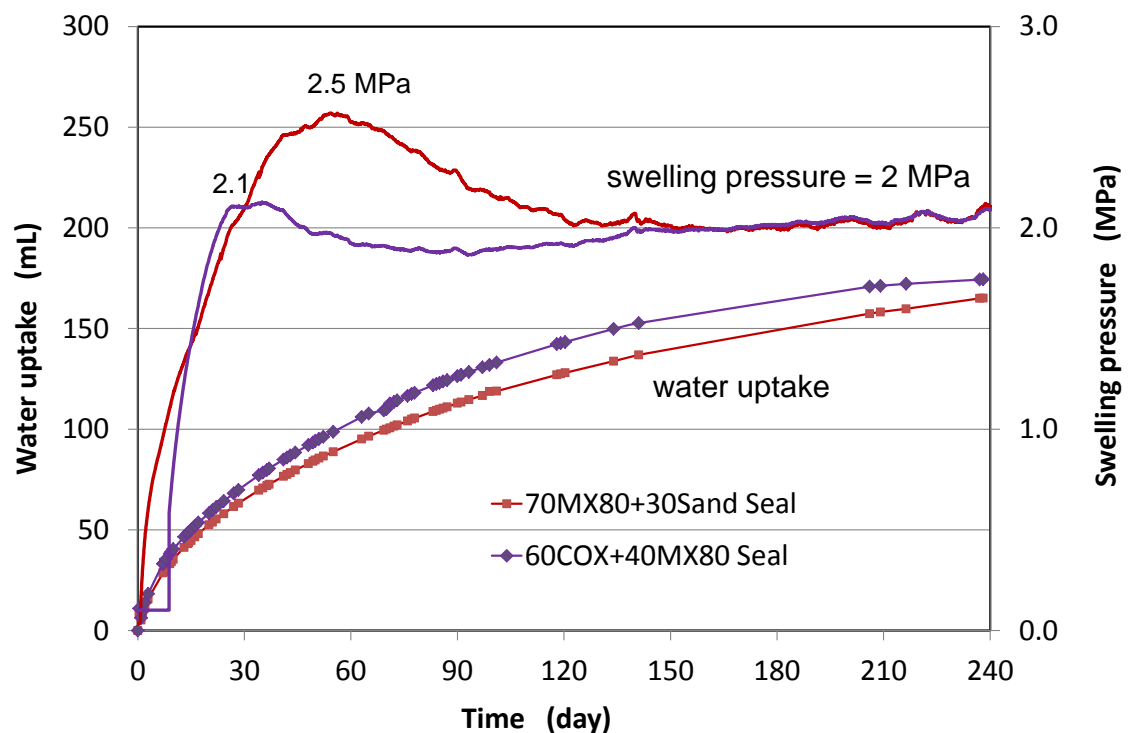


**Fig. 4.32** Water uptake and resulting swelling pressure in the claystone-bentonite and bentonite-sand seals assembled in steel cylinders during the water saturation phase

### Water injection and permeability

During the second phase with water injection, the injection pressure was increased step-by-step from 0.2 MPa to 0.6, 1.0, 1.2, 1.6 and 1.5 MPa for a year. Fig. 4.33 shows the applied water pressure and the amounts of the water injected into the claystone-bentonite and bentonite-sand seals. With increasing the injection pressure, the water inflow steadily increased. Unfortunately, the pump failed at the high pressure level of 1.6 MPa for 5 months, resulting in a large fluctuation of the pressure and slowing the water inflow. After preparation, the injection pressure could be kept relatively constant. Water outflow was observed over about 1.5 years. During the relatively constant flow over another month, the water permeability was estimated to  $K_w \approx 5 \cdot 10^{-20} \text{ m}^2$  for the claystone-bentonite seal and  $K_w \approx 3 \cdot 10^{-20} \text{ m}^2$  for the bentonite-sand seal. Both values are very close and comparable to those obtained on the individual compacted blocks (cf. Fig. 4.22). After reducing the injection pressure down to 1.5 MPa, the water flow was slowed.

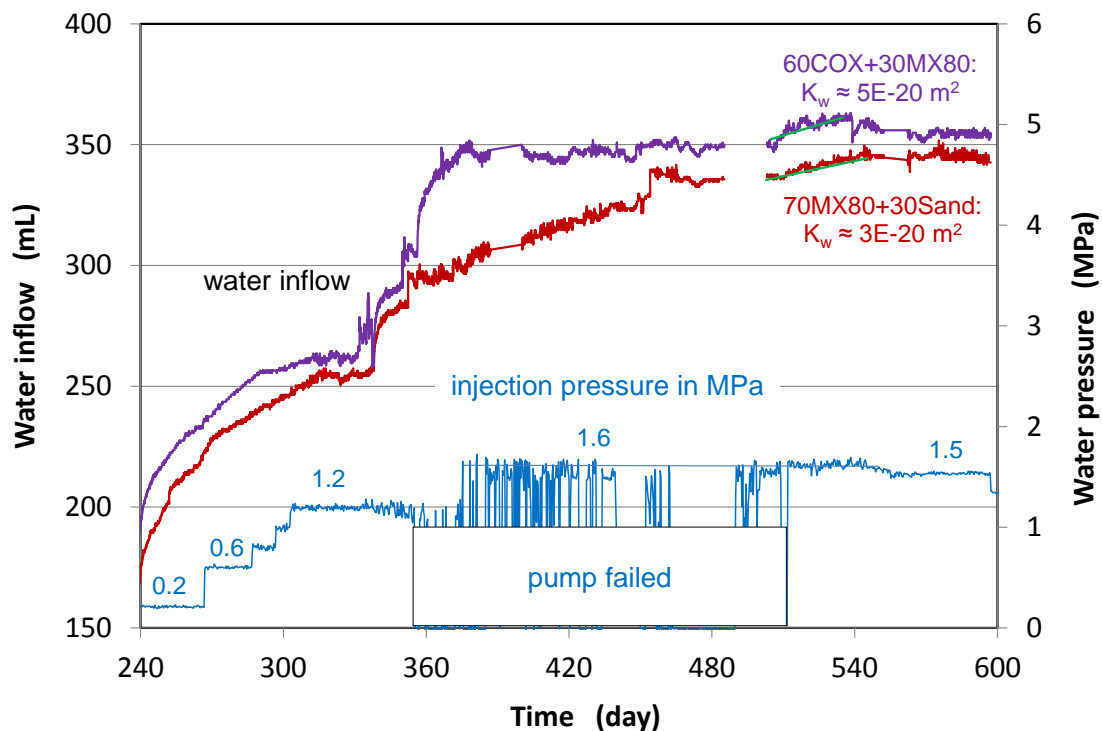


**Fig. 4.33** Water inflow into the claystone-bentonite and bentonite-sand seals assembled in steel cylinders at increased injection pressures

## **Gas migration**

After water saturation, gas testing was carried out by simultaneously injecting nitrogen gas into the upstream faces of both parallel samples. The gas injection was controlled at a low flow rate of 0.2 mL/min using a syringe-pump with a cylinder capacity of 280 mL. The downstream reservoirs of the samples were filled with the synthetic COX clay water at atmospheric pressure. Fig. 4.34 illustrates results of the tests. It can be seen that the upstream gas pressure built up gradually with time. Over 2 days, a gas breakthrough took place firstly at the claystone-bentonite seal at a peak pressure of  $P_b = 4$  MPa, whereby gas bubbles appeared in the downstream tube. Immediately switching-off the upstream led to a gradual reduction of the gas pressure down to a constant minimum value or shut-in pressure of  $P_i = 0.8$  MPa over 3 days. Injecting gas again resulted in a relatively lower breakthrough pressure of  $P_b = 3.6$  MPa and a lower shut-in pressure of  $P_i = 0.5$  MPa. The breakthrough pressure reduced further to 3.1 MPa during the third gas injection stage. The observations during the multi-stage gas tests on the claystone-bentonite seal indicate that (a) the maximal gas pressure is reached at the first breakthrough event, (b) the created pathways tend to be closed after breakthrough under effects of the increased effective stress with the gas release and pressure reduction, and (c) reopening the pathways needs sufficiently high gas pressures to overcome the rebuilt capillary thresholds, depending on the sealing intensity of the pathways.

After switching-off the upstream pressure of the claystone-bentonite seal, the gas injection continued to the bentonite-sand seal at the same flow-rate. The corresponding gas pressure increased rapidly to a high value of 8.2 MPa, then dropped suddenly down to 0.5 MPa and increased gradually again to 3 MPa, at which the gas injection was stopped. The switching-off did not lead to any change of the pressure, indicating gas tight of the seal. Further injecting gas led high pressures of about 9 MPa. The higher breakthrough pressures after the first peak seemed unusual, which cannot be explained yet.

An important finding is that the bentonite-sand seal has a high gas breakthrough pressure, being two times that of the claystone-bentonite seal. This is consistent with the observation made on the compacted blocks from both mixtures (cf. Fig. 4.23a). However, the gas breakthrough pressure values of the seals are higher than those of the compacted blocks. This might be attributed to the effects of the sample sizes and gas flow-rates. Small sample size with short pathways and low gas flow-rates usually yield relatively lower gas breakthrough pressures.

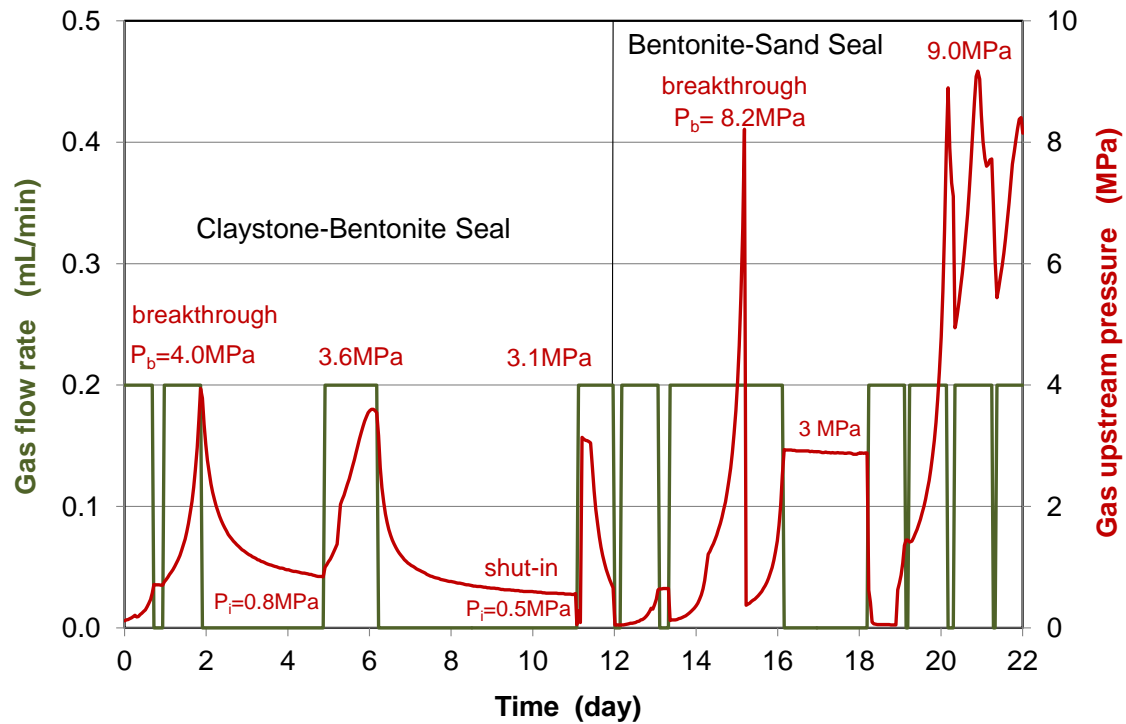


**Fig. 4.34** Results of gas injection tests on the claystone-bentonite and bentonite-sand seals assembled in steel cylinders

#### 4.9 Evaluation of the studied clay-based mixtures as seal material

As a potential material for sealing repositories in clay formations, excavated claystone mixed with bentonite was investigated in comparison to bentonite and bentonite-sand mixture. The crushed COX claystone mixed with small proportions of bentonite MX80 up to 40 %, MX80 bentonite and bentonite-sand mixture in a ratio of 70/30 were characterized with respect to the sealing properties such as compressibility and compacted density, water uptake and retention, swelling capacity, water permeability, gas entry/breakthrough pressure and permeability after full water saturation. The sealing performance of the claystone-bentonite and bentonite-sand mixtures were also examined by sealing steel tubes. The important sealing properties of the compacted mixtures are summarized in Table 4.4.

**Tab. 4.4** Summary of the key sealing properties of the compacted claystone-bentonite and bentonite-sand mixtures

Sealing properties	Crushed claystone	Claystone-bentonite (80/20)	Claystone-bentonite (60/40)	Bentonite-sand (70/30)	Bentonite (MX80)
Grain size (mm)	< 10	< 5	< 5	< 2	< 2
Dry density (g/cm <sup>3</sup> )	2.00	1.86-1.90	1.82-1.90	1.80	1.56
Water permeability (m <sup>2</sup> )	5·10 <sup>-20</sup>	(1-2)·10 <sup>-19</sup>	(1-3)·10 <sup>-20</sup>	2·10 <sup>-20</sup>	6·10 <sup>-21</sup>
Swelling pressure (MPa)	2.0	2.5	3.5	6.0	7.5
Gas breakthrough pressure (MPa)	1.0	1.2	2.5	6.0	≥7.5

Seals installed in steel tubes (L/D=100/100mm)	Claystone-bentonite (60/40)	Bentonite-sand (70/30)
Grain size (mm)	< 5	< 2
Dry density (g/cm <sup>3</sup> )	1,88	1,80
Water permeability (m <sup>2</sup> )	5·10 <sup>-20</sup>	3·10 <sup>-20</sup>
Swelling pressure (MPa)	2.0	2.0
Gas breakthrough pressure (MPa)	4.0	8.2 – 9.0

The following conclusions can be drawn from the experiments:

- **Compacted density:** The crushed claystone and claystone-bentonite mixtures (80/20; 60/40) can be compacted to higher dry densities because of the favourable grain size distributions, compared with the fine-grained bentonite and bentonite-sand mixture.
- **Mechanical stiffness:** The mechanical stiffness of the mixtures increases with dry density exponentially. At a given density, the stiffness of the claystone aggregate and claystone-bentonite mixture is higher than that of the pure bentonite and bentonite-sand mixture.
- **Water uptake and retention:** All the clay-based mixtures can take up water from humid environment. The amount of water uptake increases with increasing bentonite

content and air humidity. The maximum amounts of water uptake reached in water vapour are: 45 - 48 % at the bentonite, 32 % at the bentonite-sand mixture, 20 - 28 % for the claystone-bentonite mixtures, and 12 % at the claystone.

- Water saturation: The water saturation of the compacted clay-based mixtures is governed by diffusion of water molecules through unsaturated pores under effect of suction. The rate of water saturation is strongly dependent on the porosity or density and bentonite content. The high density and bentonite content hinder the water saturation. Under same conditions, the water saturation of the compacted claystone aggregate and claystone-bentonite mixture is faster than the bentonite and bentonite-sand mixture.
- Swelling capacity: Swelling pressure builds up upon water uptake in the compacted mixtures under confined conditions, or the volume expands under unconfined conditions. The swelling capacity of the compacted mixtures increases with increasing bentonite content and dry density.
- Water conductivity: All the compacted mixtures show very low water permeabilities of  $10^{-19} - 10^{-20} \text{ m}^2$  close to that of the intact clay rock.
- Gas migration: Gas breakthrough pressures of the compacted claystone aggregate and claystone-bentonite mixture are lower than the external confining stresses. In contrast, the gas breakthrough pressures of the compacted bentonite and bentonite-sand mixture are quite high close to and even above the confining stresses.

The test findings suggest that the compacted claystone-bentonite mixture with small proportions of bentonite less than 40 % is a suitable seal material with the favourable sealing properties. Particularly, the claystone-bentonite mixture allows gas flow through under low pressures without violating the integrity of the geological-engineered barrier system.



## 5 Modelling of hydro-mechanical processes in a seal system

For the last decade, GRS has used the FEM code CODE\_BRIGHT /UPC 15/ for analysis of coupled thermo-hydro-mechanical (THM) processes in repositories in clay formations. This code was developed by the Technical University of Catalonia in Barcelona. The theories of the THM modelling are presented by the code developer /OLI 94/, /GEN 98/06/ and /UPC 15/. There are constitutive models implemented for description of the THM behaviour of the geo-materials. For modelling and analysis of the long-term sealing processes of a seal system, one has to validate the constitutive models for the individual components of the seal system such as the clay-based seal core, concrete plugs, EDZ, host rock, and others. The associated parameters for the materials have to be determined from laboratory experiments. In order to enhance the predictive capability of the models for the long-term performance of the seal system, some of the constitutive models need to be modified or new ones to be formulated for some specific aspects, for instance, long-term deformation of clay rock, permeability changes due to damage and reconsolidation, and so on. The main objectives of the modelling work defined for this project are:

- Identification of adequate constitutive models and parameters for the studied seal materials including the compacted bentonite, bentonite-sand mixture and claystone-bentonite mixture;
- Evaluation and improvement of the existing constitutive models for the clay rock by development of new constitutive equations for the long-term deformation, fracturing-induced permeability, permeability change by compression, water permeability of fractured claystone under load, and gas migration in water-saturated and resealed claystone;
- Model simulation of typical laboratory experiments performed on the seal materials and claystone for validation of the constitutive models applied;
- Predictive modelling of the long-term sealing performance of a drift seal.

### 5.1 Fundamental theories of coupled THM modelling

#### 5.1.1 THM coupling phenomena

Geological and geotechnical porous materials are composed of three species: mineral, water and air; and distributed as three phases: solid ( $s$ ), liquid ( $l$ ) and gas ( $g$ ). The liquid phase contains liquid water and dissolved air, while the gas phase is a mixture of dry air

and water vapour. In the porous media that are simultaneously subjected to thermal, hydraulic and mechanical conditions, complex THM processes and interactions take place as for instance,

- Thermal loading inducing deformation and stress variations ( $T \rightarrow M$ ) and expansion of porewater as well as pore pressure changes ( $T \rightarrow H$ );
- Mechanical loading leading to changes in porosity / cracks and hydraulic conductivity ( $M \rightarrow H$ ) as well as thermal conductivity ( $M \rightarrow T$ );
- Pore pressure changes being directly related with the effective stress ( $H \rightarrow M$ ), and water saturation as well as water/gas flow influencing the heat transfer and the temperature field ( $H \rightarrow T$ ).

According to /GEN 06/, the important aspects of THM coupling are illustrated in Fig. 5.1.

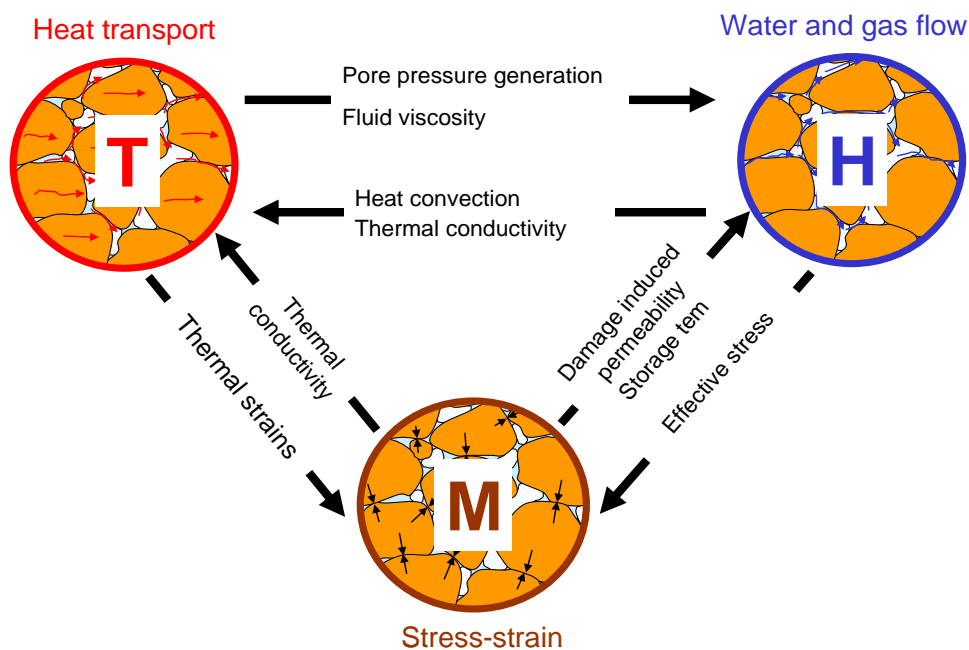


**Fig. 5.1** Main relations between THM processes in porous media /GEN 06/

The development of the code CODE\_BRIGHT takes into account the most important coupled THM phenomena /UPC 15/. A number of general assumptions are made in the formulation of the coupled THM problems encountered in unsaturated porous materials:

1. Dry air is considered a single species and, usually, it is the main component of the gaseous phase and equilibrium of dissolved air is expressed by Henry's law;

2. Vapour concentration is in equilibrium with the liquid phase, and the psychrometric law expresses its concentration;
3. Thermal equilibrium between solid-liquid-gas phases is assumed, i.e. the three phases having the same temperature;
4. Balance of momentum for the medium as a whole is reduced to the equation of stress equilibrium together with a mechanical constitutive model to relate stresses with strains;
5. Small strains and small strain rates are assumed for solid deformation;
6. State variables are solid displacements, liquid pressure, gas pressure, and temperature.

### 5.1.2 Balance equations

For the calculations of coupled THM processes in the porous media, a set of balance equations for internal energy, solid mass, water mass, air mass, and stress equilibrium are to be solved in a consistent way /UPC 15/.

#### Energy balance:

Any energy supply is balanced by the total heat flux through the medium and its total internal energy:

$$\frac{\partial}{\partial t} (E_s \rho_s (1 - \phi) + E_l \rho_l S_l \phi + E_g \rho_g S_g \phi) + \nabla \cdot (\mathbf{i}_c + \mathbf{j}_{Es} + \mathbf{j}_{El} + \mathbf{j}_{Eg}) = f^E \quad (5.1)$$

where  $E_s$ ,  $E_l$  and  $E_g$  are specific internal energies corresponding to solid, liquid and gas phase, respectively;  $\rho_s$ ,  $\rho_l$  and  $\rho_g$  are the densities of the three phases;  $\phi$  is the porosity,  $S_l$  is the volumetric liquid fraction and  $S_g$  is the volumetric gas fraction with respect to the pore volume,  $S_l + S_g = 1$ ;  $\mathbf{i}_c$  is the conductive heat flux;  $\mathbf{j}_{Es}$ ,  $\mathbf{j}_{El}$  and  $\mathbf{j}_{Eg}$  are the advective energy flux of each of the three phases with respect to a fixed reference system;  $f^E$  is the energy supply per unit volume of medium;  $t$  is time and  $\nabla$  is the divergence operator.

**Solid mass balance:**

The mass balance of solid present in the medium is expressed as:

$$\frac{\partial}{\partial t}(\rho_s(1 - \phi)) + \nabla \cdot (\mathbf{j}_s) = 0 \quad (5.2)$$

where  $\rho_s$  is the density of the solid and  $\mathbf{j}_s$  is the flux of solid.

**Water mass balance:**

Water is present in liquid and gas phases. The total mass balance of water is expressed as:

$$\frac{\partial}{\partial t}(\theta_l^w S_l \phi + \theta_g^w S_g \phi) + \nabla \cdot (\mathbf{j}_l^w + \mathbf{j}_g^w) = f^w \quad (5.3)$$

where  $\theta_l^w$  and  $\theta_g^w$  are the masses of water per unit volume of liquid and gas, respectively;  $\mathbf{j}_l^w$  and  $\mathbf{j}_g^w$  denote the total mass fluxes of water in the liquid and gas phases (water vapour), with respect to a fixed reference system.  $f^w$  is an external supply of water per unit volume of medium.

**Air mass balance:**

Dry air is present in liquid and gas phases. The total mass balance of dry air is expressed as:

$$\frac{\partial}{\partial t}(\theta_l^a S_l \phi + \theta_g^a S_g \phi) + \nabla \cdot (\mathbf{j}_l^a + \mathbf{j}_g^a) = f^a \quad (5.4)$$

where  $\theta_l^a$  and  $\theta_g^a$  are the masses of dry air per unit volume of liquid and gas, respectively;  $\mathbf{j}_l^a$  and  $\mathbf{j}_g^a$  denote the total mass fluxes of dry air in the liquid and gas phases, with respect to a fixed reference system;  $f^a$  is an external supply of dry air per unit volume of medium.

**Stress equilibrium:**

The balance of momentum for the porous medium reduces to the equilibrium equation in total stresses:

$$\nabla \cdot \boldsymbol{\sigma} + \mathbf{b} = 0 \quad (5.5)$$

where  $\boldsymbol{\sigma}$  is the stress tensor and  $\mathbf{b}$  is the vector of body forces.

### Equilibrium restrictions:

Equilibrium restrictions are given for the concentration of water vapour in gas and of dissolved air in water. The mass of water vapour per unit volume of gas ( $\theta_g^w$ ) is determined via the psychrometric law:

$$\theta_g^w = (\theta_g^w)^0 \exp \left[ \frac{-(P_g - P_l)M_w}{R(273.15 + T)\rho_l} \right] \quad (5.6)$$

where  $P_l$  and  $P_g$  are liquid and gas pressures, respectively,  $(\theta_g^w)^0$  is the vapour density in the gaseous phase in contact with a planar surface (i.e. when  $P_g - P_l = 0$ ),  $M_w$  is the molecular mass of water (0.018 kg/mol),  $R$  is the gas constant (8.314 J/mol·K) and  $T$  is the temperature (in degree Celsius).  $(\theta_g^w)^0$  is depending on temperature. The vapour partial pressure is computed by means of the ideal gas law.

The solubility of air in water is controlled by Henry's law:

$$\omega_l^a = \frac{P_a}{H} \cdot \frac{M_a}{M_w} \quad (5.7)$$

where  $\omega_l^a$  is the mass fraction of air in the liquid,  $P_a$  is the partial pressure of air,  $M_a$  is the molecular mass of air (0.02895 kg/mol) and  $H = 10000$  MPa is Henry's constant. According to the definition of partial density,  $\theta_l^a = \omega_l^a \cdot \rho_l$ .

## 5.2 Modelling of the hydro-mechanical behaviour of seal materials

### 5.2.1 Basic properties

Three seal materials are selected for modelling and analysing the long-term performance of a drift seal:

1. The compacted bentonite that has been extensively characterised as buffer/seal in HLW repositories in crystalline and clay rocks, for instance, bentonite MX80 /ÅKE 10/13/ and bentonite FEBEX /VOL 96/, /GEN 98/;
2. The compacted bentonite-sand mixture with a ratio of MX80/Sand = 70/30 that has being investigated by ANDRA for drift sealing in the COX clay rock at the MHM-URL /DEL 15/;
3. The compacted claystone-bentonite mixture with a ratio of COX/MX80 = 60/40 as a favourable alternative material for drift sealing in clay rock;

The basic properties of the selected materials are summarised in Table 5.1. The data of the bentonite MX80 are taken from literature /ÅKE 10/, while the data of the 70MX80+30Sand and 60COX+40MX80 mixtures are obtained from our own experiments presented in the previous chapter 4. Moreover, the data of the tested COX claystone are also compiled herein.

**Tab. 5.1** Basic characteristics of the selected seal materials

Material parameter	MX80 Bentonite	70MX80+30Sand	60COX+40MX80	COX Claystone
Grain density $\rho_s$ (g/cm <sup>3</sup> )	2.78	2.75	2.73	2.70
Dry density $\rho_d$ (g/cm <sup>3</sup> )	1.57	1.80	1.90	2.28
Bulk density $\rho_b$ (g/cm <sup>3</sup> )	1.84	2.00	2.03	2.41
Void ratio $e$ (-)	0.742	0.528	0.437	0.184
Porosity $\phi$ (-)	0.435	0.345	0.304	0.156
Intrinsic permeability $k_o$ (m <sup>2</sup> )	5x10 <sup>-21</sup>	2x10 <sup>-20</sup>	6x10 <sup>-20</sup>	6x10 <sup>-21</sup>
Water content $w$ (%)	17.0	9.0	7.0	5.5
Degree of water saturation $S_l$ (%)	61.0	47.0	44.0	81.0

### 5.2.2 Hydraulic constitutive models

Advective and diffusive transport of liquid and gas are considered the main processes in the drift seal. The following hydraulic models are adopted for description of the hydraulic behaviour of the selected seal materials.

### 5.2.2.1 Hydraulic conductivity

It is assumed that the advective liquid and gas flows follow Darcy's law:

$$q_\alpha = -K_\alpha(\nabla P_\alpha - \rho_\alpha \mathbf{g}) \quad (5.8)$$

where  $K_\alpha = \mathbf{k} k_{r\alpha} / \mu_\alpha$  is the permeability tensor. The intrinsic permeability tensor ( $\mathbf{k}$ ) depends on the pore structure of the porous medium. It is assumed here that the hydraulic properties are isotropic for the seal materials,  $\mathbf{k} \rightarrow k$ .  $k_{r\alpha}$  is the value of relative permeability that controls the variation of permeability in the unsaturated regime and  $\mu_\alpha$  denotes the dynamic viscosity.  $\alpha$  stands either for  $l$  or  $g$  depending on whether liquid or gas flow is considered.  $\mathbf{g}$  is the gravity vector. The variation of intrinsic permeability with porosity is given by:

$$k = k_o \cdot \frac{\phi^3}{(1-\phi)^2} \cdot \frac{(1-\phi_o)^2}{\phi_o^3} \quad (5.9)$$

where  $\phi_o$  is a reference porosity. Based on the measured data (Table 5.1), the  $k$ - $\phi$  relationships for the seal materials are illustrated in Fig. 5.2. Obviously, the permeability decreases with decreasing porosity.

### 5.2.2.2 Relative permeability

The relative permeabilities of the liquid and gas phases are dependent on the degree of liquid saturation according to:

$$k_{rl} = A \cdot S_l^\lambda \quad (5.10a)$$

$$k_{rg} = 1 - k_{rl} \quad (5.10b)$$

where  $S_l$  is the degree of liquid saturation defined in equation (5.11),  $A$  and  $\lambda$  are parameters.  $A = 1$  is commonly adapted, whereas  $\lambda$  depends on the material properties and varies in a range between 2 and 5 for the clay-based materials. Fig. 5.3 illustrates the relative liquid and gas permeability with  $\lambda = 2, 3, 4, 5$  as a function of degree of water saturation. It is obvious that the effective liquid flow is strongly dependent on the  $\lambda$ -value. High  $\lambda$ -values yield low relative water permeabilities at a given degree of water saturation and conversely high relative gas permeabilities.

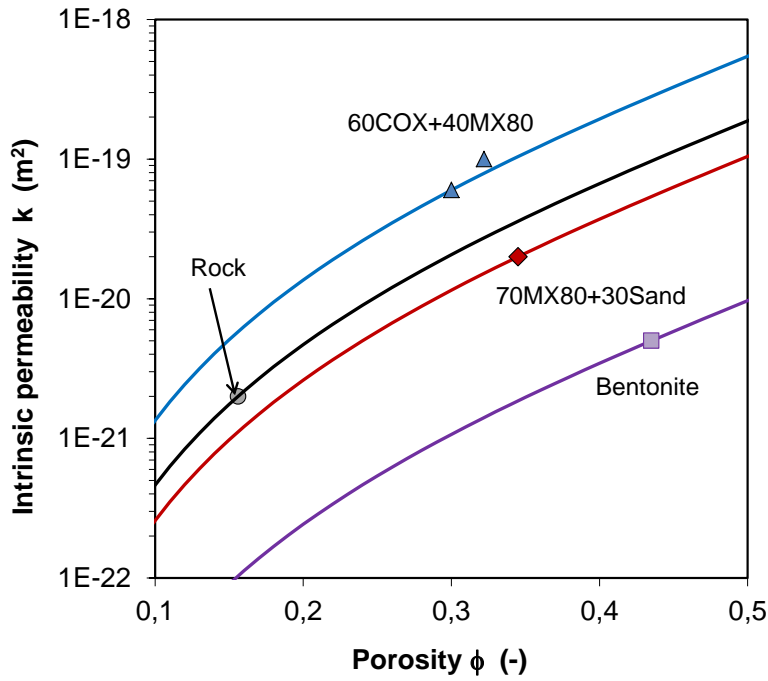


Fig. 5.2 Intrinsic permeability as a function of porosity for the seal materials

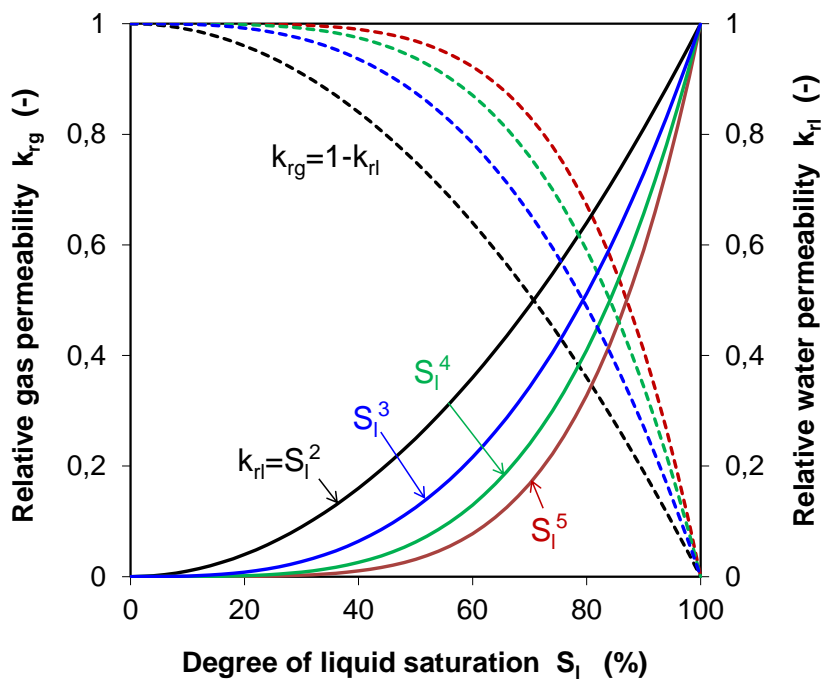


Fig. 5.3 Relative water and gas permeability as a function of water saturation

The degree of liquid saturation  $S_l$  is defined as

$$S_l = \frac{\rho_d \cdot W}{\rho_l \cdot \phi} \quad (5.11)$$

where  $w$  is the liquid water content,  $\rho_l$  the liquid density,  $\rho_d$  the dry density and  $\phi$  the porosity of the solid material.

### 5.2.2.3 Vapour diffusion

The molecular diffusion of vapour is governed by Fick's law:

$$\mathbf{i}_g^w = -\mathbf{D}_g^w \nabla \omega_g^w = -(\phi \rho_g S_g \tau \mathbf{D}_m^w I + \rho_g \mathbf{D}'_g) \cdot \nabla \omega_g^w \quad (5.12)$$

where  $\mathbf{i}_g^w$  is the non-advective mass flux of water in gas,  $\mathbf{D}_g^w$  is the dispersion tensor,  $\omega_g^w$  is the mass fraction of water in gas,  $\tau$  is the tortuosity and  $\mathbf{D}'_g$  is the mechanical dispersion tensor. Usually, a constant dispersion coefficient corresponding to the molecular diffusion of vapour in air is assumed:

$$D_m^w = \tau D \left( \frac{(273.15+T)^n}{P_g} \right) \quad (5.13)$$

where  $P_g$  is given in MPa. The parameters  $\tau = 1$ ,  $n = 2.3$  and  $D = 5.9 \cdot 10^{-12}$  m<sup>2</sup>/s are adopted for the seal materials.  $\mathbf{D}'_g$  can be neglected if air flow is insignificant.

### 5.2.2.4 Water retention curve

In the highly compacted clay-based materials, the hydration is an essential process of water transport in humid conditions, which is governed by the relationship between degree of water saturation  $S_l$  and matric suction  $s (= P_g - P_l)$ , usually called water retention curve. The suction is determined by the psychrometric law (equation 4.1 or 5.6). The van Genuchten model /VAN 80/ is usually applied for approaching the  $S_l - s$  relationship

$$S_l = \left[ 1 + \left( \frac{s}{P_o} \right)^{\frac{1}{1-\beta}} \right]^{-\beta} \quad (5.14)$$

where  $P_o$  and  $\beta$  are the material parameters. Based on the test data presented in section 4.3 (cf. Fig.4.8a-d), the retention parameters of the selected seal materials will be estimated below.

Taking the density of normal water  $\rho_w = 1.0$  g/cm<sup>3</sup> and the parameters  $\rho_d$  and  $\phi$  constant for the materials in volume-constraint conditions, the degree of water saturation  $S_l$  is obtained from the measured water content  $w$  according to equation (5.11). Fig. 5.4 shows the water retention curves for the bentonite (a), bentonite-sand mixture (b), claystone-

bentonite mixture (c), and claystone (d), respectively. It can be identified that the  $S_l$ -values at low suctions close and equal to zero are over 100 % indicating “oversaturation”. The maximum values are  $S_{lm} = 170$  % for the compacted bentonite with a dry density of  $1.57 \text{ g/cm}^3$ ,  $S_{lm} = 150$  % for 70MX80+30Sand mixture,  $S_{lm} = 120$  % for 60COX+40MX80 mixture, and  $S_{lm} = 120$  % for the claystone. A major reason for the calculated “oversaturation” may be that the actual density of water in such highly-compacted clay materials is higher than the normal one. Values of up to  $1.4 \text{ g/cm}^3$  are reported in literature /MIT 76/ for the density of adsorbed water on sodium montmorillonite (a  $10 \text{ \AA}$  thick layer). Moreover, due to the compressibility of water, the water density in the highly-compacted clay materials may increase with swelling pressure in rigid confinement.

The “oversaturation” brings difficulties for the determination of the water retention curve. Taking into account the confined and unconfined conditions of the samples, two evaluation methods are preliminarily suggested for approximation of the  $S_l - s$  relationship.

When the water content – suction ( $w - s$ ) data are obtained from unconfined samples (free swelling), the corresponding degrees of water saturation  $S_l$  for a given porosity ( $\varphi$ ) and dry density ( $\rho_d$ ) may be obtained according to equation (5.11) using the normal water density of  $\rho_w = 1.0 \text{ g/cm}^3$ . The part of the “oversaturation” with  $S_l > 100$  % is neglected, for instance, for the compacted bentonite in Fig. 5.4a.

When the  $w - s$  data are obtained from volume-constraint samples, the maximum water content reached at zero suction may be considered corresponding to the full saturation,  $w_m \rightarrow S_{lm} = 100$  %, and the degree of water saturation at any suction is defined as a ratio of the water content to its maximum

$$S_l = \frac{w}{w_m} = \frac{S_l}{S_{lm}} \quad (5.15)$$

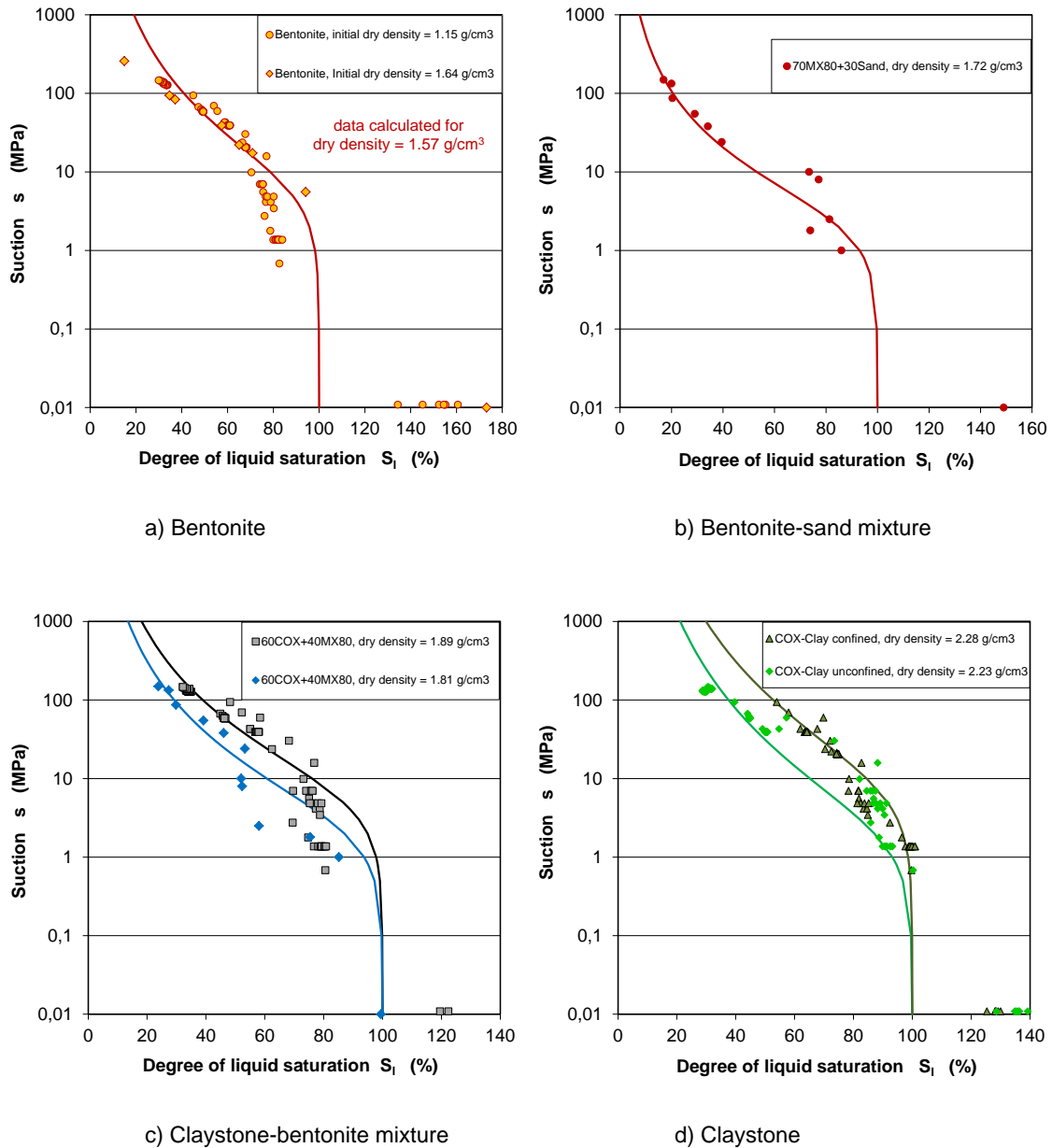


**Fig. 5.4** Water retention curves expressed by the van Genuchten model for the selected seal materials (a-d)

Based on the measured  $w - s$  data from the confined and unconfined mixtures, the  $S_l - s$  relationships approached by the van Genuchten model (Eq. 5.14) are established for each material. The associated parameter values are summarized in Table 5.2.

Fig. 5.5 illustrates the water retention curves for the compacted bentonite with a dry density of  $1.57 \text{ g/cm}^3$  (a), the bentonite-sand mixture (70/30) with a dry density of  $1.72 \text{ g/cm}^3$  (b), the claystone-bentonite mixture (60/40) with dry densities of  $1.89$  and  $1.81 \text{ g/cm}^3$  (c), and the claystone with dry densities of  $2.28$  and  $2.23 \text{ g/cm}^3$  (d), respectively. For the

bentonite two water retention curves are established: curve A matching the data in the low saturation area ( $S_l < 80\%$ ) and curve B closing to the data in the high saturation range. It is difficult for the van Genuchten model to gather a unique curve for the whole range. The retention curve for the compacted bentonite-sand mixture is determined by the evaluated saturation degree according to equation (5.15). For the compacted claystone-bentonite mixture, two curves are estimated for the upper and low boundary respectively. For the claystone at a given suction, the degree of saturation in unconfined condition (b) seems to be relatively lower than in confined condition (a). A reversal conclusion shall be reasonable. More precise tests are needed to confirm the conclusion.

It can also be recognized that the van Genuchten model largely overestimates the suctions in the low saturation area and  $s \rightarrow \infty$  as  $S_l \rightarrow 0$ . This shortage may be overcome by adding a term for suction to approach the upper limit /UPC 15/

$$S_l = \left[ 1 + \left( \frac{s}{P_o} \right)^{\frac{1}{1-\beta}} \right]^{-\beta} \cdot \left[ 1 - \frac{s}{P_1} \right]^{-\gamma} \quad (5.16)$$

where  $P_o$ ,  $\beta$ ,  $P_1$  and  $\gamma$  are the material parameters. The parameters are estimated by fitting the data and summarized in Table 5.3. The parameter  $\gamma = 1$  and the maximum suction  $P_1 = 350 \text{ MPa}$  are taken for all the materials. The modified retention curves are compared with the data in Fig. 5.6. It is obvious that the modified model fits the data for the whole range and  $s \rightarrow P_1$  as  $S_l \rightarrow 0$ .

**Tab. 5.2** Water retention parameters associated in the van Genuchten model for the seal materials

Material parameter	MX80 bentonite-a	MX80 bentonite-b	70MX80+ 30Sand	60COX+ 40MX80-a	60COX+ 40MX80-b	COX Clay-a	COX Clay-b
$P_o$ (MPa)	6.5	2.0	0.3	0.5	0.1	0.5	0.2
$\beta$ (-)	0.25	0.15	0.25	0.15	0.16	0.15	0.15

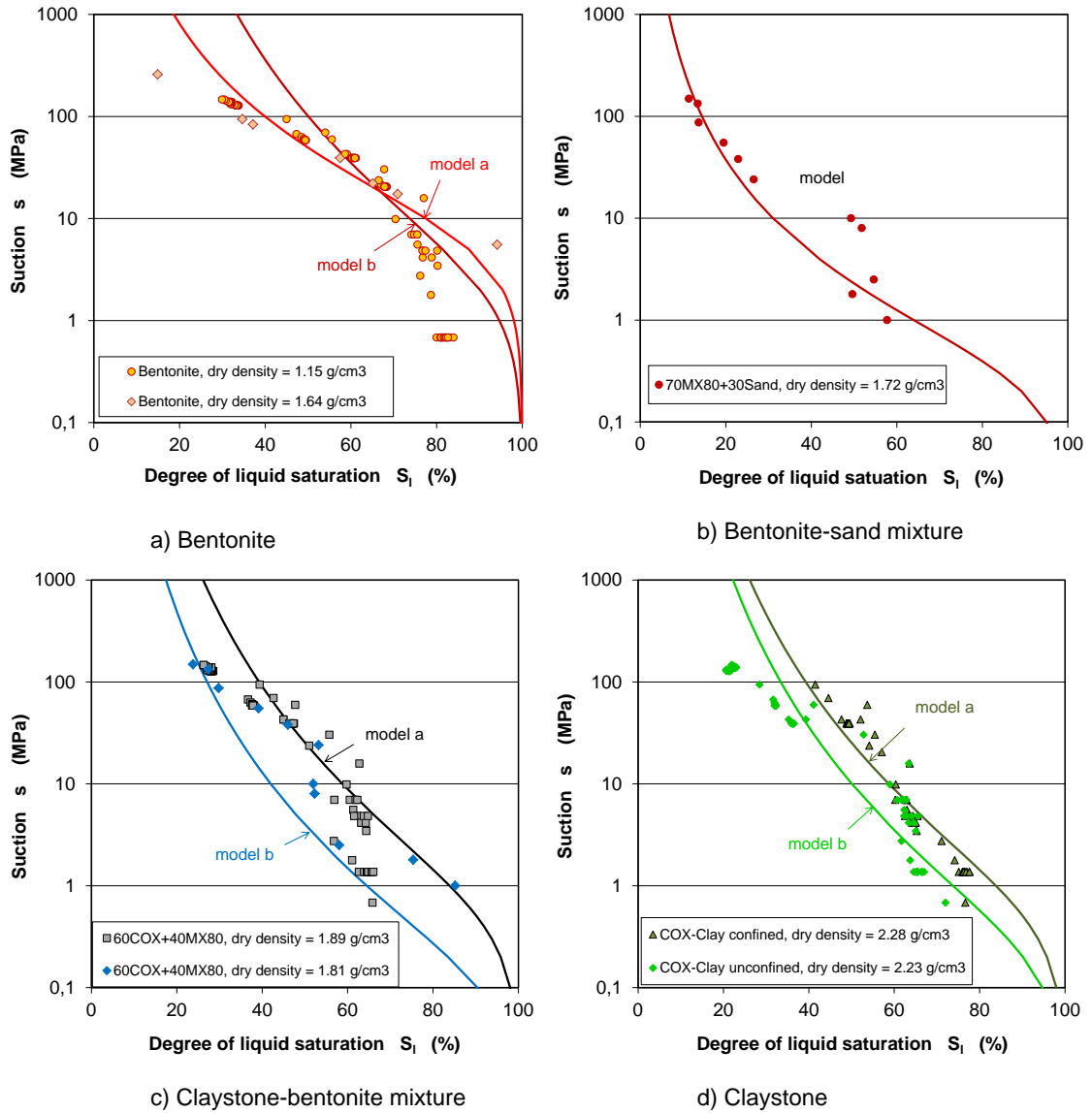


**Fig. 5.5** Water retention curves expressed by the van Genuchten model for the selected seal materials (a-d)

**Tab. 5.3** Water retention parameters associated in the modified van Genuchten model for the seal materials

Material parameter	MX80 bentonite	70MX80+30Sand	60COX+40MX80-a	60COX+40MX80-b	COX Clay-a	COX Clay-b
$P_o$ (MPa)	1.1	0.2	0.1	0.03	0.15	0.05
$\beta$ (-)	0.1	0.2	0.1	0.1	0.1	0.1
$P_l$ (MPa)	350	350	350	350	350	350
$\gamma$ (-)	1	1	1	1	1	1

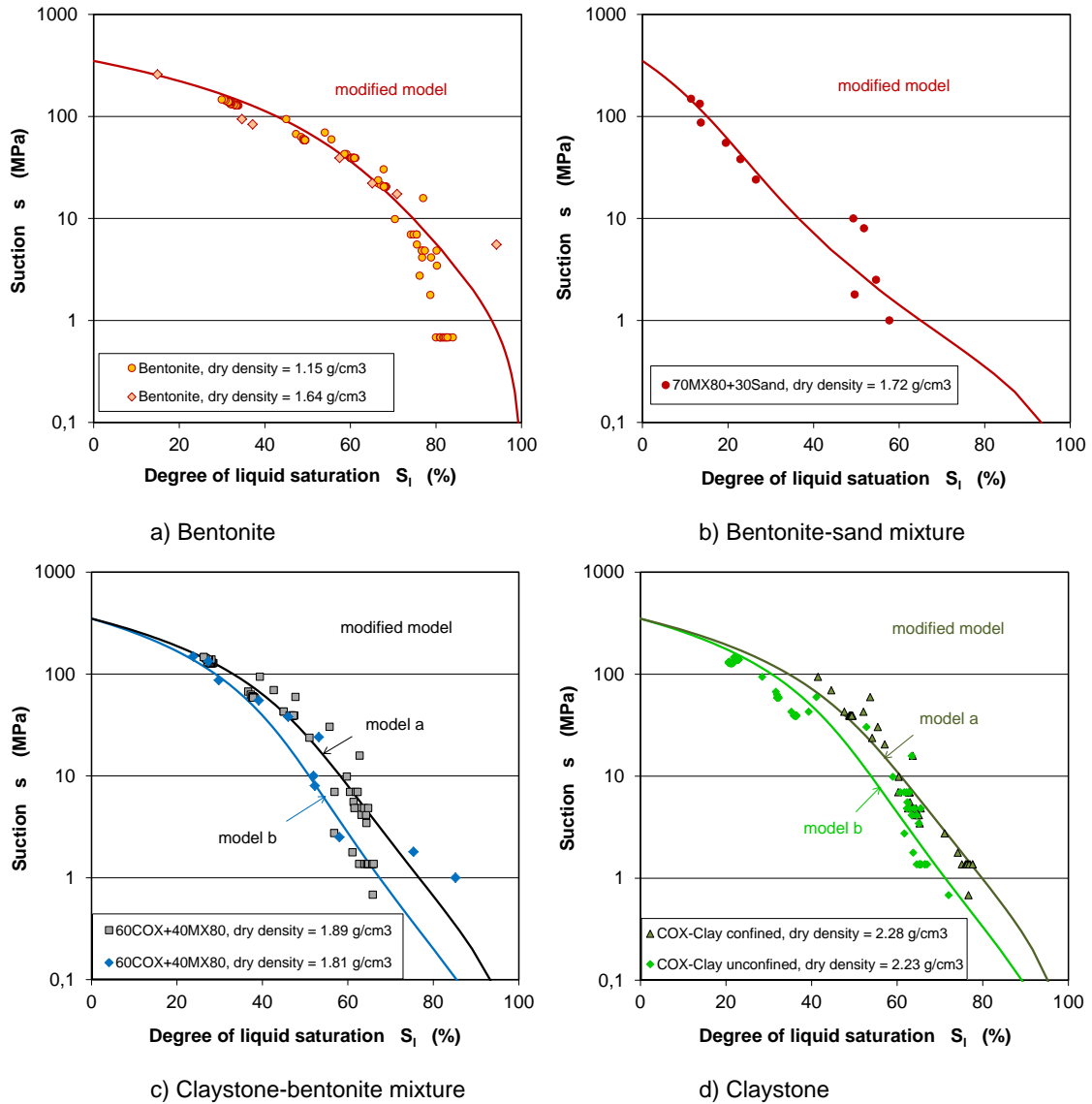


**Fig. 5.6** Water retention curves expressed by the modified van Genuchten model for the selected seal materials (a-d)

## 5.2.3 Mechanic constitutive models

### 5.2.3.1 Stress invariants

$$\text{Mean effective stress: } p = \frac{1}{3}(\sigma'_x + \sigma'_y + \sigma'_z) \quad (5.17)$$

where  $\sigma'_x, \sigma'_y, \sigma'_z$  are the effective stresses.

Second stress invariant:

$$J = \sqrt{\frac{1}{2} \text{trace}(\mathbf{s} : \mathbf{s})} = \frac{1}{\sqrt{3}} q, \quad \mathbf{s} = \boldsymbol{\sigma} - p\mathbf{I} \quad (5.18)$$

$$q = \frac{1}{\sqrt{2}} \sqrt{(\sigma'_x - \sigma'_y)^2 + (\sigma'_y - \sigma'_z)^2 + (\sigma'_z - \sigma'_x)^2 + 6(\tau'_{xy} + \tau'_{yz} + \tau'_{zx})} \quad (5.19)$$

where  $q$  is the deviatoric stress,  $\tau'_{xy}, \tau'_{yz}, \tau'_{zx}$  are the shear stresses.

$$\text{Lode's angle: } \theta = -\frac{1}{3} \sin^{-1} (1.5\sqrt{3} \det \mathbf{s} / J^3) \quad (5.20)$$

$\theta = -\pi/6$  means triaxial compression and  $\theta = \pi/6$  extension.

### 5.2.3.2 Elasto-plastic model (BBM)

In saturated porous materials, the mechanical behaviour is best understood in terms of effective stress  $\boldsymbol{\sigma}' = \boldsymbol{\sigma} - P_l \mathbf{m}$ , where  $\mathbf{m}^T$  is an auxiliary vector [1,1,1,0,0,0]. For unsaturated materials it is necessary to consider two independent stress variables: net stresses  $(\boldsymbol{\sigma} - P_l \mathbf{m})$  and capillary suction  $s = (P_g - P_l)$ . The net stress is the excess of total stress over gas pressure. If full saturation is achieved, the net stress becomes effective stress. The mechanical constitutive equation takes the incremental form:

$$d\boldsymbol{\sigma}' = \mathbf{D}d\boldsymbol{\varepsilon} + \mathbf{h}ds \quad (5.21)$$

where  $\boldsymbol{\sigma}'$  is used for net stresses,  $\boldsymbol{\varepsilon}$  is the strain tensor.  $\mathbf{D}$  is the constitutive stiffness matrix, defined by Young's modulus  $E$ , shear modulus  $G$  and Poisson's ratio  $\nu$ , and  $\mathbf{h}$  is a constitutive vector relating changes of suction to changes in net stress.

An elasto-plastic model named Barcelona Basic Model (BBM) is implemented in CODE\_BRIGHT, which is able to represent many mechanical features of unsaturated materials. The yield function is expressed by

$$q^2 - M^2(p + p_s)(p_o - p) = 0 \quad (5.22)$$

where  $p_o$  the net isotropic yield stress,  $p_s$  the isotropic tensile strength depending on suction  $s$ , and  $M$  a constant value characterising the critical failure state line

$$q = M \cdot p \quad (5.23)$$

It is assumed that the apparent cohesion increases with suction by

$$p_s = p_{so} + k \cdot s \quad (5.24)$$

where  $p_{so}$  is the isotropic tensile strength in saturated conditions,  $k$  is a parameter.

The net isotropic yield stress  $p_o$  is considered to be dependent on suction through

$$p_o = p^c \left( \frac{p_o^*}{p^c} \right)^{\frac{\lambda(o) - k_{io}}{\lambda(s) - k_{io}}} ; \quad \lambda(s) = \lambda(o) \left[ (1 - r) \exp(-\beta \cdot s) + r \right] \quad (5.25)$$

where  $p_o^*$  is the net yield stress for saturated conditions,  $\lambda(o)$  and  $\lambda(s)$  are the slopes of the virgin compression lines for saturated and unsaturated conditions,  $r$  is a constant related to the matrix stiffness,  $\beta$  provides the rate of change of  $\lambda(s)$  with suction,  $k_{io}$  is the initial slope of the isotropic unloading-reloading paths for saturated conditions,  $p^c$  is a reference stress.

Hardening depends on plastic strain according to

$$\frac{dp_o^*}{p_o^*} = \frac{v}{\lambda(o) - k_{io}} d\varepsilon_v^p \quad (5.26)$$

where  $v = 1 + e$  is the specific volume,  $e$  is the void ratio.

Volumetric elastic strains induced by changes of net mean stress and suction are given by

$$d\varepsilon_v^e = d\varepsilon_{vp}^e + d\varepsilon_{vs}^e \quad (5.27a)$$

$$d\varepsilon_{vp}^e = \frac{k_i}{v} \frac{dp}{p} ; \quad k_i = k_{io} (1 + \alpha_i s) \quad (5.27b)$$

$$d\varepsilon_{vs}^e = \frac{k_s}{v} \frac{ds}{s + p_{at}} ; \quad k_s = k_{so} \left( 1 + \alpha_{sp} \ln \left( \frac{p}{p_{ref}} \right) \right) \exp(\alpha_{ss} s) \quad (5.27c)$$

where  $k_{io}$  and  $k_i$  are the slopes of the isotropic unloading-reloading paths for saturated and unsaturated conditions, respectively,  $k_{so}$  and  $k_s$  are the slopes of the wetting-drying paths for saturated and unsaturated conditions at a given stress  $p$  in the elastic domain,

$p_{at}$  and  $p_{ref}$  are the atmospheric pressure and the reference pressure,  $\alpha_i$ ,  $\alpha_{sp}$  and  $\alpha_{ss}$  are parameters.

Deviatoric elastic deformations are computed through shear modulus  $G$  and the Poisson ratio  $\nu$ :

$$d\varepsilon_q^e = \frac{G}{3} dq; \quad G = \frac{3(1-2\nu)(1+e)}{2(1+\nu)k_i} p \quad (5.28)$$

### 5.2.3.3 Parameters

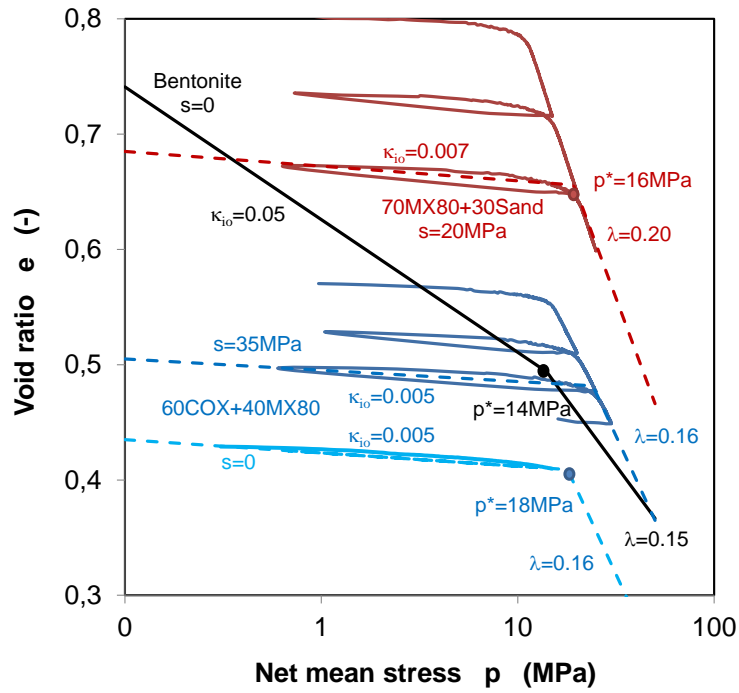
For the MX80 bentonite with a dry density of 1.57 g/cm<sup>3</sup> in the BRIE experiment /ÅKE 13/, the parameter values were obtained on the basis of the data of the FEBEX bentonite with a dry density of 1.55 g/cm<sup>3</sup> /GEN 98/. Only the parameter  $k_{io}$ -value is changed from 0.05 (FEBEX) to 0.02 (MX80) for matching the relatively higher swelling pressure measured on MX80 bentonite. Most of the mechanical parameters for the 70MX80+30Sand and 60COX+40MX80 mixtures are obtained directly from our laboratory experiments and partly by back calculations.

Fig. 5.7 shows the compaction curves of the bentonite-sand and claystone-bentonite mixtures, based on which the elastic and plastic stiffness parameters  $k_{io}$  and  $\lambda(s)$  as well as the yield stress  $p_o^*$  are obtained. Since the parameter  $k_{io}$  of the claystone-bentonite mixture shows almost independence of the water saturation, the parameter  $\alpha_i = 0$  is thus assumed. The comparison between the compaction curves indicates that both the compacted mixtures are much stiffer than the pure bentonite.

The initial elastic parameters  $K$ ,  $G$  and  $E$  are calculated for saturated conditions at  $p = 1$  MPa and  $e = e_o$

$$K = p(1+e)/k_{io}, \quad G = 3K(1-2\nu)/2(1+\nu), \quad E = 2G(1+\nu).$$

The swelling parameters  $k_{so}$ ,  $\alpha_{sp}$  and  $\alpha_{ss}$  are estimated by back calculations of the swelling pressures measured on the bentonite-sand and claystone-bentonite mixtures (see later). The estimated values of the BBM parameters are summarized in Table 5.4 for the selected seal materials.



**Fig. 5.7** Determination of the compaction parameters for the seal materials

**Tab. 5.4** BBM model parameters for the selected seal materials

Parameter in equation	Symbol	Unit	Bentonite	70MX80+30Sand	60COX+40MX80
5.27b	$k_{io}$	-	0.05/0.02	0.007	0.005
5.27b	$\alpha_i$	-	0.003	-	-
5.27c	$k_{so}$	-	0.3	0.3	0.022
5.27c	$\alpha_{sp}$	-	-0.1638	-	-
5.27c	$\alpha_{ss}$	MPa <sup>-1</sup>	-0.03	-	-
5.27c	$p_{ref}$	MPa	0.01	-	-
5.28	$\nu$	-	0.4	0.35	0.35
Bulk modulus	$K$	MPa	35	285	340
Shear modulus	$G$	MPa	7.5	95	113
Young's modulus	$E$	MPa	20	255	305
5.23	$M$	-	1.0	-	-
5.24	$k$	-	-0.1	-	-
5.25	$p^c$	MPa	0.1	-	-
5.25	$p_o^*$	MPa	14	16	18
5.25/5.26	$\lambda(o)$	-	0.15	0,2	0,16
5.25	$r$	-	0.75	-	-
5.25	$\beta$	MPa <sup>-1</sup>	0.05	-	-

## 5.2.4 Simulations of water uptake and swelling pressure evolution

### 5.2.4.1 Water uptake

The water saturation tests on the compacted 70MX80+30Sand and 60COX+40MX80 mixtures as well as the COX claystone were described in section 4.4. Most of them are modelled in this section. Additionally, the previous hydration tests performed on the pure MX80 bentonite /KRÖ 04/ are also simulated. The basic characteristics of the samples are summarized in Table 5.5.

**Tab. 5.5** Basic characteristics of the samples in the water saturation tests: MX80 bentonite, 70MX80+30Sand and 60COX+40MX80 mixtures, and COX claystone

Parameter	Bentonite	70MX80+30Sand		60COX+40MX80			COX Clay
		1 group-II	2 group-III	1 group-I	2 group-III	3 group-III	
Test	/KRÖ 04/						
$D$ (mm)	50.0	50.0	50,0	50.0	50,0	50,0	47.2
$L$ (mm)	10.0	98.0	100,0	100.0	100,0	100,0	101.3
$\rho_d$ (g/cm <sup>3</sup> )	1.52	1.49	1,79	1.79	1,87	1,91	2.29
$\phi$ (%)	45.7	46.0	35,0	34.5	31,0	30,0	15.1
$w$ (%)	10.0	9.0	9,0	5.45	7,0	7,0	3.70
$S_l$ (%)	33.3	32.7	46,0	30.0	41,6	44,4	58.3

The initially unsaturated samples were placed in steel cylinders of 50 mm diameter and 100 mm length and wetted from an end face with the synthetic clay water at atmospheric pressure. The tests are modelled using CODE\_BRIGTH (v3 $\beta$ ) as a coupled HM problem by an axisymmetric geometry with 100 elements as shown in Fig. 5.8. The liquid pressure at the entire face is kept at atmospheric level,  $P_l = 0.1$  MPa, and the atmospheric gas pressure is kept for the whole sample,  $P_g = 0.1$  MPa. The other boundaries are isolated with zero fluid flow,  $Q_l = 0$ . The initial suction  $s_o$  is obtained from the water retention curve and the initial water saturation  $S_{l0}$  for each sample. The initial stress is nearly zero:  $\sigma_1 = \sigma_2 = \sigma_3 = 0.15$  MPa. A constant temperature maintains at 20 °C. The calculations are performed by solving the balance equations of solid (Eq. 5.2), water mass (Eq. 5.3) and

stress equilibrium (Eq. 5.5). As a result, the distribution of water saturation in the sample at the end of each saturation period is predicted.

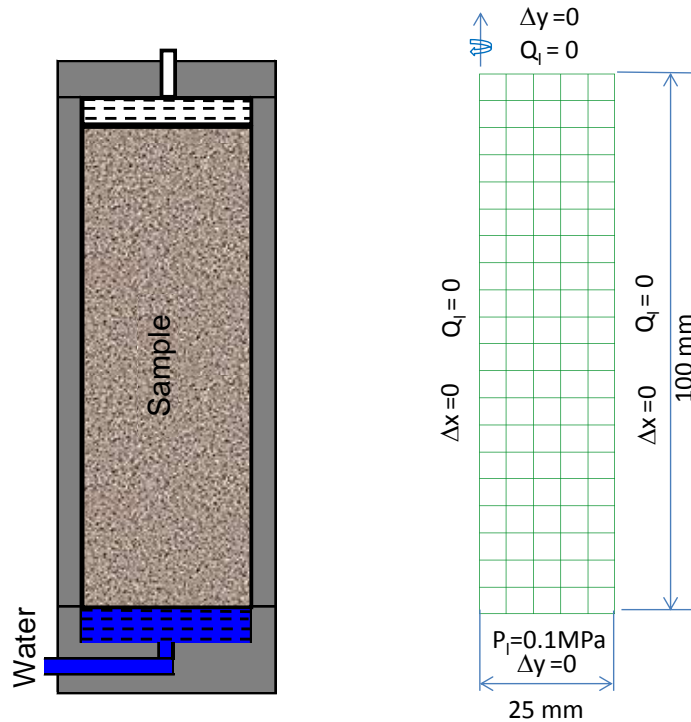


**Fig. 5.8** Model geometry and boundary conditions for modelling the water saturation of the seal materials

#### 5.2.4.1.1 Bentonite

The hydration tests on the compacted MX80 bentonite in /KRÖ 04/ are predicted using different sets of the hydraulic parameters, which are established here or taken from literature /ÅKE 13/ for the bentonite used in the BRIE-Experiment in Äspö-URL in Sweden and from /GEN 98/ for the bentonite used in the FEBEX-Experiment in Grimsel-URL in Switzerland. The hydraulic parameters and the water retention parameters of the van Genuchten model (Eq. 5.14) are summarized in Table 5.6. Fig. 5.9 shows the water retention curves together with the test data. GRS-A and BRIE model curves are close to each other and agree well with the data in the low saturation range of  $S_l < 80\%$ . FEBEX model curve exhibits the same shape but lies slightly below the other curves. GRS-B curve is more close to the data in the high saturation range and below the other curves in this region. For the initial degree of water saturation of  $S_{l0} = 33.3\%$  in the bentonite

samples, the corresponding suction values  $s_o$  are determined from the respective retention curves. The exponent of the power law for the relative permeability,  $k_{rl} = S_l^\lambda$ , is differing from a model to another with  $\lambda = 3, 4$  and  $5$ .

**Tab. 5.6** Summary of the hydraulic parameters in different models for the bentonite

Material parameter	GRS-A Model	GRS-B Model	BRIE Model /ÅKE 13/	FEBEX Model /VOL 96/
$\phi_o$ (-)	0.43	0.43	0.44	0.43
$k_o$ (m <sup>2</sup> )	$6 \times 10^{-21}$	$6 \times 10^{-21}$	$6.4 \times 10^{-21}$	$6 \times 10^{-21}$
$k_{rl}$ (-)	$S_l^5$	$S_l^5$	$S_l^4$	$S_l^3$
$P_o$ (MPa)	6.5	2.0	10.0	7.0
$\beta$ (-)	0.25	0.15	0.28	0.35
$s_o$ (MPa)	180	1000	165	58

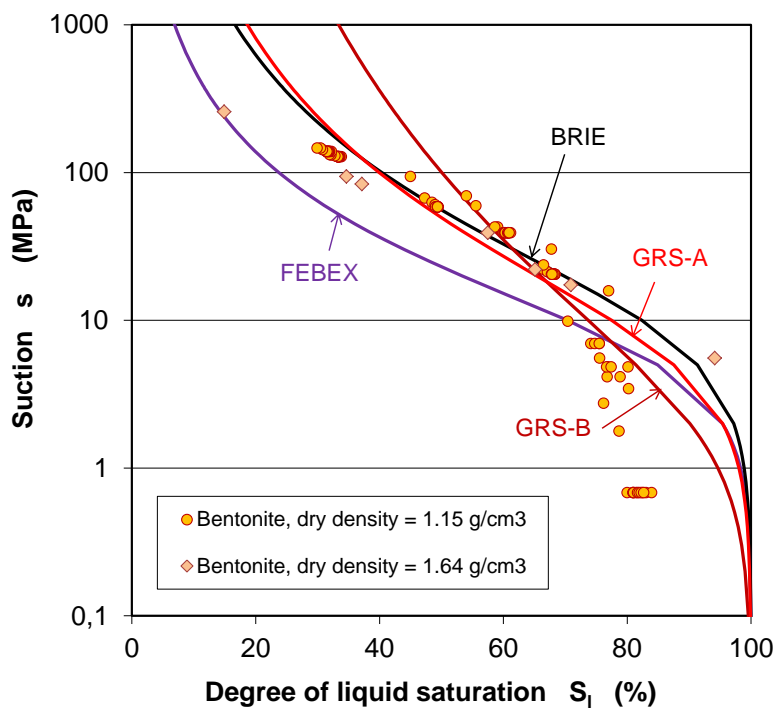
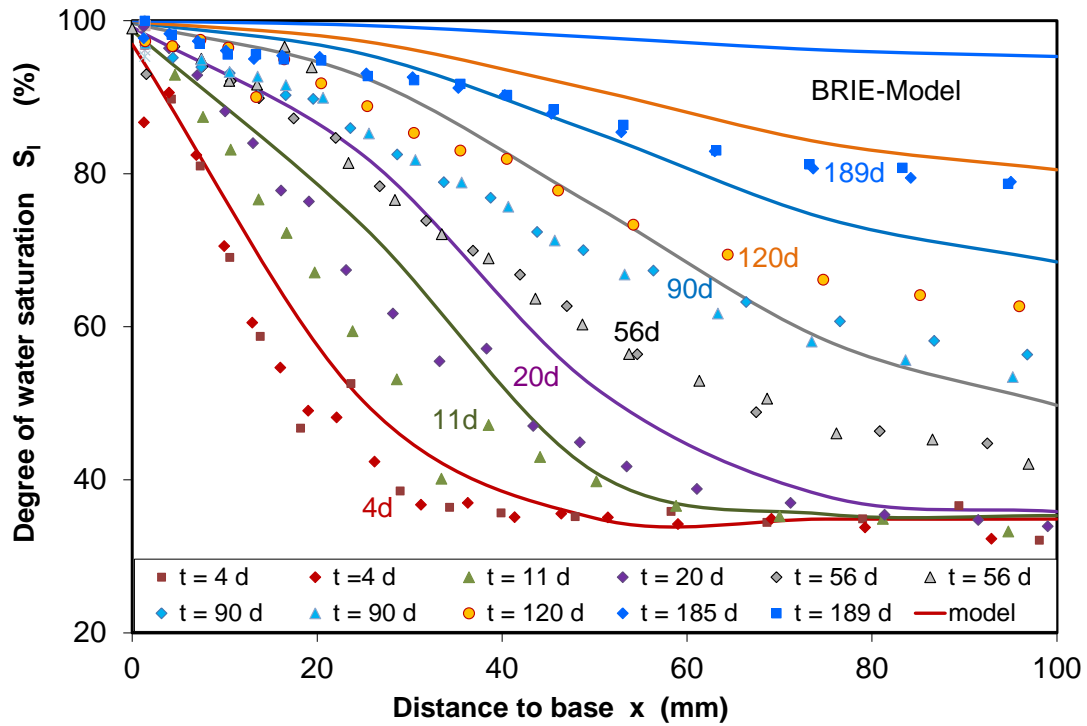


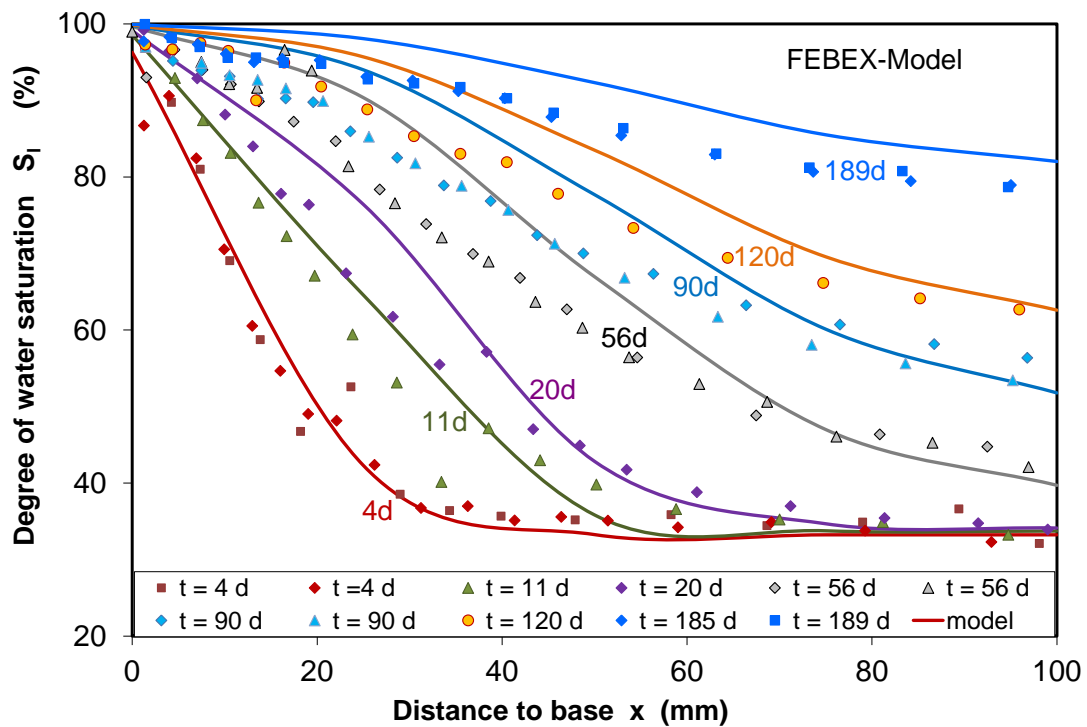
**Fig. 5.9** Water retention curves used for modelling the water uptake of the compacted bentonite

The modelling results are compared in Fig. 5.10 with the measured distributions of water saturation in the samples at different time periods using models: (a) BRIE, (b) FEBEX, (c) GRS-A, and (d) GRS-B. It can be seen that the application of the retention curves of

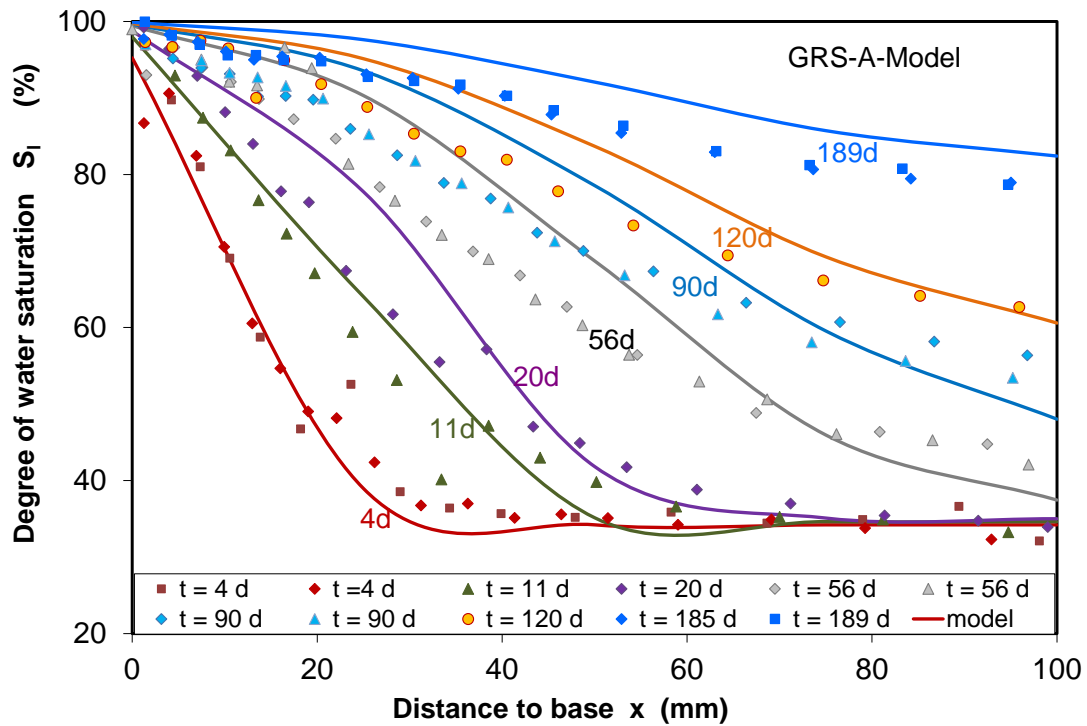
BRIE, FEBEX and GRS-A more or less overestimates the hydration rate, particularly for the long saturation durations after a month. In contrast, GRS-B model provides an excellent agreement with the measurements at the various saturation periods.



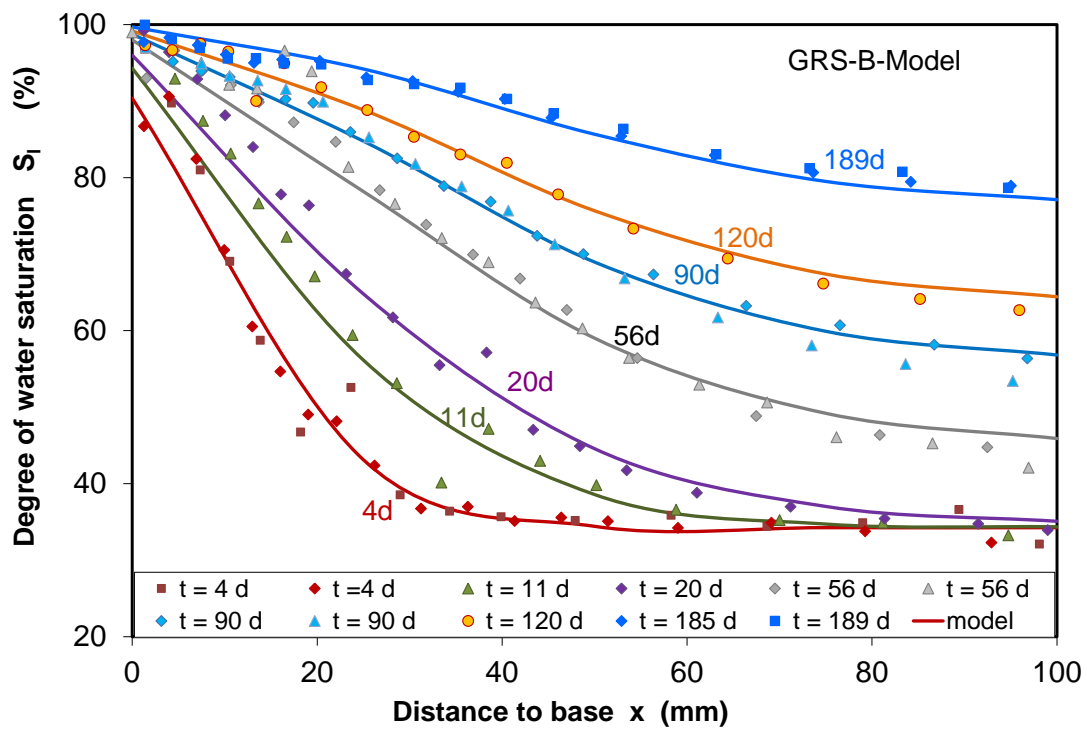
a) Prediction using BRIE model parameters



b) Prediction using FEBEX model parameters



c) Prediction using GRS-A model parameters



d) Prediction using GRS-B model parameters

**Fig. 5.10** Comparison of water saturation measured on MX80 bentonite /KRÖ 04/ and predicted using the different hydraulic parameters (a-d)

Additionally, the modified retention curve in Fig. 5.6a with the associated parameters in Table 5.3 is also used for modelling the hydration tests. The initial suction of  $s_o = 154$  MPa is resulted from the initial saturation degree of  $S_{o} = 33.3$  %. Fig. 5.11 shows the comparison between the model prediction and the data. A good agreement between them is also reached.

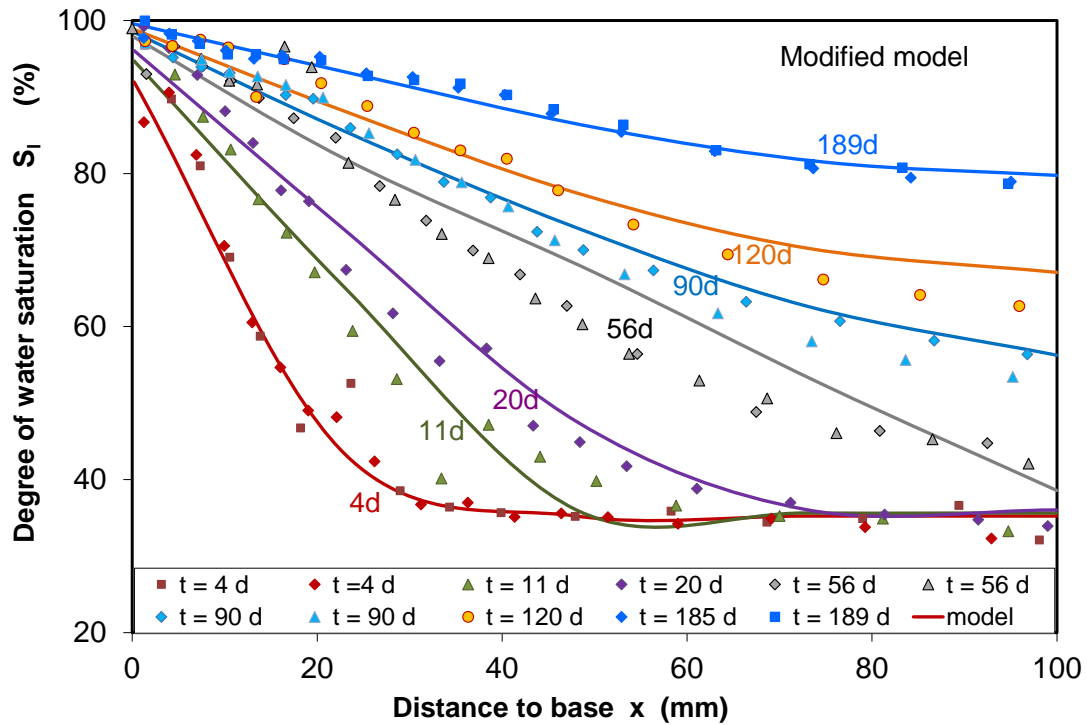


**Fig. 5.11** Comparison of water saturation measured on MX80 bentonite /KRÖ 04/ and predicted using the modified water retention curve

#### 5.2.4.1.2 Bentonite-sand mixture

Two water saturation tests on the bentonite-sand mixture 70MX80+30Sand are simulated using both the van Genuchten retention curve (Fig. 5.5b) and the modified model (Fig. 5.6b). The associated retention parameters, the other hydraulic parameters, and the initial properties of these two samples are summarized in Table 5.7. The modelling results are compared in Figs. 5.12 with the measured distributions of water saturation in the samples at different time periods. The distribution of water saturation of sample 1 with a porosity of 46 % at 9.5 months can be very well predicted by the models with both the retention curves, while the water saturation in sample 2 with a low porosity of 35 % at 14 months is largely overestimated. But the model for  $t = 14$  months is close to the data obtained on sample 3 at 23 months. The saturation time is largely dependent on the porosity of the material. The lower the porosity, the longer the saturation is required.

**Tab. 5.7** Hydraulic parameters of the bentonite-sand mixture

Hydraulic parameters	$\phi_o = 0.345, k_o = 2 \times 10^{-20} \text{ m}^2, k_{rl} = S_l^5$
van Genuchten model (1)	$P_o = 0.3 \text{ MPa}, \beta = 0.25$
Modified model (2)	$P_o = 0.2 \text{ MPa}, \beta = 0.2, P_I = 350 \text{ MPa}, \lambda = 1$
Initial properties of sample 1	$\phi_o = 0.46, S_{lo} = 32.7 \%, s_{o-1} = 9 \text{ MPa}, s_{o-2} = 15 \text{ MPa}$
Initial properties of sample 2	$\phi_o = 0.35, S_{lo} = 46.0 \%, s_{o-1} = 3 \text{ MPa}, s_{o-2} = 4 \text{ MPa}$

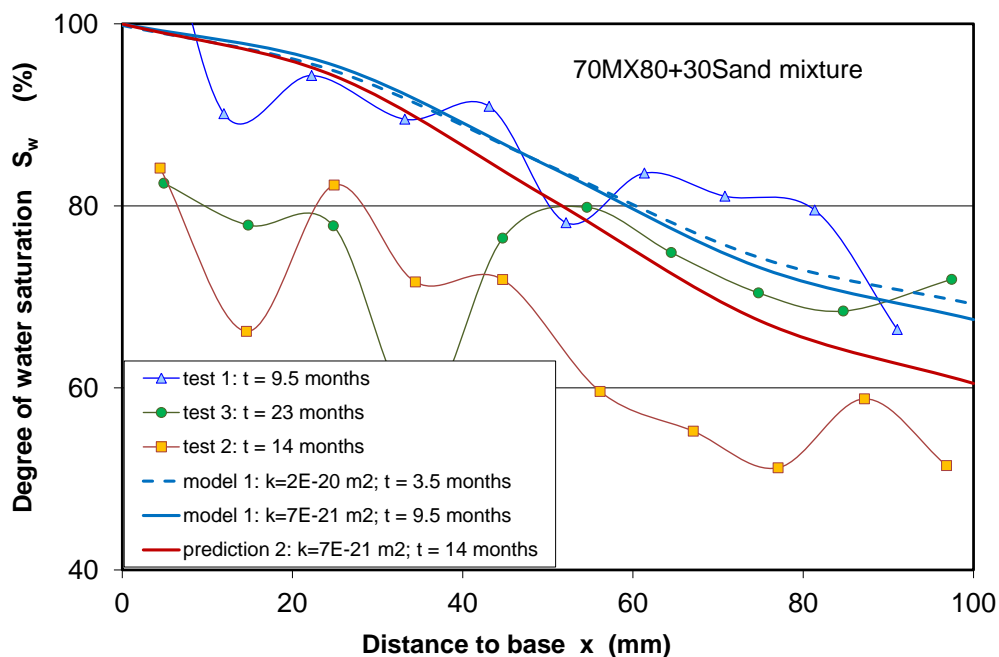


**Fig. 5.12** Predictions of the water saturation in the bentonite-sand mixture using the van Genuchten model (solid line) and the modified model (dash line)

### 5.2.4.1.3 Claystone-bentonite mixture

Three water saturation tests on the claystone-bentonite mixture 60COX+40MX80 are simulated using both the van Genuchten retention curve b in Fig. 5.5c and the modified model b in Fig. 5.6c for a dry density of  $1.81 \text{ g/cm}^3$ . The associated retention parameters, the other hydraulic parameters, and the initial properties of the tested samples are summarized in Table 5.8. The modelling results are illustrated in Fig. 5.13 with the measured distributions of water saturation in the samples at different time periods. The predictions using the van Genuchten retention curve (solid line) and the modified retention curve (dash line) are close to the measured data for sample 1 but slightly overestimate for the

other two samples. The measured low degrees of water saturation in the water entrance sides are probably caused by measurement errors.

**Tab. 5.8** Hydraulic parameters of the claystone-bentonite mixture

Hydraulic parameters	$\phi_o = 0.304, k_o = 6 \times 10^{-20} \text{ m}^2, k_{rl} = S_l^5$
van Genuchten model (1)	$P_o = 0.1 \text{ MPa}, \beta = 0.16$
Modified model (2)	$P_o = 0.03 \text{ MPa}, \beta = 0.1, P_I = 350 \text{ MPa}, \lambda = 1$
Sample-1 initial properties	$\phi_o = 0.345, S_{lo} = 30.0 \%, s_{o-1} = 400 \text{ MPa}, s_{o-2} = 87 \text{ MPa}$
Sample-2 initial properties	$\phi_o = 0.31, S_{lo} = 41.6 \%, s_{o-1} = 75 \text{ MPa}, s_{o-2} = 35 \text{ MPa}$
Sample-3 initial properties	$\phi_o = 0.30, S_{lo} = 44.4 \%, s_{o-1} = 50 \text{ MPa}, s_{o-2} = 22 \text{ MPa}$

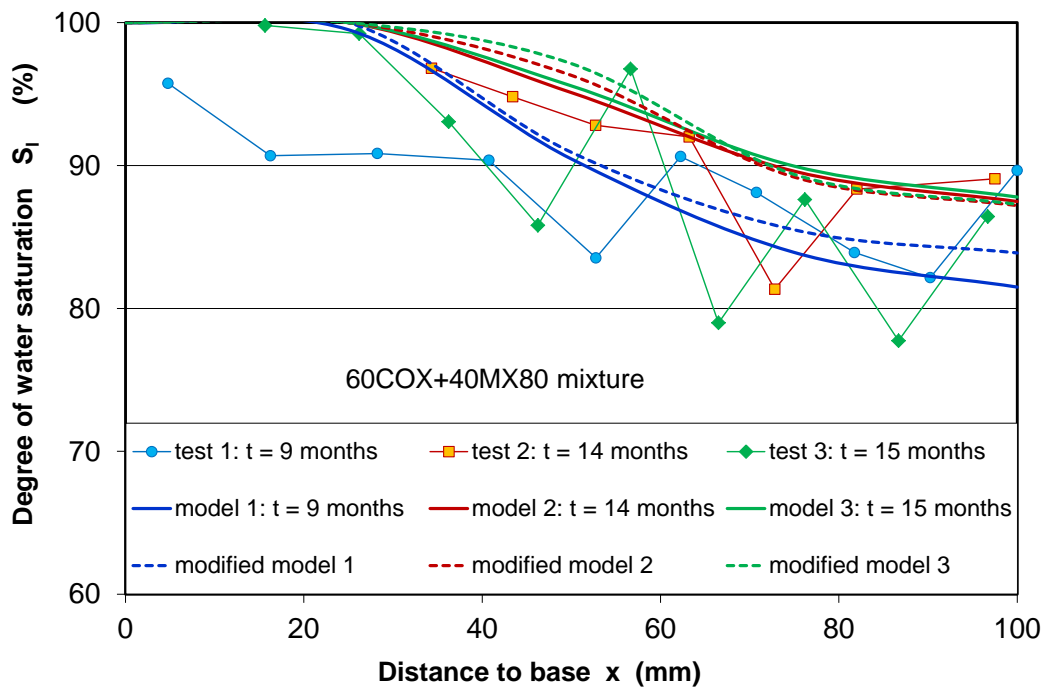


**Fig. 5.13** Predictions of the water saturation in the claystone-bentonite mixture using the van Genuchten model (solid line) and the modified model (dash line)

#### 5.2.4.1.4 Claystone

A water saturation test on the COX claystone is simulated using both the van Genuchten retention curve b in Fig. 5.5d and the modified model b in Fig. 5.6d obtained from the unconfined samples. The associated retention parameters, the other hydraulic parameters, and the initial properties of the sample are summarized in Table 5.9. The modelling results based on both the water retention models are shown in Fig. 5.14 together with the measured distribution of water saturation in the sample after testing at 9.5 months. The model curves lie within the scatter of the data.

**Tab. 5.9** Hydraulic parameters of the COX claystone

Hydraulic parameters	$\phi_o = 0.156, k_o = 6 \times 10^{-21} \text{ m}^2, k_{rl} = S_l^5$
van Genuchten model (1)	$P_o = 0.2 \text{ MPa}, \beta = 0.15$
Modified model (2)	$P_o = 0.05 \text{ MPa}, \beta = 0.1, P_1 = 350 \text{ MPa}, \lambda = 1$
Sample initial properties	$\phi_o = 0.151, S_{lo} = 58.3 \%, s_{o-1} = 4 \text{ MPa}, s_{o-2} = 6 \text{ MPa}$

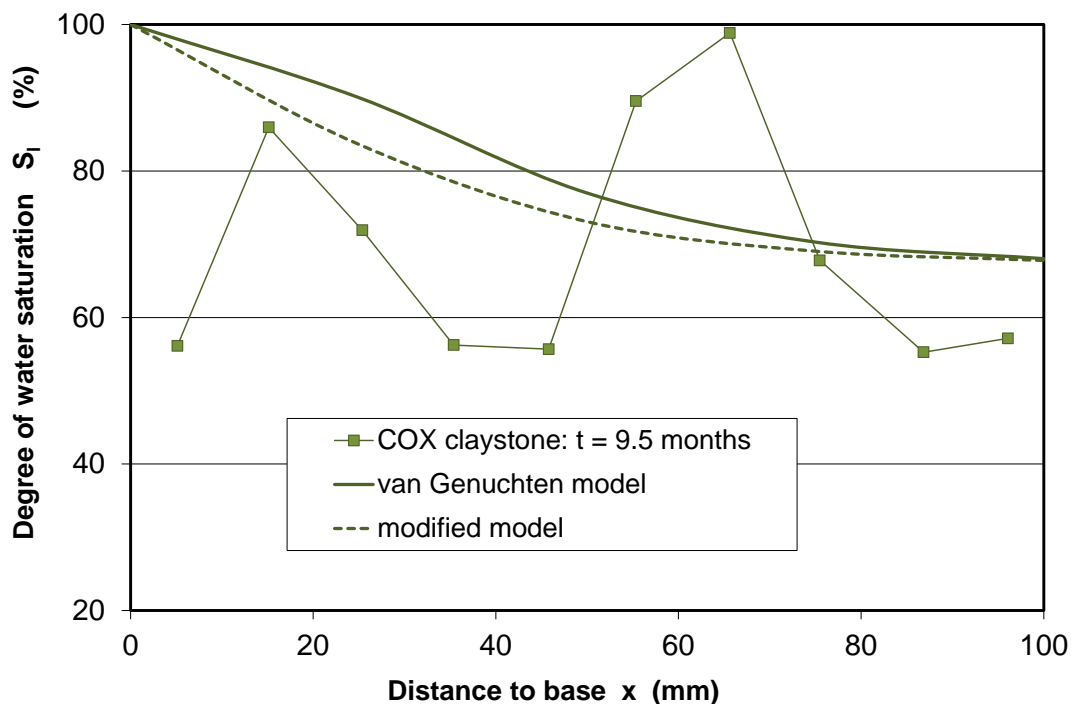


**Fig. 5.14** Predictions of the water saturation in the claystone mixture using the van Genuchten model (solid line) and the modified model (dash line)

## 5.2.4.2 Swelling pressure

### 5.2.4.2.1 Bentonite-sand and claystone-bentonite mixtures

The swelling pressure tests on the compacted bentonite-sand (70MX80+30Sand) and claystone-bentonite (60COX+40MX80) mixtures were described in section 4.5 and selected for modelling. The initial unsaturated samples in steel cells of 50 mm diameter and 30 mm height are modelled by an axisymmetric geometry with 50 elements, see Fig. 5.15. The initial properties of the mixtures are

- 70MX80+30Sand:  $\rho_d = 1.82 \text{ g/cm}^3$ ,  $\phi = 34.0 \%$ ,  $w_o = 11.0 \%$ ,  $S_{l0} = 59.0 \%$   $\text{g/cm}^3$
- 60COX+40MX80:  $\rho_d = 1.86 \text{ g/cm}^3$ ,  $\phi = 32.0 \%$ ,  $w_o = 10.0 \%$ ,  $S_{l0} = 58.0 \%$   $\text{g/cm}^3$

The samples are confined with the fixed boundaries. The liquid pressure at the bottom is kept at atmospheric level,  $P_l = 0.1 \text{ MPa}$ , and the gas pressure is atmospheric,  $P_g = 0.1 \text{ MPa}$ . The other boundaries are isolated with zero fluid flow,  $Q_l = 0$ . A low initial stress state is applied with  $\sigma_1 = \sigma_2 = \sigma_3 = 0.11 \text{ MPa}$ . A constant temperature is kept at  $20 \text{ }^\circ\text{C}$ . The calculations are performed by solving the balance equations of solid (Eq. 5.2), water mass (Eq. 5.3) and stress equilibrium (Eq. 5.5).

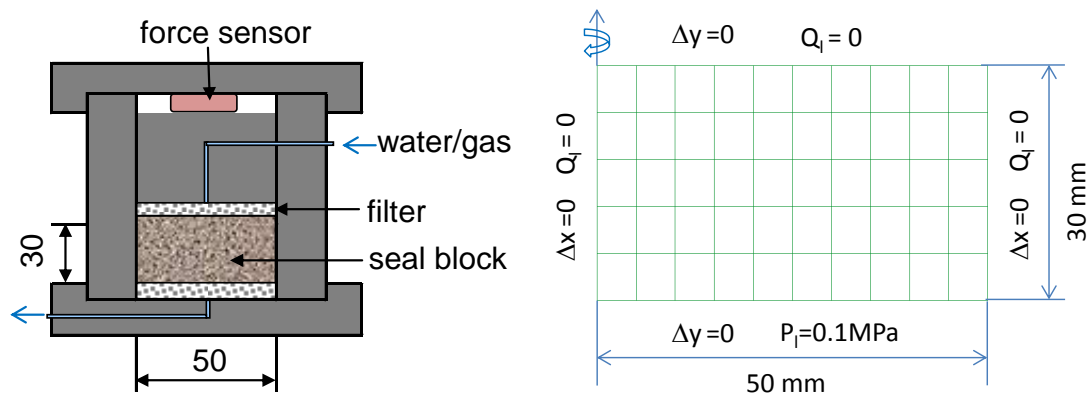
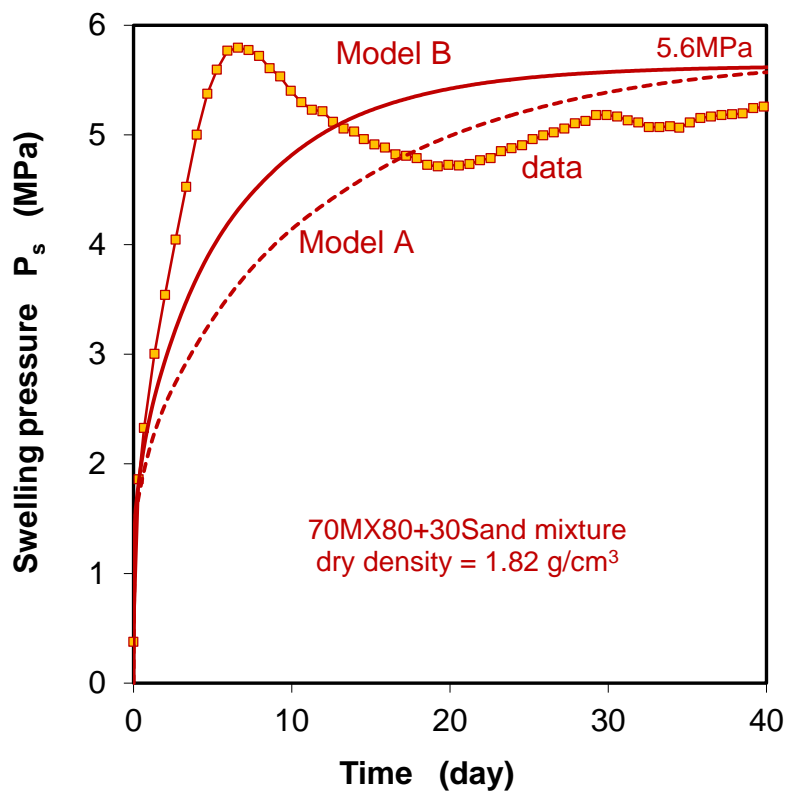


**Fig. 5.15** Model geometry and boundary conditions for modelling the swelling pressure of the seal materials

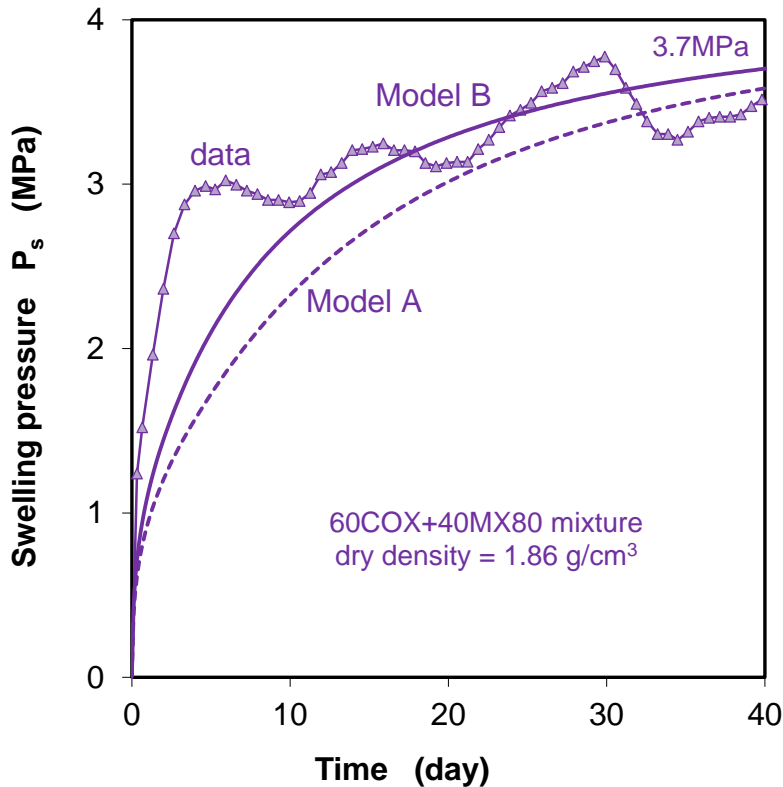
The BBM model with the mechanical parameters summarized in Table 5.4 is adopted for the mechanical behaviour of the seal materials. The hydraulic models and parameters in Table 5.1 are adopted. The water retention curve in Fig. 5.5b and the curve b in Fig. 5.5c are adopted for 70MX80+30Sand and 60COX+40MX80 mixture, respectively. Both retention curves are also used for modelling the water saturation tests (Figs. 5.12 and

5.13). The initial suctions are obtained to be  $s_0 = 1.4$  MPa for 70MX80+ 30Sand and  $s_0 = 2$  MPa for 60COX+40MX80.

Fig. 5.16 compares the modelled and measured evolution of swelling pressure for 70MX80+30Sand (a) and 60COX+40MX80 (b) mixture respectively. The sensitivity of the relative permeability parameter  $\lambda$  is examined using two values of  $\lambda = 5$  for model A and  $\lambda = 3$  for model B. The calculated development of swelling pressure with  $\lambda = 3$  (model B) is faster than using  $\lambda = 5$ . But the increased rates are still lower than the observations in the beginning. Obviously, the evolution of swelling pressure is directly related to the hydration process. The swelling pressure calculated tends to the maximum of  $p_s = 5.6$  MPa at the bentonite-sand mixture over 40 days and  $p_s = 3.7$  MPa at the claystone-bentonite mixture over 50 days. These values are consistent with the measured data. Since the swelling pressures are much lower than those pre-consolidation pressures of 14 to 18 MPa, the seal materials remain in the elastic domain during hydration and thus the plastic parameters do not play any role in the computation /GEN 98/.



a) Bentonite-sand mixture



b) Claystone-bentonite mixture

**Fig. 5.16** Predictions of the swelling pressure developed in the compacted bentonite-sand (a) and claystone-bentonite (b) mixture during hydration

#### 5.2.4.2.2 Bentonite

Within the framework of the Bentonite Rock Interaction Experiment (BRIE) in Äspö-URL, water uptake tests were performed on the compacted MX80 bentonite blocks by Clay Technology /ÅKE 13/. The blocks with a dry density = 1.587 g/cm<sup>3</sup> were sized to a height of 100 mm and diameter of 298 mm. A hole of 40 mm was drilled in the centre of each block. The blocks were installed in steel cylinders with steel lids mounted on the top and the bottom. A plastic filter was mounted on the inside of the cylinder for water supply, while the central hole was sealed with a dummy. The cylinder and the top lid were equipped with holes for measurements of total pressure and relative humidity. Fig. 5.17 illustrates schematically the setup of the test and positions of the measurements.

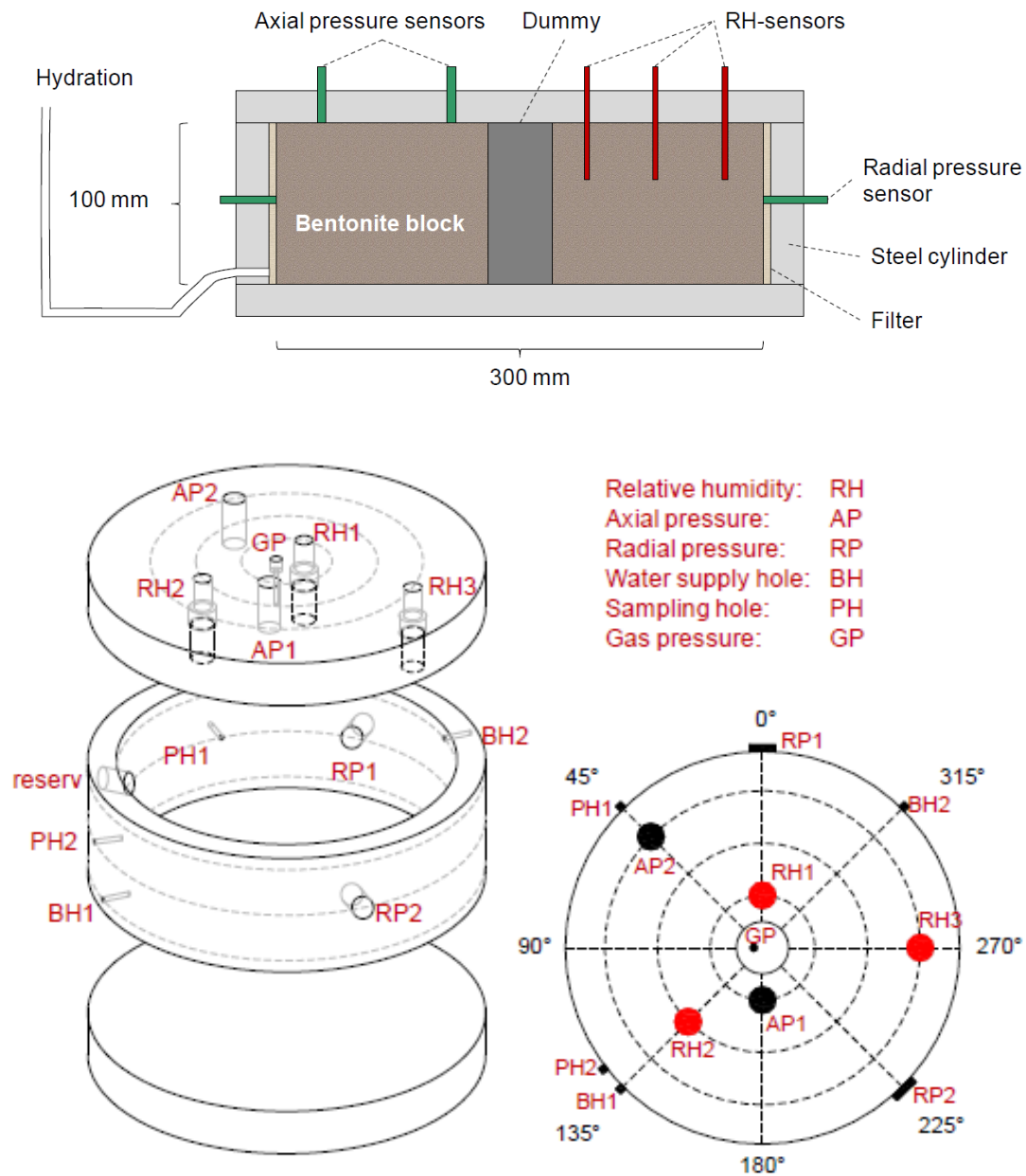


**Fig. 5.17** Schematic setup of BRIE water uptake tests on the compacted bentonite and measurement locations /ÅKE 13/

The conditions of BRIE-test 1 are selected for modelling the hydration process and the resultant buildup of swelling pressure in the compacted bentonite. An axisymmetric geometry with 120 elements is established for the hollow cylinder, see Fig. 5.18. Considering the initial water filling of the outer slot, the outer diameter of 145 mm is defined for the model. The sample is characterized with a dry density = 1.587 g/cm<sup>3</sup>, porosity = 44.0 %, water content = 11.75 %, and saturation degree = 42.0 %. The block is fixed with zero boundary deformation. The liquid pressure at the outer boundary is kept at atmospheric

level,  $P_l = 0.1$  MPa, and the gas pressure is atmospheric,  $P_g = 0.1$  MPa. The rest boundaries are isolated with zero fluid flow,  $Q_l = 0$ . A low initial stress is applied with  $\sigma_1 = \sigma_2 = \sigma_3 = 0.15$  MPa. A constant temperature remains at 20 °C. GRS-A, GRS-B and BRIE models with the hydraulic parameters are applied (see Table 5.6). However, a unique value of the relative permeability parameter  $\lambda = 4$  is obtained from back analysis for all the models. In correspondence to the initial saturation of  $S_{o} = 42.0$  %, an initial suction of  $s_o = 95$  MPa is obtained for GRS-A and BRIE model, while  $s_o = 290$  MPa for GRS-B. The BBM parameters for the bentonite are adopted (see Table 5.4). Coupled HM calculations are performed by solving the balance equations of solid (Eq. 5.2), water mass (Eq. 5.3) and stress equilibrium (Eq. 5.5).

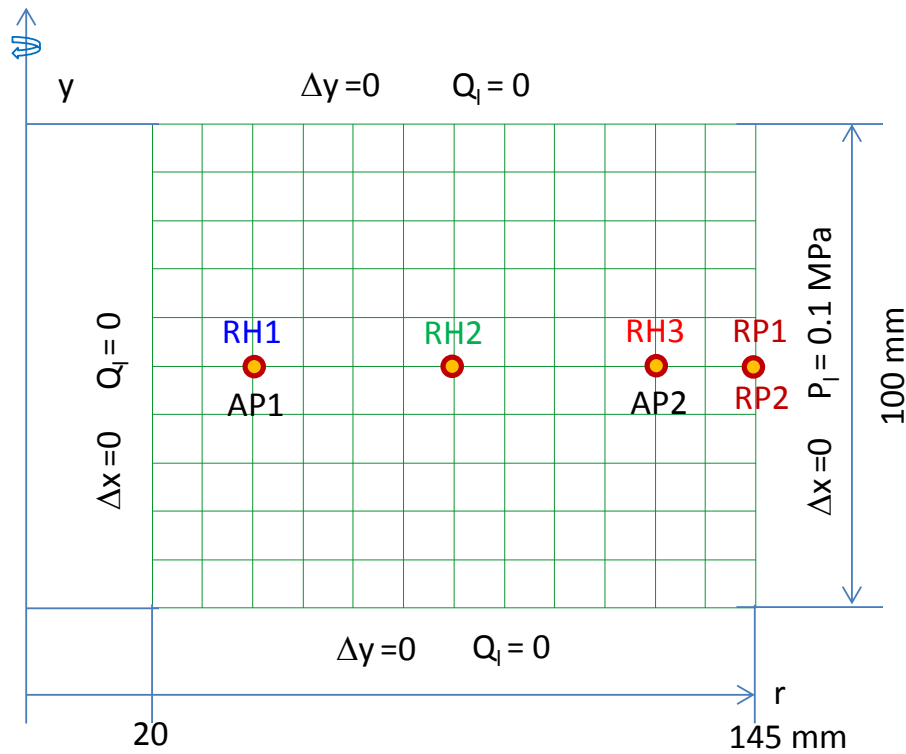


**Fig. 5.18** Model geometry and boundary conditions for modelling the hydration and swelling pressure in the compacted bentonite in BRIE-tests

Modelling results are compared with the evolution of measured relative humidity ( $RH$ ) and total or swelling pressures ( $AP$ ,  $RP$ ) in the sample at the different locations. The distributions of water saturation in the samples after testing at 107 days (test 2) and 203 days (test 1) are also predicted.

From the computing output of the degree of water saturation  $S_i$ , one can derive the  $RH$ -values by reformulating and combining equations (4.1) and (5.14)

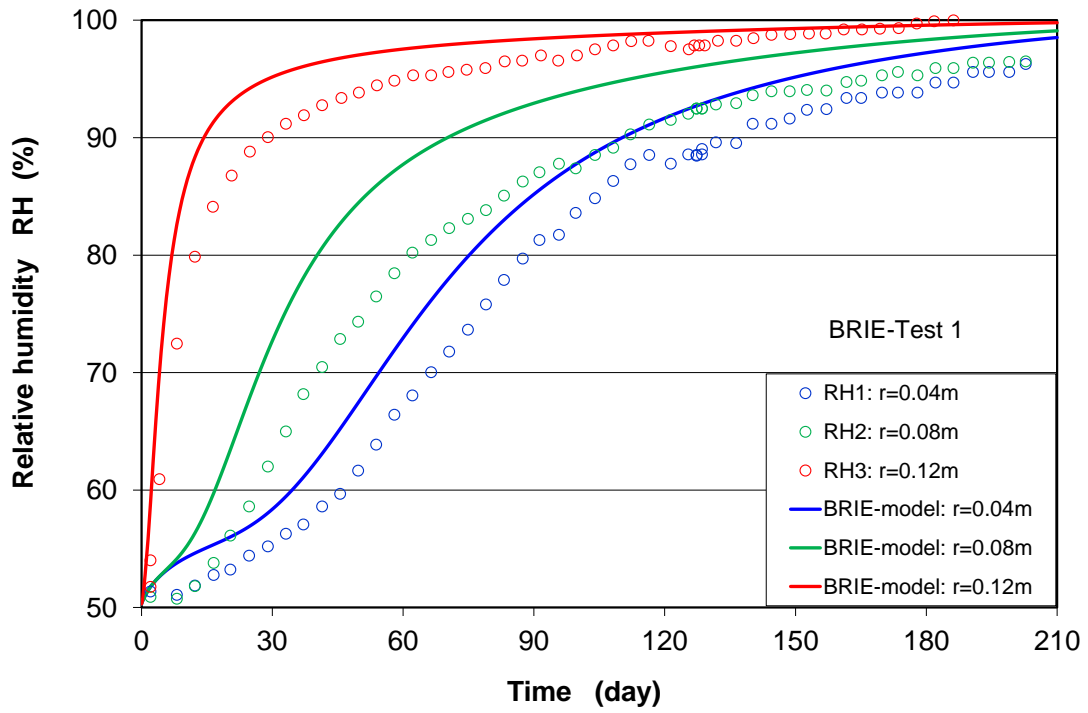
$$RH = \exp \left[ -\frac{v_{wo} \omega_v}{RT} \cdot s \right] \quad (5.29)$$

with  $s = P_o \cdot \left[ S_i^{-1/\beta} - 1 \right]^{(1-\beta)}$

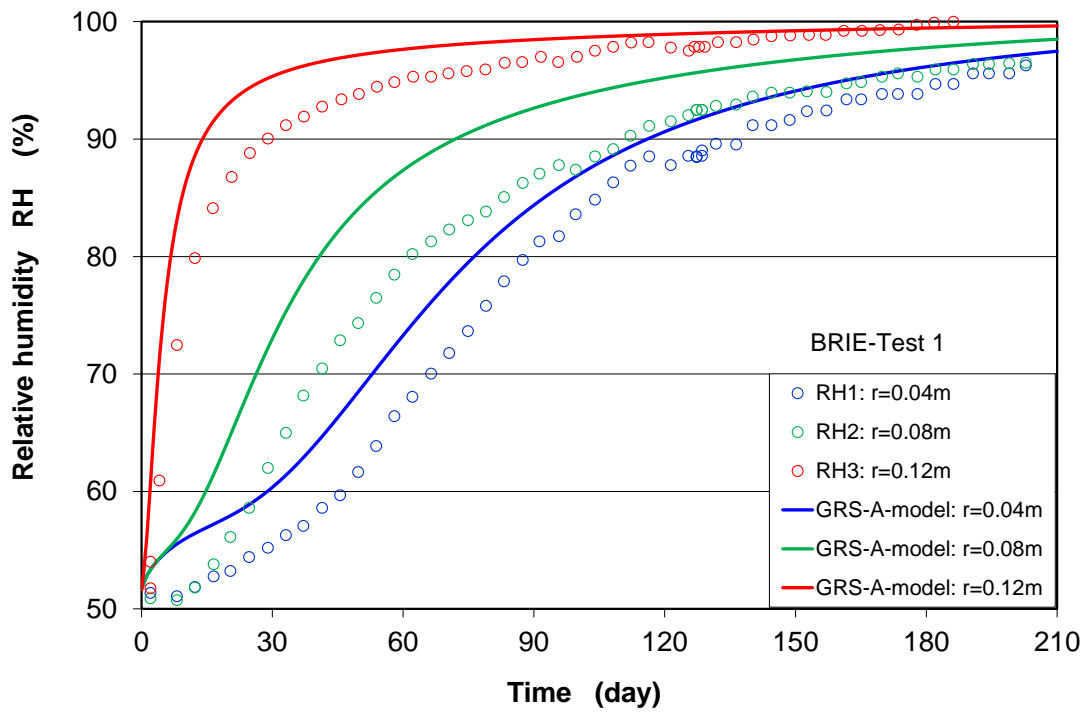
Fig. 5.19 shows the modelling results of the  $RH$ -evolution at the different positions in the sample using the model BRIE (a), GRS-A (b) and GRS-B (c), respectively. It can be recognized that both BRIE and GRS-A models are close to but somewhat overestimate the measured relative humidities, whereas GRS-B model provides much lower  $RH$ -values for the first two months but agrees well with the data for the later stages.

The modelling results for the distribution of water saturation are illustrated in Fig. 5.20 together with the data at 107 days (test 2) and 203 days (test 1). Whereas BRIE model systematically overestimates (Fig. 5.20a) and GRS-B contrarily underdetermines the water saturation (Fig. 5.20b), GRS-A model delivers a very close agreement with the distributions of water saturation at those saturation times, see Fig. 5.20a.

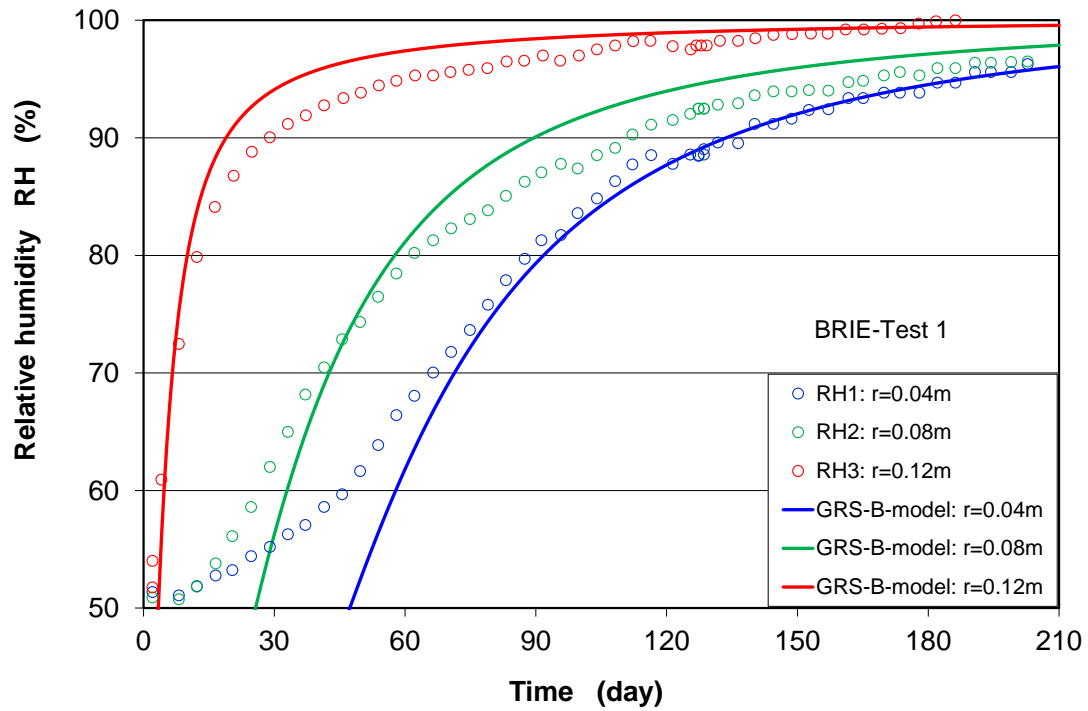
Finally, the development of swelling pressure during the water saturation is predicted using the most adequate water retention model GRS-A. Fig. 5.21 shows the modelling results in comparison with the observed buildup of swelling pressure at the different locations. It is obvious that the swelling pressures in radial direction RP at the outer side ( $r = 0.145$  m) and in axial direction at the position  $r = 0.04$  m are well captured by the model. The measured axial swelling pressures at  $r = 0.12$  m are overestimated by the model, but the calculated axial swelling pressures match the upper curve of the radial swelling pressure. Generally speaking, the hydration process and the resulting swelling pressure in the bentonite can be reasonably revealed by the coupled HM modelling with GRS-A water retention parameters.



a) Prediction using BRIE model parameters

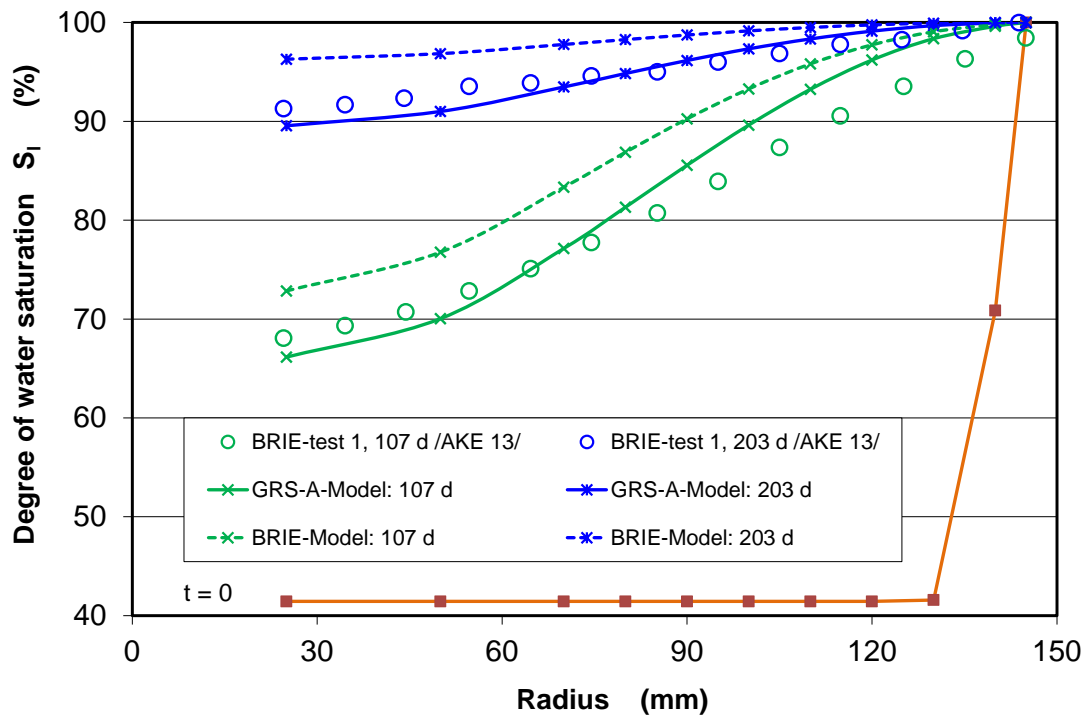


b) Prediction using GRS-A model parameters

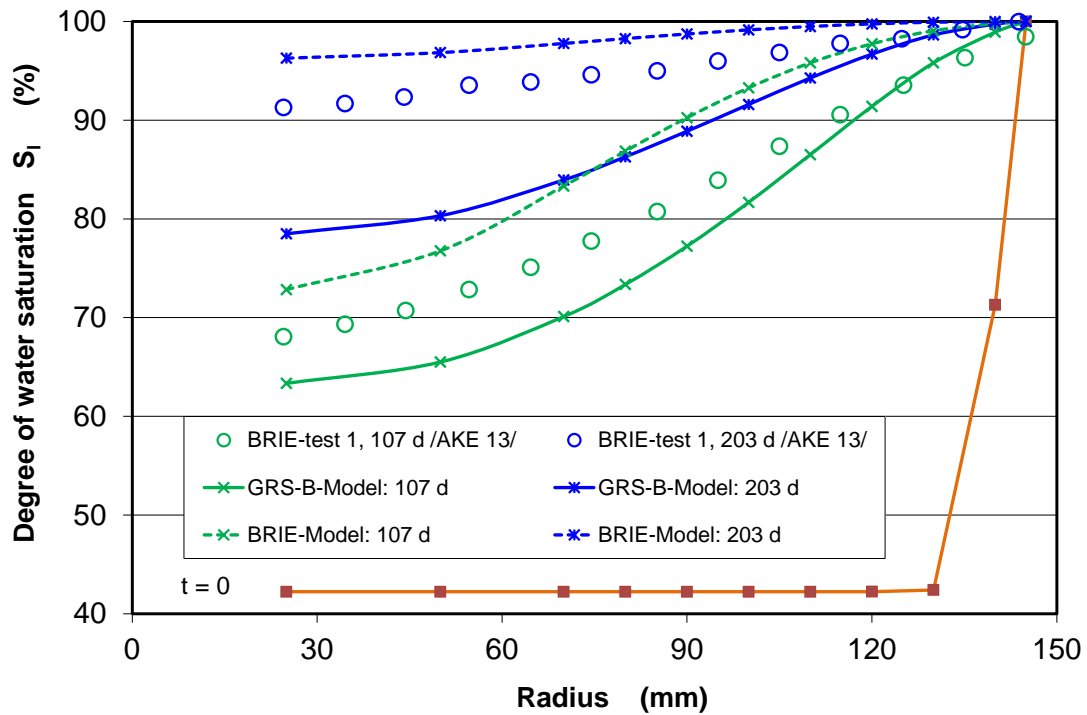


c) Predictions using GRS-B model parameters

**Fig. 5.19** Modelled evolution of water saturation of the compacted bentonite at different locations during the laboratory BRIE test (a-c) /ÅKE 13/



a) Predictions using BRIE and GRS-A model parameters



b) Predictions using BRIE and GRS-B model parameters

**Fig. 5.20** Modelled distributions of water saturation in the compacted bentonite at different times during the laboratory BRIE-test (a-b) /ÅKE 13/

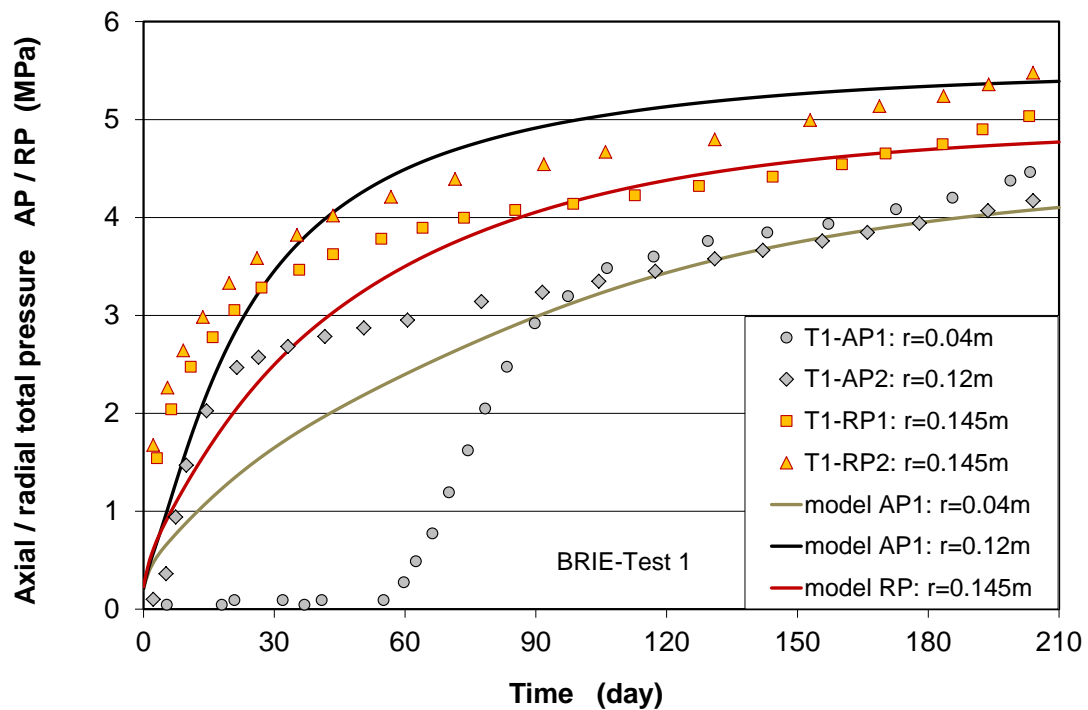


**Fig. 5.21** Modelling results of swelling pressure development in the compacted bentonite during the BRIE water uptake test /ÅKE 13/

### **5.3 Modelling of the hydro-mechanical behaviour of clay rock**

From comprehensive modelling exercises during the last decade, it was recognized that the existing constitutive models for clay rock are to be improved for reliable prediction of the long-term behaviour of the clay host rock during the repository operation and post-closure phases, especially with regard to the long-term deformation, permeability variations with damage and recompaction, water conductivity of fractured claystone, and gas migration behaviour. In the framework of this project, it was attempted to establish some specific functions for improving the existing models with aspects of

- time-dependent deformation of water-saturated claystone;
- fracturing-induced permeability changes;
- recompaction and permeability changes of fractured claystone; and
- gas migration behaviour of fractured and resealed claystone.

These model formulations were based on the laboratory observations. More details are presented in the project interim reports and publications /ZHA 13a/114b/14c/15a/16/. These constitutive equations will be briefly summarized in the following.

#### **5.3.1 Hydraulic constitutive models**

The hydraulic laws adopted for the compacted seal materials (section 5.2.2) may be applied for modelling of the hydraulic behaviour of the intact clay rock. As the clay rock is subjected to fracturing by mechanical loading, for instance, with the generation and development of the EDZ near the underground openings, the permeability increases with fracturing. The cubic law for porous media with interconnected pores or cracks (Eq. 5.9) is no more adequate for the fracturing-induced permeability. Based on the laboratory experiments and fracture percolation theory, a new permeability model has been established for the prediction of the permeability evolution in the EDZ.

##### **5.3.1.1 A permeability model for damage and recompaction of claystone**

Considering the varying stress conditions subject to the clay rock in the near-field of a potential repository, its hydro-mechanical responses were experimentally investigated on the COX claystone with measurements of deformation and gas permeability during damage and recompression /ZHA 13a/16/. The main results are overviewed in chapter 3.

The complete behaviour of the claystone before and after failure is schematically highlighted in Fig. 5.22 in terms of differential stress ( $\Delta\sigma = \sigma_1 - \sigma_3$ ), volumetric strain ( $\varepsilon_v$ ), and permeability ( $k$ ) vs. axial strain ( $\varepsilon_1$ ).

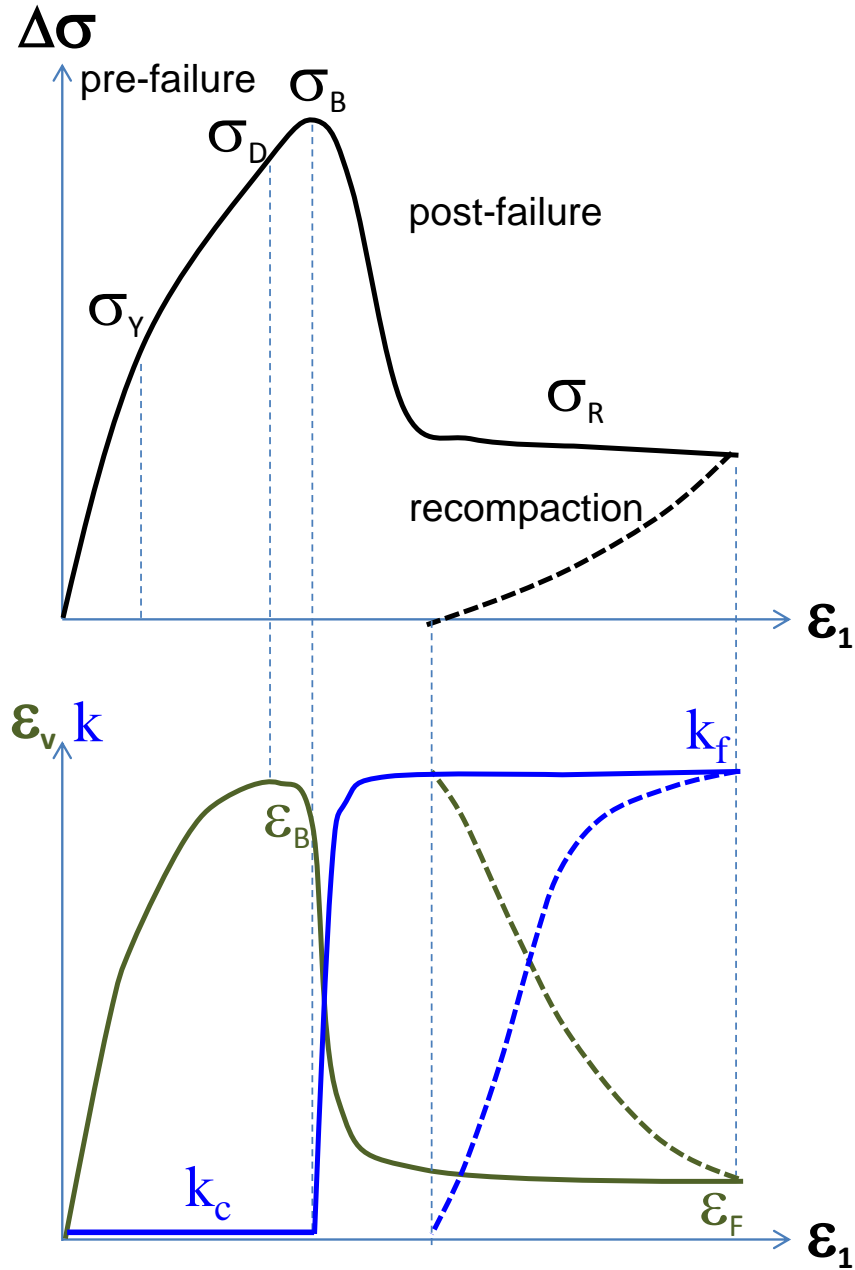


**Fig. 5.22** Stress-strain-permeability behaviour of claystone during damage and recompaction ( $\sigma_Y$  = yield stress,  $\sigma_D$  = dilatancy threshold,  $\sigma_B/\varepsilon_B$  = peak failure stress/volumetric strain,  $\sigma_R$  = residual strength,  $k_c$  = initial permeability,  $\varepsilon_F$  = volumetric strain at ultimate fracturing and  $k_f$  = final fracture permeability)

The claystone behaves elasto-plastically with volume compaction until the onset of dilatancy at a high stress  $\sigma_D$ . The volume compaction closes up the pores and fissures so that the permeability does not increase. Further increasing the stress leads to initiation and propagation of microcracks. As the peak stress  $\sigma_B$  is reached, the microcracks coalesce to a continuous network or shear fracture resulting in a spontaneous increase in permeability. The increased permeability remains relatively constant after the fracture percolation over the post-failure phase. When the minor principal stress  $\sigma_3$  in the damaged claystone (EDZ) increases ( $\Delta\sigma$  decreases), for instance, with the convergent compression of the surrounding rock and the resistance of the lining or backfill, the fractures tend to closure ( $\varepsilon_v$  decreases) and the permeability reduces. A high degree (if not full) of the fracture reseal can be expected over long time periods under combined impact of the mechanical load and the moisture-induced swelling of clay into the fracture interstices.

Based on the experimental results, a new model was established for approaching the permeability variations with deformation, damage and recompaction:

$$k = \begin{cases} k_c & (\sigma_1 - \sigma_3) < \sigma_B & (5.30a) \\ k_o \cdot \exp(-r\sigma_3) \cdot \left(1 - \exp\left(-\frac{\Delta\varepsilon_D}{\varepsilon_B}\right)\right) & \sigma_B \geq (\sigma_1 - \sigma_3) \geq \sigma_R & (5.30b) \\ D \cdot (\Delta\varepsilon_R)^3 & (\sigma_1 - \sigma_3) < \sigma_R & (5.30c) \end{cases}$$

Before failure at  $(\sigma_1 - \sigma_3) < \sigma_B$ , the very low permeability of the natural intact claystone does not increase but decreases slightly with some compaction of the pores. For the purpose of simplification, the very low permeability values of the highly-consolidated clay rocks can be assumed constant (Eq. 5.30a). As measured,  $k_c$ -values of the COX and OPA claystones are in a very low range of  $10^{-20}$ – $10^{-21}$  m<sup>2</sup>, practically impermeable.

After failure at  $\sigma_B \geq (\sigma_1 - \sigma_3) \geq \sigma_R$ , the fracturing-induced permeability increases spontaneously, which is contributed by the connectivity and the conductivity of cracks. It can be expressed with the percolation probability of cracks belonging to the conducting part of a network and the ultimate permeability after fully fracturing (Eq. 5.30b). The percolation probability is expressed as an exponential function of crack dilatancy:  $p = (1 - \exp(-\Delta\varepsilon_D/\varepsilon_B))$ , where  $\Delta\varepsilon_D = |\varepsilon_v - \varepsilon_B|$  is the dilatancy with reference to the volumetric strain  $\varepsilon_B$  at the percolation threshold assumed to be equal to the peak stress  $\sigma_B$ . The ultimate fracture permeability increases exponentially with decreasing the minor principal stress:  $k_f = k_o \cdot \exp(-r\sigma_3)$ , where  $k_o$  is the permeability at zero minor principal stress  $\sigma_3$

$= 0$  and  $\gamma$  is a parameter characterizing the dilatibility of the interconnected cracks. The values of the parameters are estimated to be  $k_o = 3 \cdot 10^{-13} \text{ m}^2$  and  $\gamma = 1.9 \text{ MPa}^{-1}$  for the COX claystone. The comparison with the test data in Fig. 3.4 confirms the percolation model.

When the fractured claystone is recompacted with increasing  $\sigma_3$  or decreasing the differential stress to  $(\sigma_1 - \sigma_3) < \sigma_R$ , the fracture permeability tends to decrease following the cubic law (Eq. 5.30c), where  $\Delta\varepsilon_R = |\varepsilon_F - \varepsilon_v|$  represents the residual void in the fractures,  $\varepsilon_F$  is the maximum dilatancy at the final damaged state and  $D = k_f / \varepsilon_F^3$  is a parameter characterising the final damaged state. As the residual fracture void tends to zero,  $\Delta\varepsilon_R \rightarrow 0$ , the fracture permeability will disappear. The parameter  $D$  is estimated from the data to lie in a range of  $7 \cdot 10^{-10} \text{ m}^2$  to  $1 \cdot 10^{-7} \text{ m}^2$ , depending on the damage intensity of the claystone. A comparison made in Fig. 3.9 shows a satisfactory agreement of the cubic law with the data obtained from the hydrostatic and deviatoric recompressions.

### 5.3.1.2 A water permeability model for sealing of fractured claystone

Note that the above mentioned permeability model is based on the gas permeability measurements under mechanical loads. It cannot be directly applied for modelling the water permeability because the significant water-enhanced sealing effects are not involved. As observed in our experiments (section 3.4), the water permeability of the fractured claystone is several orders of magnitude lower than the gas permeability. Based on the data obtained during the long-term sealing tests, an empirical equation was established for the water permeability of fractured claystone in relation with effective confining stress (Eq. 3.7):

$$K_w = K_{wo} \cdot \exp(-\beta \cdot \sigma') \quad (5.31)$$

where  $\sigma' = \sigma - p_w$  is the effective isostatic stress,  $\sigma$  is the total isostatic stress,  $p_w$  is the porewater pressure,  $K_{wo}$  is the initial water permeability at zero effective confining stress  $\sigma' = 0$ , and  $\beta$  is a parameter characterising the compressibility of the water flow pathways.  $K_{wo}$ -values determined on the artificially-fractured COX samples are quite low ranging from  $2 \times 10^{-16}$  to  $4 \times 10^{-20} \text{ m}^2$  compared with their gas permeability of  $\sim 10^{-13} \text{ m}^2$ . A unique  $\beta$ -value of  $0.6 \text{ MPa}^{-1}$  is obtained. This model matches the test data well (cf. Fig. 3.12) and, therefore, it can be used for modelling the water permeability of fractured claystone during recompaction.

### 5.3.1.3 A gas flow model for water-saturated and resealed claystone

Gas flow through a fractured claystone could be modelled by using Darcy's law and the new permeability model (equations 5.30b-c), which was based on the gas permeability data obtained on the fractured COX claystone. As the fractures become water-saturated, however, gas entry and flow through needs driving forces to overcome capillary thresholds which are built up in the fractures after water saturation. The gas migration behaviour of the water-saturated and resealed claystone can be characterised with two key parameters, namely gas breakthrough pressure and permeability. They are strongly related with the intrinsic (water) permeability of the claystone and external confining stress. Based on the experimental data, the respective relationships were formulated in /ZHA 14c/ and represented below as a gas flow model for water-saturated and resealed claystone.

The gas breakthrough pressure can be expressed as function of intrinsic permeability and minimum confining stress (Eq. 3.8)

$$P_b = B \cdot (K_{wo})^{-1/n} \cdot \exp(-\gamma\sigma_{min}) \quad (5.32)$$

where  $P_b$  is the gas breakthrough pressure,  $K_{wo}$  is the initial intrinsic permeability at zero minor confining stress  $\sigma_{min} = 0$ ,  $B$ ,  $n$  and  $\gamma$  are parameters. Their values are estimated to be  $B = 2 \times 10^{-7} \text{ MPa} \cdot \text{m}^{2/3}$ ,  $n = 3$  and  $\gamma = 0.2 \text{ MPa}^{-1}$  for the fractured claystone with very low water permeabilities of  $K_{wo} = 5 \times 10^{-19}$  to  $5 \times 10^{-20} \text{ m}^2$ . The model prediction provides a reasonable agreement with the data (Fig. 3.15). Obviously, the gas breakthrough pressures are below the conservative fracturing condition by neglecting the tensile strength,  $P_b < \sigma_3$ . This model is also applicable for the intact claystone as a fully resealed material with lower permeabilities of  $K_{wo} < 1 \times 10^{-20} \text{ m}^2$ .

Gas pressure rising reopens some weakly-resealed fissures and then dilates the gas-occupied pathways. The growth of the fissure network allows gas to flow easier, so that the effective gas permeability increases with increasing gas pressure (see Fig. 3.16). The gas breakthrough permeability can be expressed as a function of gas pressure  $P_b$ :

$$K_g = K_{go} \cdot \exp[\omega(P_b - P_{bo})] \quad (5.33)$$

where  $K_{go}$  is the gas permeability at the initial breakthrough pressure  $P_{bo}$ ,  $\omega$  is the parameter characterising the dilatability and interconnectivity of the gas pathways. Fitting the data leads to  $\omega = 1.5$  to  $2.5 \text{ MPa}^{-1}$ , depending on the resealing degree of the fractures.

Actually, the dilation of the pathways and the resulting permeability increase is determined by the effective confining stress, namely the difference between the total stress and pore pressure. Therefore, the gas breakthrough permeability can also be related to the minor effective principal stress  $\sigma'_{min}$

$$K_g = K_{go} \cdot \exp[-\mu\sigma'_{min}] \quad (5.34)$$

where  $\sigma'_{min} = \sigma_{min} - (P_g + P_o)/2$ ,  $K_{go}$  is the gas permeability at  $\sigma'_{min} = 0$ , and  $\mu$  is a parameter characterising the dilatability and interconnectivity of the gas pathways. The parameters were estimated to be  $K_{go} = 1 \times 10^{-10} - 3 \times 10^{-7} \text{ m}^2$  and  $\mu = 3.5 \text{ MPa}^{-1}$ . A comparison in Fig. 3.17 shows good agreement between the model and the data.

### 5.3.2 Mechanical constitutive models

An elastoplastic damage model was originally developed by /VAU 03/ for description of the mechanical behaviour of clay rock. This model considers the claystone as a composite material composed of a clay matrix connected by bonds. The clay matrix behaves like a typical elastoplastic soil, while the bonds (mainly carbonates) behave like a typical quasi-brittle material that can be represented by a damage elastic law. The stress-strain behaviour of the composite material is assumed to be determined by coupling both responses of matrix and bonds under compatible conditions.

However, the microstructural observations made on the relatively clay-rich COX and OPA claystones /AND 05/and /BOC 10/ show that the hard mineral grains (quartz, calcite and others) are embedded in the clay matrix and the connections between neighbouring clay particles are mainly through adsorbed porewater. The effects of the solid-bonds should not be significant. So the behaviour of the clay matrix is dominating. Currently, this model has been enhanced by introducing a modified Lemaitre law for the viscoplastic deformation of claystone /RUI 15/. This so called visco-elastoplastic model is briefly overviewed below.

The visco-elastoplastic model is formulated for claystone in water-saturated and unsaturated conditions. The Mohr-Coulomb criterion is adopted for yield surface in the stress space that separates the elastic and plastic parts of the mechanical response.

$$\text{Elastic law: } d\sigma_{ij} = D_{ijkl}^e \left( d\varepsilon_{kl} - \delta_{kl} \frac{ds}{K_s} - d\varepsilon_{kl}^{vp} \right) \quad (5.35)$$

where  $\sigma_{ij}$  = effective stresses

$\varepsilon_{kl}$  = total strains

$\varepsilon_{kl}^{vp}$  = viscoplastic strains

$D_{ijkl}^e$  = elastic stiffness matrix

$K_s$  = bulk modulus against suction change  $ds$  ( $s = p_g - p_t$ )

$\delta_{kl}$  = Kronecker delta.

For the simplicity, the claystone is here assumed to be isotropic. The linear elastic stiffness  $D_{ijkl}^e$  is determined by Young's modulus  $E$  and Poisson's ratio  $\nu$  of the claystone. Volumetric swelling of the claystone is assumed to be linearly related to suction change  $ds$  by the bulk modulus  $K_s$ . Wetting (suction decrease) leads to swelling and in contrast drying (suction increase) results in shrinkage:

$$d\varepsilon_v^s = \frac{ds}{K_s} \quad (5.36)$$

Mohr-Coulomb yield function:

$$F = \left( \cos \theta + \frac{1}{\sqrt{3}} \sin \theta \cdot \sin \varphi \right) J - \sin \varphi \cdot (c \cot \varphi + p_t) \geq 0 \quad (5.37)$$

where  $\theta$  is Lode's angle (Eq. 5.20),  $\varphi$  is the friction angle,  $c$  is the cohesion, which depends on suction following the law:  $c = c_o + s \cdot \tan \varphi$ , and  $p_t = c \cdot \cot \varphi$  represents the isostatic tensile strength.

Plastic potential:

$$G = \left( \cos \theta + \frac{1}{\sqrt{3}} \sin \theta \cdot \sin \varphi \right) J - \omega \cdot \sin \varphi \cdot (p + p_t) \quad (5.38)$$

where  $\omega$  is a parameter defining the non-associativity of the plastic flow:  $\omega = 1$  when associated and  $\omega = 0$  for zero dilatancy.

#### Hardening-softening law:

An isotropic hardening-softening law is considered, governed by the evolution of the strength parameters  $(\varphi, c)$ . The equivalent plastic deformation is the selected state variable to control this evolution, which is defined as:

$$\varepsilon_{eq}^p = \left( \frac{2}{3} \boldsymbol{\varepsilon}^p : \boldsymbol{\varepsilon}^p \right)^{1/2} \quad (5.39)$$

where  $\boldsymbol{\varepsilon}^p$  is the plastic deformation tensor.

The way in which the angle of friction varies depends on the equivalent plastic deformation, as outlined in Fig. 5.23. The laws of evolution in each one of the listed areas are shown in Table 5.10. Cohesion evolves as a function of the mobilized friction angle and at any point is given by the following expression:  $c_{mov} = c_{peak} \cdot \cot \varphi_{ini} \cdot \tan \varphi_{mov}$ .

#### Creep law

For description of the creep deformation of claystone, a modified Lemaitre law is adopted taking into account strain-hardening effect. The strain rate is expressed as function of deviatoric stress and equivalent plastic strain

$$\dot{\boldsymbol{\varepsilon}}^{vp} = \frac{2}{3} \frac{\dot{\varepsilon}_{eq}^{vp}}{q} \mathbf{s} \quad (5.40) \quad \dot{\varepsilon}^{vp} = \gamma (q - \sigma_s)^n (1 - \varepsilon_{eq}^{vp})^m \quad (5.41)$$

where  $\gamma$  is a parameter of viscosity,  $\sigma_s$  is a threshold of the deviatoric stress from which the viscoplastic deformation is activated,  $n$  and  $m$  are material constants and  $\varepsilon_{eq}^{vp}$  is the state variable of the viscoplastic response, defined as:

$$\varepsilon_{eq}^{vp} = \int \left( \frac{2}{2} \dot{\boldsymbol{\varepsilon}}^{vp} : \dot{\boldsymbol{\varepsilon}}^{vp} \right)^{1/2} dt \quad (5.42)$$

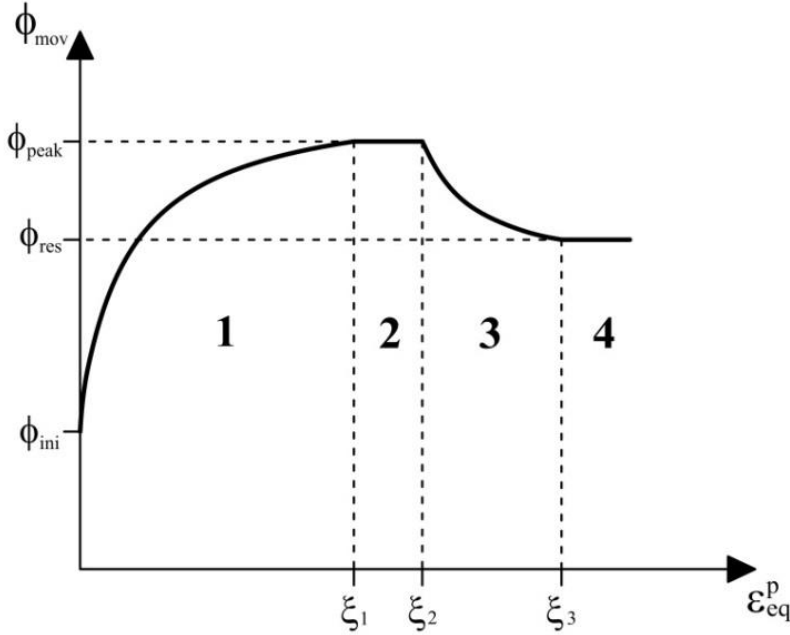


**Fig. 5.23** Evolution of the friction angle

**Tab. 5.10** Laws of evolution of the friction angle

Zone 1	$\varphi_{mov} = \varphi_{ini} + \frac{\varepsilon_{eq}^p}{a_{hard} + \frac{\varepsilon_{eq}^p}{\Delta\varphi_{hard}}}, \quad \Delta\varphi_{hard} = \frac{\xi_1}{\frac{\xi_1}{\varphi_{peak} - \varphi_{ini}} - a_{hard}}$
Zone 2	$\varphi_{mov} = \varphi_{peak}$
Zone 3	$\varphi_{mov} = \varphi_{peak} - \frac{\varepsilon_{eq}^p - \xi_2}{a_{soft} + \frac{\varepsilon_{eq}^p - \xi_2}{\Delta\varphi_{soft}}}, \quad \Delta\varphi_{soft} = \frac{\xi_3 - \xi_2}{\frac{\xi_3 - \xi_2}{\varphi_{peak} - \varphi_{res}} - a_{soft}}$
Zone 4	$\varphi_{mov} = \varphi_{res}$

$\varphi_{mov}$  = mobilized friction angle,  $\varphi_{ini}$  = initial friction angle at yield surface,  $\varphi_{peak}$  = peak friction angle at peak failure strength,  $\varphi_{res}$  = residual friction angle at residual strength,  $\xi_1$  = equivalent plastic strain at which the maximum strength is reached,  $\xi_2$  = equivalent plastic strain at which softening begins,  $\xi_3$  = equivalent plastic strain at which the residual strength is reached,  $a_{hard}$  = constant that controls the curvature of the function in the hardening branch,  $a_{soft}$  = constant that controls the curvature of the function in the softening branch.

The long-term creep experiments performed on the claystone /ZHA 13a/16/ showed that the typical creep strain curve can be divided into three sequential stages, transient creep with decreasing rates, stationary creep with a constant rate, and tertiary creep with increasing rate to failure. The modified Lemaitre law features the transient creep with rate decrease.

Based on the long-term creep test data, a model was formulated for the stationary creep of the claystone by modification of the Mitchell law /MIT 92/ that had been derived through thermodynamically analysis of soil flow by application of absolute reaction rate theory

$$\dot{\varepsilon}^{vp} = A \exp\left(-\frac{Q}{RT}\right) \sinh(\alpha \cdot q) \quad (5.43)$$

where  $T$  is the absolute temperature (K),  $R$  is the universal gas constant ( $8.32 \cdot 10^{-3} \text{ kJmol}^{-1} \text{ K}^{-1}$ ),  $Q$  is the apparent activation energy ( $\text{kJmol}^{-1}$ ),  $A$  is a parameter in  $\text{s}^{-1}$ , and  $\alpha$  is a parameter in  $\text{MPa}^{-1}$ .

If  $\alpha q < 1$ , then  $\sinh(\alpha q) \approx \alpha q$ , and the strain rate is directly proportional to  $q$

$$\dot{\varepsilon}^{vp} = A \exp\left(-\frac{Q}{RT}\right) (\alpha \cdot q) \quad (5.44)$$

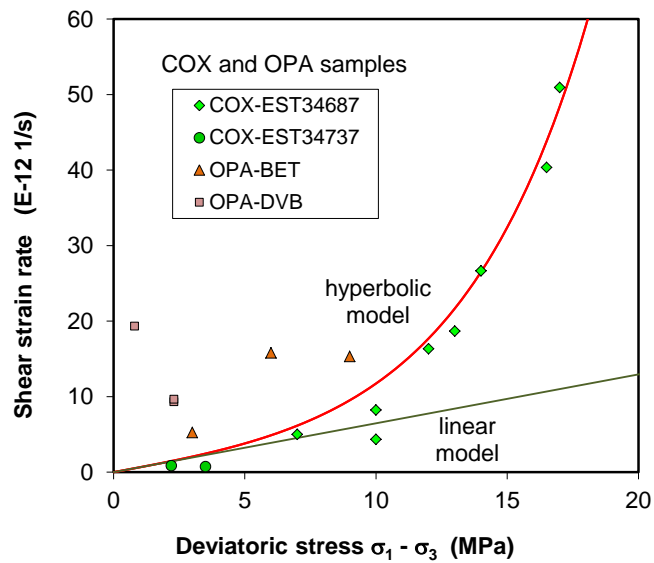
This is the case for ordinary Newtonian fluid flow and diffusion. According to /RUT 93/, the linear stress/strain rate relation implicates that the viscoplastic deformation of the saturated claystone is controlled by diffusive mass transfer or pressure solution processes in interfaces between grains.

For most deformation problems of soils and rocks,  $\alpha q > 1$ , so then  $\sinh(\alpha q) \approx 1/2 \exp(\alpha q)$ , and equation (5.43) becomes

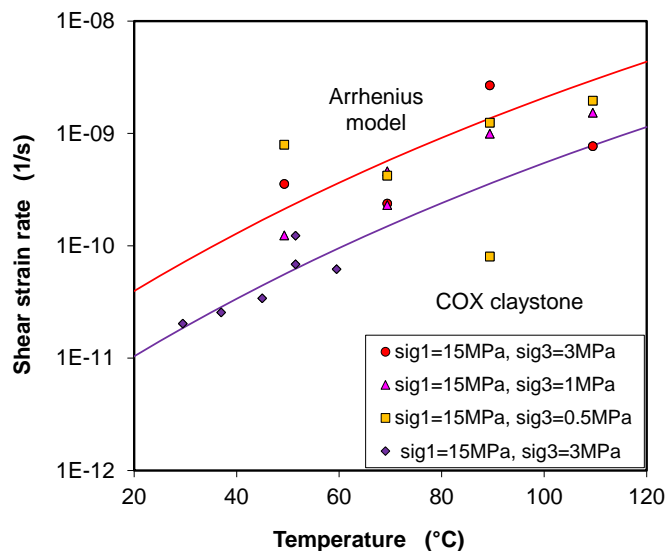
$$\dot{\varepsilon}^{vp} = \frac{A}{2} \exp\left(-\frac{Q}{RT}\right) \exp(\alpha \cdot q) \quad (5.45)$$

It is considerable to incorporate the stationary creep model into the code for prediction of the long-term deformation of clay host rock during the repository post-closure phase.

For the water-saturated COX claystone, the parameters are established:  $A = 2.2 \cdot 10^{-4} \text{ s}^{-1}$ ,  $\alpha = 0.2 \text{ MPa}^{-1}$ , and  $Q = 45 \text{ kJmol}^{-1}$ . Fig. 5.24 compares the creep model with the measured creep rates as function of deviatoric stress (a) and temperature (b). A reasonable agreement can be found for the COX claystone. The creep rates obtained for the OPA claystone are relatively higher due to the high content of clay minerals, compared to the COX claystone. As mentioned earlier, the creep under low stresses of  $\Delta\sigma < 10 \text{ MPa}$  varies almost linearly with stress, which is probably controlled by diffusion in bound water-films between solid particles. Beyond that the creep is additionally contributed by microcracking.



a) Creep rate – stress relation



b) Creep rate – temperature relation

**Fig. 5.24** Stationary shear creep rate of the water-saturated COX claystone as function of deviatoric stress (a) and temperature (b)

### 5.3.2.1 Mechanical parameters

#### Elastic parameters

In the framework of an ANDRA-GRS joint programme /ZHA 15b/ for the characterisation of the anisotropic behaviour of the COX claystone, the elastic parameters were determined in directions parallel and perpendicular to the bedding planes. Fig. 5.25 shows the averaged Young's modulus  $E_1$  / Poisson's ratio  $\nu_1$  parallel to bedding and  $E_2$  /  $\nu_2$  normal to bedding as a function of deviatoric stress at lateral stress of 5 MPa. The elastic parameters increase in the beginning of  $\Delta\sigma < 10$  MPa due to hardening effect and then tend to constant until damage and failure. The constant values shall be representative for the intact claystone, while the low values may be for the disturbed state. The five independent elastic parameters and the anisotropic parameters are summarized in Table 5.11 and compared with the OPA clay /BOC 10/ and the Tournemire shale /NIA 97/. One can identify that the elastic stiffness of the COX claystone is higher than that of the Opalinus claystone but lower than the Tournemire shale. The elastic anisotropy of the COX clay rock is less significant compared with the other two clay rocks.

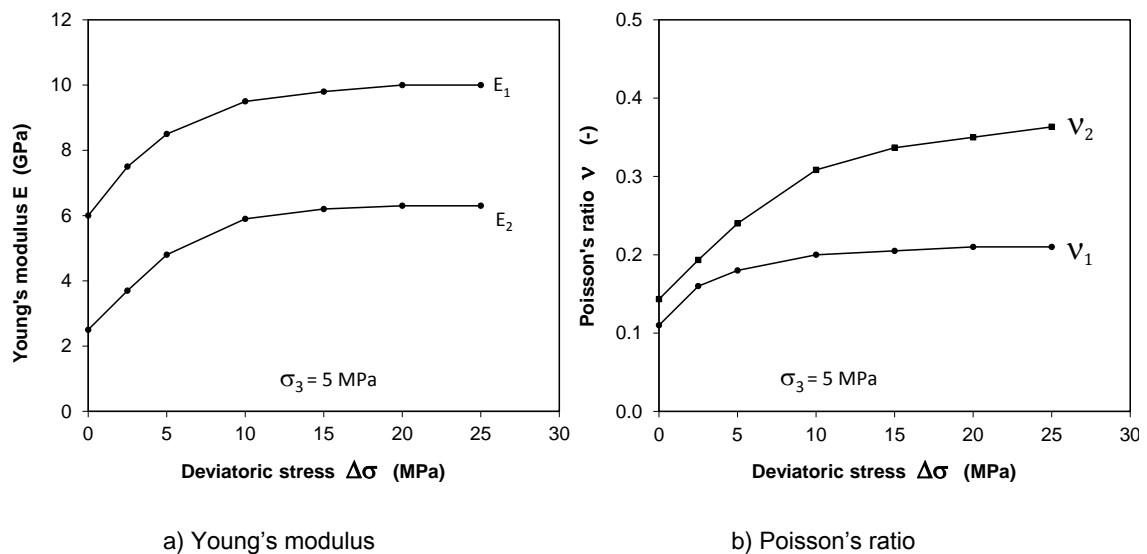


**Fig. 5.25** Anisotropic elastic parameters of the COX claystone as a function of deviatoric stress: Young's modulus / Poisson's ratio  $E_1$  /  $\nu_1$  parallel and  $E_2$  /  $\nu_2$  normal to bedding planes

**Tab. 5.11** Anisotropic elastic parameters of three clay rocks

Clay rock	$E_1$ (GPa)	$E_2$ (GPa)	$G_2$ (GPa)	$\nu_1$	$\nu_2$	$R_E=E_1/E_2$	$R_\nu=\nu_2/\nu_1$
COX Bure-490m /ZHA 15b/	10.0	6.3	5.0	0.21	0.35	1.6	1.7
OPA, Mont-Terri /BOC 10/	10.0	4.0	3.5	0.25	0.35	2.5	1.4
Tournemire /NIA 97/	30.0	10.0	5.0	0.15	0.30	3.0	2.0

Neglecting the anisotropy, the isotropic elastic parameters can be obtained:

$$E = \frac{2E_1 + E_2}{3}; \quad \nu = \frac{2\nu_1 + \nu_2}{3}; \quad G = \frac{E}{2(1+2\nu)}; \quad K = \frac{E}{3(1-2\nu)} \quad (5.46)$$

where  $E$  = Young's modulus,  $\nu$  = Poisson's ratio,  $K$  = bulk modulus, and  $G$  = shear modulus. The calculated data for the COX claystone are summarized in Table 5.12 and illustrated in Fig. 5.26.

**Tab. 5.12** Isotropic elastic parameters of COX claystone at radial stress of 5 MPa

$\Delta\sigma$ (MPa)	$E$ (GPa)	$\nu$	$G$ (GPa)	$K$ (GPa)
0	4.83	0.12	1.95	2.13
2.5	6.23	0.17	2.32	3.16
5	7.27	0.20	2.60	4.04
10	8.30	0.24	2.82	5.24
15	8.60	0.25	2.87	5.71
20	8.80	0.26	2.90	6.00
25	8.80	0.26	2.88	6.12

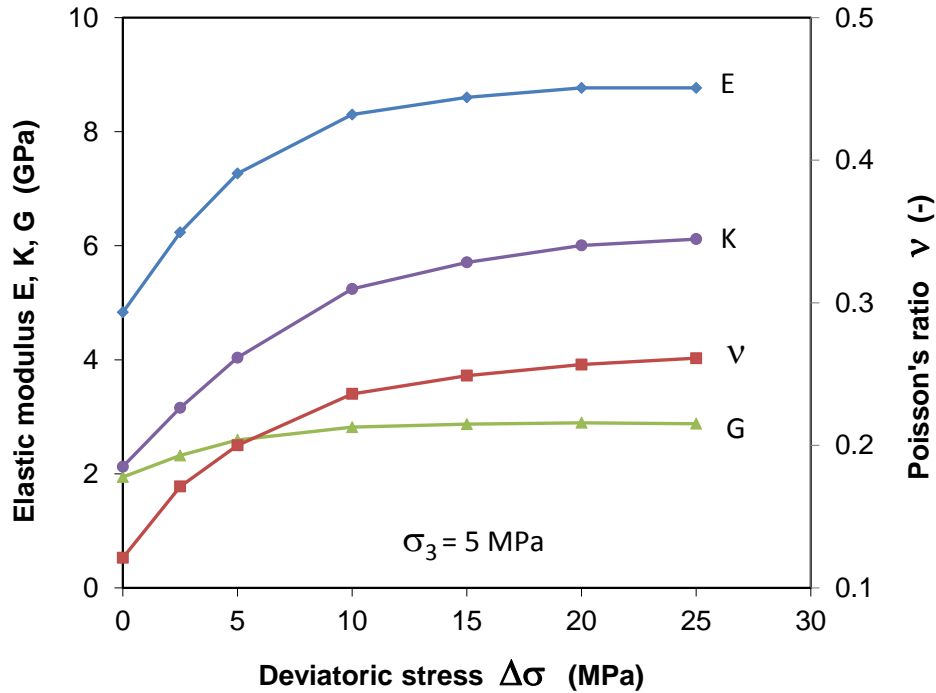


**Fig. 5.26** Isotropic elastic parameters of the COX claystone as a function of deviatoric stress

### Swelling parameters

The swelling and shrinking of the claystone is assumed to be linearly related with suction (Eq. 5.35). The swelling bulk modulus  $K_s$  is estimated on the basis of the test data as shown in Fig. 5.27. The COX and OPA samples were dried at a low humidity of  $RH = 23\%$  (suction  $s = 206$  MPa) and then wetted with vapour at  $RH = 100\%$  ( $s = 0$ ). The volume expansion from the wetting part up to the full saturation ( $s = 206$  MPa  $\rightarrow$  0) was measured to  $d\varepsilon_v \approx 1.5\%$  yielding  $K_s \approx 14$  GPa. The free swelling after water saturation has to be considered for the complete swelling behaviour of the claystone in the future.

### Yield parameters

The yield parameters in (Eq. 5.36) are determined from the triaxial compression tests ( $\theta = -\pi/6$ ) for the COX claystone:  $c = 2.5$  MPa and  $\varphi = 26^\circ$ . Fig. 5.28 compares the yield boundary with the measured data for the COX claystone. Beyond the yield limit, further load leads to initiation and growth of microcracks until the peak failure. The evolution of the stress-strain is modelled through hardening plasticity. The peak strength parameters are determined to  $c = 6$  MPa and  $\varphi = 26^\circ$ .

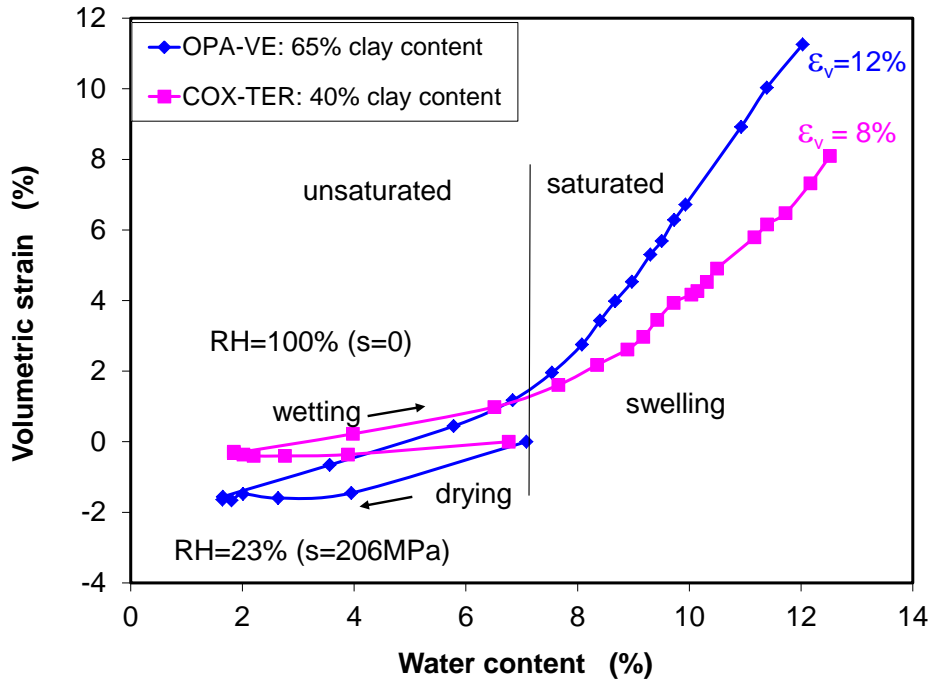


**Fig. 5.27** Swelling and shrinkage of the COX and OPA claystones as a function of water content

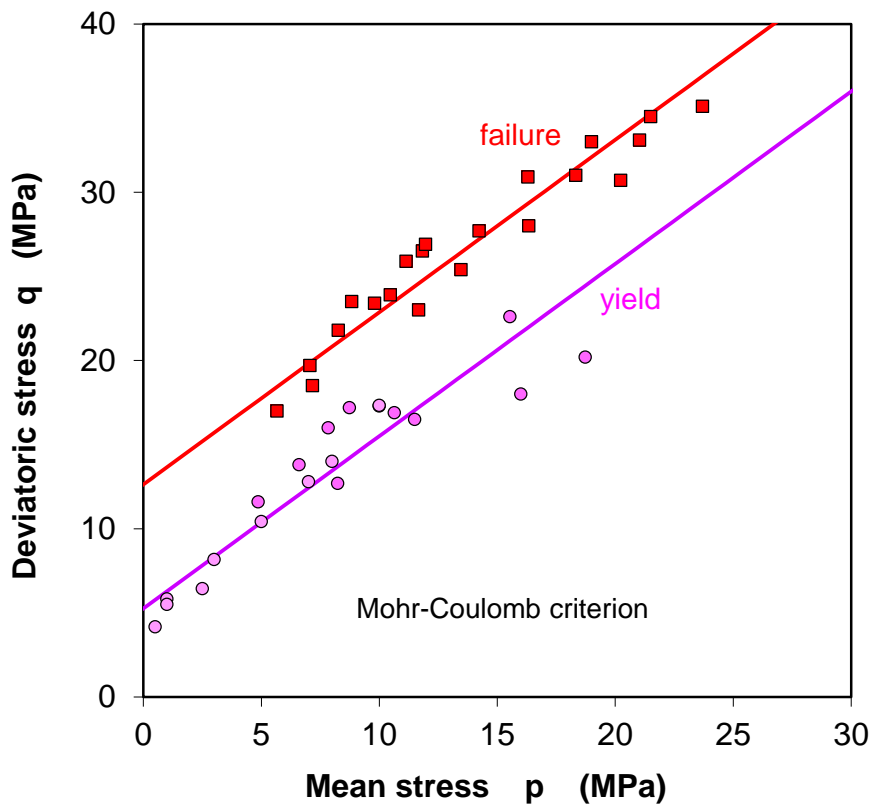


**Fig. 5.28** Yield and peak failure boundaries of the COX claystone

## Creep parameters

The creep parameters in equation (5.42) for the stationary creep of the claystone have been established:  $R= 8.32 \cdot 10^{-3} \text{ kJmol}^{-1}\text{K}^{-1}$ ,  $Q= 45 \text{ kJmol}^{-1}$ ,  $A= 2.5 \cdot 10^{-4} \text{ s}^{-1}$ ,  $\alpha= 0.2 \text{ MPa}^{-1}$ . Fig. 5.29 shows the comparison of this hyperbolic model with the creep rates as a function of deviatoric stress. Taking the creep threshold  $\sigma_s = 2.0 \text{ MPa}$  and  $\varepsilon_{eq}^{vp} = 0$ , fitting the data yields the parameters of the Lemaitre power law (Eq. 5.40):  $\gamma = 4.5 \cdot 10^{-9} \text{ d}^{-1}$ ,  $n = 2.5$  and  $m = 530$ .

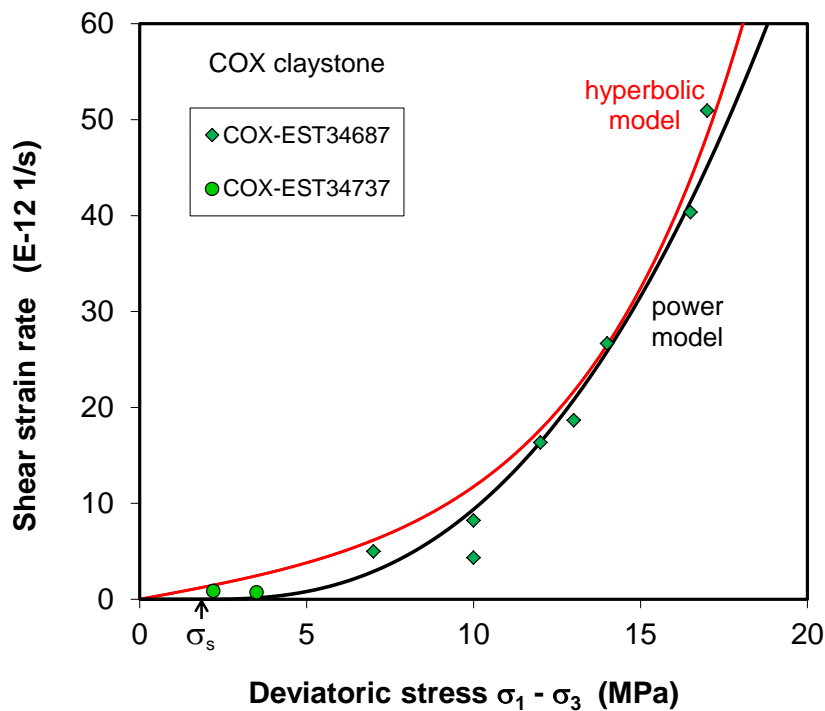


Fig. 5.29 Creep models for the stationary creep of the COX claystones

### 5.3.3 Simulations of short- and long-term deformation

The short- and long-term deformation behaviour of the COX claystone are simulated by HM coupling calculations using the visco-elastoplastic model for the mechanical behaviour and the relevant hydraulic laws for the response of pore pressure. The mechanical parameters are partly determined above based on the test data and partly through back calculations, depending on individual samples because of their different properties. However, the same hydraulic parameters are adopted for all the samples and given in Table 5.13.

**Tab. 5.13** Key hydraulic parameters obtained for modelling the COX claystone

Permeability-porosity relation	$k = k_o \cdot \frac{\phi^3}{(1-\phi)^2} \cdot \frac{(1-\phi_o)^2}{\phi_o^3}$ ; $\phi_o = 0.17, k_o = 1 \cdot 10^{-20} \text{ m}^2$
Relative permeability	$k_{rl} = A \cdot S_l^\lambda$ ; $k_{rg} = 1 - k_{rl}$ ; $A = 1, \lambda = 5$
Water retention curve	$S_l = \left[ 1 + (s/P_o)^{\frac{1}{1-\beta}} \right]^{-\beta}$ ; $P_o = 20 \text{ MPa}, \beta = 0.35$

**5.3.3.1 Short-term deformation**

A series of triaxial compression tests presented in /ZHA 13a/ are simulated by solving the balance equations of solid (Eq. 5.2), water mass (Eq. 5.3) and stress equilibrium (Eq. 5.5). The initial properties of the samples are characterized by a porosity of 17 %, water content of 6.5 % and saturation degree of 90 %. The corresponding suction is determined to  $s_o = 10 \text{ MPa}$ . The cylindrical samples of 70 mm diameter and 140 mm length were loaded at an axial strain rate of  $10^{-6} \text{ s}^{-1}$  under different lateral stresses of 0 to 12 MPa to the peak stress and beyond that to the residual strength. The drained conditions are applied by keeping atmospheric pressure at both end faces,  $P_l = P_g = 0.1 \text{ MPa}$ . The circumference surface is isolated against fluid,  $Q_l = 0$ . The cylindrical samples are represented by a 3D cubic body (Fig. 5.30).

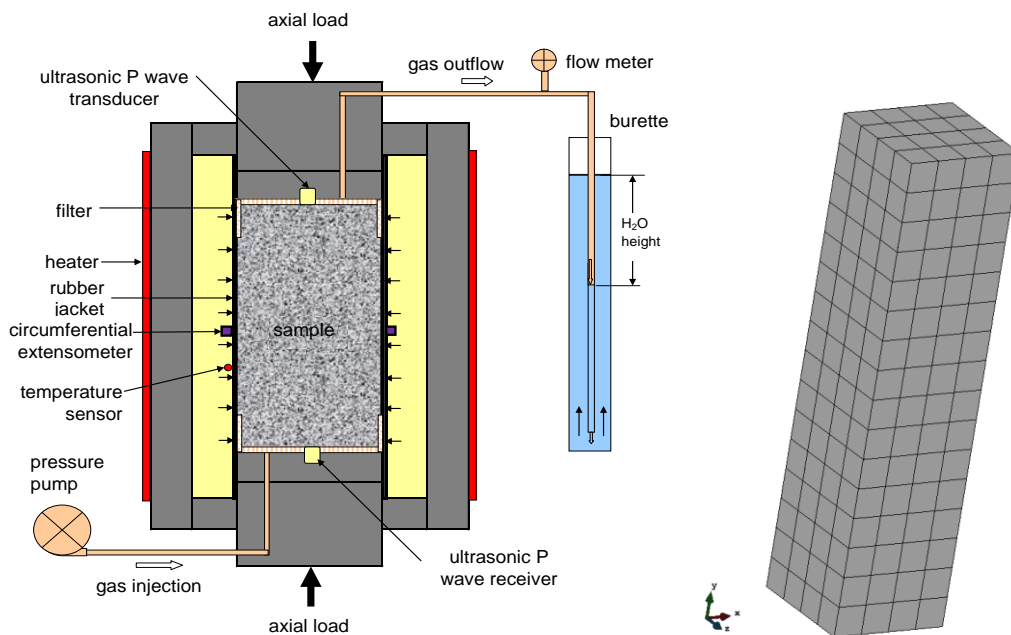


**Fig. 5.30** 3D model geometry for modelling the triaxial tests on COX claystone

In the calculations, the Biot effective stress concept is applied:  $p^b = p^t - Bp^l$ , where  $p^t$  is the total mean stress,  $p^l$  is the porewater pressure and  $p^b$  is the effective stress. The mechanical parameters used are summarized in Table 5.14.

**Tab. 5.14** Mechanical parameters adopted for modelling the short-term deformation behaviour of the COX claystone

Biot stress parameter	$p^b = p - Bp^l: B = 0.6$
Elastic modulus (Eq. 5.34)	$E = 6.3 \text{ GPa}, \nu = 0.2, K_s = 1E7 \text{ MPa}$
Yield parameters (Eq. 5.36/37)	$c = 6 \text{ MPa}, \varphi = 26^\circ, \varpi = 0.1, \theta = 25^\circ$
Hardening-softening parameters (Table 5.11)	$\beta^{ini} = \varphi_{ini} / \varphi_{peak} = 0.42, \alpha_{hard} = 0.0035$ $\beta^{res} = \varphi_{ires} / \varphi_{peak} = 0.8, \alpha_{soft} = 0.07$ $\xi_1 = 0.001\sigma_3 + 0.001, \xi_2 = 0.001\sigma_3 + 0.002$ $\xi_3 = 0.001\sigma_3 + 0.012$
Creep parameters (Eq. 5.40)	$\sigma_s = 2 \text{ MPa}, \varepsilon_{eq}^{vp} = 0, \gamma = 4.5 \cdot 10^{-9} \text{ d}^{-1}, n = 2.5, m = 530$

Modelling results are illustrated in Fig. 5.31 together with the test data. It is obvious that the elastoplastic response with hardening and softening effects can be reasonably represented by the model. The model shows the volumetric compression until the peak stress and then the following dilatancy progressing during the softening phase. There are some quantitative discrepancies between the calculated and measured volumetric strains. It is also to be pointed out that the equivalent plastic strain parameters  $\xi_1, \xi_2, \xi_3$  are not constant but vary with the confining stress  $\sigma_3$ . This is due to the increased ductility of the claystone at high confining stresses. In the calculations, the plastic strain parameters are preliminarily assumed to be linearly related with the confining stress as shown in Fig. 5.32 and Table 5.14. Obviously, this assumption provides the sound modelling results. These equations shall be implemented in the code.

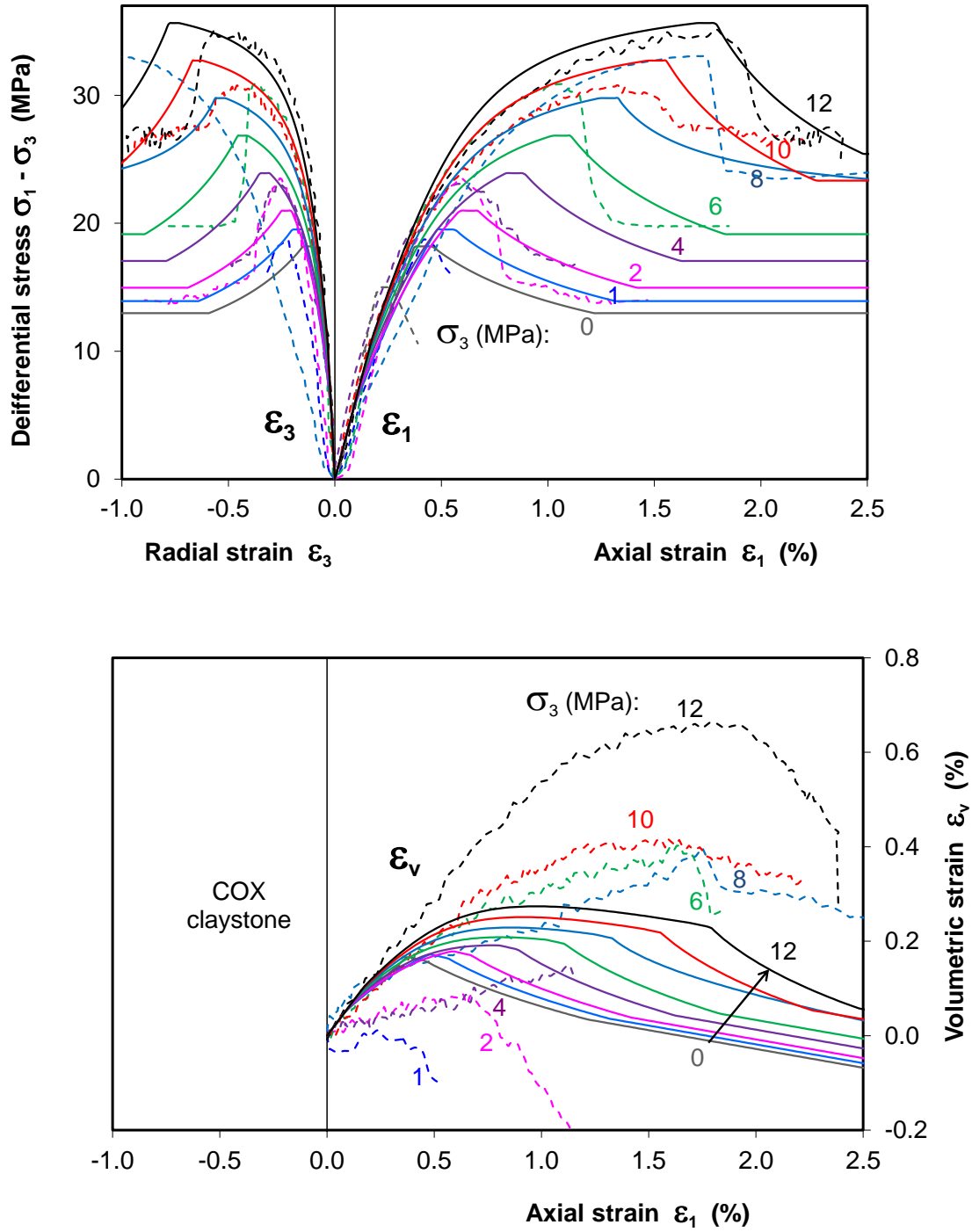


**Fig. 5.31** Modelling results of the short-term deformation behaviour of the COX claystone during triaxial loading

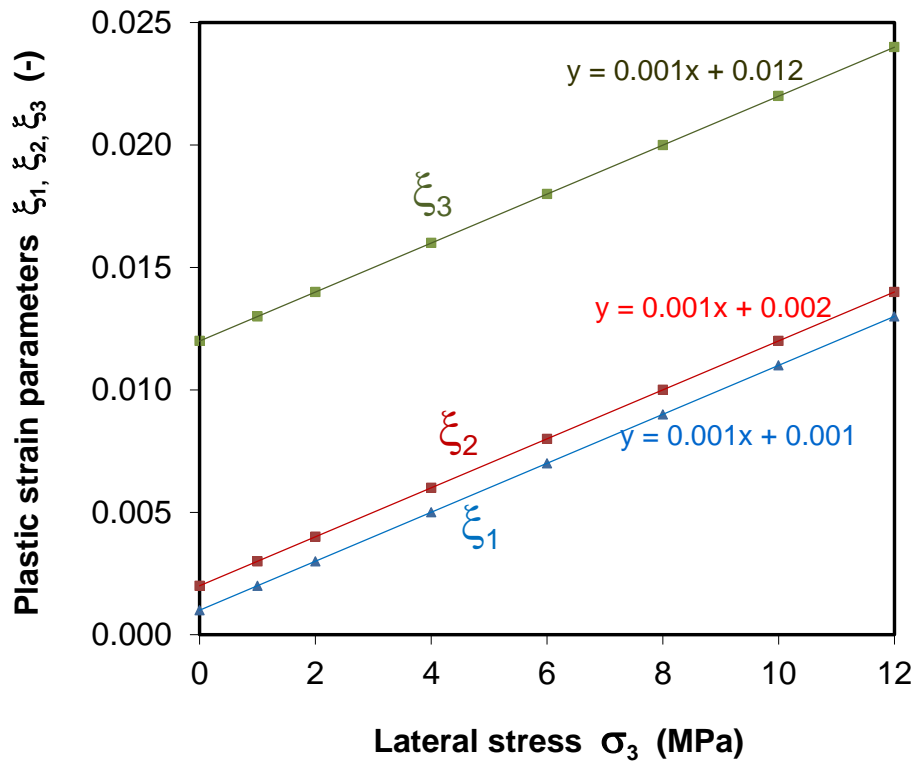


Fig. 5.32 Plastic strain parameters as function of the minor confining stress

### 5.3.3.2 Long-term deformation

The long-term deformation behaviour of the claystone was investigated in triaxial creep tests. One of them was performed on a COX sample EST34678 with a porosity of 15 % and water saturation degree of 97 %. The corresponding suction is determined to  $s_o = 5$  MPa. The cylindrical sample of 100 mm diameter and 190 mm length is represented by a 3D cubic body (Fig. 5.30). The drained conditions are applied by keeping atmospheric pressure at both end faces,  $P_l = P_g = 0.1$  MPa. The circumference surface is isolated against fluid,  $Q_l = 0$ . The creep test was performed in three phases under different triaxial loads.

Fig. 5.33a shows the evolution of applied stresses. During the first phase at axial stress  $\sigma_1 = 15$  MPa, the lateral stress  $\sigma_3$  was stepwise reduced down to 5, 3, 2, 1 and 0.5 MPa. In the second phase, the lateral stress of 0.5 MPa maintained and the axial stress was increased up to 17, 17.5 and 18.5. The third phase was carried out by increasing the lateral stress up to 1, 2 and 3 MPa under constant  $\sigma_1 = 18.5$  MPa. The test is simulated by solving the balance equations of solid (Eq. 5.2), water mass (Eq. 5.3) and stress equi-

librium (Eq. 5.5). The parameter values used in the modelling of the short-term deformation above (Table 5.14) are adopted for modelling the long-term deformation. Moreover, sensibility of some parameters is examined in the simulation of the creep test, such as the Young's modulus  $E$  and plastic strain parameters  $\xi_1, \xi_2, \xi_3$ . All the parameters are listed in Table 5.15.

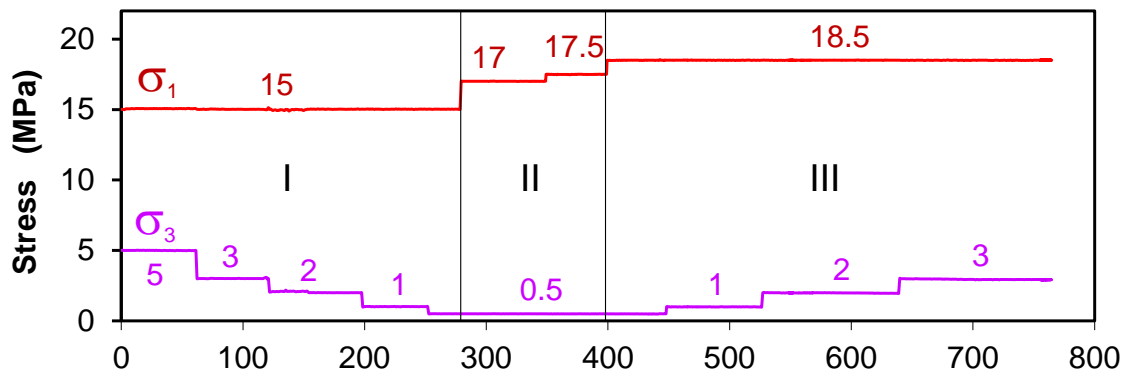
**Tab. 5.15** Mechanical parameters for modelling the short-term deformation behaviour of the COX claystone

Biot stress parameter	$p^b = p - Bp^l$ ; $B = 0.6$
Creep parameters	$\sigma_s = 2.0$ MPa, $\varepsilon_{eq}^{vp} = 0$ , $\gamma = 4.5 \cdot 10^{-9} \text{ d}^{-1}$ , $n = 2.5$ , $m = 530$
Elastic parameters	$\nu = 0.25$ , $K_s = 1\text{E}7$ MPa
Hardening-softening parameters	$\beta^{ini} = \varphi_{ini} / \varphi_{peak} = 0.42$ , $\alpha_{hard} = 0.0035$ $\beta^{res} = \varphi_{ires} / \varphi_{peak} = 0.8$ , $\alpha_{soft} = 0.07$
Model	Varying parameters
A	$E = 6.3$ GPa, $\xi_1 = 0.0015$ , $\xi_2 = 0.003$ , $\xi_3 = 0.012$
B	$E = 8.8$ GPa, $\xi_1 = 0.003$ , $\xi_2 = 0.004$ , $\xi_3 = 0.014$
C	$E = 88$ GPa, $\xi_1 = 0.0015$ , $\xi_2 = 0.003$ , $\xi_3 = 0.012$

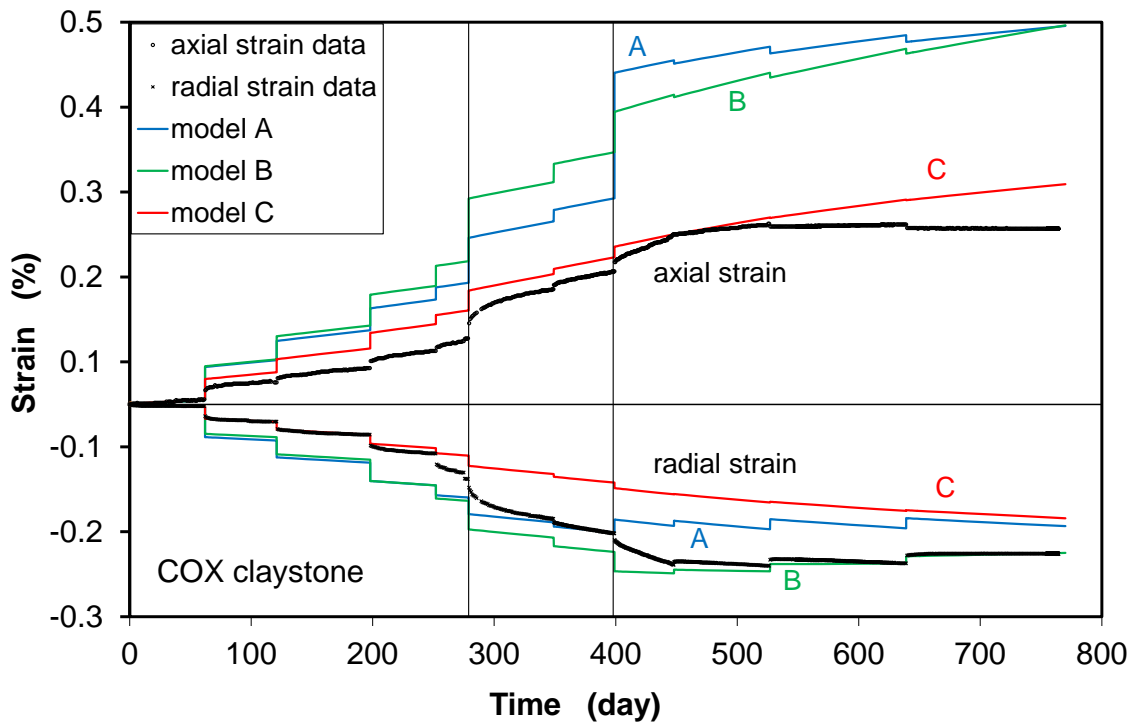
Fig. 5.33b compares the calculated strains with the measured data. Model A uses the same parameters as in the simulation of the short-term tests, resulting in relatively large deformation. Model B takes relatively large  $E$ -value of 8.8 GPa and plastic strains, providing slightly larger strains for the first and second phases compared to that of Model A. Taking a very large  $E$ -value of 88 GPa and smaller plastic strain parameters, Model

C produces the strain curves more close to the measured ones. This indicates the extremely high stiffness of this sample. For the most samples, the parameters of Model B seem to be more adequate.

The calculated creep strains for each step are almost in steady state because the applied very large  $m$ -value of 530 limits the strain hardening effect. The slope of the creep curve or creep rate is more comparable with the last part of each creep step. However, the creep rates during the third phase under increased lateral stresses are overestimated by the models. The dependency of the creep on the loading path has to be examined further.



a) Axial and radial stresses applied



b) Comparison between calculated and measure strains

**Fig. 5.33** Modelling results of the long-term deformation behaviour observed during a triaxial creep test on COX claystone (a-b)

Another triaxial creep test performed on the COX claystone under very low deviatoric stresses is also simulated. Fig. 5.34 shows the modelling results in comparison with the measured data. For fitting the data, the creep parameters are redetermined:  $\sigma_s = 1.0$  MPa,  $\gamma = 2.0 \cdot 10^{-7} \text{ d}^{-1}$ ,  $n = 2.5$ ,  $m = 530$ . The other parameters used are:  $E = 3.2$  GPa,  $\nu = 0.25$ ,  $\xi_1 = 0.003$ ,  $\xi_2 = 0.004$ ,  $\xi_3 = 0.012$ . The model curves are close to the measured ones. But the short transient creep stage cannot be well matched by the model. This may be not significant for prediction of the long-term deformation of the clay rock during the repository post-closure phase over hundreds of thousands of years.

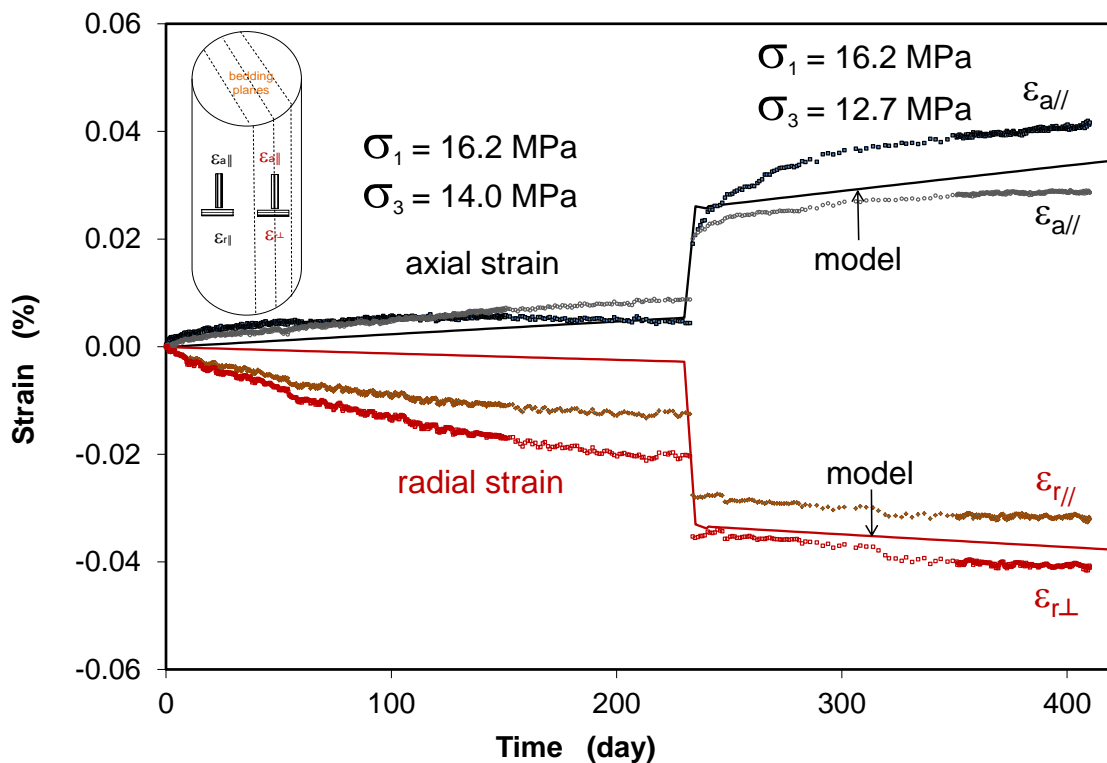


**Fig. 5.34** Modelling results of the long-term deformation behaviour of the COX claystone under low deviatoric stresses

## **5.4 Predictive modelling of the long-term performance of a drift seal**

The long-term performance of a drift seal system depends on the hydro-mechanical properties and responses of the seal components and the surrounding rock, particularly the damaged zone near the drift wall. In the framework of this project, a drift seal is predictively modelled in order to provide an insight into the hydro-mechanical processes during the long-term repository closure phase. The investigated seal materials, namely the compacted bentonite, bentonite-sand and claystone-bentonite mixtures, are taken for the swelling core in the drift seal system (s. Fig. 2.3), so that their sealing performance can be compared under the repository relevant conditions.

### **5.4.1 Numerical model of a drift seal**

The preliminary model prediction focuses on the central swelling core of the France reference drift seal without considering the concrete plugs and drift lining (cf. Fig. 2.3). Fig. 5.35 shows the geometry of the model for the seal. In the model simulation, the prevailing conditions in the MHM-URL are taken into account /AND 15/. It is assumed that a horizontal access drift (or an ILW disposal vault) is excavated at a depth of 500 m parallel to the major horizontal stress direction. It has a diameter of 9.0 m and a length of 40 m. It is supported by a concrete lining of 0.5 meter, which will be removed as the seal will be installed. An axisymmetric model is chosen involving a large rock mass of 60 m radius and 40 m length. According to the in situ observations /ARM 14/, the rock properties in the EDZ are differing from a location to another. Therefore, the total EDZ is divided into three bands with a thickness of 1 m each (EDZ1/2/3). The anisotropic stress state is considered by applying the major horizontal stress of 17 MPa in direction parallel to the drift and the minor horizontal and vertical stress of 13 MPa in direction perpendicular to the drift. The initial porewater pressure of 4.5 MPa is applied to the boundary of the surrounding rock.

The sequence of the drift excavation, operation, and sealing is simulated. The excavation of the drift is simulated by removing the rock mass in one step within 6 months until installation of the concrete lining. The drift is ventilated during the operation phase with relative humidity of about 50 %. The air humidity is imposed to the drift wall by applying a suction of 95 MPa. The operation phase is assumed to take a time period of 100 years. Before installation of the seal, the concrete lining is removed in order to avoid possible pathways through it due to the alteration over time. The lining withdrawal needs 1 month. Following that, the seal is constructed for permanent sealing of the drift. The sealing



The clay rock and seal are assumed homogeneous and isotropic. A constant temperature of 20 °C is assumed, so that the performance of the drift seal is modelled by coupled hydro-mechanical calculations with solving the balance equations of solid (Eq. 5.2), water mass (Eq. 5.3), stress equilibrium (Eq. 5.5), and the constitutive equations for the rock, EDZ and seals. For the preliminary prediction, the issue of gas generation and migration is not taken into account.

#### **5.4.2 Material parameters**

The drift seal is composed by four materials: the intact host rock, the EDZ, the concrete lining for supporting the drift during the operation phase, and the seal core for the entire life of the repository. These materials are described by the physical properties and the constitutive models for the HM behaviour.

##### ***Host rock and EDZ***

The constitutive models and parameters applied to the clay rock and EDZs are summarized in Table 5.16. The hydro-mechanical behaviour of the intact rock and EDZs are described with the same constitutive models but with different permeability values:  $k_o = 5 \cdot 10^{-18} \text{ m}^2$  for EDZ1,  $1 \cdot 10^{-18} \text{ m}^2$  for EDZ2,  $1 \cdot 10^{-19} \text{ m}^2$  for EDZ3, and  $1 \cdot 10^{-20} \text{ m}^2$  for the rock in the far field. These values represent the average in situ hydraulic conductivities around a drift parallel to the horizontal major stress direction /AGM 14/, as shown in Fig. 5.36 ( $1 \text{ m/s} \approx 1 \cdot 10^{-7} \text{ m}^2$ ). Most of the other parameters determined in section 5.3 are adopted. A few parameters are revalued for fitting the in situ observations of rock deformation. The mechanical behaviour of the intact rock and EDZs are uniquely described by the visco-elastoplastic model with the Mohr-Coulomb yield criterion, hardening-softening and creep equations (section 5.3.2). But the EDZ development, namely damage and permeability change, recompaction and sealing, cannot be yet simulated. It is foreseen to implement some newly formulated constitutive models (Eqs. 5.30 - 5.34) into the code for enhancing the capacities of the models.

##### ***Concrete lining***

The concrete lining is modelled by linear elasticity as a first approximation (Table 5.17). The concrete has an initial porosity of 20 % and is partly water-saturated with a degree of 30 %, corresponding to a suction of 55 MPa.

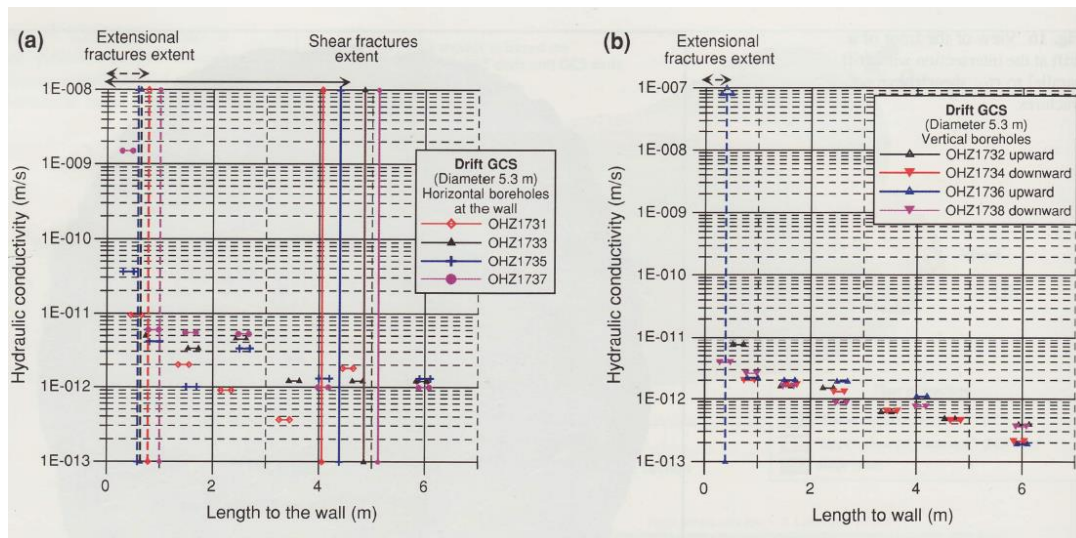


**Fig. 5.36** Hydraulic conductivity measured around a drift parallel to the horizontal major stress direction in the MHM-URL: (a) horizontal borehole at the wall and (b) vertical boreholes at floor and ceiling / ARM 14/

### Seal materials

The compacted bentonite, bentonite-sand mixture (70/30) and claystone-bentonite mixture (60/40) are modelled for the seal core, respectively. They are characterized with the same constitutive models and own parameter values. The mechanical behaviour is described by a nonlinear elasticity model simplified from the elastoplastic BBM model (section 5.2.3.2). The deformation of the seal materials is nonlinearly related to mechanical load and hydraulic suction. Most of the parameters are taken from the results obtained in section 5.2. However, some of them are revalued under consideration of the realistic conditions of the seals after construction. For instance, the initial stiffness and swelling pressure of the realistic seals may become relatively low due to the imperfectly filled gaps between seal and rock. This is adjusted by input of low initial stiffness moduli for all the materials:  $K_i = 5 \text{ MPa}$ ,  $E_i = 4.5 \text{ MPa}$ ,  $G_i = 1.7 \text{ MPa}$  and  $\nu = 0.3$ . Similarly, relative higher permeabilities than the measured values are taken:  $k_o = 1 \cdot 10^{-19} \text{ m}^2$  to  $5 \cdot 10^{-19} \text{ m}^2$  for the bentonite seal,  $k_o = 5 \cdot 10^{-19} \text{ m}^2$  for the bentonite-sand seal, and  $k_o = 5 \cdot 10^{-19} \text{ m}^2$  to  $1 \cdot 10^{-18} \text{ m}^2$  for the claystone-bentonite seal. These values are about one order of magnitude higher than those obtained on the individual compacted blocks. The models and the associated parameter values are summarized in Table 5.18.

**Tab. 5.16** Constitutive models and parameters for the clay rock and EDZ

Parameters	EDZ1	EDZ2	EDZ3	Rock
Porosity $\phi$ (-)	0.17	0.17	0.17	0.17
Permeability-porosity relation $k = k_o \cdot \frac{\phi^3}{(1-\phi)^2} \cdot \frac{(1-\phi_o)^2}{\phi_o^3}$	$k_o=5 \cdot 10^{-18} \text{ m}^2$	$k_o=1 \cdot 10^{-18} \text{ m}^2$	$k_o=1 \cdot 10^{-19} \text{ m}^2$	$k_o=1 \cdot 10^{-20} \text{ m}^2$
Water retention curve	$S_l = \left[ 1 + (s/P_o)^{\frac{1}{1-\beta}} \right]^{-\beta}$ ; $P_o = 15 \text{ MPa}$ , $\beta = 0.35$			
Relative permeability	$k_{rl} = A \cdot S_l^\lambda$ ; $k_{rg} = 1 - k_{rl}$ ; $A = 1$ , $\lambda = 3$			
Biot stress parameter	$p^b = p - Bp^l$ ; $B = 0.6$			
Elastic parameters	$d\sigma_{ij} = D_{ijkl}^e \left( d\varepsilon_{kl} - \delta_{kl} \frac{ds}{K_s} - d\varepsilon_{kl}^{vp} \right)$ ; $E = 6 \text{ GPa}$ , $\nu = 0.25$ , $K_s = 14 \text{ GPa}$			
Creep parameters	$\dot{\varepsilon}^{vp} = \gamma (q - \sigma_s)^n (1 - \varepsilon_{eq}^{vp})^m$ $\gamma = 1 \cdot 10^{-8} \text{ d}^{-1}$ , $\sigma_s = 2 \text{ MPa}$ , $\varepsilon_{eq}^{vp} = 0$ , $n = 2.5$ , $m = 530$			
Mohr-Coulomb yield function and plastic potential	$F = \left( \cos \theta + \frac{1}{\sqrt{3}} \sin \theta \cdot \sin \varphi \right) J - \sin \varphi \cdot (c \cot \varphi + p) \geq 0$ $G = \left( \cos \theta + \frac{1}{\sqrt{3}} \sin \theta \cdot \sin \varphi \right) J - \omega \cdot \sin \varphi \cdot (p + p_t)$ $c = 6 \text{ MPa}$ , $\varphi = 26^\circ$ , $\omega = 1$ , $\theta = 25^\circ$			
Hardening-softening	$\beta^{ini} = \varphi_{ini} / \varphi_{peak} = 0.42$ , $\alpha_{hard} = 0.0035$ $\beta^{res} = \varphi_{ires} / \varphi_{peak} = 0.8$ , $\alpha_{soft} = 0.07$ $\xi_1 = 0.008$ , $\xi_2 = 0.01$ , $\xi_3 = 0.02$			

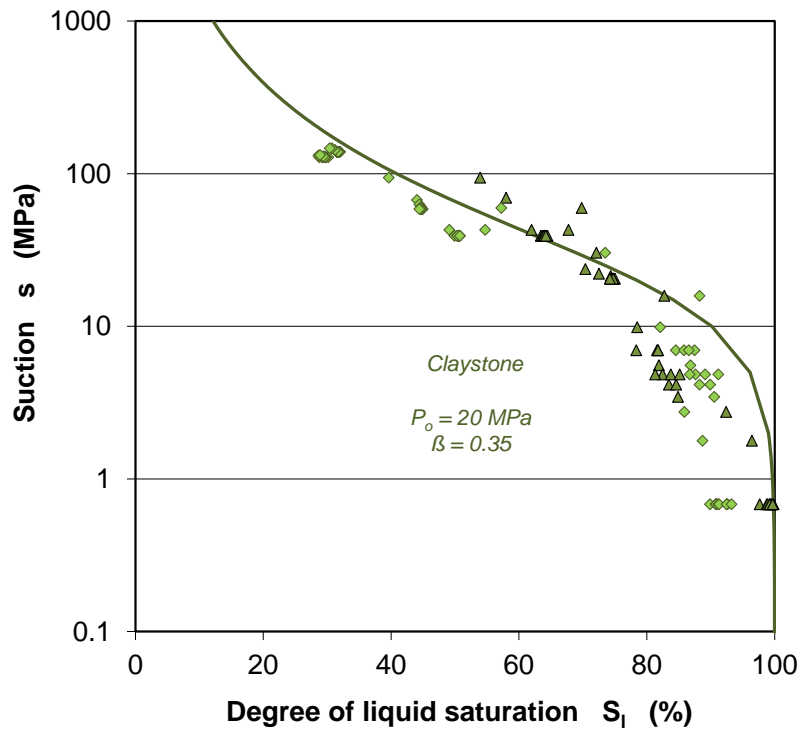
**Tab. 5.17** Constitutive models and parameters for the concrete lining

Initial properties	Lining
Permeability-porosity relation	$k = k_o \cdot \frac{\phi^3}{(1-\phi)^2} \cdot \frac{(1-\phi_o)^2}{\phi_o^3}$ ; $\phi_o = 0.2$ , $k_o=1 \times 10^{-19} \text{ m}^2$
Water retention curve	$S_l = \left[ 1 + (s/P_o)^{\frac{1}{1-\beta}} \right]^{-\beta}$ ; $P_o = 2 \text{ MPa}$ , $\beta = 0.35$
Relative permeability	$k_{rl} = A \cdot S_l^\lambda$ ; $k_{rg} = 1 - k_{rl}$ ; $A = 1$ , $\lambda = 3$
Linear elastic parameters	$E = 40 \text{ GPa}$ , $\nu = 0.3$

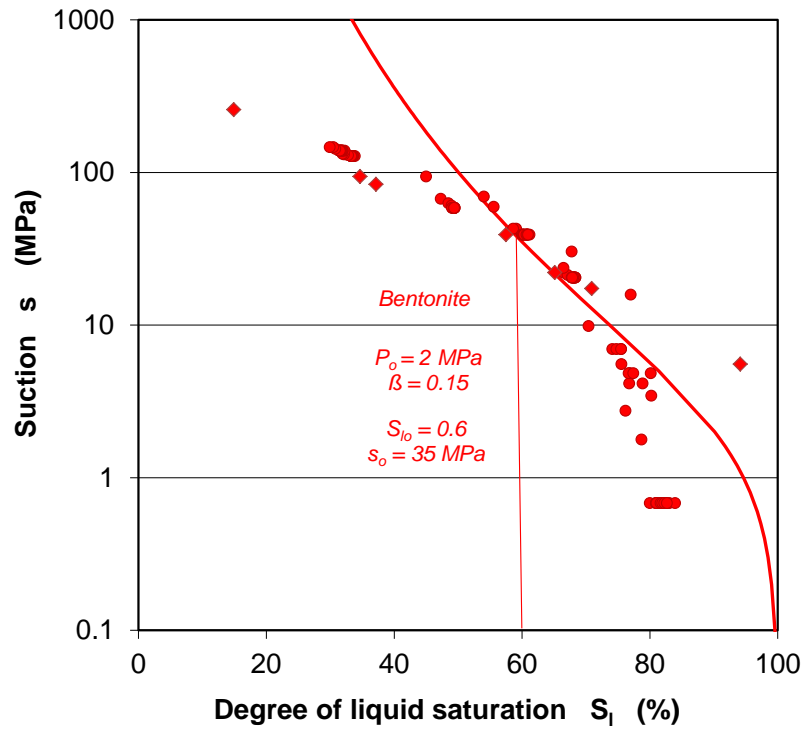
**Tab. 5.18** Constitutive models and parameters for the seal materials: bentonite, bentonite-sand mixture (70/30) and claystone-bentonite mixture (60/40)

Parameters	Bentonite MX80	Bentonite-sand (70/30)	Claystone-bentonite (60/40)
Dry density $\rho_d$ (g/cm <sup>3</sup> )	1.57	1.80	1.90
Porosity $\phi$ (-)	0.44	0.35	0.30
Void ratio $e$ (-)	0.74	0.54	0.44
Water saturation degree $S_l$ (%)	60.0	51.0	53.0
Suction $s_o$ (MPa)	35.0	20.0	32.0
Permeability-porosity relation $k = k_o \cdot \frac{\phi^3}{(1-\phi)^2} \cdot \frac{(1-\phi_o)^2}{\phi_o^3}$	$k_o = 1 \cdot 10^{-19} \text{ m}^2$ $5 \cdot 10^{-19} \text{ m}^2$	$k_o = 5 \cdot 10^{-19} \text{ m}^2$	$k_o = 5 \cdot 10^{-19} \text{ m}^2$ $1 \cdot 10^{-18} \text{ m}^2$
Water retention curve $S_l = \left[ 1 + (s/P_o)^{\frac{1}{1-\beta}} \right]^{-\beta}$	$P_o = 2 \text{ MPa}$ $\beta = 0.15$	$P_o = 3 \text{ MPa}$ $\beta = 0.3$	$P_o = 3 \text{ MPa}$ $\beta = 0.25$
Relative permeability	$k_{rl} = A \cdot S_l^\lambda$ ; $k_{rg} = 1 - k_{rl}$ ; $A = 1$ , $\lambda = 5$		
Volumetric strains $d\varepsilon_v = \Delta e / (1 + e) = a_1 \Delta \ln(p')$ $+ a_2 \Delta \ln(s + 0.1/0.1)$ $+ a_3 \Delta \ln(p' / p_{ref}) \Delta \ln(s + 0.1/0.1)$ $+ a_4 s \Delta \ln(p')$	$a_1 = -0.02$ $a_2 = -0.017$ $a_3 = 0.022$ $a_4 = 2\text{E-}4$	$a_1 = -0.02$ $a_2 = -0.01$ $a_3 = 0.022$ $a_4 = 2\text{E-}4$	$a_1 = -0.02$ $a_2 = -0.007$ $a_3 = 0.022$ $a_4 = 2\text{E-}4$
Deviatoric elastic strains $d\varepsilon_q = G/3 \cdot dq$	$K = p(1+e) / k_i$ ; $G = 3K(1-2\nu) / 2(1+\nu)$ ; $E = 2G(1+\nu)$ $K_i = 5 \text{ MPa}$ , $\nu = 0.3$ , $G_i = 1.7 \text{ MPa}$ , $E_i = 4.5 \text{ MPa}$		

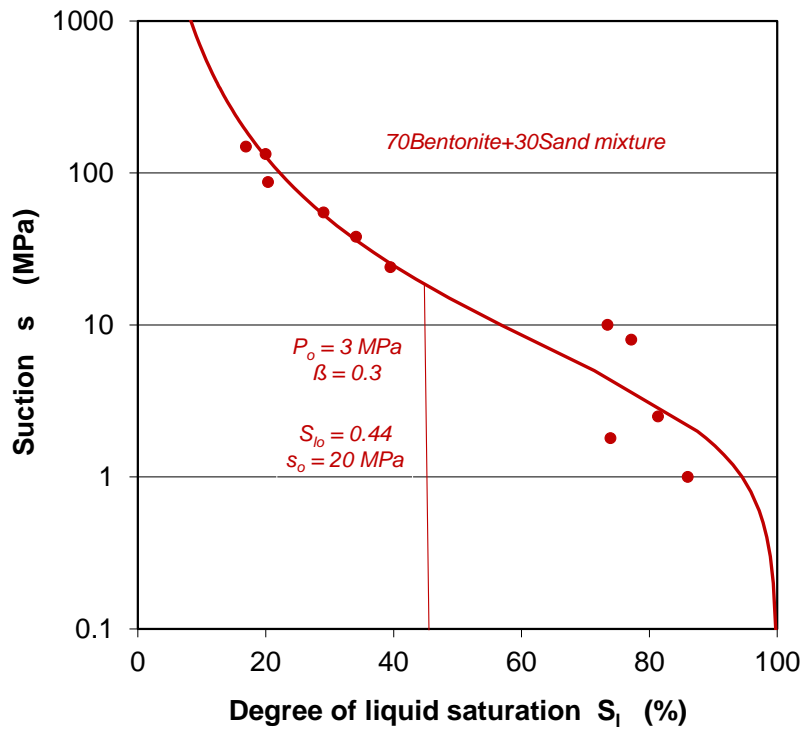
For modelling the hydraulic behaviour of the seal system, the water retention curve, the variation of the intrinsic permeability with porosity, and the variation of the relative hydraulic conductivity for water and gas as a function of water saturation degree are applied. Among them, the water retention behaviour is particularly important, which dominates the water resaturation in the seal system. The water retention curves of the individual seal materials are depicted in Fig. 5.37 with the remarked initial degrees of water saturation and suctions. The water saturation in turn controls the development of swelling pressure in the seal and interactions between the rock and the seal.



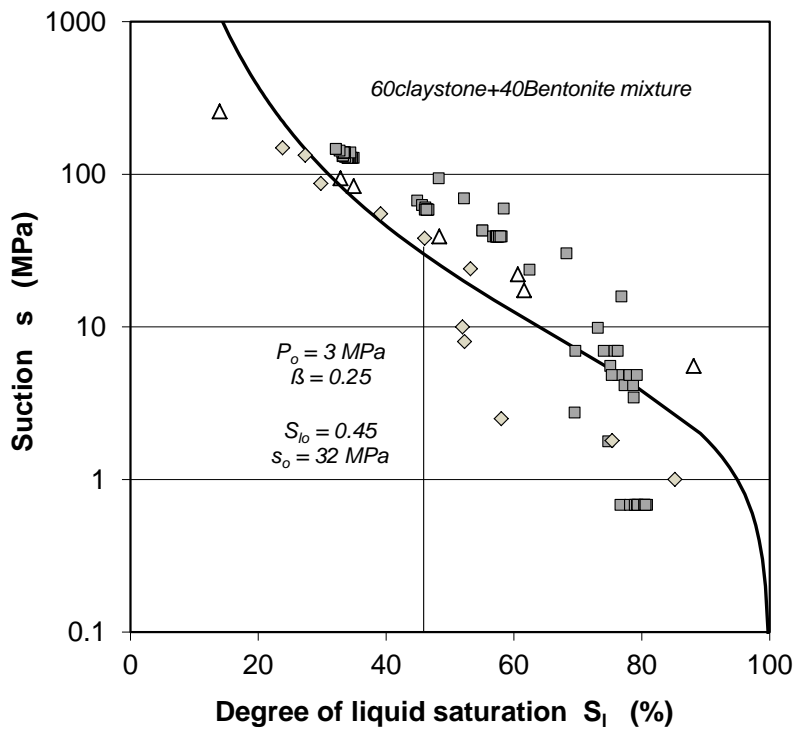
a) Water retention curve for clay rock and EDZ



b) Water retention curve for bentonite



c) Water retention curve for bentonite-sand mixture



d) Water retention curve for claystone-bentonite-mixture

**Fig. 5.37** Water retention curves used for the clay rock and EDZ (a), bentonite (b), bentonite-sand mixture (c), and claystone-bentonite mixture (d)

### **5.4.3 Results and analysis**

#### **5.4.3.1 Effects of drift excavation and support**

##### **5.4.3.1.1 Mechanical response**

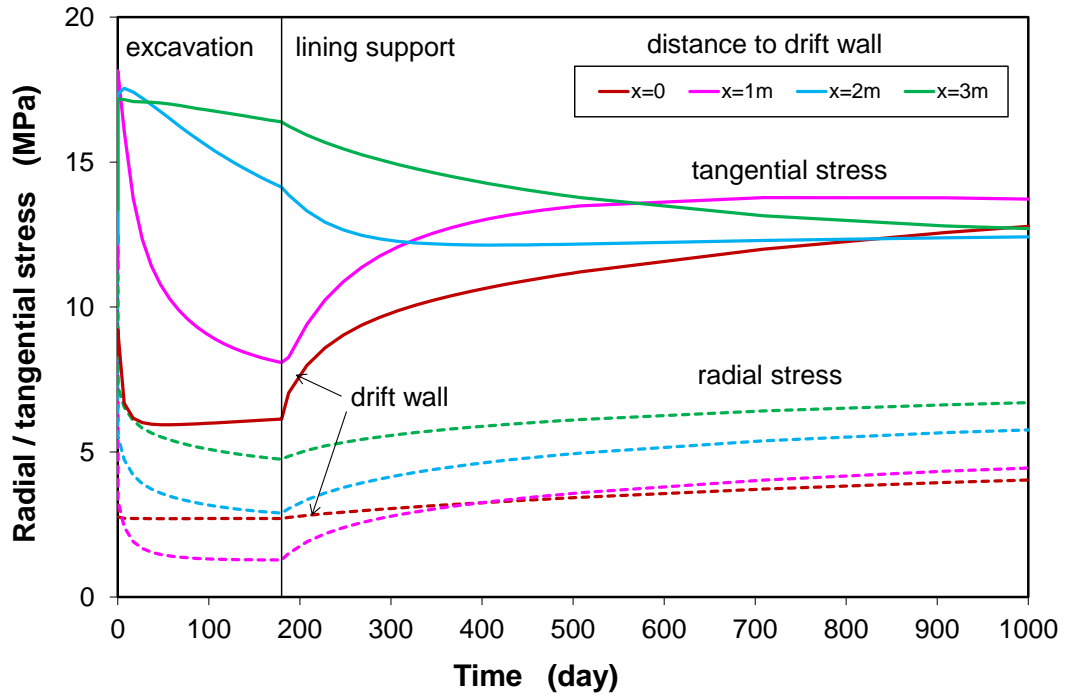
Fig. 5.38 shows the calculated evolution of radial and tangential stresses (a) and convergent displacement (b) in the surrounding rock after drift excavation and support over 1000 days. As the drift is excavated at  $t = 0$ , the radial stress relaxes suddenly and correspondingly the tangential stress arises. The resulting high deviatoric loads in the EDZ ( $x = 0$  to 3 m to the rock wall) cause large sudden convergent deformation and plastic damage. Following that, the stresses decrease gradually with the continuing convergent creep of the rock.

When the concrete lining is installed, the relatively high stiffness of the lining provides resistance against the rock deformation (Fig. 5.38b). The drift convergence is thus decelerated due to the decrease of the deviatoric stress, which is resulted from the difference between the increasing radial stress and decreasing tangential stress. It is to be noted that the predicted drift convergence is fortunately consistent with the average in situ measurements in the MHM-URL (cf. Fig. 5.39 after /ARM 14/).

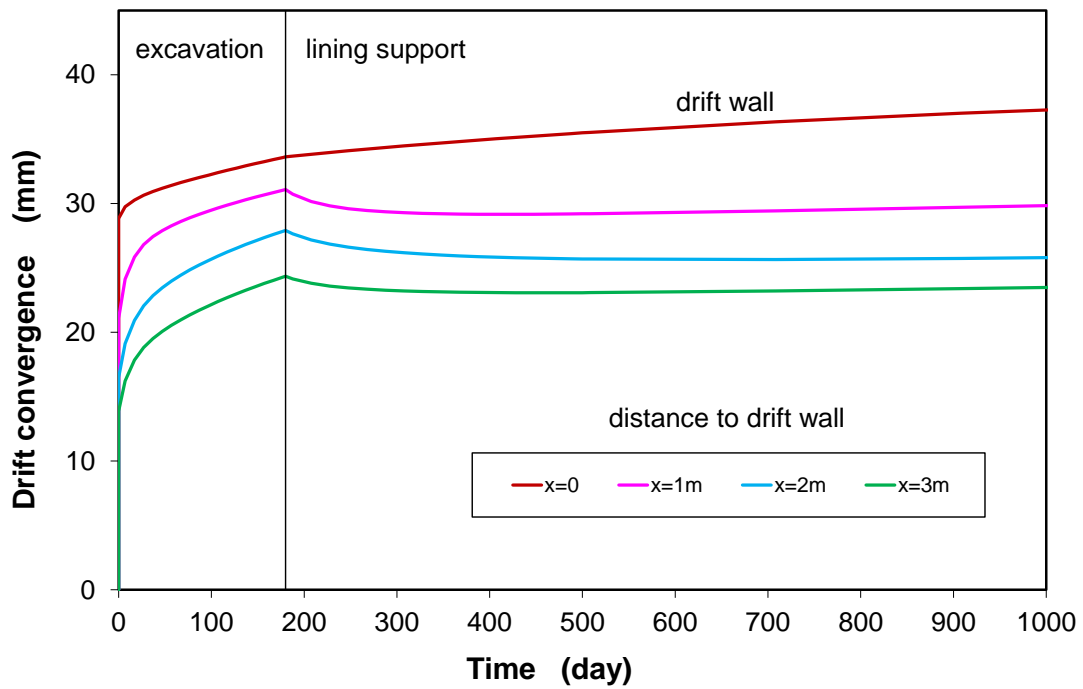
##### **5.4.3.1.2 Hydraulic response**

The hydraulic response of the rock mass to the excavation and ventilation as well as support of the drift is shown in Fig. 5.40 in terms of porewater pressure (a) and water saturation (b). The drift excavation and ventilation with relative humidity of 50 % (suction = 95 MPa) results in negative porewater pressures and desaturation in the rock near the drift wall. Under the effect of suction, the porewater pressure decreases gradually with time, forming a gradient with the lowest value of -95 MPa at the wall and the unchanged initial value of 4.5 MPa in the far-field of the rock. The desaturated area extends from the drift wall to a depth of ~ 3.5 m into the rock mass over the first 6 months.

The installation of the concrete lining with a relatively high degree of water saturation hinders the development of desaturation in the near-field. In the far-field, the decrease of the porewater pressure continues to equilibrium with the lining boundary value of  $P_l = -55$  MPa.



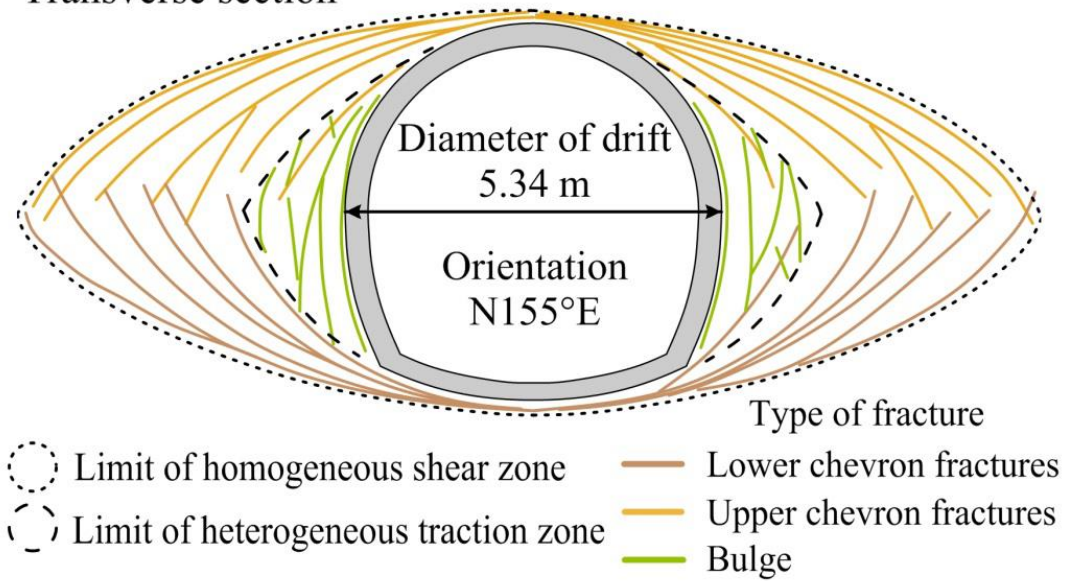
a) Radial and tangential stress



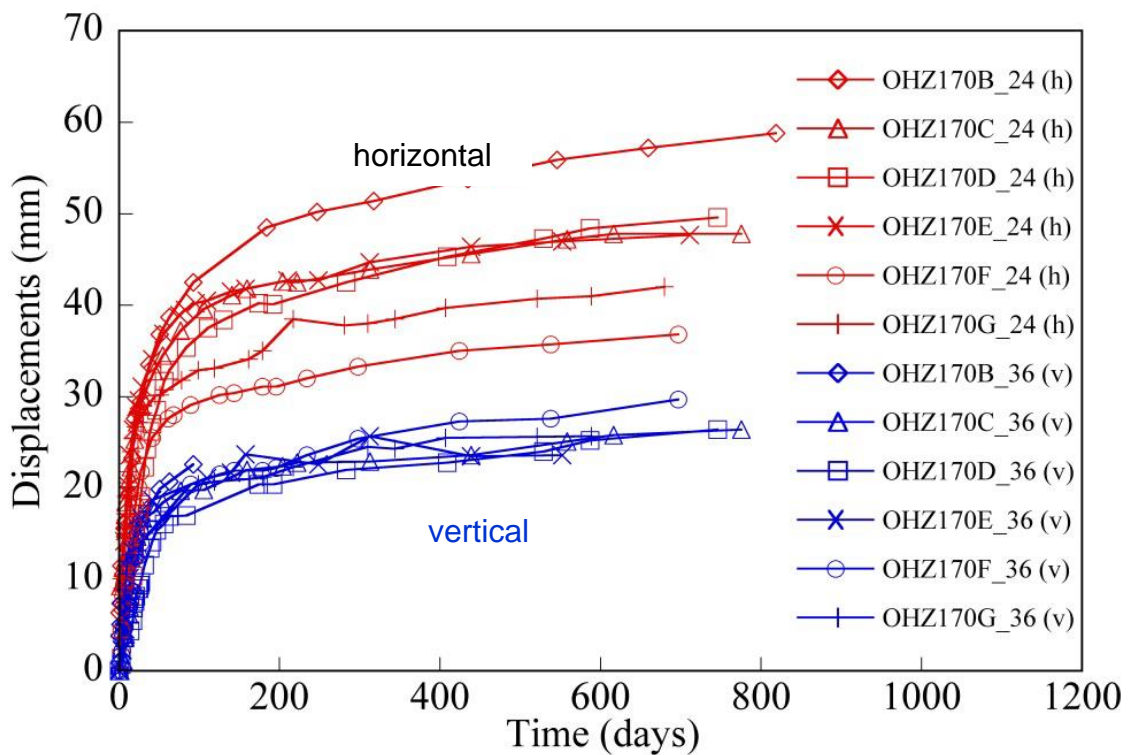
b) Convergent displacement

**Fig. 5.38** Evolution of the radial and tangential stresses (a) and the convergent displacements (b) in the surrounding rock after drift excavation and support

### Transverse section

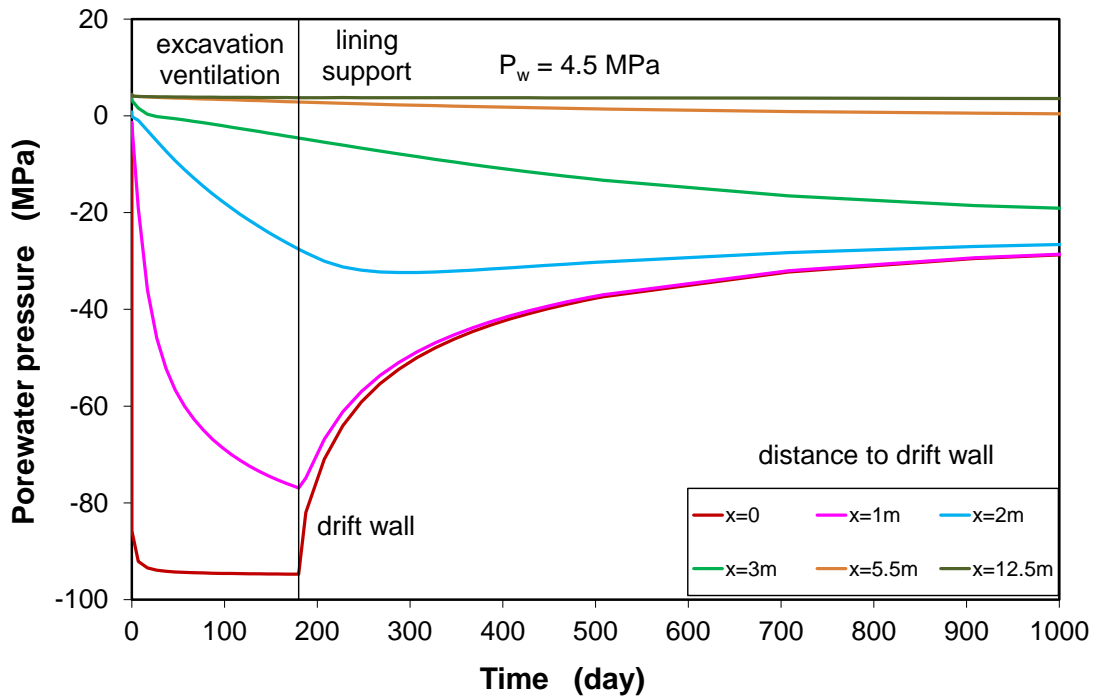


a) Fracture patterns in the EDZ around a drift oriented parallel to the major horizontal stress direction

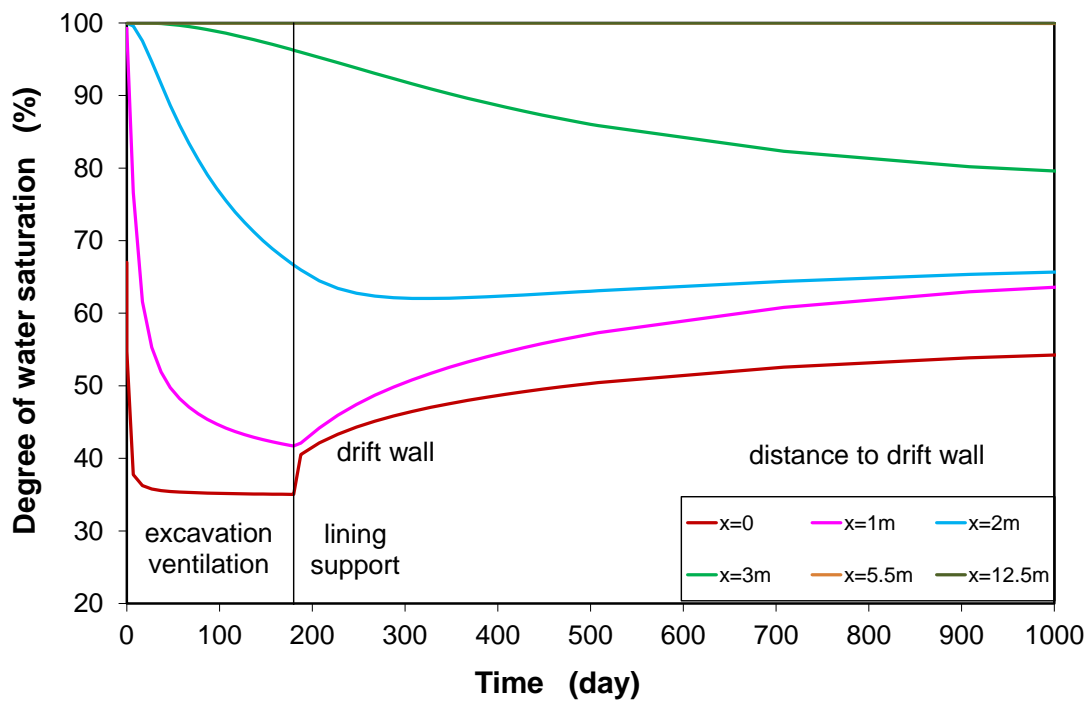


b) Drift convergence measured in the horizontal and vertical directions

**Fig. 5.39** EDZ and convergence of a drift parallel to the horizontal major stress direction observed in the MHM-URL (a-b) /ARM 14/



a) Porewater pressure



b) Water saturation

**Fig. 5.40** Evolution of the porewater pressure (a) and water saturation (b) in the surrounding rock with the drift ventilation after excavation and support

### 5.4.3.2 Hydro-mechanical processes in the drift seal

After the installation of the seal in the drift, hydro-mechanical processes and interactions take place in the seal-rock-system. Because the processes are qualitatively identical for the different seal materials, only the results obtained for the claystone-bentonite mixture are presented for the process analyses. The results obtained from the bentonite and bentonite-sand mixture are compared in terms of the performance indicators later.

#### 5.4.3.2.1 Hydraulic process

The claystone-bentonite seal with permeability of  $1 \cdot 10^{-18} \text{ m}^2$  and water saturation degree of 53 % is installed in the drift. The suction of 32 MPa in the seal and the hydraulic gradient in the EDZ and rock drives porewater migrating from the saturated far-field to the unsaturated EDZ and seal. Fig. 5.41 shows the evolution of porewater pressure in the centre of the seal, EDZ1 / 2 / 3 and in the near-field of the rock ( $r = 12 \text{ m}$ ) for 4000 years. Under the suction effect, the unsaturated seal, EDZ and near-field rock take up water from the saturated far-field, increasing the water saturation (see Fig. 5.42). Simultaneously, the suction is decreasing or the porewater pressure is increasing (Fig. 5.41). Because of the different water saturation degrees and uptake capacities, the evolution of water saturation is differing from the seal to the EDZ and rock. A full water saturation of the seal-rock-system is reached at time  $t = 2700$  years, i.e. the net saturation duration being 2600 years exclusive of the drift operation phase of 100 years. After water saturation, the porewater pressures become positive and increase with time. Over another 1000 years, the original porewater pressure of 4.5 MPa is recovered in the entire seal-rock-system, so that a hydraulic stabilization is reached.

#### 5.4.3.2.2 Mechanical response

The water saturation results in buildup of swelling pressure in the seal, which in turn gives rise to withstand the development of the EDZ. Fig. 5.42 shows the evolution of swelling pressure and porosity in the seal. In correspondence with the increase of the water saturation (cf. Fig. 5.42), the swelling pressure increases gradually with time. As the full saturation is reached at  $t = 2700$  years, the maximum swelling pressure of 2.8 MPa is achieved. Because of the low stiffness applied to the seal, the material is initially more compacted under impacts of the rock creep and the swelling of the wetted seal near the rock.

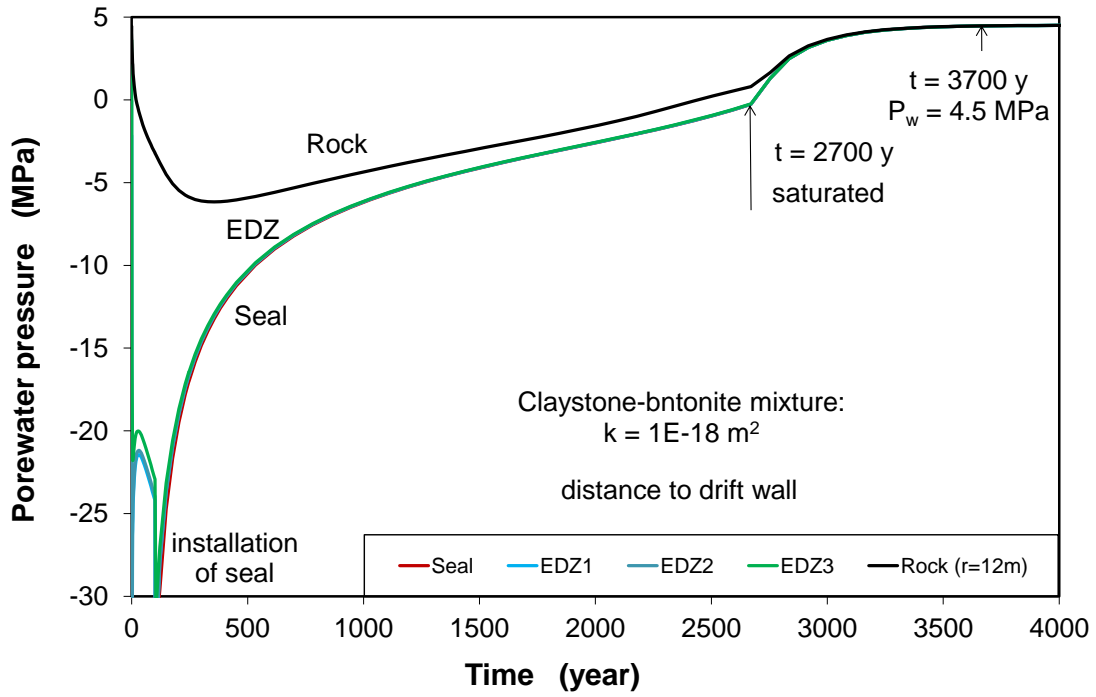


Fig. 5.41 Long-term evolution of porewater pressure in the seal, EDZ and rock

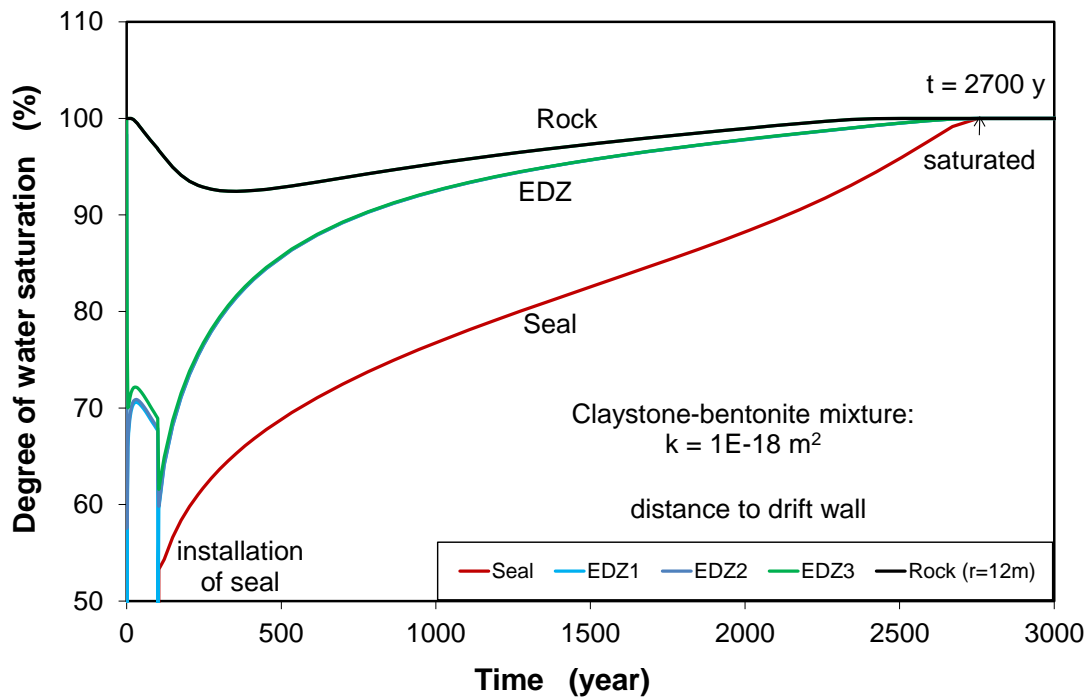
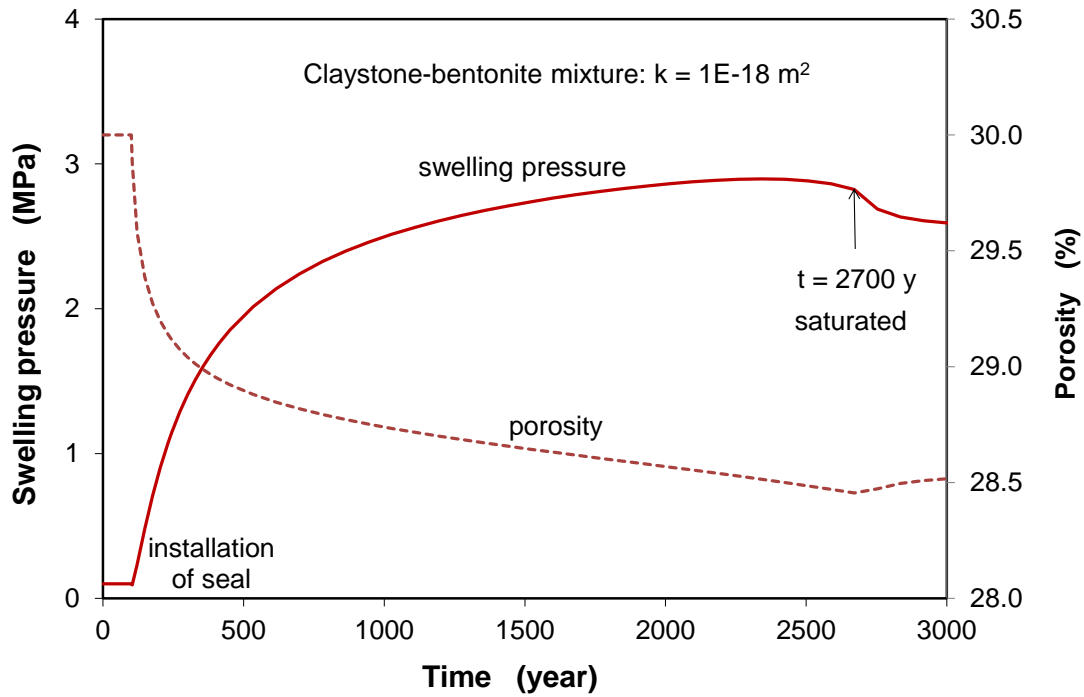


Fig. 5.42 Long-term evolution of water saturation in the seal, EDZ and rock



**Fig. 5.43** Development of swelling pressure and porosity in the seal during water saturation

The increasing swelling pressure provides withstand against the development of the EDZ. This increases the radial stresses in the EDZ and the near-field rock (Fig. 5.44) and slows the convergent deformation (Fig. 5.45). After full saturation, the porewater pressure in the seal increases relatively fast. The resultant total stress increases too. The high stress in the seal hinders the convergent deformation of the EDZ and rock, and even causes some divergence. After reaching the hydraulic stabilization at  $t = 3700$  years, the original mechanical conditions with the given stress state of  $\sigma_h = \sigma_v = 13$  MPa and  $\sigma_H = 17$  MPa are not yet recovered. Reaching mechanical equilibrium needs much longer time.

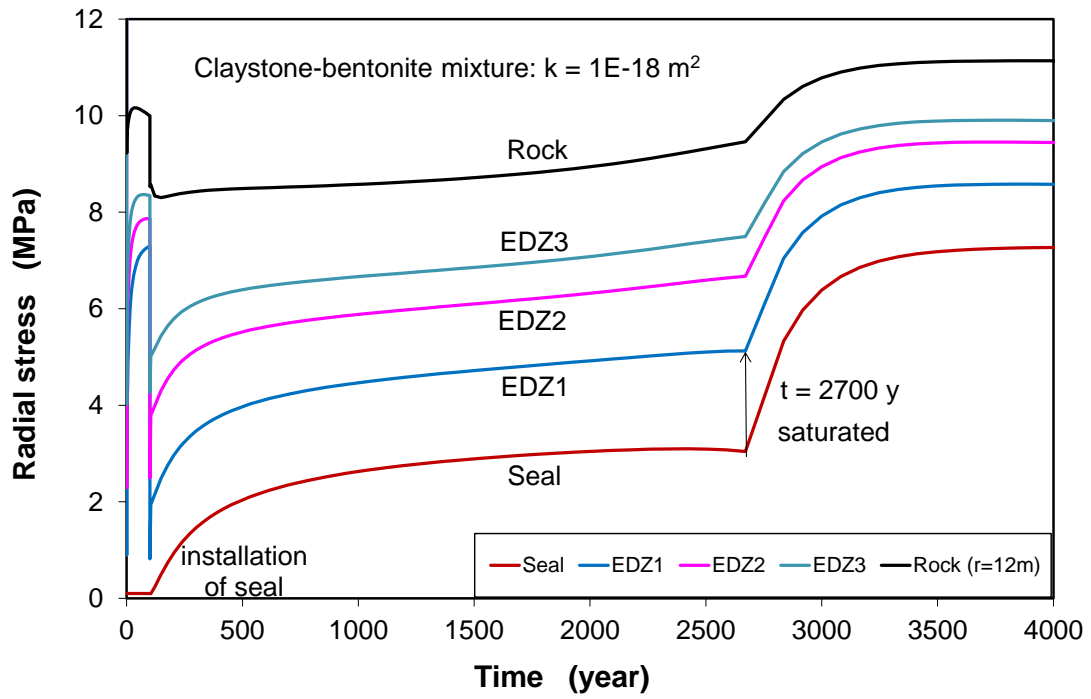


Fig. 5.44 Development of total radial stress in the seal-rock-system

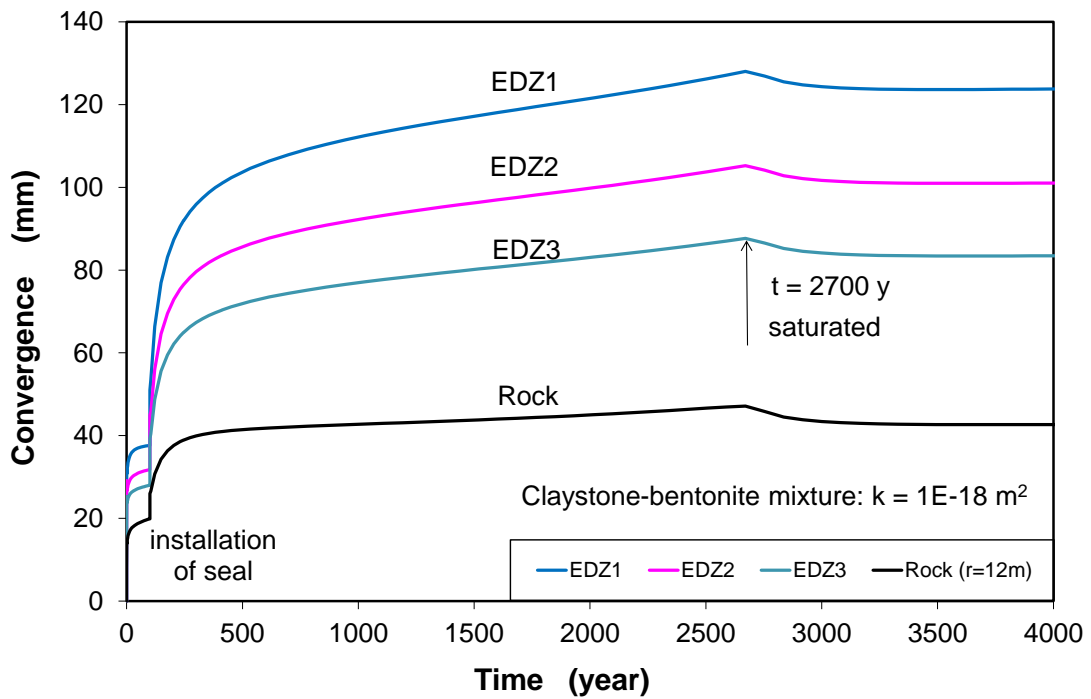


Fig. 5.45 Development of convergent displacement of the EDZ and rock

#### 5.4.3.2.3 Comparison of the sealing performance of the seal materials

The performance and effects of the compacted bentonite, bentonite-sand and claystone-bentonite mixtures for the drift sealing are compared in terms of resaturation duration and swelling pressure in the seal, and back-pressure against the drift convergence. A same permeability value of  $5 \cdot 10^{-19} \text{ m}^2$  is assumed for all the materials, whereas the other properties and parameters remain for the individual materials.

The most important process is the water saturation of the seal, with which the other hydro-mechanical processes and the reactions of the surrounding EDZ evolve. Fig. 5.46 illustrates the evolution of water saturation in the seal centre of the selected sealing materials. The water saturation of each material is determined by its inherent properties such as porosity, initial saturation degree, permeability and particularly water retention capacity. The water resaturation of the pure bentonite increases rapidly to 85 % during the first 400 years ( $\Delta t = 500\text{y} - 100\text{y}$ ), while the resaturation of the other mixtures are relatively slow to a degree of 70 % at the claystone-bentonite seal and 63 % at the bentonite-sand seal for the same time period. The full saturation needs a much longer time over 2600 years for the claystone-bentonite seal, 2800 years for the bentonite and 2900 years for the bentonite-sand seal. The differences in water saturation durations are relatively small for these three materials.

In correspondence with the water saturation, swelling pressure built up in each seal, as shown in Fig. 5.47. Over the 400 years resaturation, different swelling pressures are reached in the seals: 3 MPa in the bentonite, 2 MPa in the claystone-bentonite and 1.2 MPa in the bentonite-sand seal, respectively. The maximum swelling pressures are achieved after full water saturation: 4.4 MPa at the bentonite, 3.1 MPa at the bentonite-sand and 2.8 MPa at the claystone-bentonite seal. All the seal materials are more or less consolidated by the rock compression. In view of the EDZ sealing, a fast buildup of swelling pressure is desired.

The stress reaction at drift wall to the development of swelling pressure in each seal is depicted in Fig. 5.48. The evolution of the total radial stress during the saturation phase is similar to the swelling pressure development. After full water saturation, the total stress increases with the increase of the porewater pressure. Under the support effect from the seal, the drift convergence is decelerated as shown in Fig. 5.49. The higher the swelling pressure is developed in the seal, the higher the support effect with smaller drift convergence, so that the sealing of the EDZ will be enhanced. The impacts of the seal on the

EDZ sealing will be studied in the future with implementation of the new HM models (Eqs. 5.30 - 5.34) for clay rock during damage and recompaction.

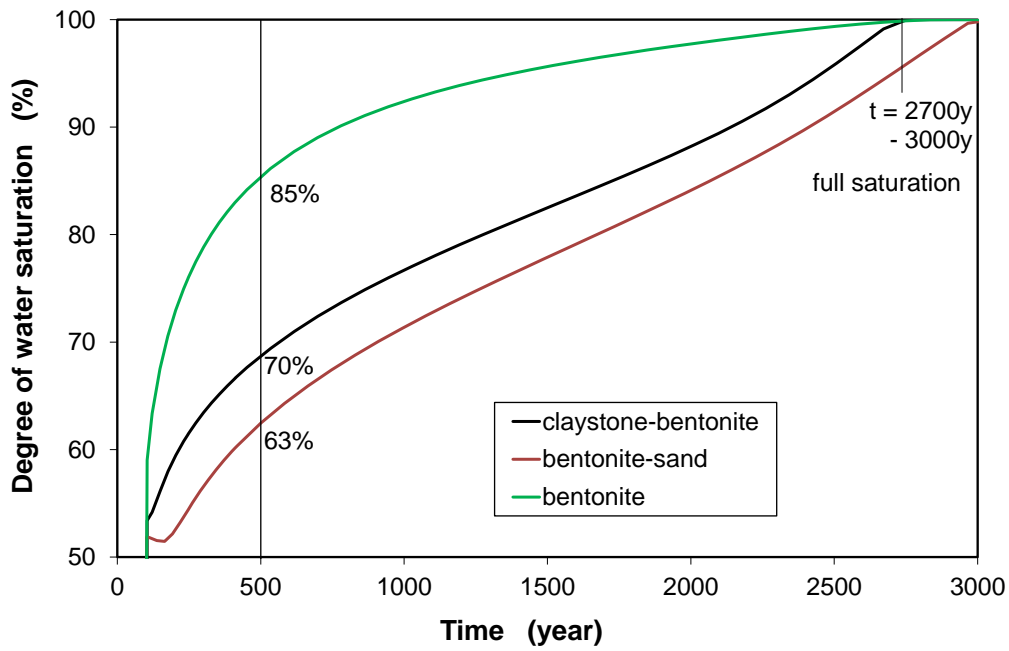


Fig. 5.46 Evolution of water saturation in the seal materials

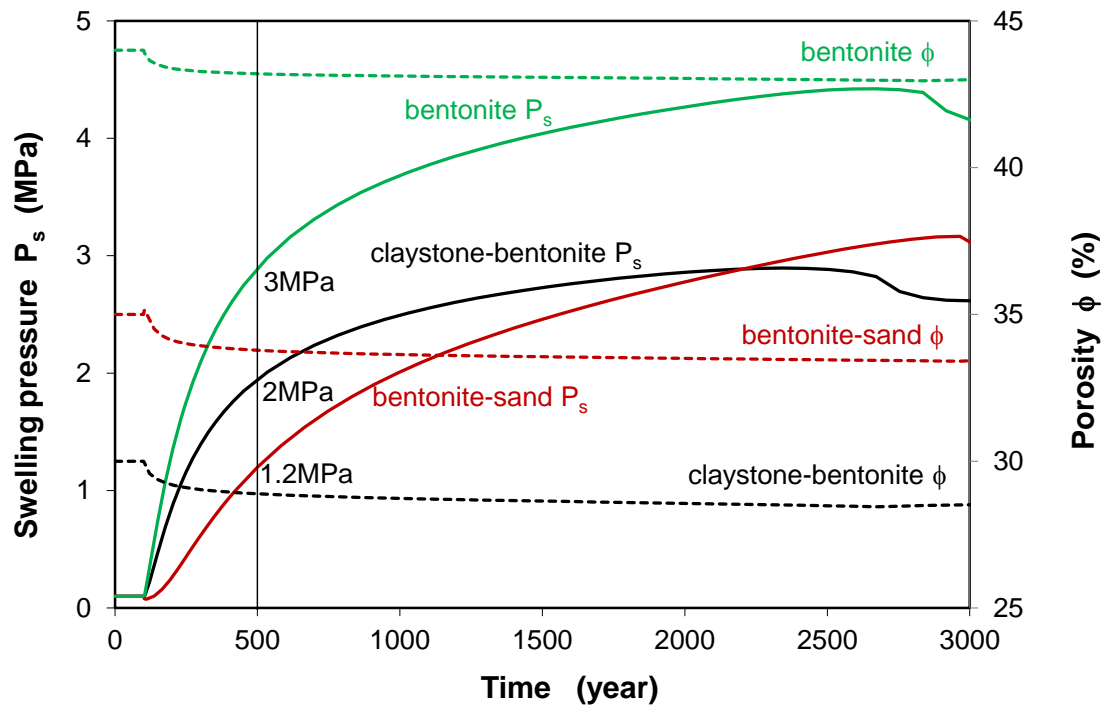
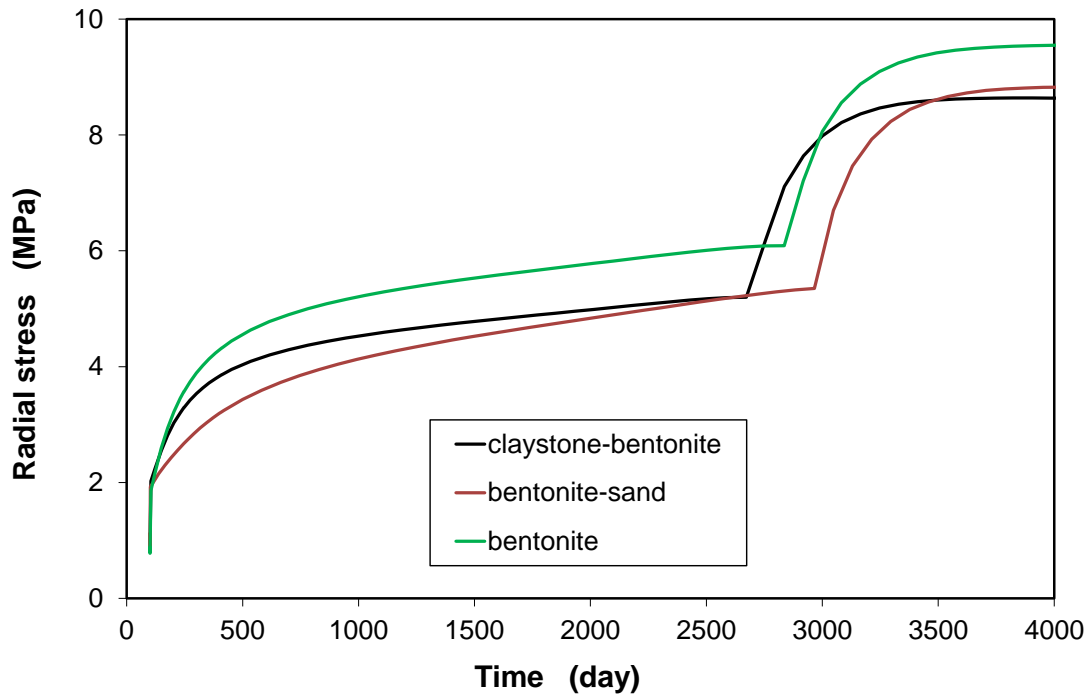
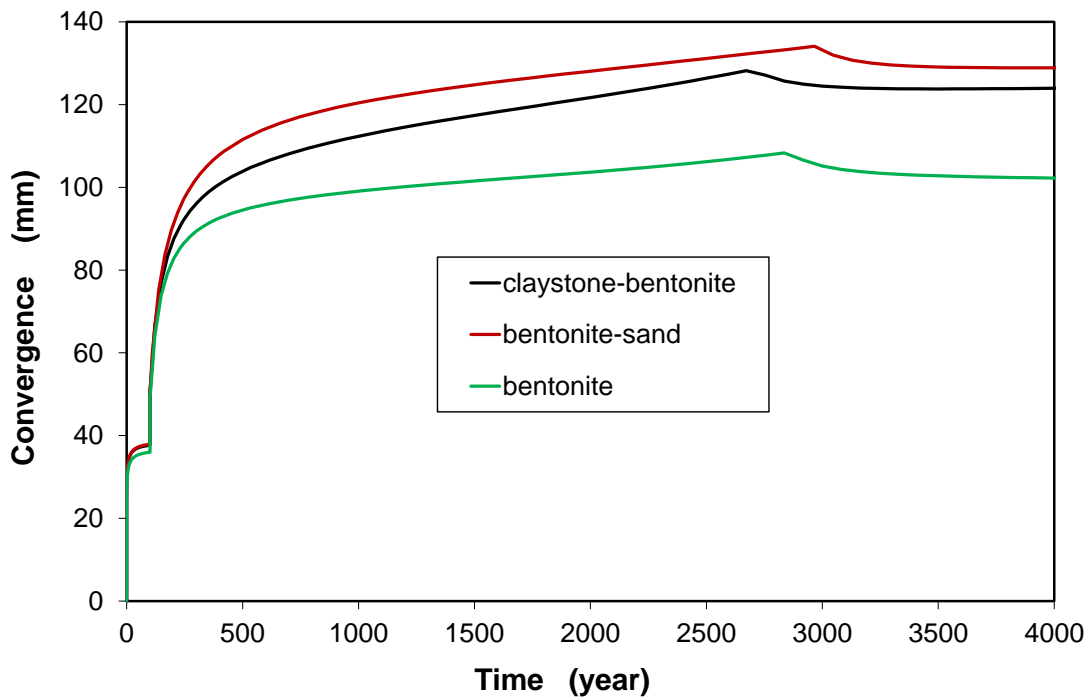


Fig. 5.47 Development of swelling pressure and porosity in the seal materials



**Fig. 5.48** Stress reaction at drift wall to the swelling pressure in the seal



**Fig. 5.49** Impact of swelling pressure in the seal on the drift convergence

## **5.5 Lessons learnt from the modelling exercises**

For the prediction and assessment of the long-term performance of the drift seal in clay rock, extensive modelling exercises have been done using the THM computing code CODE\_BRIGTH, including

- validation of the existing constitutive models for the mathematical description of the hydro-mechanical behaviour of the clay rock and clay-based seal materials;
- development of some specific constitutive equations to enhance the capability of the existing models for the clay rock;
- determination of the associated parameters for the clay rock and seal materials;
- simulation of the laboratory experiments for the validation and demonstration of the predictability of the applied models; and
- predictive modelling of the long-term sealing performance of a drift seal.

### **5.5.1 Modelling of the HM behaviour of the seal materials**

The HM behaviour of the compacted bentonite, bentonite-sand (70/30) and claystone-bentonite (60/40) mixtures is mathematically represented by a same set of constitutive equations but different parameter values.

The elasto-plastic model BBM adopted is adequate for describing the mechanical responses of the clay-based materials such as the stress-driven deformation and suction-driven swelling. However, the time-dependent behaviour of the materials is not yet explicitly involved, which is of most importance for predicting the long-term behaviour of the seal.

The Darcy's law is applied for the advective liquid and gas flow in the seal materials together with additional relationships such as intrinsic permeability – porosity, relative liquid/gas permeability, and suction – water saturation or water retention curve. In unsaturated state, water resaturation is the dominating process, which results in significant responses of the compacted clay-based materials such as buildup of swelling pressure in confined conditions or expansion in unconfined conditions, variations of porosity, permeability, stiffness and strength.

The simulations of the laboratory experiments with the water saturation and swelling of the bentonite, bentonite-sand and claystone-bentonite mixtures provide satisfactory agreements between the modelling results and the measured data. However, some uncertainty in the model parameters is to be minimized through further investigations.

### **5.5.2 Modelling of the HM behaviour of the clay rock**

The visco-elastoplastic model newly modified by UPC is adopted for the mechanical behaviour of the clay rock, which is able to represent the short-term elastoplastic deformation with hardening/softening and compaction/dilatancy, and the transient creep with strain hardening. Using the parameters obtained on the COX claystone, this model provides the reasonable modelling results compared with the observations during the short- and long-term deformation tests. Based on the long-term creep tests on the claystone, a stationary creep model was established to enhance the existing model for predicting the long-term creep of the clay host rock.

Most of the hydraulic models available from the code are applicable for conventional porous media without significant fractures. They are not adequate for the clay rock during stress-driven fracturing. Based on the gas permeability measurements during mechanical loading, a percolation permeability model was formulated for the fracturing-induced permeability during damage and failure as function of minimum principal stress and dilatancy. Recompression decreases the permeability of fractured clay rock, which is related to the change in fracture space by a cubic law approximately.

Because of the significant swelling effects, the water permeability of the fractured claystone is several orders of magnitude lower than the gas permeability. Based on the measurements of water permeability of the fractured claystone, a relationship was established for the water permeability to effective confining stress.

For modelling of gas migration in water-saturated and fracture-resealed claystone, empirical models were formulated for the gas breakthrough pressure as a function of the water permeability and the minimum confining stress and for the gas permeability as a function of gas pressure or the effective confining stress.

These specific constitutive equations shall be implemented in CODE\_BRIGHT for modelling the excavation induced damage zone (EDZ) and the long-term sealing process in it.

### **5.5.3 Predictive modelling of a drift seal**

The long-term performance of a drift seal was preliminarily predicted by coupled HM modelling. The drift seal section is assumed to be excavated to a diameter of 9.5 m and a length of 40 m at a depth of 500 m. The drift is supported with concrete lining. After an operational phase over 100 years, a seal is installed. The compacted bentonite, bentonite-sand (70/30) and claystone-bentonite (60/40) mixtures are respectively applied for the seal. The hydro-mechanical processes in the seal system including the seal, EDZ and intact rock are modelled.

The most important process is the water uptake of the seal, with which the sealing effects develop. Full water saturation takes very long time periods of about 3000 years for all the selected seal materials. In correspondence with the water saturation, swelling pressure built up in the seal up to 3 MPa at the bentonite, 2 MPa at the claystone-bentonite and 1.2 MPa at the bentonite-sand during the first 400 years. The higher the swelling pressure is developed in the seal, the more effective the support effect on the sealing of the EDZ. However, the development of the EDZ cannot be yet represented by using the existing constitutive models for the clay rock. New adequate models, for instance, the above-mentioned models for the fracturing-induced permeability, fracture closure and permeability reduction, swelling-enhanced sealing or permeability reduction, and gas migration through water-saturated fractures, are required for further modelling the long-term behaviour of the EDZ.



## 6 Summary and conclusions

The geological disposal concepts for radioactive waste are generally based on a multi-barrier system comprising the natural geological formations and engineered barriers. After emplacement of the waste, the disposal cells, access drifts and shafts will be back-filled and sealed with suitable materials to prevent release of radionuclides into the biosphere. In the framework of the joint R&D programme by the German project THM-TON for the investigation of the THM behaviour of clay rock and the European project DOPAS for the demonstration of the feasibility of plugs and seals for safe sealing repositories, GRS performed comprehensive experimental investigations and modelling exercises, including

- Examination of self-sealing of fractures in clay rock by measurements of fracture closure, water permeability and gas migration;
- Characterization of crushed claystone-bentonite mixture as seal material in comparison to bentonite and bentonite-sand mixture with respect to safe sealing properties such as compacted density, mechanical stability, water uptake and retention, swelling capacity, water permeability and gas migration;
- Development of specific constitutive relationships for the seal materials and the clay rock in order to enhance the predictability of numerical models for the long-term sealing performance of seal systems in repositories;
- Model validation by simulating the hydro-mechanical behaviour of the seal materials and the clay rock observed during laboratory experiments;
- Model prediction and analysis of the long-term performance of a reference drift seal constructed using the compacted claystone-bentonite mixture, bentonite and bentonite-sand mixture, respectively.

The experiments were carried out on the Callovo-Oxfordian claystone taken from the MHM-URL in France. The self-sealing capability of the claystone was investigated on the artificially-fractured samples, whereas the suitability of the crushed claystone mixed with bentonite for sealing repositories was examined in comparison with pure bentonite and bentonite-sand mixture. The modelling work was conducted by using the THM computing code CODE\_BRIGHT. The main results and important conclusions drawn from the studies are summarized as follows.

## 6.1 Self-sealing of fractures in claystone

High stresses in the region between the damage and failure boundaries generate microcracks, which propagate and coalesce to a network when the peak failure stress is reached. The fracturing results in a spontaneous increase of the permeability by up to several orders of magnitude, depending on the minor principal stress. The intensity of created fractures and the permeability decrease with increasing the minor principal stress. The fracturing-induced permeability is contributed by the connectivity and the conductivity of created cracks.

Fractures in claystone tend to close up when the stress normal to the fracture planes is increased. Correspondingly, the fracture permeability reduces, which depends on the fracture feature such as fracture geometry, size, roughness, density and connectivity. The permeability reduction is related to the fracture closure approximately following the cubic law.

As water enters and flows through fractures, the clay matrix takes up the water and expands into the interstices. The water-induced swelling, weakening and slaking of the claystone leads to clogging and sealing of the fractures. Consequently, the hydraulic conductivity decreases by several orders of magnitude down to very low levels of  $10^{-19}$  to  $10^{-21}$  m<sup>2</sup> even at low confining stresses of 2 - 4 MPa. This process observed in the laboratory experiments is completed within relatively short periods of times, i.e. months to years, compared with the repository post-closure phase of tens of thousands of years. Moreover, the sealing of the fractures is not significantly affected by the thermal loading in the testing range between 20 °C and 90 °C. The very low water permeabilities of the resealed fractures are in the same order as that of the intact claystone.

Before full water saturation, fractures in the claystone act as preferential pathways for gas. However, after full water saturation, gas entry and subsequent penetration into the resealed fractures require a certain gas pressure to overcome the capillary thresholds. The gas entry/breakthrough pressure is controlled by the degree of fracture sealing which is in turn depending on the confining stress. It was observed that the gas breakthrough pressures in the water-saturated and highly-resealed claystones are still lower than the confining stresses. It implies that the EDZ, even when highly resealed, will still have the capacity for gas flow without over-pressurisation.

Generally speaking, the high self-sealing capacity of the fractured claystone hinders water transport and thus radionuclides migration through the EDZ, but allows gas flow without over-pressurisation and without fracturing the host rock. These significant advantages guarantee the long-term sealing functions of the plug/seal systems and hence the long-term safety of the repositories.

## **6.2 Sealing properties of clay-based materials**

As a potential material for sealing repositories in clay formations, excavated claystone mixed with bentonite was investigated in comparison to bentonite and bentonite-sand mixture. The crushed COX claystone mixed with small fractions of bentonite MX80 up to 40 %, MX80 bentonite and bentonite-sand mixture in a ratio of 70/30 were characterized with respect to the sealing properties such as compacted density, mechanical stability, water uptake and retention, swelling capacity, water permeability, gas entry/break-through pressure and permeability after full water saturation. The sealing performance of the claystone-bentonite and bentonite-sand mixtures were also examined by small-scale sealing tests in steel tubes. The following conclusions can be drawn from the experiments:

Compacted density: The claystone-bentonite mixture can be compacted to high dry densities compared to the pure bentonite and the bentonite-sand mixture. At a given load of 15 MPa in oedometer compression, the dry densities achieved were: 2.0 g/cm<sup>3</sup> at the crushed claystone, 1.85 - 1.90 g/cm<sup>3</sup> at the claystone-bentonite mixture (80/20; 60/40), 1.80 g/cm<sup>3</sup> at the bentonite-sand mixture (70/30) and 1.65 g/cm<sup>3</sup> at the bentonite. These compacted mixtures with the respective densities were furthermore investigated to determine the sealing properties and behaviour.

Mechanical stiffness: The mechanical stiffness of the mixtures increases exponentially with the dry density. At a given density, the stiffness of the claystone-bentonite mixture is higher than that of the bentonite and the bentonite-sand mixture. This implies that a seal constructed with compacted claystone-bentonite blocks will be more stable against external loading and can provide high backpressures enhancing the sealing of the surrounding EDZ.

Water uptake and retention: Water uptake of compacted clay-based materials is governed by diffusion of water molecules through unsaturated pores under suction effect. The rate of water uptake is strongly dependent on the porosity or density as well as on the bentonite content. High density and bentonite content hinder the water uptake. The maximum amounts of water uptake in vapour were determined: 12 % at the compacted crushed claystone, 20 - 28 % at the claystone-bentonite mixture, 32 % at the bentonite-sand mixture, and 45 - 48 % at the bentonite.

Swelling capacity: Upon water uptake the compacted clay-based mixtures tend to expansion. The swelling capacity of the compacted mixtures increases with increasing bentonite content and dry density. The maximum swelling pressures of the compacted mixtures were achieved at full water saturation: 2.0 MPa at the compacted crushed claystone, 2.5 - 3.5 MPa at the claystone-bentonite mixture, 6.0 MPa at the bentonite-sand mixture, and 7.5 MPa at the bentonite.

Water conductivity: The compacted clay-based mixtures show very low water permeabilities at full saturation:  $5 \cdot 10^{-20} \text{ m}^2$  at the compacted crushed claystone,  $2 \cdot 10^{-19}$ – $1 \cdot 10^{-20} \text{ m}^2$  at the claystone-bentonite mixture,  $2 \cdot 10^{-20} \text{ m}^2$  at the bentonite-sand mixture, and  $< 10^{-20} \text{ m}^2$  at the bentonite. These permeability values are close to that of the intact clay rock.

Gas migration: After full water saturation, gas needs to overcome the capillary thresholds before it can migrate through the compacted mixtures. This gas breakthrough pressure was measured for each mixture. It was observed that the gas breakthrough pressures of the compacted claystone-bentonite mixtures were lower than the external confining stresses which are in contrast quite high, close to or even above the confining stresses or swelling pressures for the bentonite-based materials.

Generally speaking, the compacted claystone-bentonite mixtures have similar sealing properties like the compacted bentonite and bentonite-sand mixtures with one exception: compacted claystone-bentonite mixtures as sealing material allow for gas release already at low and moderate pressures without compromising the integrity of the geological-engineered barrier system. Claystone-bentonite mixtures thus appear to be a preferable material for sealing repositories.

### **6.3 Modelling of the sealing performance of the clay-based materials**

The modelling work was performed by using the THM computer code CODE\_BRIGHT. In order to enhance the predictive capability of the numerical models for the long-term performance of the sealing systems in repositories, the constitutive models available for the description of the hydro-mechanical behaviour of the clay-based materials and the clay rock were validated by simulating the laboratory experiments and matching the measured data. Some new constitutive equations were formulated for the claystone to enhance the model capability for predicting the hydro-mechanical behaviour of the EDZ. Based on the experimental results, the model parameters were determined for the seal materials and the clay rock. They were applied for predictive modelling of the long-term performance of a reference drift seal under repository relevant conditions.

#### ***Modelling of the seal materials***

The hydro-mechanical behaviour of the compacted bentonite, bentonite-sand and claystone-bentonite mixtures is mathematically represented by a same set of constitutive equations but different parameter values. The elasto-plastic model (BBM) developed by UPC is basically validated for the description of responses of the clay-based materials to variations of hydro-mechanical conditions, such as the stress-driven deformation and suction-driven swelling. However, the time-dependence of the deformation is not yet explicitly involved, which is of most importance for predicting the long-term performance of the seal materials. As a main hydraulic process in the highly-compacted materials, the water saturation is governed by suction. The relationship between them (called water retention curve) was established for each mixture with the associated parameters. The application of the mechanical and hydraulic models for modelling the water saturation and swelling pressure evolution observed in the laboratory tests provided a satisfactory agreement with the measured data for each mixture. However, some parameters need to be determined in more precise experiments.

#### ***Modelling of the clay rock***

The visco-elastoplastic model advanced by UPC is basically validated by simulating and matching the triaxial short- and long-term experiments on the COX claystone. This model is capable of representing the short-term elastoplastic deformation with hardening/softening and the transient creep with strain hardening. For predicting the long-term creep of the claystone, a new creep equation was established for the stationary creep. For

prediction of the water and gas transport process in the EDZ, a set of equations for water permeability, gas breakthrough pressure and permeability were developed on the bases of the experimental observations:

- The fracturing-induced permeability (to gas) is expressed by a percolation model as function of dilatancy and minimum principal stress;
- The fracture permeability decreases with recompaction following a cubic law;
- The water conductivity of fractures in the claystone is several orders of magnitude lower than the gas permeability because of the swelling effects, which is expressed as an exponential function of minimum principal stress;
- Gas migration through water-saturated fractures in the claystone is described with two terms - gas breakthrough pressure and permeability; the gas breakthrough pressure is exponentially related to the water permeability and the minimum confining stress, whereas the gas permeability is exponentially related to the gas pressure after breakthrough.

These specific constitutive equations shall be implemented in the computer code CODE\_BRIGTH to enhance the predictability of numerical modelling.

### ***Prediction of the long-term performance of a drift seal***

The preliminary model prediction focused on the central swelling core of the France reference drift seal without considering concrete plugs at the end faces of the core. The hydro-mechanical conditions in the MHM-URL are taken into account. A horizontal access drift (or ILW vault) of 9.5 m diameter is excavated at a depth of 500 m. A seal (swelling core) is constructed in a section of 40 m length. An axisymmetric model is chosen involving a large rock mass of 60 m radius and 40 m length. The operational phases are simulated with drift excavation and support within 6 months, drift operation period of 100 years, removal of the support lining within a month and installation of the seal, and the subsequent post-closure phase. The compacted bentonite, bentonite-sand (70/30) and claystone-bentonite (60/40) blocks are respectively utilized for the construction of the seal. The EDZ surrounding the seal is characterized by relatively high permeabilities of  $5 \cdot 10^{-18} \text{ m}^2$  to  $1 \cdot 10^{-19} \text{ m}^2$  from the drift wall to 3 m in depth, compared to that of  $1 \cdot 10^{-20} \text{ m}^2$  for the host rock. The constitutive models validated for the compacted seal materials and the clay rock are used. The hydro-mechanical processes in the seal system including the seal, EDZ and intact rock are modelled in a coupling way until the hydraulic process reaches equilibrium.

The modelling results show that the most important process is the water saturation of the seal, which leads to development of its sealing effects such as building up of swelling pressure, slowing down of the convergent deformation, etc. Full water saturation needs long time periods of about 3,000 years for all the selected seal materials that show the similar saturation process. The water saturation leads to a development of swelling pressure to 3 MPa in the bentonite seal, 2 MPa in the claystone-bentonite seal and 1.2 MPa in the bentonite-sand seal during the first 400 years. The swelling pressure hinders the development of the EDZ and decelerates the drift convergence. In the future, more precise model predictions have to be done with the help of advancing constitutive models for all the components of the seal system.



## **Acknowledgements**

The research work was co-funded by the German Federal Ministry for Economic Affairs and Energy (BMWi) under contract number 02E10377 and by the European Commission (EC) as the part of the Euratom's Seventh Framework Programme FP7/2007-2013 under grant agreement no. 323273 for the DOPAS project.

We also gratefully acknowledge the support from the French Agence Nationale pour la Gestion des Déchets Radioactifs (ANDRA) for providing the testing material and fruitful discussions, and the support from the Geotechnical Engineering Department of the Technical University of Catalonia in Barcelona (UPC) with regard to modelling work.



## References

- /ÅKE 10/ Åkesson, M., Kristensson, O., Börgensson, L., Dueck, A. (2010): THM modelling of buffer, backfill and other system components – Critical processes and scenarios. SKB Technical Report TR-10-11, March 2010.
- /ÅKE 13/ Åkesson, M. and Andersson, L. (2013): BRIE Water-uptake test Clay Technology AB, Lund, Sweden, April / September 2013.
- /AND 05/ ANDRA DOSSIER (2005): Synthesis – Evaluation of the feasibility of a geological repository in an argillaceous formation.
- /AND 15/ ANDRA (2015): Status of the Cigéo Project in France - French Industrial Geological Disposal Project, in the Proceedings of the LUCOEX Conference and Workshop, June 2-4, 2015, Oskarshamn, Sweden.
- /ARM 14/ Armand, G., Leveau, F., Nussbaum, C., de La Vaissiere, R., Noiret, A., Jaeggi, D., Landrein, P., Righini, C. (2014): Geometry and Properties of the Excavation-Induced Fractures at the Meuse/Haute-Marne URL Drifts, *Rock Mech Rock Eng* (2014) 47, 21-41.
- /BGR 07/ Hoth, P., Wirth, H., Reinhold, K., Bräuer, V., Krull, P., Feldrappe, H. (2007): Untersuchung und Bewertung von Tongesteinsformationen, Bundesanstalt für Geowissenschaften und Rohstoffe, Berlin/Hannover, April 2007.
- /BIR 13/ Birgersson, M., Karnland O. (2013): Gas intrusion in bentonite – Results of small scale experiments, FORGE International Symposium and Workshop on Gas Generation and Migration, February 5-7, 2013, Luxembourg.
- /BLU 07/ Blümling, P., Bernier, F., Lebon, P., Martin, C.D. (2007): The excavation damaged zone in clay formations: time-dependent behaviour and influence on performance assessment, *Physics and Chemistry of the Earth*, 32, 588-599.

- /BMW 12/ BMWi und PTKA-WTE (2012): Schwerpunkte zukünftiger FuE-Arbeiten bei der Endlagerung radioaktiver Abfälle (2011 – 2014), Bundesministerium für Wirtschaft und Technologie (BMWi) und Projektträger Karlsruhe Wassertechnologie und Entsorgung (PTKA-WTE).
- /BOC 10/ Bock, H., Dehandschutter, B., Martin, C.D., Mazurek, M., Haller, A.D., Skoczylas, F., Davy, C. (2010): Self-Sealing of Fractures in Argillaceous Formations in the Context of Geological Disposal of Radioactive Waste – Review and Synthesis. Clay Club Report, OECD, NEA No. 6184.
- /BOS 04/ Bossart, P., Trick, T., Meier, P.M., Mayor, J.C. (2004): Structural and hydrogeological characterisation of the excavation-disturbed zone in the Opalinus Clay (Mont Terri Project. Switzerland), Applied Clay Science 26, 429-448.
- /DEL 13/ de La Vaissiere, R. and Talandier J. (2013): Gas Injection Test in the Meuse/Haute Marne Underground Research Laboratory, FORGE International Symposium and Workshop on Gas Generation and Migration, February 5-7, 2013, Luxembourg.
- /DEL 15a/ de La Vaissiere, R., Conil, N; Leveau, F., Armand, G. (2015): Large-Scale Sealing Experiment in the Meuse/Haute Marne Underground Research Laboratory, The 6th International Clay conference – Clays in Natural & Engineered Barriers for Radioactive Waste Confinement, March 23-26, 2015, Brussels.
- /DEL 15b/ de La Vaissiere, R., Armand, G., Talandier, J. (2015): Gas and water flow in an excavation-induced fracture network around an underground drift: A case study for a radioactive waste repository in clay rock, Journal of Hydrology 521 (2015) 141 – 156.
- /DOP 12/ DOPAS project (2012): Technical feasibility and long-term performance of repository components – Full-scale demonstration of plugs and seals, the European Union's European Atomic Energy Community's (Euratom) Seventh Framework Programme FP7/2007-2011 under Grant agreement no 323273.

- /FOI 15/ Foin, R., Bosgiraud, J.-M., Armand, G., Noiret, A. (2015): Technical feasibility of the Cigéo Project seals, in the Proceedings of the LUCOEX Conference and Workshop, June 2-4, 2015, Oskarshamn, Sweden.
- /FRE 93/ Fredlund, D.G., Rahardjo, H. (1993): Soil Mechanics for Unsaturated Soils. John Wiley & Sons, INC.
- /GEN 98/ Gens, A., Garcia-Molina, A.J., Olivella, S., Alonso, E.E., Huertas, F. (1998): Analysis of a Full Scale in-situ Test Simulating Repository Conditions. Int. J. Numer. Anal. Meth. Geomech., 22, 515-548, 1998.
- /GEN 06/ Gens, A. A., Olivella, S.: Coupled Thermo-Hydro-Mechanical Analysis of Engineered Barriers for High-Level Radioactive Waste, in Chinese Journal of Rock Mechanics and Engineering, 2006, 25(4), 670 -680.
- /HAN 13/ Hansen, J., Holt, E., Palmu, M. (2013): DOPAS: 'Full-scale in situ Demonstration of Tunnel Plugs and shaft Seal in Clay, Crystalline and Salt Repository Host-Rock Formations', EURADWASTE'13 – 8<sup>th</sup> EC Conference on the Management of Radioactive Waste Community Policy and Research on Disposal, 14-17 October 2013, Vilnius, Lithuania.
- /HAN 14/ Hansen, J. (2014): A general overview of DOPAS project and first year achievements for full-scale demonstration of plugs and seals, PEBS International Conference on the Performance of Engineered Barriers, February 6-7, 2014, Hannover.
- /HER 15/ Herold, P., Gruner, M., Jobmann, M., Kudla, W. (2015): Konzeptentwicklung für Schachtverschlüsse im Ton- und Salzgestein, Technischer Bericht (Entwurf), DBE TECHNOLOGY GmbH, TU Bergakademie Freiberg (in German).
- /IAE 90/ IAEA (1990): Sealing of Underground Repositories for Radioactive Wastes. Technical Report Series No. 319.
- /IAE 92/ IAEA (1992): Performance of Engineered Barriers in Deep Geological Repositories. Technical Report Series No. 342.

- /JOB 15a/ Jobmann, M., Meleshyn, A., Maßmann, J., Polster, M. (2015): Quantifizierung von Kriterien für Integritätsnachweise, Technischer Bericht (Entwurf), BGR, GRS, DBE TECHNOLOGY GmbH, Ber. Nr.: TEC-08-2013-AP, Peine (in German).
- /JOB 15b/ Jobmann, M. & Lommerzheim, A. (2015): Endlagerkonzept sowie Verfüll- und Verschlusskonzept für das Endlagerstandortmodell SÜD, Technischer Bericht (Entwurf), DBE TECHNOLOGY GmbH, Peine (in German).
- /KAR 08/ Karnland, O., Nilsson, U., Weber, H., Wersin, P. (2008): Sealing ability of Wyoming bentonite pellets foreseen as buffer material – Laboratory tests, *Physics and Chemistry of the Earth* 33, 472-475
- /KÖH 15/ Köhler, S., Fries, T., Müller, H.R., Gaus, I. (2015): Swiss Backfilling Concept – Requirements and Approaches for Optimization of the Bentonite Barrier around SF/HLW Disposal Canisters, The 6th International Clay conference – Clays in Natural & Engineered Barriers for Radioactive Waste Confinement, March 23-26, 2015, Brussels.
- /KRÖ 04/ Kröhn, K.-P. (2004): Modelling the re-saturation of bentonite in final repositories in crystalline rock, final report, GRS – 199.
- /LOM 15/ Lommerzheim, A. & Jobmann, M. (2015): Endlagerkonzept sowie Verfüll- und Verschlusskonzept für das Endlagerstandortmodell NORD, Technischer Bericht (Entwurf), DBE TECHNOLOGY GmbH, Peine (in German).
- /MIT 76/ Mitchell, J.K. (1976): *Fundamentals of Soil Behavior*. University of California, Berkeley, USA
- /MUL 15/ Müller, H.R., Vogt, T., Garritte B., Köhler, S., Sakaki, T., Weber, H., Vietor, T. (2015): The Full-Scale Emplacement Experiment – Implementation of a Multiple Heater Experiment at the Mont Terri URL, The 6th International Clay conference – Clays in Natural & Engineered Barriers for Radioactive Waste Confinement, March 23-26, 2015, Brussels.

- /NAG 02/ NAGRA (2002): Project Opalinus Clay, Models, Codes and Data for Safety Assessment – Demonstration of disposal feasibility for spent fuel, vitrified high-level waste and long-lived intermediate-level waste
- /NIA 97/ Niandou, H., Shao, J.F., Henry, J.P., Fourmaintraux, D. (1997): Laboratory Investigation of the Mechanical Behaviour of Tournemire Shale, *Int. J. Rock Mech. Min. Sci.* Vol 34, No. 1, pp. 3-16
- /MIT 92/ Mitchell, J.K. (1992): Characteristics and Mechanisms of Clay Creep and Creep Rupture, in “Clay-water interface and its rheological implications, *Clay Mineral society*”, Vol.4, 212-244.
- /OEC 03/ OECD (2003): Engineered Barrier Systems and the Safety of Deep Geological Repositories – State-of-the-art Report. EUR 19964 EN.
- /OEC 04/ OECD (2004): Safety of Disposal of Spent Fuel, HLW and Long-lived ILW in Switzerland – An international peer review of the post-closure radiological safety assessment for disposal in the Opalinus Clay of the Zürcher Weinland. NEA No. 5568.
- /OLI 94/ Olivella, S.; Carrera, J.; Gens, A.; Alonso, E.E. (1994): Nonisothermal Multi-phase Flow of Brine and Gas Through Saline Media. *Transport in Porous Media*, 15, 271-293 (1994).
- /POP 07/ Popp, T. and Salzer, K. 2007: Anisotropy of seismic and mechanical properties of Opalinus clay during triaxial deformation in a multi-anvil apparatus, *Physics and Chemistry of the Earth*, 32, 879-888.
- /REI 13/ Reinhold, K., Jahn, S., Kühnlenz, T., Ptock, L. & Sönke, J. (2013): Projekt AnSichT – Methodenentwicklung und Anwendung eines Sicherheitsnachweiskonzeptes für einen generischen HAW-Endlagerstandort im Tonstein. Endlagerstandortmodell NORD. Teil I: Beschreibung des geologischen Endlagerstandortmodells. – Bundesanstalt für Geowissenschaften und Rohstoffe (BGR), Zwischenbericht: 71 S.; Berlin und Hannover.

- /REI 16/ Reinhold, K., Stark, L., Kühnlenz, T. & Ptock, L. (2016): Projekt AnSichT - Methodenentwicklung und Anwendung eines Sicherheitsnachweiskonzeptes für einen generischen HAW-Endlagerstandort im Tonstein. Endlagerstandortmodell SÜD – Teil I: Beschreibung des geologischen Endlagerstandortmodells. – Bundesanstalt für Geowissenschaften und Rohstoffe (BGR), Ergebnisbericht: 71 S; Hannover/Berlin.
- /RUI 15/ Ruiz, D.F., Vaunat, J., Gens, A., Manica, M., Pasteau, A. (2015): Insights into the response of a gallery sealing over the entire life of a deep repository, The 6th International Clay Conference – Clays in Natural & Engineered Barriers for Radioactive Waste Confinement, March 23-26, 2015, Brussels.
- /RUT 83/ Rutter, E.H. (1983): Pressure solution in nature, theory and experiment, Journal of Geological Society. London, Vol. 140, pp. 725-740.
- /SHA 15/ Shaw, R.P. (editor): Gas Generation and Migration in Deep Geological Radioactive Waste Repositories, Special Publication 415 of the Geological Society of London, 2015.
- /UPC 15/ UPC (2015): User's Guide of CODE\_BRIGHT - A 3-D Program for Thermo-Hydro-Mechanical Analysis in Geological Media, Department of Geotechnical Engineering and Geosciences of Technical University of Catalonia (UPC), Barcelona, Spain.
- /VAN 80/ Van Genuchten, M.T. (1980): A Closed-Form Equation for predicting the hydraulic Conductivity of Unsaturated Soils. -Soil Sci. Soc. Am. J., 44:892-898
- /VAU 03/ Vaunat, J., Alonso, E.E., Gens, A. (2003): constitutive model of short and long term behaviour of the Meuse/Haute-Marne argillite. Deliverable 2&3 of the EC project MODEX-REP, FIKW-CT2000-00029.
- /VIG 11/ Viggiani, G., Bésuelle, P, Desrues, J. (2011): X-ray Micro Tomography as a Tool for Studying Localized Damage / Deformation in Clay Rock, NEA CLAY CLUB Workshop Proceedings – Clay characterisation from nanoscopic to microscopic resolution, Karlsruhe, Germany, September 2011.

- /VOL 96/ Volckaert,G.; Bernier,F.; Alonso,E.; Gens,A.; Samper,J.; Villar,M.; Martin-Martin,P.L.; Cuevas,J.; Campos,R.; Thomas,H.; Imbert,C.; Zingarelli,V. (1996): Thermo-hydraulic-mechanical and geochemical behaviour of the clay barrier in radioactive waste repositories (model development and validation), Final report, EUR 16744 EN.
- /WHI 14/ White, M., Doudou, S., Neall, F. (2014): DOPAS Work Package 2 - Deliverable D2.1: Design Bases and Criteria.
- /ZHA 08a/ Zhang, C.L., Rothfuchs, T., Dittrich, J., Müller, J. (2008): Investigations on self-sealing of indurated clay – part of the EC NFPRO project, Bericht GRS-230, Gesellschaft für Anlagen- und Reaktorsicherheit (GRS) mbH, Braunschweig.
- /ZHA 08b/ Zhang, C.L., Rothfuchs, T. (2008): Damage and sealing of clay rocks detected by measurements of gas permeability, Physics and Chemistry of the Earth, Vol. 33, 363-373
- /ZHA 09/ Zhang C.L. (2009): Self-sealing of Fractures in Argillites under Repository conditions, The international conference and workshop in the framework of the EC TIMODAZ and THERESA projects, Sept. 2009, Luxembourg
- /ZHA 10a/ Zhang, C.L., Czaikowski, O., Rothfuchs, T. (2010): Thermo-Hydro-Mechanical Behaviour of the Callovo-Oxfordian Clay Rock – Final report of the BURE-HAUPT/EC-TIMODAZ project, Bericht GRS-266, Gesellschaft für Anlagen- und Reaktorsicherheit (GRS) mbH, Braunschweig.
- /ZHA 10b/ Zhang, C.L., Wieczorek, K., Xie, M. L. (2010): Swelling experiments on mudstones, Journal of Rock Mechanics & Geotechnical Engineering, 2(1) 41-47
- /ZHA 11/ Zhang C.L. (2011): Experimental Evidence for Self-sealing of Fractures in Claystone, Physics and Chemistry of the Earth, Vol. 36: 1972-1980.

- /ZHA 13a/ Zhang, C.L., Czaikowski, O., Rothfuchs, T., Wieczorek, K. (2013): Thermo-Hydro-Mechanical Processes in the Nearfield around a HLW Repository in Argillaceous Formations - Volume I: Laboratory Investigations, May 2007 to May 2013, Bericht GRS-312, Gesellschaft für Anlagen- und Reaktorsicherheit (GRS) mbH, Braunschweig.
- /ZHA 13b/ Zhang C.L. (2013): Sealing of Fractures in Claystone, Journal of Rock Mechanics and Geotechnical Engineering 5, 214-220.
- /ZHA 14a/ Zhang, C.L., Czaikowski, O., Komischke, M., Wieczorek, K. (2014): Thermo-Hydro-Mechanical Processes in the Nearfield around a HLW Repository in Argillaceous Formations - Volume II: In-situ-Investigations and Interpretative Modelling, May 2007 to May 2013, Bericht GRS-313, Gesellschaft für Anlagen- und Reaktorsicherheit (GRS) mbH, Braunschweig.
- /ZHA 14b/ Zhang C.L. (2014): Status report for the EC DOPAS project Deliverable (D5.5): Characterization and modelling of clay rock and claystone-based seal material, Bericht GRS-A-3761, Gesellschaft für Anlagen- und Reaktorsicherheit (GRS) mbH, Braunschweig.
- /ZHA 14c/ Zhang C.L. (2014): Investigation of gas migration in damaged and resealed claystone, Proceedings – Gas Generation and Migration in Deep Geological Radioactive Waste Repositories (edited by SHAW, R.P.), The Geological Society of London, 2014.
- /ZHA 14d/ Zhang, C.L. (2014): Characterization of Excavated Claystone and Claystone-Bentonite Mixtures as Backfill/Seal Material, Geological Society Special Publication 400 – Clays in Natural and Engineered Barriers for Radioactive Waste Confinement (edited by Norris et al.), The Geological Society of London, 2014, 323-337.
- /ZHA 14e/ Zhang, C.L. (2014): Investigations of Excavated Claystone as Backfill/Seal Material, PEBS International Conference on the Performance of Engineered Barriers, February 6-7, 2014, Hannover.
- /ZHA 15a/ Zhang, C.L. (2015): Deformation of Clay Rock under THM Conditions, Geomechanics and Tunnelling 8 (2015), No. 5, 426-435.

- /ZHA 15b/ Zhang, C.L., Armand, G., Conil, N. (2015): Investigation on the Anisotropic Mechanical Behaviour of the Callovo-Oxfordian Clay Rock, Final Report of the ANDRA/GRS Experimental Programme, Bericht GRS-360, Gesellschaft für Anlagen- und Reaktorsicherheit (GRS) mbH, Braunschweig.
- /ZHA 16/ Zhang, C.L. (2016): The Stress-Strain-Permeability Behaviour of Clay Rock during Damage and Recompression, Journal of Rock Mechanics and Geotechnical Engineering 8 (2016), 16-26.
- /ZHA 17A/ Zhang, C.L. (2017): Examination of Effective Stress in Clay Rock, Journal of Rock Mechanics and Geotechnical Engineering, 2017, 9(2).
- /ZHA 17B/ Zhang, C.L., Conil, N., Armand, G. (2017): Thermal effects on clay rocks for deep disposal of high-level radioactive waste, Journal of Rock Mechanics and Geotechnical Engineering 2017, 9(2)



## List of figures

Fig. 2.1	Swiss repository concept for SF and HLW disposal in horizontal drifts in the Opalinus clay formation (a-b) /NAG 02/.....	7
Fig. 2.2	French repository concept for HLW and ILW disposal in horizontal boreholes and drifts in the Callovo-Oxfordian clay formation /AND 15/ .....	8
Fig. 2.3	French reference drift sealing and backfilling concept /FOI 15/ .....	9
Fig. 2.4	Longitudinal view of the FSS experiment made by ANDRA /FOI 15/.....	10
Fig. 2.5	General layout of the NSC experiment in the MHM-URL (a) and seal construction in the drift using bentonite-sand blocks and bentonite pellets (b) /DEL 15a/ .....	11
Fig. 2.6	German concept for HLW disposal in horizontal drifts in Opalinus Clay (a-b) /JOB 15b/ .....	13
Fig. 2.7	German concept for HLW disposal in vertical boreholes in Lower Cretaceous Clay /LOB 15/ .....	14
Fig. 2.8	German drift backfilling and sealing concept /LOB 15/ .....	15
Fig. 3.1	Stress-strain-permeability behaviour of COX claystone including thresholds of yield $\sigma_Y$ , dilatancy $\sigma_D$ , percolation $\sigma_P$ , and peak failure $\sigma_B$ (a-b) .....	19
Fig. 3.2	Dependency of the deformation and permeability of COX claystone on lateral confining stress (a-c) .....	21
Fig. 3.3	Stress boundaries of yield, dilatancy, percolation and peak failure of the claystone .....	22
Fig. 3.4	Prediction of the fracturing-induced permeability in the claystone using the percolation model .....	24
Fig. 3.5	Volume compaction (a) and permeability changes (b) of fractured COX claystone during hydrostatic loading and unloading.....	26
Fig. 3.6	Fracture closure as a function of normal stress (a) and permeability reduction with fracture closure (b) .....	26
Fig. 3.7	Stress-strain-permeability behaviour of fractured claystone during multistep deviatoric loading (a-b) .....	29
Fig. 3.8	Residual strength of fractured COX claystone as a function of minor confining stress .....	30

Fig. 3.9	Variation in permeability of fractured claystone with volume compaction during hydrostatic loading (a) and multistep deviatoric loading (b) .....	32
Fig. 3.10	Sealing of fractures in COX claystone under various confining stresses .....	33
Fig. 3.11	Long-term evolution of water permeability obtained on fractured claystones under confining stresses of 2 to 3.5 MPa and temperatures of 20 °C to 90 °C (a-b) .....	34
Fig. 3.12	Dependence of stabilized water permeability of fractured claystone on effective confining stress .....	35
Fig. 3.13	Gas breakthrough pressures measured on highly-resealed claystones under different confining stresses (a-b).....	37
Fig. 3.14	Gas pressure induced dilatancy in a highly-resealed claystone sample under triaxial compression.....	38
Fig. 3.15	Gas breakthrough pressure of highly-resealed claystones in comparison with a conservative fracturing criterion without considering tensile strength .....	39
Fig. 3.16	Dependence of gas permeability on gas pressure after breakthrough.....	40
Fig. 3.17	Dependence of gas permeability on effective minimum stress after breakthrough .....	40
Fig. 4.1	Grain size distributions of crushed claystone, bentonite, sand and mixtures.....	45
Fig. 4.2	Normal (a) and large (b) oedometers used for compaction of seal materials.....	46
Fig. 4.3	Compacted dry densities of the claystone-bentonite and bentonite-sand mixtures in normal oedometer (a-b) .....	47
Fig. 4.4	Elastic bulk modulus of the compacted claystone-bentonite and bentonite-sand mixtures as function of dry density .....	48
Fig. 4.5	Dry densities of the compacted crushed claystone, bentonite, claystone-bentonite and bentonite-sand mixtures in large oedometer cell (a-b) .....	50
Fig. 4.6	Compacted dry densities obtained on six samples of the claystone-bentonite mixtures in large oedometer cell .....	51

Fig. 4.7	Measurement of water retention properties of the clay-based materials in desiccators at different air humidities (a-c) .....	55
Fig. 4.8	Relationships of water content to suction for the seal materials: bentonite, bentonite-sand mixture, claystone-bentonite mixture, intact and crushed claystone (a-d).....	57
Fig. 4.9	Setup of water saturation measurements on the compacted seal mixtures in steel cylinders .....	59
Fig. 4.10	Evolution of cumulative water uptake of compacted seal materials in contact with synthetic clay water at atmospheric pressure (a-d).....	62
Fig. 4.11	Water uptake (a) and free swelling (b) measured on the compacted claystone-bentonite mixtures at different suctions .....	64
Fig. 4.12	Free swelling of the compacted seal materials with increasing water content .....	64
Fig. 4.13	Pictures of the compacted claystone-bentonite samples after free swelling at a high relative humidity of 96 % over 6 months (a-d) .....	65
Fig. 4.14	Test setup for swelling pressure measurements on seal samples.....	66
Fig. 4.15	Development of swelling pressure in the compacted claystone-bentonite and bentonite-sand mixtures during wetting with synthetic clay water .....	67
Fig. 4.16	Uniaxial swelling deformation of the compacted claystone-bentonite and bentonite-sand mixtures in oedometers at axial load of 1 MPa during wetting with synthetic clay water .....	68
Fig. 4.17	Schematic of triaxial swelling test on a claystone-bentonite sample.....	69
Fig. 4.18	Triaxial swelling deformation of the compacted claystone-bentonite sample at a confining stress of 2 MPa during water injection at pressures of 1.0 and 1.5 MPa .....	70
Fig. 4.19	Schematic of large-scale swelling test on compacted crushed claystone .....	71
Fig. 4.20	Testing conditions applied to the compacted crushed claystone .....	72
Fig. 4.21	Testing conditions applied to the compacted crushed claystone (a-c).....	73
Fig. 4.22	Water permeabilities of the compacted crushed claystone, claystone-bentonite and bentonite-sand mixtures .....	75
Fig. 4.23	Gas breakthrough pressures and permeability of the compacted claystone-bentonite and bentonite-sand mixtures (a-b) .....	78

Fig. 4.24	Gas breakthrough permeability as a function of gas pressure .....	78
Fig. 4.25	Schematic illustration of the water and gas flow tests with seal mixtures.....	79
Fig. 4.26	Gas breakthrough pressures and permeabilities obtained on the compacted and water-saturated claystone aggregate at different confining stresses .....	80
Fig. 4.27	Gas breakthrough pressure and permeability as function of confining stress.....	81
Fig. 4.28	Evolution of gas injection pressure after switching off the inlet to the water-saturated claystone-bentonite mixture .....	82
Fig. 4.29	Gas flow through the water-saturated and compacted claystone aggregate .....	82
Fig. 4.30	Installation of small-scale borehole sealing tests in steel cylinders with compacted blocks of the claystone-bentonite and bentonite-sand mixtures and bentonite powder filling the gaps .....	84
Fig. 4.31	Setup of the small-scale borehole sealing tests in steel cylinders with compacted blocks of claystone-bentonite and bentonite-sand mixtures (a-b) .....	85
Fig. 4.32	Water uptake and resulting swelling pressure in the claystone-bentonite and bentonite-sand seals assembled in steel cylinders during the water saturation phase .....	86
Fig. 4.33	Water inflow into the claystone-bentonite and bentonite-sand seals assembled in steel cylinders at increased injection pressures.....	87
Fig. 4.34	Results of gas injection tests on the claystone-bentonite and bentonite-sand seals assembled in steel cylinders .....	89
Fig. 5.1	Main relations between THM processes in porous media /GEN 06/ .....	94
Fig. 5.2	Intrinsic permeability as a function of porosity for the seal materials .....	100
Fig. 5.3	Relative water and gas permeability as a function of water saturation ...	100
Fig. 5.4	Water retention curves expressed by the van Genuchten model for the selected seal materials (a-d) .....	103
Fig. 5.5	Water retention curves expressed by the van Genuchten model for the selected seal materials (a-d) .....	105
Fig. 5.6	Water retention curves expressed by the modified van Genuchten model for the selected seal materials (a-d) .....	106

Fig. 5.7	Determination of the compaction parameters for the seal materials .....	110
Fig. 5.8	Model geometry and boundary conditions for modelling the water saturation of the seal materials .....	112
Fig. 5.9	Water retention curves used for modelling the water uptake of the compacted bentonite .....	113
Fig. 5.10	Comparison of water saturation measured on MX80 bentonite /KRÖ 04/ and predicted using the different hydraulic parameters (a-d).....	115
Fig. 5.11	Comparison of water saturation measured on MX80 bentonite /KRÖ 04/ and predicted using the modified water retention curve.....	116
Fig. 5.12	Predictions of the water saturation in the bentonite-sand mixture using the van Genuchten model (solid line) and the modified model (dash line) .....	117
Fig. 5.13	Predictions of the water saturation in the claystone-bentonite mixture using the van Genuchten model (solid line) and the modified model (dash line) .....	118
Fig. 5.14	Predictions of the water saturation in the claystone mixture using the van Genuchten model (solid line) and the modified model (dash line)....	119
Fig. 5.15	Model geometry and boundary conditions for modelling the swelling pressure of the seal materials .....	120
Fig. 5.16	Predictions of the swelling pressure developed in the compacted bentonite-sand (a) and claystone-bentonite (b) mixture during hydration .....	122
Fig. 5.17	Schematic setup of BRIE water uptake tests on the compacted bentonite and measurement locations /ÅKE 13/ .....	123
Fig. 5.18	Model geometry and boundary conditions for modelling the hydration and swelling pressure in the compacted bentonite in BRIE-tests .....	124
Fig. 5.19	Modelled evolution of water saturation of the compacted bentonite at different locations during the laboratory BRIE test (a-c) /ÅKE 13/ .....	127
Fig. 5.20	Modelled distributions of water saturation in the compacted bentonite at different times during the laboratory BRIE-test (a-b) /ÅKE 13/.....	128
Fig. 5.21	Modelling results of swelling pressure development in the compacted bentonite during the BRIE water uptake test /ÅKE 13/.....	128
Fig. 5.22	Stress-strain-permeability behaviour of claystone during damage and recompaction ( $\sigma_Y$ = yield stress, $\sigma_D$ = dilatancy threshold, $\sigma_B/\varepsilon_B$ =	

	peak failure stress/volumetric strain, $\sigma_R$ = residual strength, $k_c$ = initial permeability, $\varepsilon_F$ = volumetric strain at ultimate fracturing and $k_f$ = final fracture permeability) .....	130
Fig. 5.23	Evolution of the friction angle .....	137
Fig. 5.24	Stationary shear creep rate of the water-saturated COX claystone as function of deviatoric stress (a) and temperature (b).....	139
Fig. 5.25	Anisotropic elastic parameters of the COX claystone as a function of deviatoric stress: Young's modulus / Poisson's ratio $E_1 / \nu_1$ parallel and $E_2 / \nu_2$ normal to bedding planes .....	140
Fig. 5.26	Isotropic elastic parameters of the COX claystone as a function of deviatoric stress .....	142
Fig. 5.27	Swelling and shrinkage of the COX and OPA claystones as a function of water content .....	143
Fig. 5.28	Yield and peak failure boundaries of the COX claystone .....	143
Fig. 5.29	Creep models for the stationary creep of the COX claystones .....	144
Fig. 5.30	3D model geometry for modelling the triaxial tests on COX claystone ...	145
Fig. 5.31	Modelling results of the short-term deformation behaviour of the COX claystone during triaxial loading .....	147
Fig. 5.32	Plastic strain parameters as function of the minor confining stress .....	148
Fig. 5.33	Modelling results of the long-term deformation behaviour observed during a triaxial creep test on COX claystone (a-b).....	151
Fig. 5.34	Modelling results of the long-term deformation behaviour of the COX claystone under low deviatoric stresses.....	151
Fig. 5.35	Axisymmetric model for the drift seal after drift lining (a) and sealing (b).....	153
Fig. 5.36	Hydraulic conductivity measured around a drift parallel to the horizontal major stress direction in the MHM-URL: (a) horizontal borehole at the wall and (b) vertical boreholes at floor and ceiling / ARM 14/ .....	155
Fig. 5.37	Water retention curves used for the clay rock and EDZ (a), bentonite (b), bentonite-sand mixture (c), and claystone-bentonite mixture (d).....	159
Fig. 5.38	Evolution of the radial and tangential stresses (a) and the convergent displacements (b) in the surrounding rock after drift excavation and support .....	161

Fig. 5.39	EDZ and convergence of a drift parallel to the horizontal major stress direction observed in the MHM-URL (a-b) /ARM 14/.....	162
Fig. 5.40	Evolution of the porewater pressure (a) and water saturation (b) in the surrounding rock with the drift ventilation after excavation and support .....	163
Fig. 5.41	Long-term evolution of porewater pressure in the seal, EDZ and rock ...	165
Fig. 5.42	Long-term evolution of water saturation in the seal, EDZ and rock.....	165
Fig. 5.43	Development of swelling pressure and porosity in the seal during water saturation.....	166
Fig. 5.44	Development of total radial stress in the seal-rock-system .....	167
Fig. 5.45	Development of convergent displacement of the EDZ and rock .....	167
Fig. 5.46	Evolution of water saturation in the seal materials .....	169
Fig. 5.47	Development of swelling pressure and porosity in the seal materials.....	169
Fig. 5.48	Stress reaction at drift wall to the swelling pressure in the seal .....	170
Fig. 5.49	Impact of swelling pressure in the seal on the drift convergence.....	170

## Appendix A

Fig. A. 1	Water uptake and free deformation of compacted bentonite in different humid conditions .....	208
Fig. A. 2	Water uptake and free deformation of compacted claystone-bentonite mixture (80/20) in different humid conditions.....	209
Fig. A. 3	Water uptake and free deformation of compacted claystone-bentonite mixture (60/40) in different humid conditions.....	210
Fig. A. 4	Water uptake and free deformation of compacted claystone aggregate in different humid conditions .....	211
Fig. A. 5	Water uptake of compacted claystone-bentonite (60/40) and bentonite-sand (70/30) mixtures in desiccator 1 .....	212
Fig. A. 6	Water uptake of compacted claystone-bentonite (60/40) and bentonite-sand (70/30) mixtures in desiccator 2 .....	212
Fig. A. 7	Water uptake of compacted claystone-bentonite (60/40) and bentonite-sand (70/30) mixtures in desiccator 3 .....	213

Fig. A. 8	Water uptake of compacted claystone-bentonite (60/40) and bentonite-sand (70/30) mixtures in desiccator 4 .....	213
Fig. A. 9	Water uptake of compacted claystone-bentonite (60/40) and bentonite-sand (70/30) mixtures in desiccator 5 .....	214
Fig. A. 10	Water uptake of compacted claystone-bentonite and bentonite powder, claystone in desiccator 1 .....	215
Fig. A. 11	Water uptake of compacted claystone-bentonite and bentonite powder, claystone in desiccator 2 .....	215
Fig. A. 12	Water uptake of compacted claystone-bentonite and bentonite powder, claystone in desiccator 3 .....	216
Fig. A. 13	Water uptake of compacted claystone-bentonite and bentonite powder, claystone in desiccator 4 .....	216
Fig. A. 14	Water uptake of compacted claystone-bentonite and bentonite powder, crushed claystone and claystone core in desiccator 5 .....	217
Fig. A. 15	Water uptake of compacted claystone-bentonite and bentonite powder, crushed claystone and claystone core in desiccator 6 .....	217
Fig. A. 16	Water uptake of compacted claystone-bentonite and bentonite powder, crushed claystone and claystone core in desiccator 7 .....	218
Fig. A. 17	Water uptake of compacted claystone-bentonite and bentonite powder, crushed claystone and claystone core in desiccator 8 .....	218

## **Appendix B**

Fig. B. 1	Evolution of water uptake by the compacted claystone-bentonite mixture .....	220
Fig. B. 2	Distributions of bulk/dry density, water content and saturation of compacted claystone aggregate after a saturation time period of 9 months .....	220
Fig. B. 3	Distributions of bulk/dry density, water content and saturation of compacted claystone-bentonite mixture (80/20) after a saturation time period of 9 months.....	221
Fig. B. 4	Distributions of bulk/dry density, water content and saturation of compacted claystone-bentonite mixture (60/40) after a saturation time period of 9 months.....	221
Fig. B. 5	Evolution of water uptake by the compacted claystone-bentonite and bentonite-sand mixtures .....	222

Fig. B. 6	Distributions of bulk/dry density, water content and saturation of compacted claystone-bentonite mixture (60/40) after a saturation time period of 9.5 months.....	223
Fig. B. 7	Distributions of bulk/dry density, water content and saturation of compacted bentonite-sand mixture (70/30) after a saturation time period of 9.5 months .....	223
Fig. B. 8	Distributions of bulk/dry density, water content and saturation of compacted bentonite after a saturation time period of 9.5 months .....	224
Fig. B. 9	Distributions of bulk/dry density, water content and saturation of a claystone core after a saturation time period of 9.5 months.....	224
Fig. B. 10	Evolution of water uptake by the compacted claystone-bentonite and bentonite-sand mixtures .....	226
Fig. B. 11	Distributions of bulk/dry density, water content and saturation of compacted claystone-bentonite mixture (60/40) after a saturation time period of 15 months.....	226
Fig. B. 12	Distributions of bulk/dry density, water content and saturation of compacted claystone-bentonite mixture (60/40) after a saturation time period of 14 months.....	227
Fig. B. 13	Distributions of bulk/dry density, water content and saturation of compacted bentonite-sand mixture (70/30) after a saturation time period of 15 months .....	227
Fig. B. 14	Distributions of bulk/dry density, water content and saturation of compacted bentonite-sand mixture (70/30) after a saturation time period of 14 months .....	228



## List of tables

Tab. 4.1	Basic properties of the samples prepared from the different clay-based mixtures for determination of the water retention curves.....	52
Tab. 4.2	Parameters of the water retention curves in expression of water content .....	58
Tab. 4.3	Characteristics of the water-saturated and compacted claystone-bentonite and bentonite-sand mixtures for gas testing.....	76
Tab. 4.4	Summary of the key sealing properties of the compacted claystone-bentonite and bentonite-sand mixtures .....	90
Tab. 5.1	Basic characteristics of the selected seal materials .....	98
Tab. 5.2	Water retention parameters associated in the van Genuchten model for the seal materials.....	104
Tab. 5.3	Water retention parameters associated in the modified van Genuchten model for the seal materials .....	105
Tab. 5.4	BBM model parameters for the selected seal materials.....	110
Tab. 5.5	Basic characteristics of the samples in the water saturation tests: MX80 bentonite, 70MX80+30Sand and 60COX+40MX80 mixtures, and COX claystone .....	111
Tab. 5.6	Summary of the hydraulic parameters in different models for the bentonite .....	113
Tab. 5.7	Hydraulic parameters of the bentonite-sand mixture.....	117
Tab. 5.8	Hydraulic parameters of the claystone-bentonite mixture .....	118
Tab. 5.9	Hydraulic parameters of the COX claystone .....	119
Tab. 5.10	Laws of evolution of the friction angle .....	137
Tab. 5.11	Anisotropic elastic parameters of three clay rocks .....	141
Tab. 5.12	Isotropic elastic parameters of COX claystone at radial stress of 5 MPa.....	141
Tab. 5.13	Key hydraulic parameters obtained for modelling the COX claystone ....	145
Tab. 5.14	Mechanical parameters adopted for modelling the short-term deformation behaviour of the COX claystone.....	146

Tab. 5.15	Mechanical parameters for modelling the short-term deformation behaviour of the COX claystone .....	149
Tab. 5.16	Constitutive models and parameters for the clay rock and EDZ .....	156
Tab. 5.17	Constitutive models and parameters for the concrete lining .....	156
Tab. 5.18	Constitutive models and parameters for the seal materials: bentonite, bentonite-sand mixture (70/30) and claystone-bentonite mixture (60/40) .....	157

### **Appendix A**

Tab. A. 1	Properties of the seal mixtures prepared for determination of the water retention properties in three groups .....	207
-----------	--	-----

### **Appendix B**

Tab. B. 1	Initial characteristics of the samples tested in group I .....	219
Tab. B. 2	Initial characteristics of the samples tested in group II .....	222
Tab. B. 3	Initial characteristics of the samples tested in group III .....	225

## Appendix A: Water retention data obtained on the seal materials

**Tab. A. 1** Properties of the seal mixtures prepared for determination of the water retention properties in three groups

Test group I				
Material property	MX80 bentonite	80 COX+ 20 MX80	60 COX+ 40 MX80	Crushed COX claystone
Grain size $d_{max}$ (mm)	0.5	5.0	5.0	5.0
Grain density $\rho_s$ (g/cm <sup>3</sup> )	2.78	2.72	2.73	2.70
Dry density $\rho_d$ (g/cm <sup>3</sup> )	1.64	1.95	1.88	2.05
Porosity $\phi$ (%)	41.1	28.2	31.2	24.2
Water content $w$ (%)	9.67	4.50	5.45	3.0
Max. water content $w_m$ (%)	48.0	19.0	28.0	12.0

Test group	II		III			
Material property	70MX80+ 30Sand	60COX+ 40MX80	MX80 bentonite	60COX+ 40MX80	COX clays-tone	Crushed clays-tone
Grain size $d_{max}$ (mm)	2.0	5.0	2.0	5.0		
Grain density $\rho_s$ (g/cm <sup>3</sup> )	2.75	2.73	2.74	2.73	2.70	2.70
Dry density $\rho_d$ (g/cm <sup>3</sup> )	1.72	1.81	1.15	1.89	2,28	2.23
Porosity $\phi$ (%)	37.5	33.5	58.0	30.7	15.5	17.5
Water content $w$ (%)	7.0	5.5	11.0	6.0	5.5	5.5
Max. water content $w_m$ (%)	18.0	32,0	45,0	20.0	8.8	11.0

**Group I:**

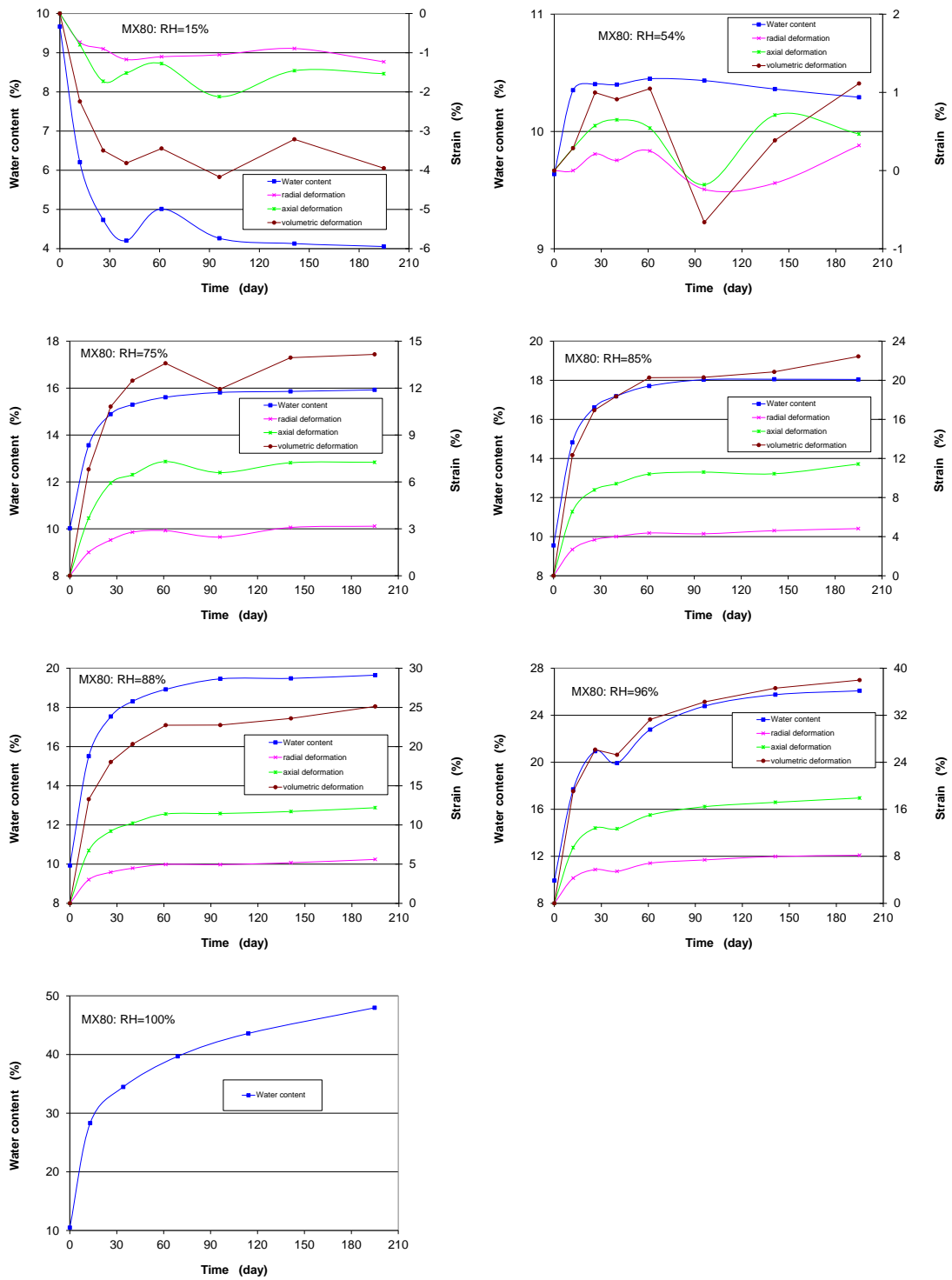


**Fig. A. 1** Water uptake and free deformation of compacted bentonite in different humid conditions

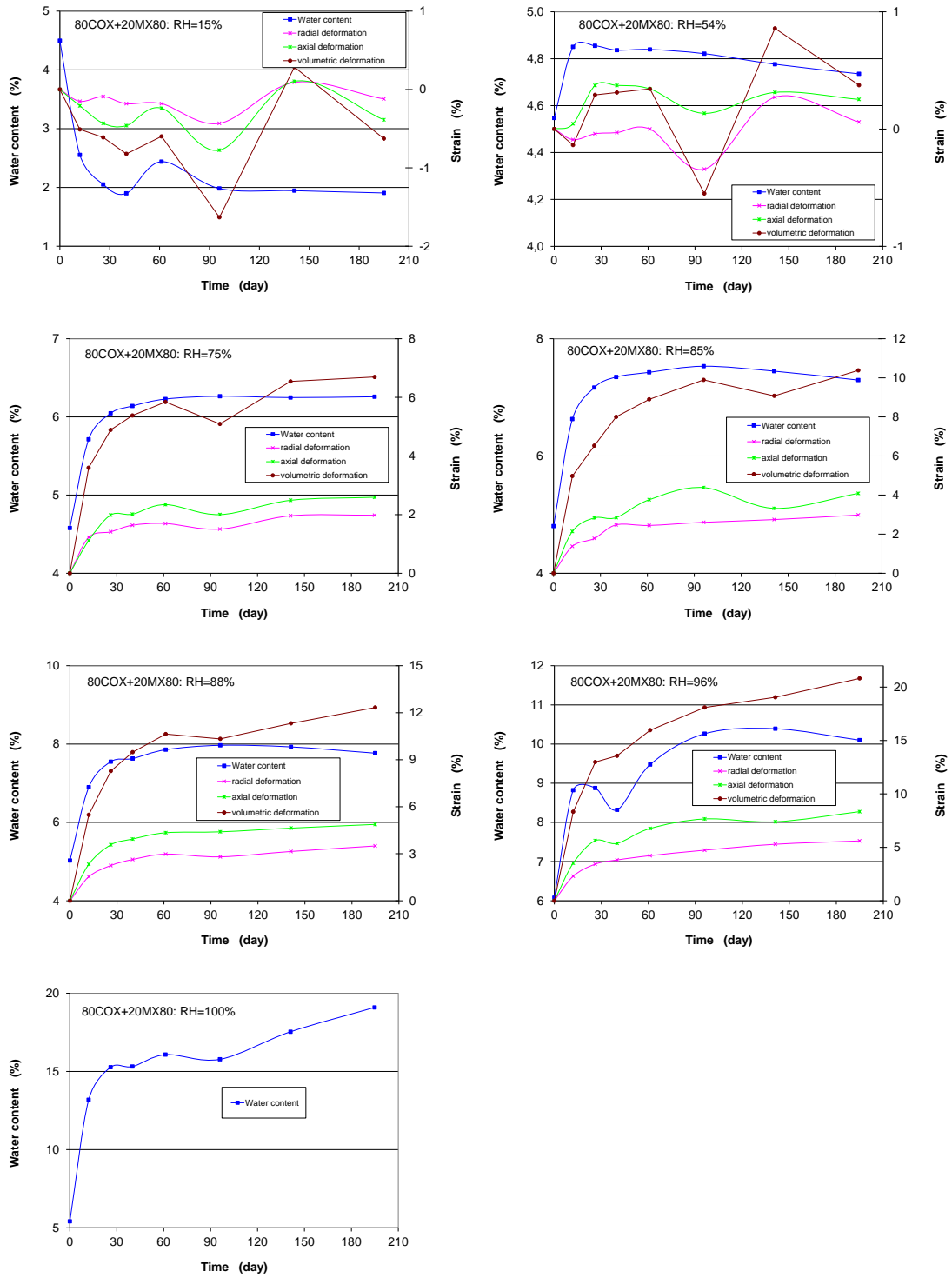


**Fig. A. 2** Water uptake and free deformation of compacted claystone-bentonite mixture (80/20) in different humid conditions

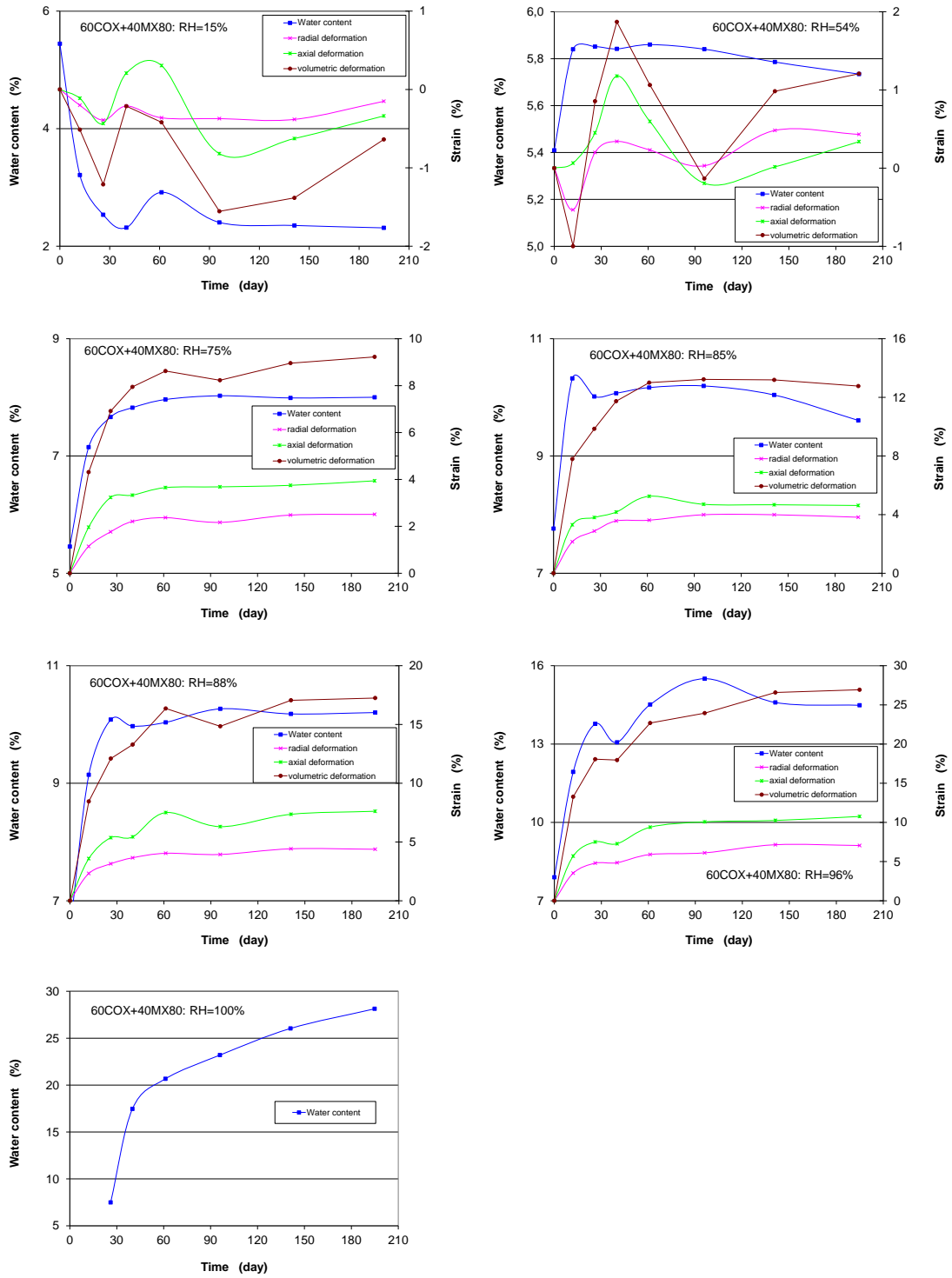


**Fig. A. 3** Water uptake and free deformation of compacted claystone-bentonite mixture (60/40) in different humid conditions

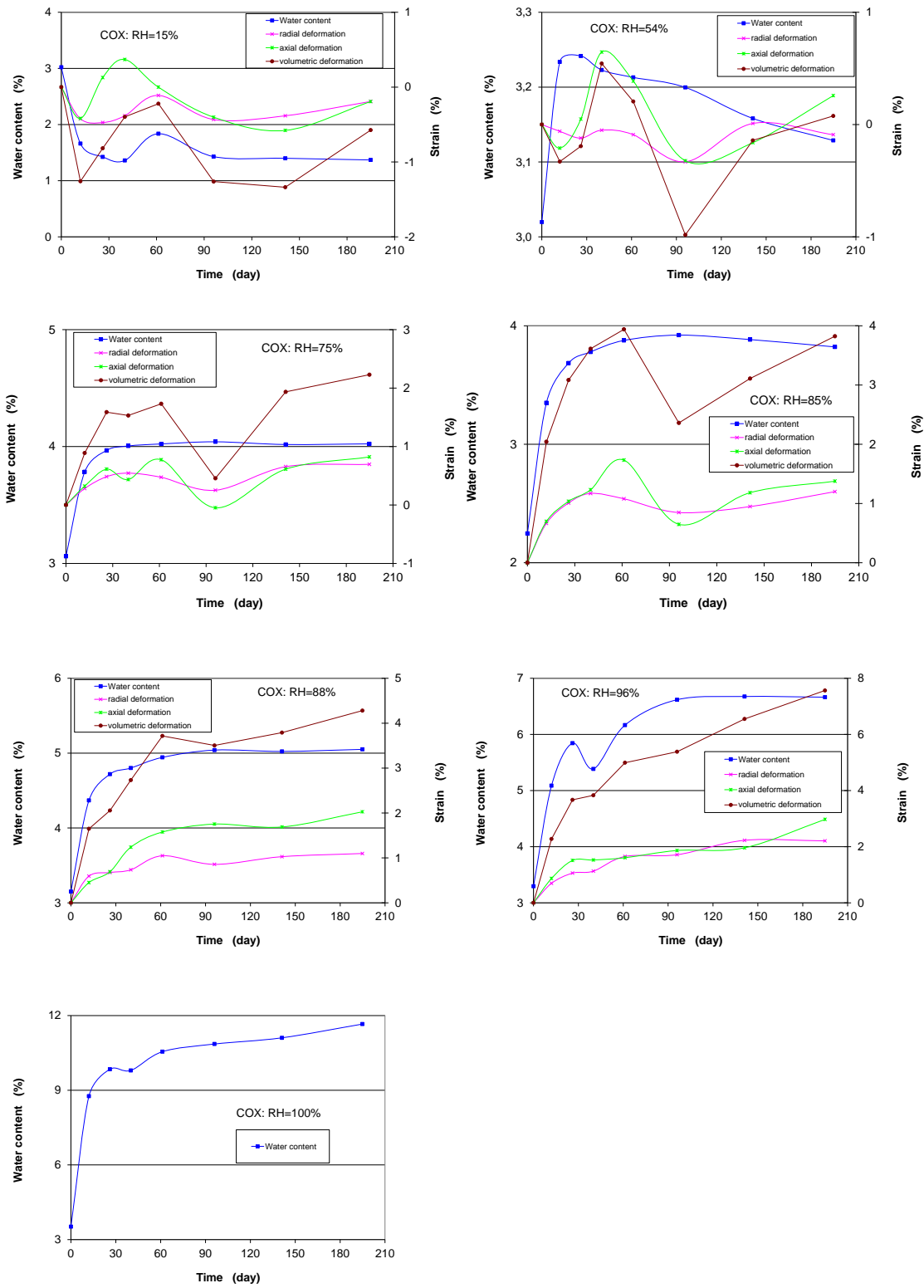


**Fig. A. 4** Water uptake and free deformation of compacted claystone aggregate in different humid conditions

**Group II:**

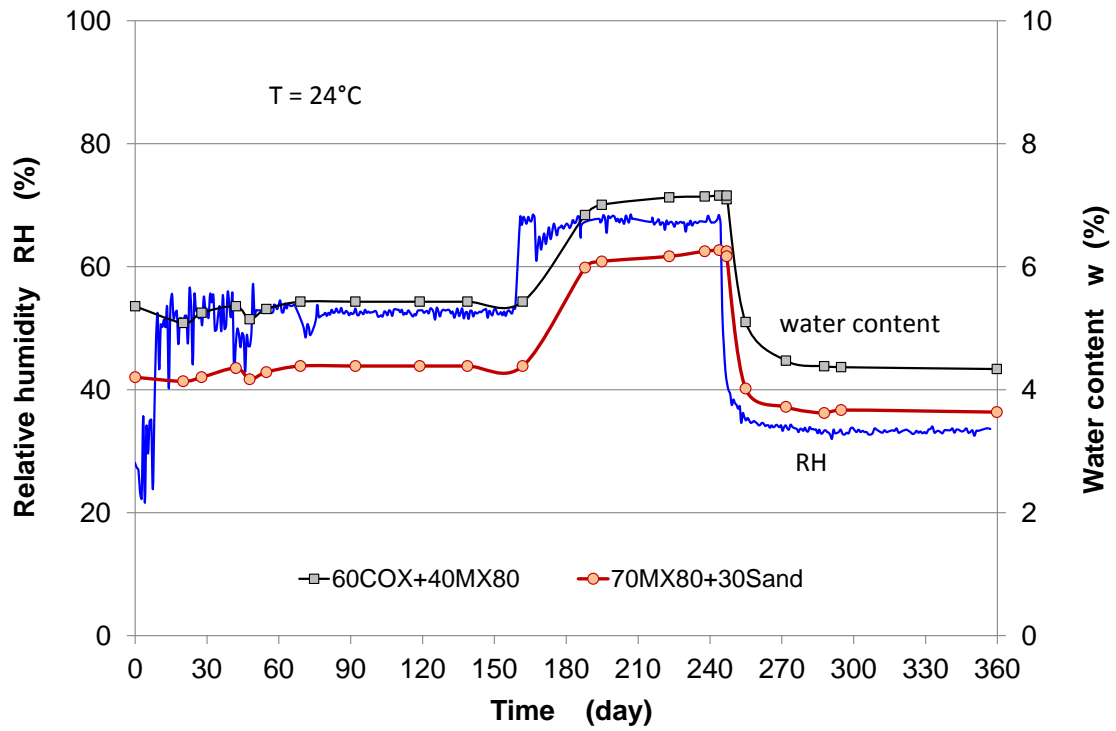


**Fig. A. 5** Water uptake of compacted claystone-bentonite (60/40) and bentonite-sand (70/30) mixtures in desiccator 1

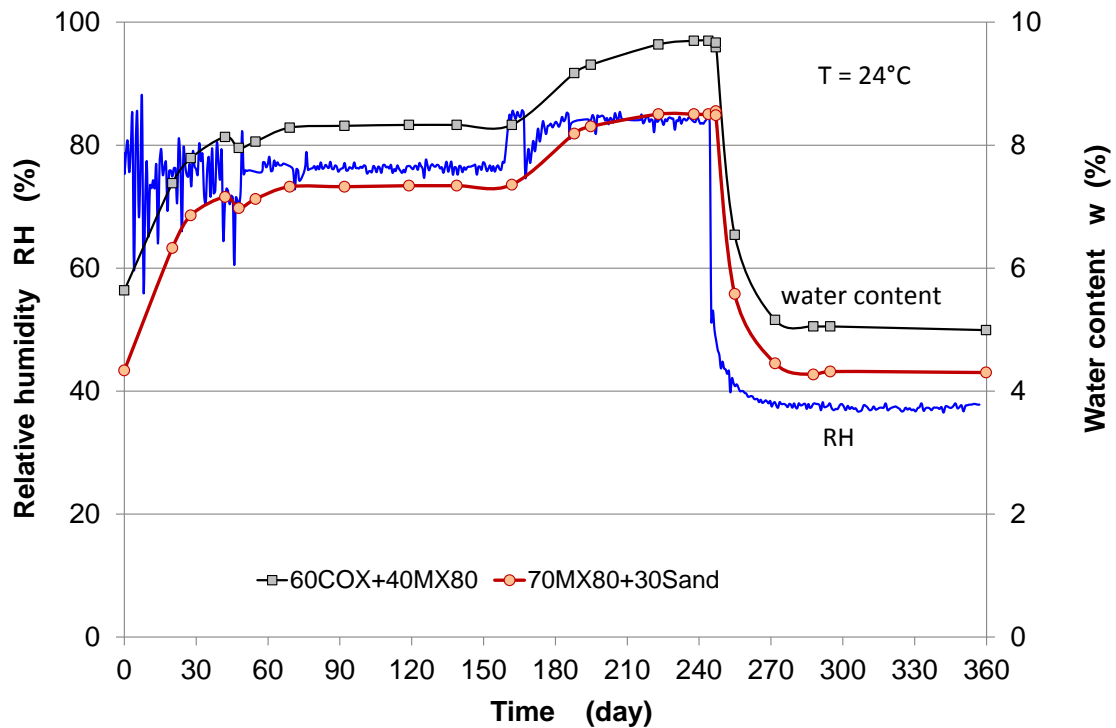


**Fig. A. 6** Water uptake of compacted claystone-bentonite (60/40) and bentonite-sand (70/30) mixtures in desiccator 2

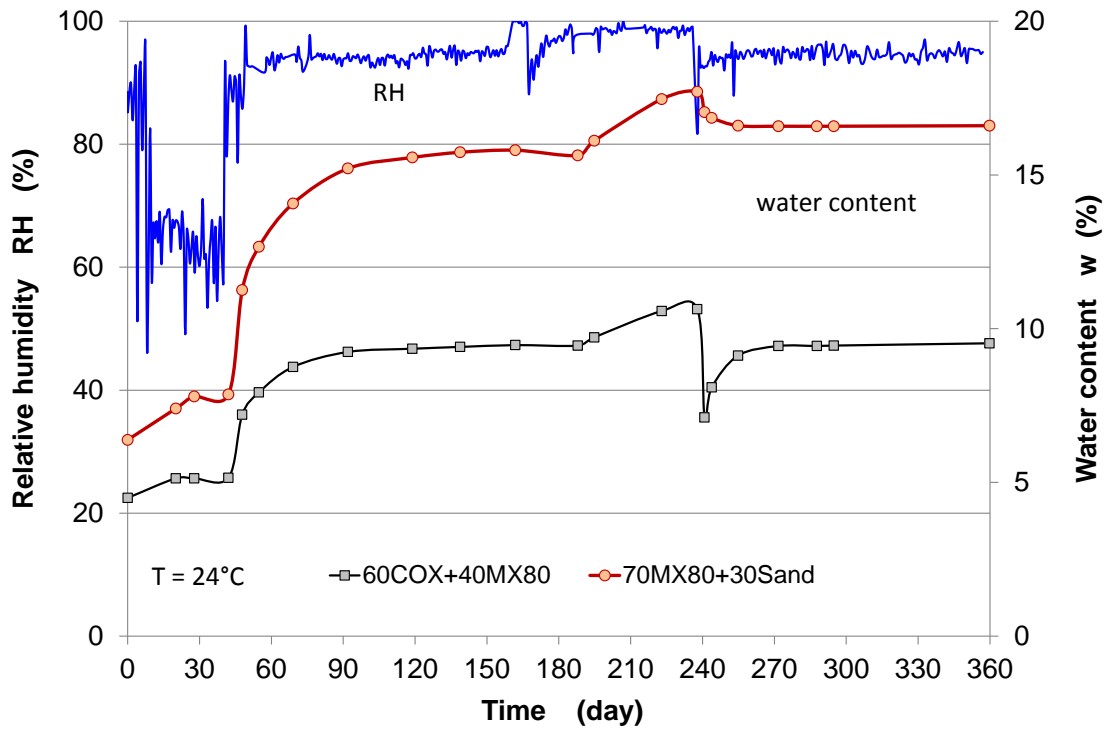


**Fig. A. 7** Water uptake of compacted claystone-bentonite (60/40) and bentonite-sand (70/30) mixtures in desiccator 3

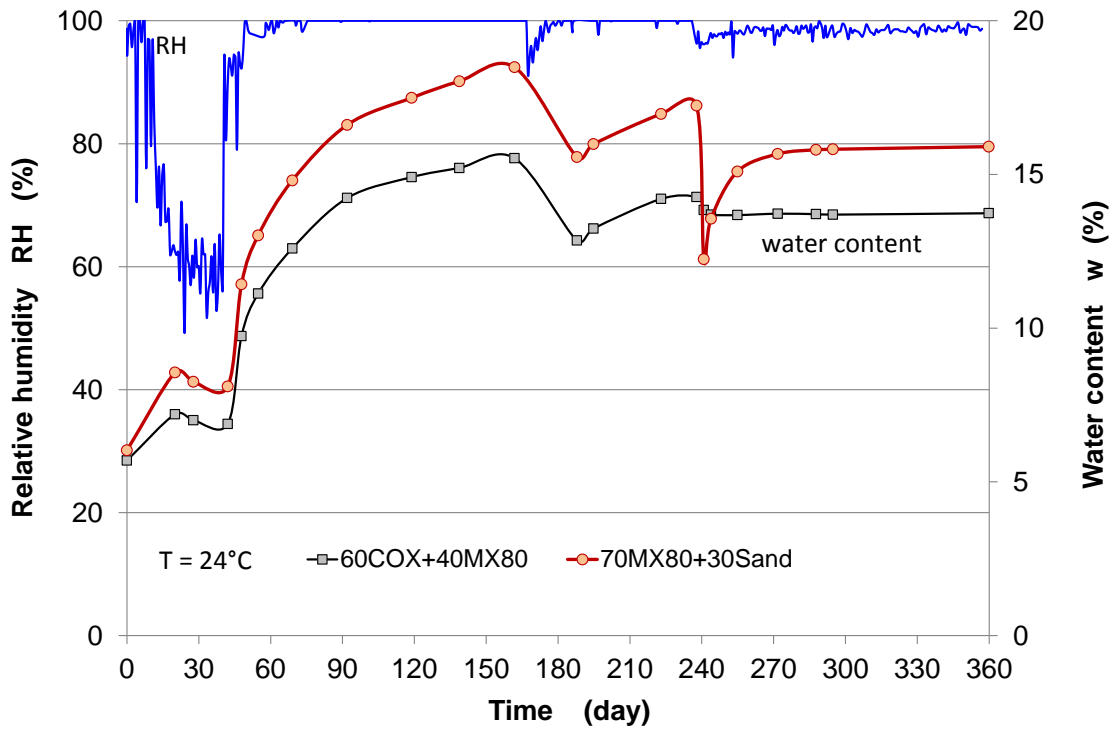


**Fig. A. 8** Water uptake of compacted claystone-bentonite (60/40) and bentonite-sand (70/30) mixtures in desiccator 4

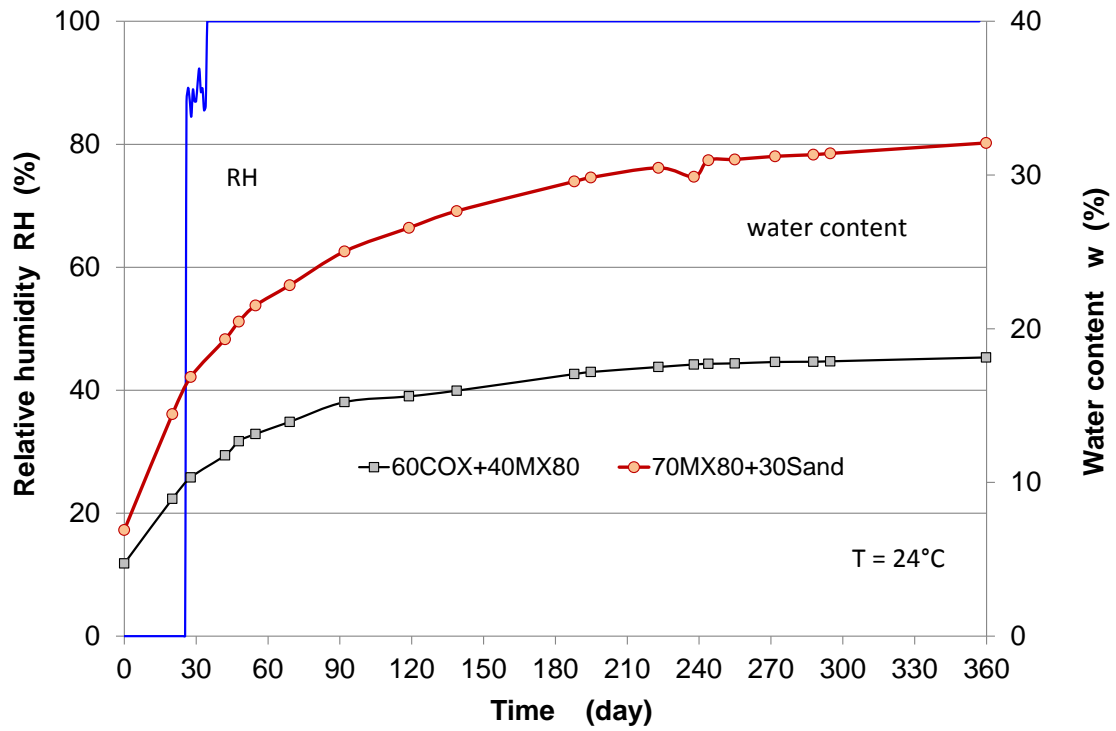


**Fig. A. 9** Water uptake of compacted claystone-bentonite (60/40) and bentonite-sand (70/30) mixtures in desiccator 5

**Group III:**

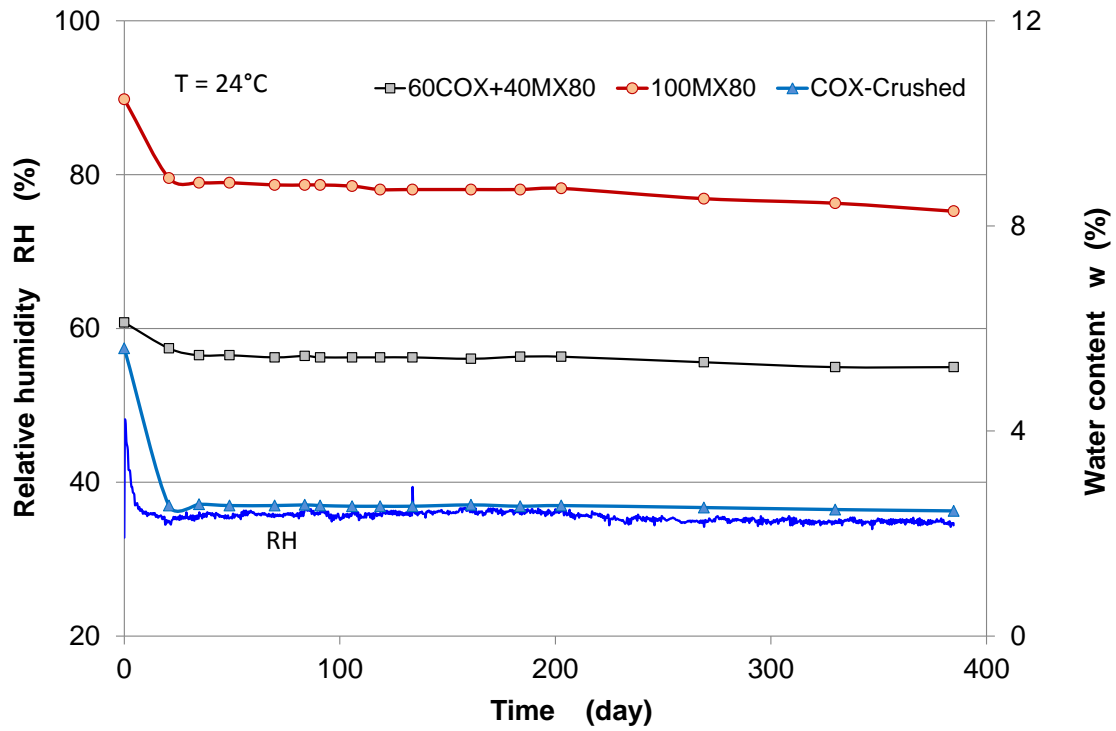


**Fig. A. 10** Water uptake of compacted claystone-bentonite and bentonite powder, claystone in desiccator 1

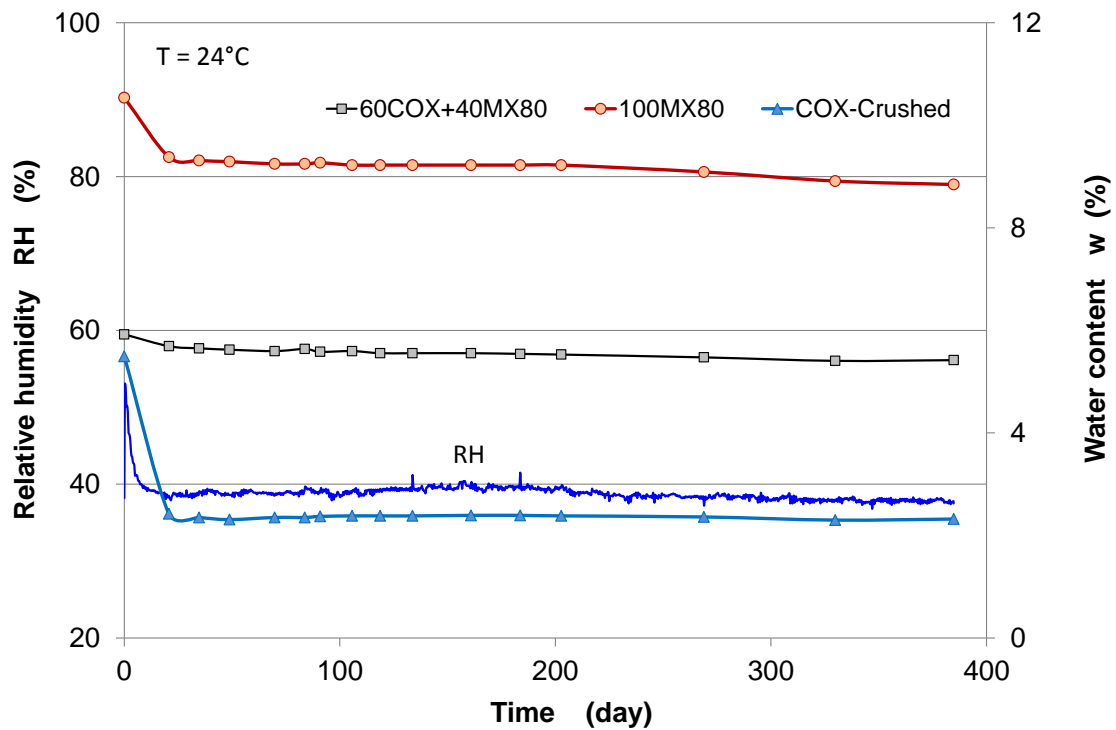


**Fig. A. 11** Water uptake of compacted claystone-bentonite and bentonite powder, claystone in desiccator 2

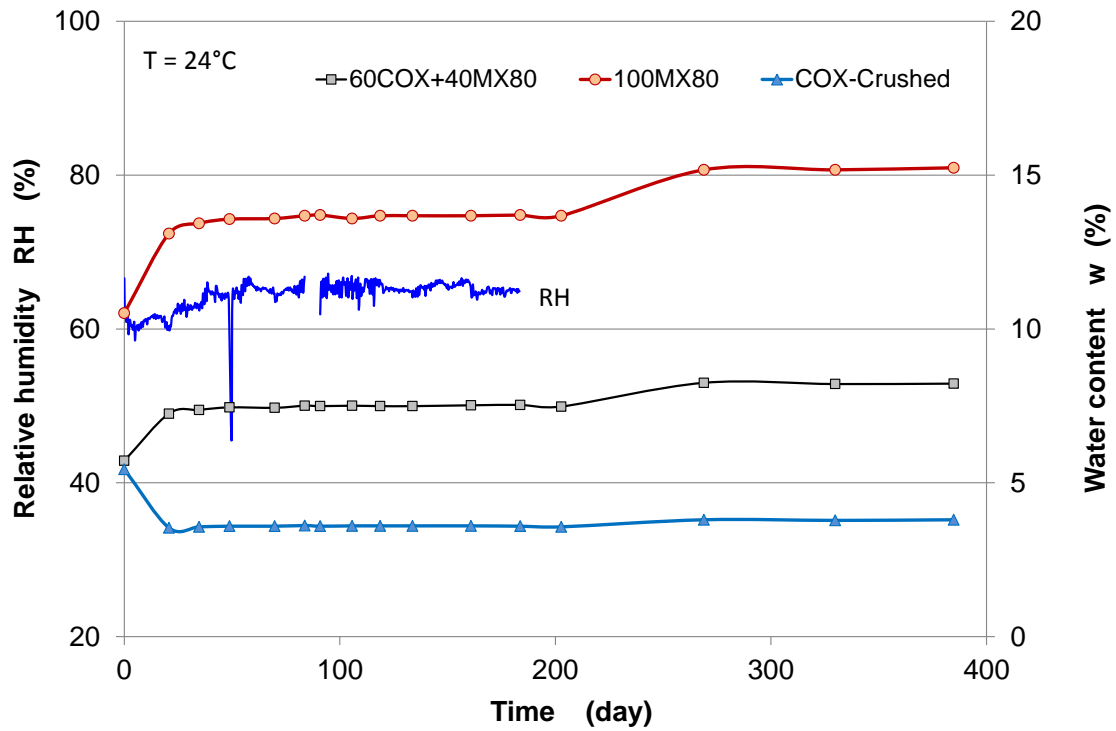


Fig. A. 12 Water uptake of compacted claystone-bentonite and bentonite powder, claystone in desiccator 3

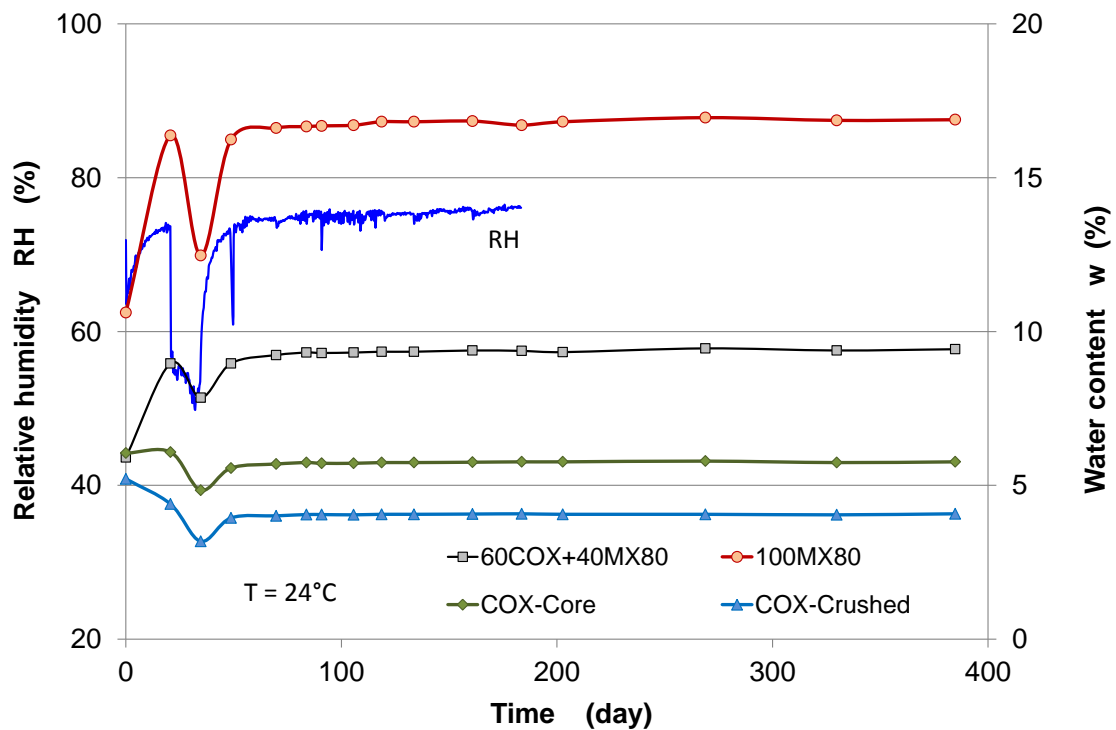
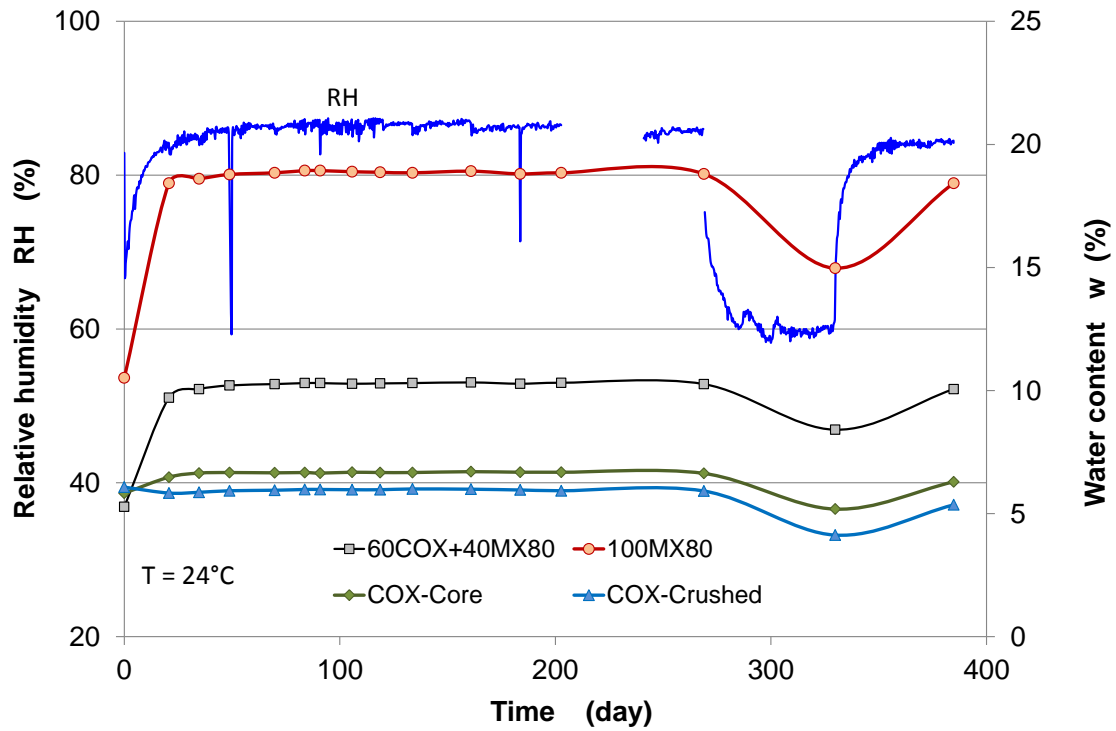
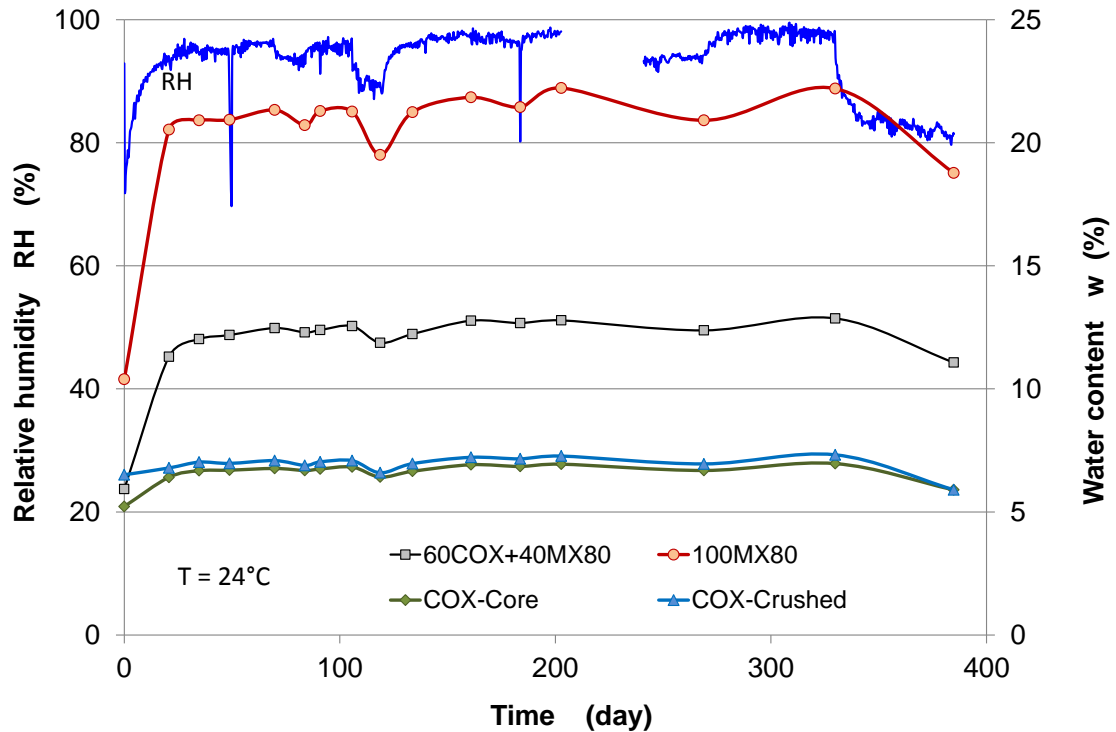


Fig. A. 13 Water uptake of compacted claystone-bentonite and bentonite powder, claystone in desiccator 4



**Fig. A. 14** Water uptake of compacted claystone-bentonite and bentonite powder, crushed claystone and claystone core in desiccator 5



**Fig. A. 15** Water uptake of compacted claystone-bentonite and bentonite powder, crushed claystone and claystone core in desiccator 6

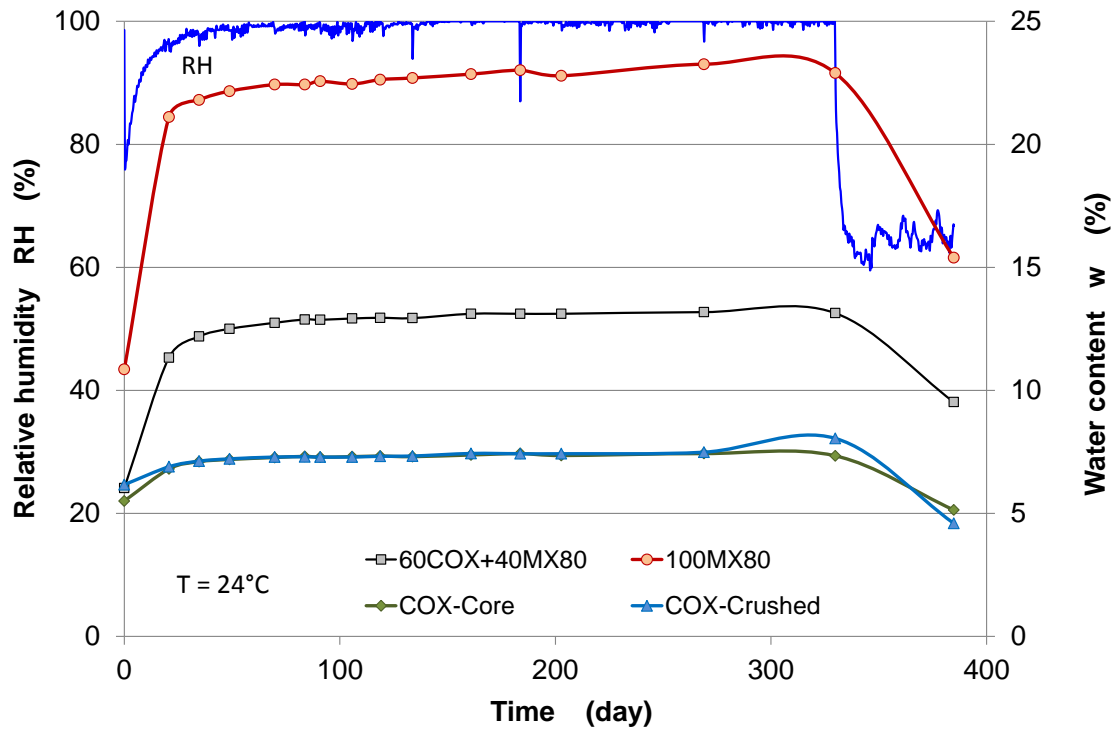


**Fig. A. 16** Water uptake of compacted claystone-bentonite and bentonite powder, crushed claystone and claystone core in desiccator 7

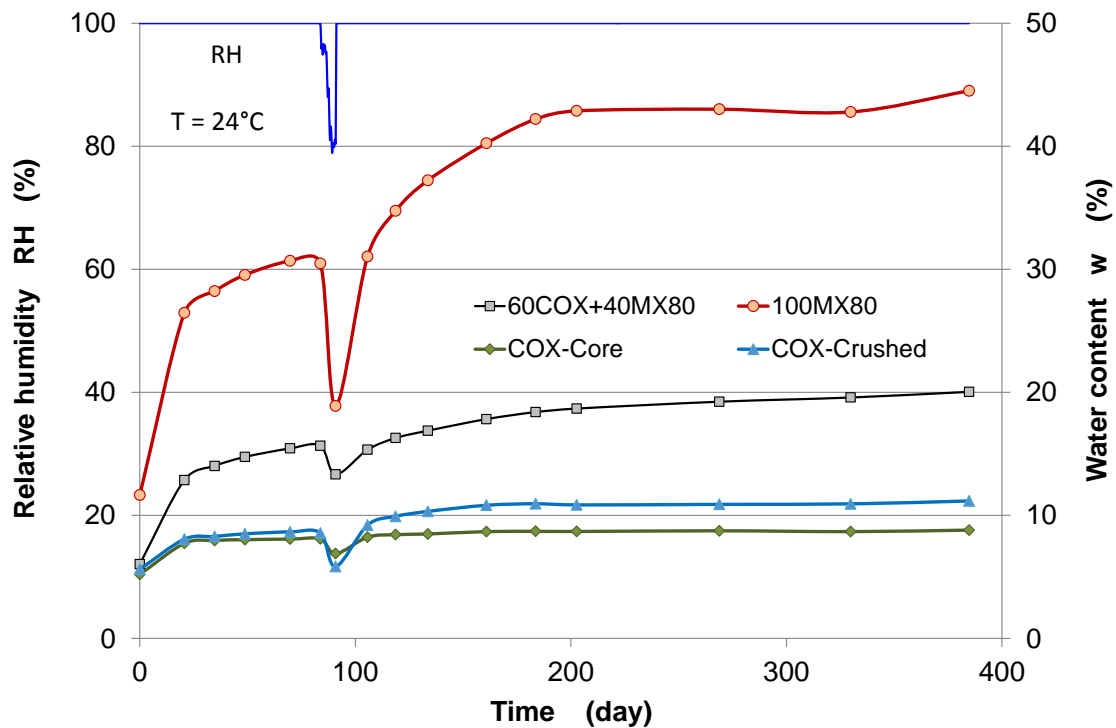


**Fig. A. 17** Water uptake of compacted claystone-bentonite and bentonite powder, crushed claystone and claystone core in desiccator 8

## Appendix B: Water saturation data obtained on the seal materials

Tab. B. 1 Initial characteristics of the samples tested in group I

Property	COX aggregate	MX80 bentonite	80COX+ 20MX80	60COX+ 40MX80
Diameter D (mm)	50.0	50.0	50.0	50.0
Height H (mm)	95.5	104.0	97.0	100.0
Grain size d (mm)	< 10.0	< 0.5	< 10.0	< 10.0
Water content w (%)	3.00	9.67	4.50	5.45
Bulk density $\rho_b$ (g/cm <sup>3</sup> )	2.10	2.00	2.10	1.89
Dry density $\rho_d$ (g/cm <sup>3</sup> )	2.04	1.81	2.01	1.79
Grain density $\rho_s$ (g/cm <sup>3</sup> )	2.70	2.78	2.72	2.73
Total porosity $\phi$ (%)	24.6	35.0	26.3	34.5
Water saturation $S_w$ (%)	25.7	55.2	36.0	30.0

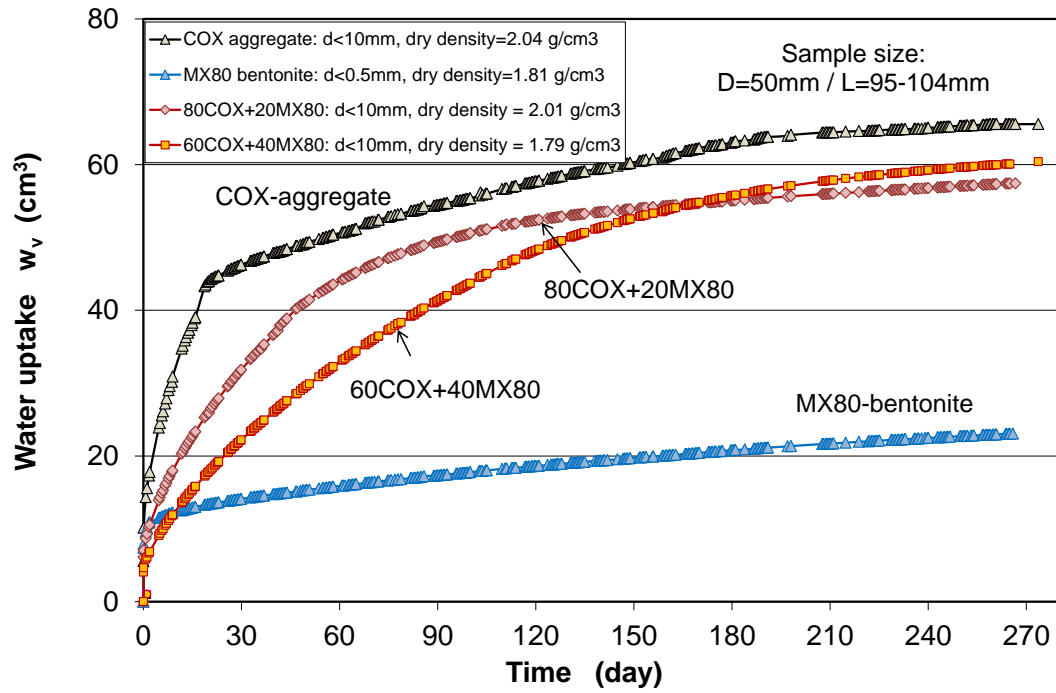


Fig. B. 1 Evolution of water uptake by the compacted claystone-bentonite mixture

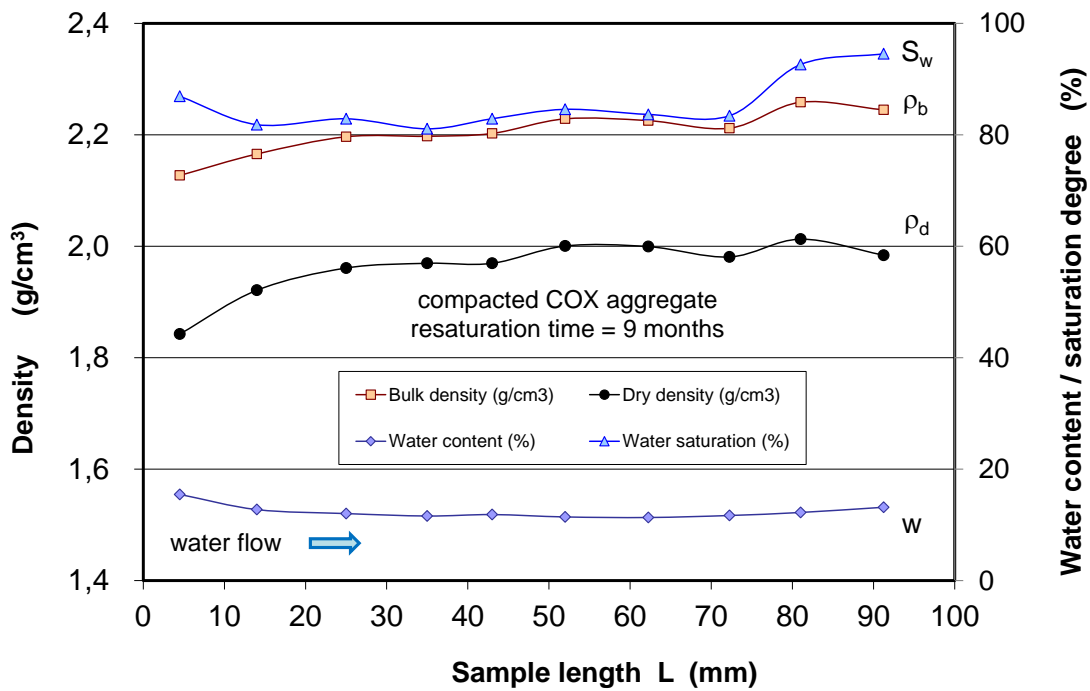
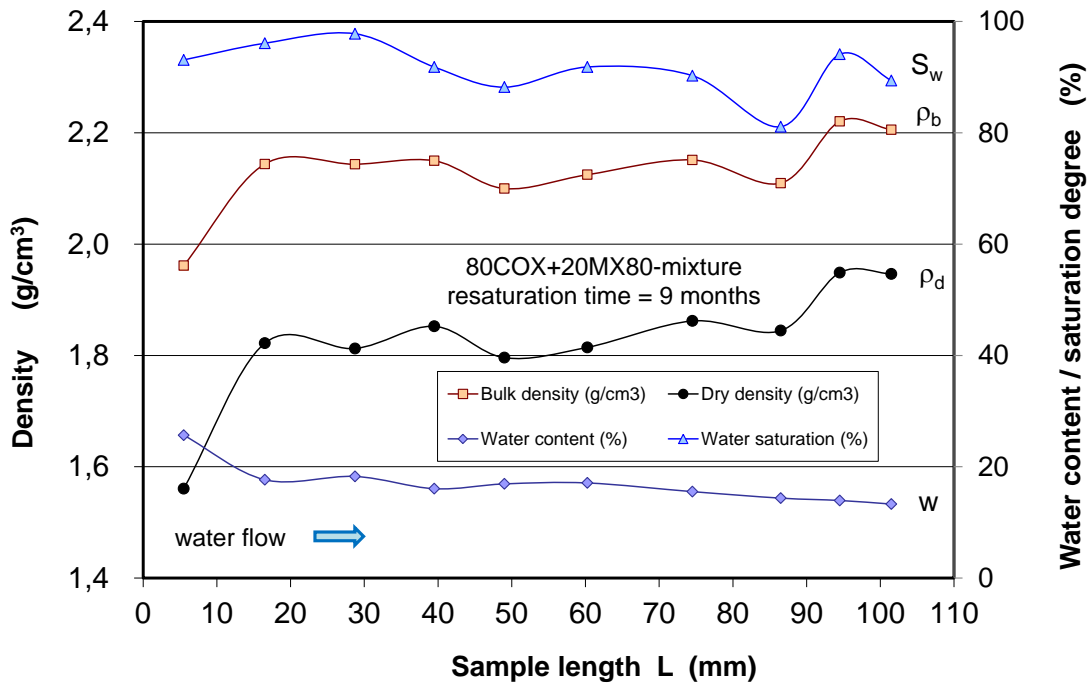
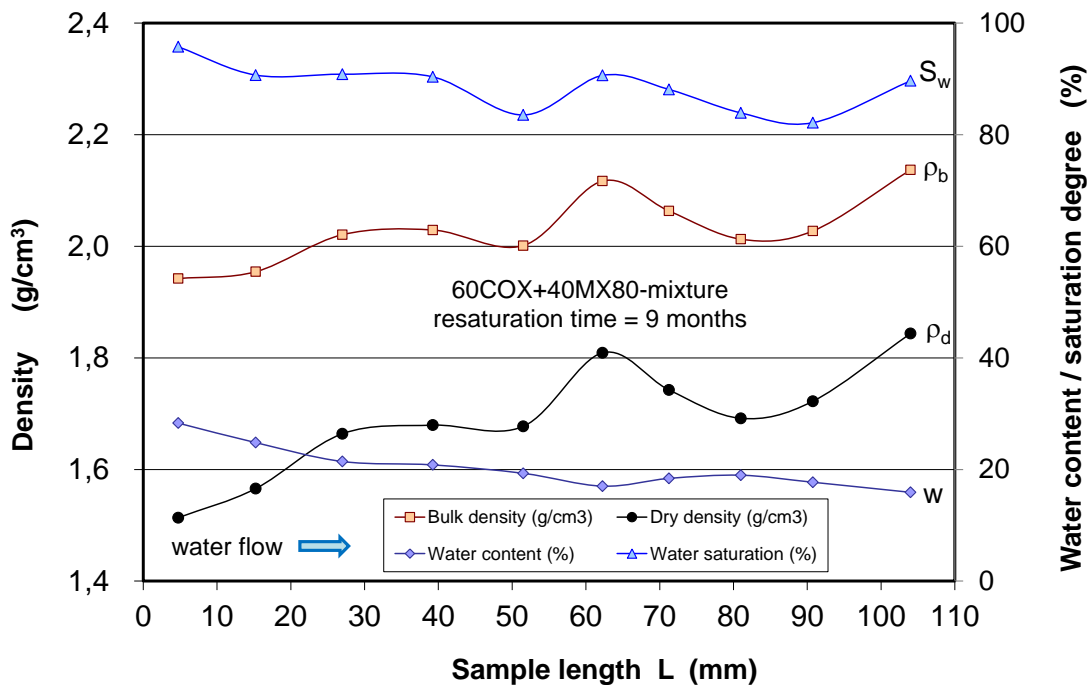


Fig. B. 2 Distributions of bulk/dry density, water content and saturation of compacted claystone aggregate after a saturation time period of 9 months



**Fig. B. 3** Distributions of bulk/dry density, water content and saturation of compacted claystone-bentonite mixture (80/20) after a saturation time period of 9 months



**Fig. B. 4** Distributions of bulk/dry density, water content and saturation of compacted claystone-bentonite mixture (60/40) after a saturation time period of 9 months

**Tab. B. 2** Initial characteristics of the samples tested in group II

Property	60COX+40MX80	70MX80+30Sand	MX80 bentonite	COX-claystone
Diameter D (mm)	50.0	50.0	50.0	47.2
Height H (mm)	100.0	98.0	97.0	101.3
Grain size d (mm)	< 10.0	< 2.0	< 2.0	
Water content w (%)	3.04	9.0	9.0	3.70
Bulk density $\rho_b$ (g/cm <sup>3</sup> )	1.80	1.64	1.20	2.38
Dry density $\rho_d$ (g/cm <sup>3</sup> )	1.75	1.49	1.09	2.29
Grain density $\rho_s$ (g/cm <sup>3</sup> )	2.73	2.75	2.78	2.70
Total porosity $\phi$ (%)	36.0	46.0	61.0	15.1
Water saturation $S_w$ (%)	15.1	32.7	17.8	58.3

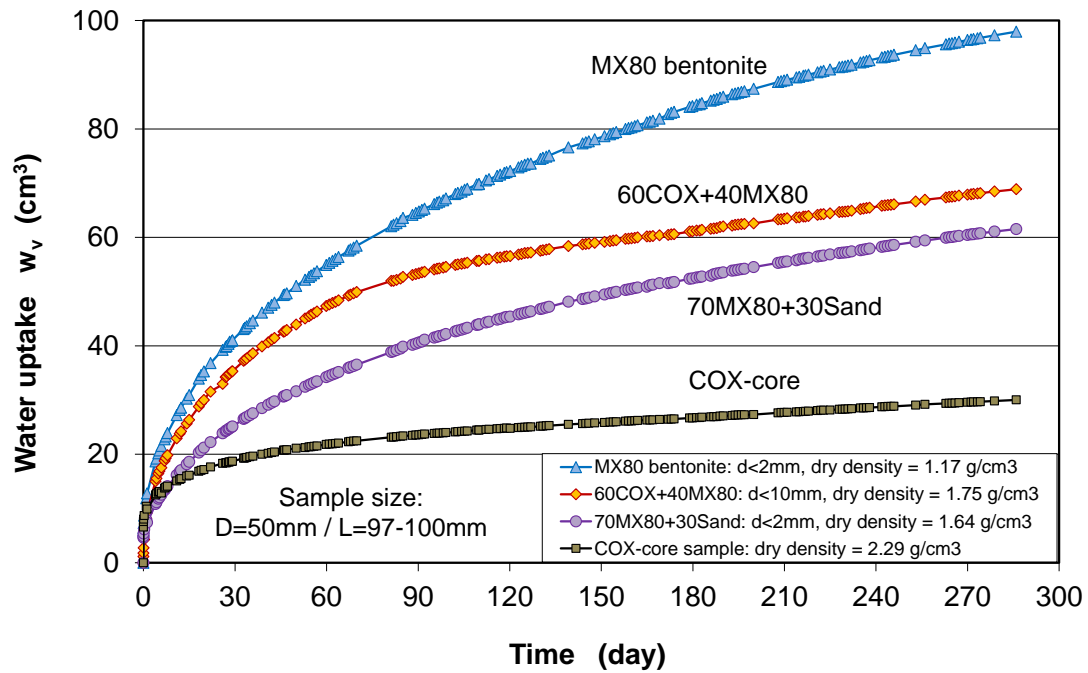


**Fig. B. 5** Evolution of water uptake by the compacted claystone-bentonite and bentonite-sand mixtures

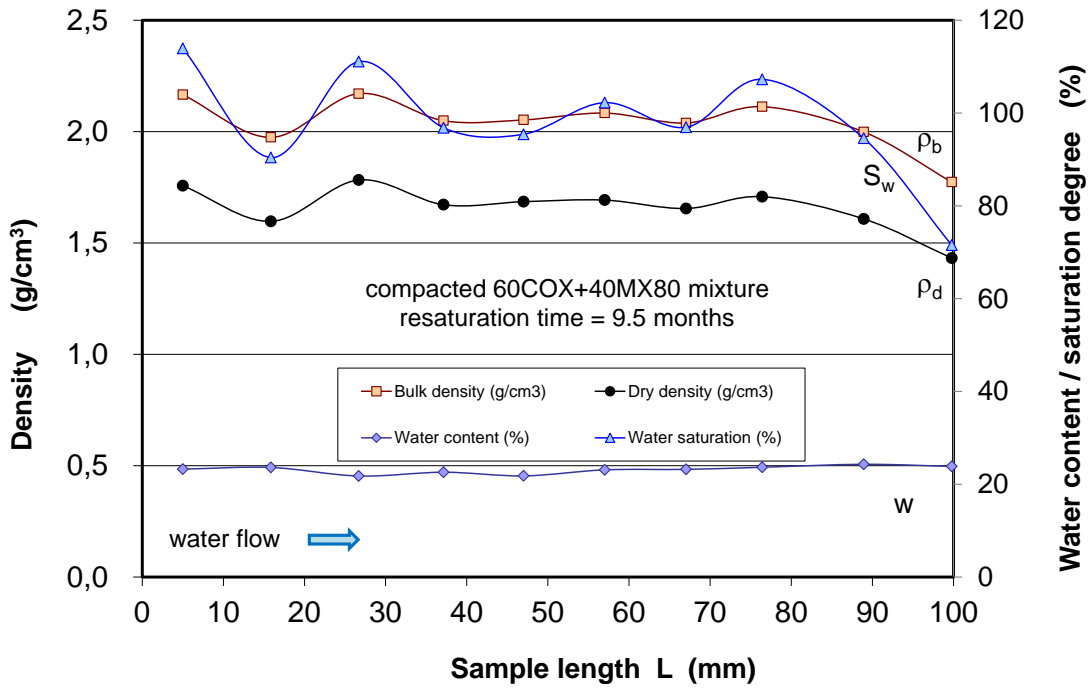


**Fig. B. 6** Distributions of bulk/dry density, water content and saturation of compacted claystone-bentonite mixture (60/40) after a saturation time period of 9.5 months

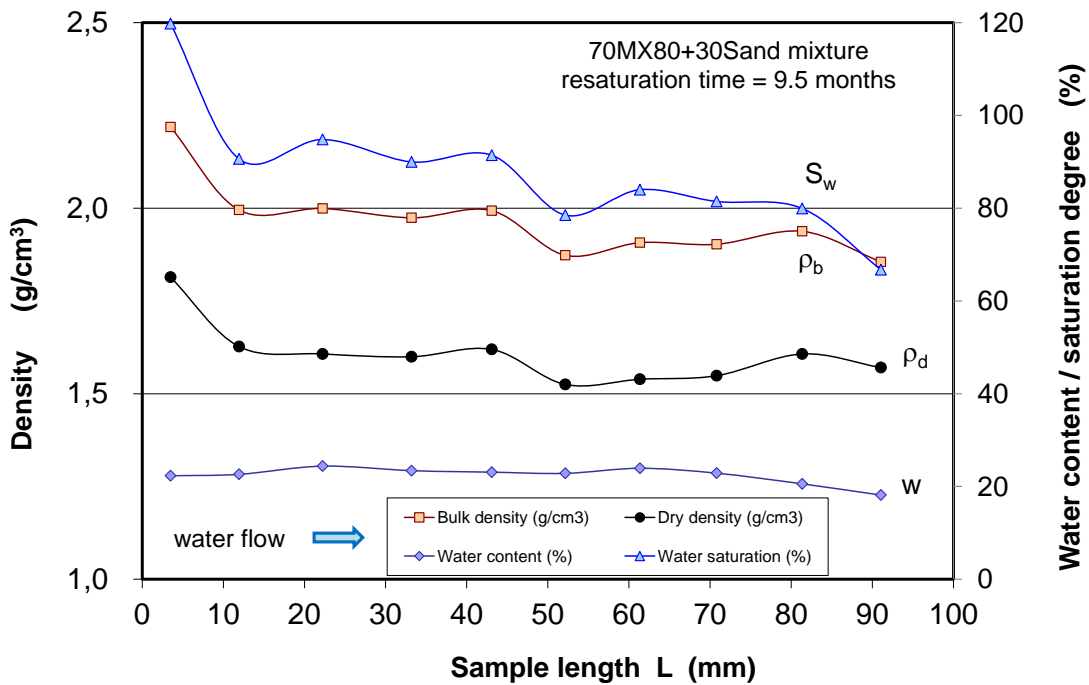


**Fig. B. 7** Distributions of bulk/dry density, water content and saturation of compacted bentonite-sand mixture (70/30) after a saturation time period of 9.5 months

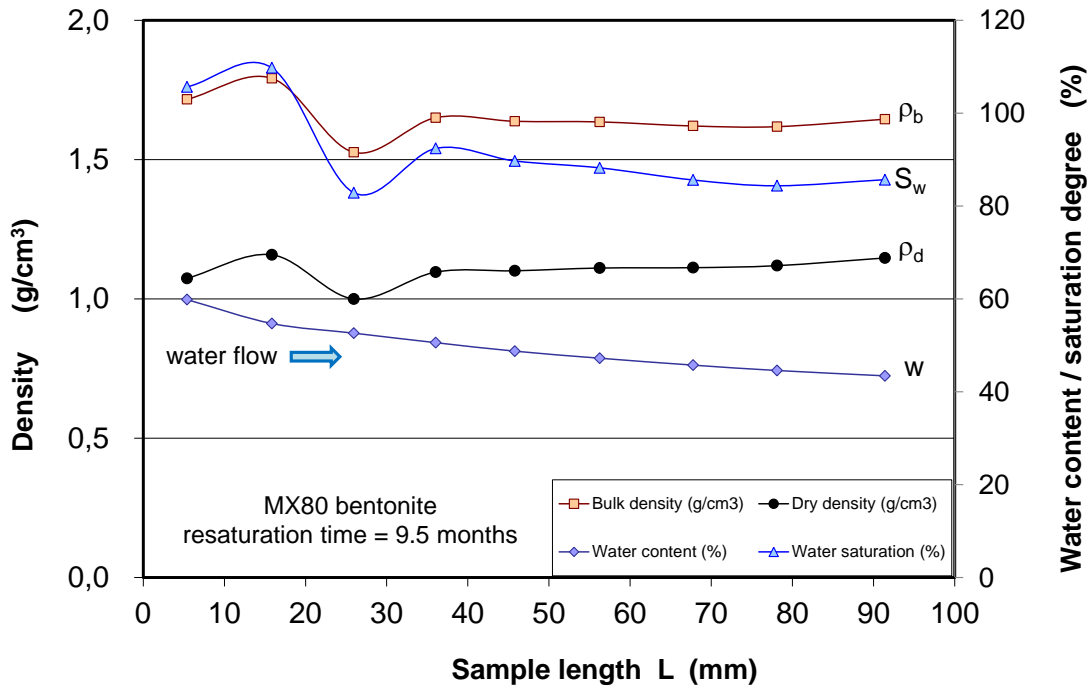


**Fig. B. 8** Distributions of bulk/dry density, water content and saturation of compacted bentonite after a saturation time period of 9.5 months

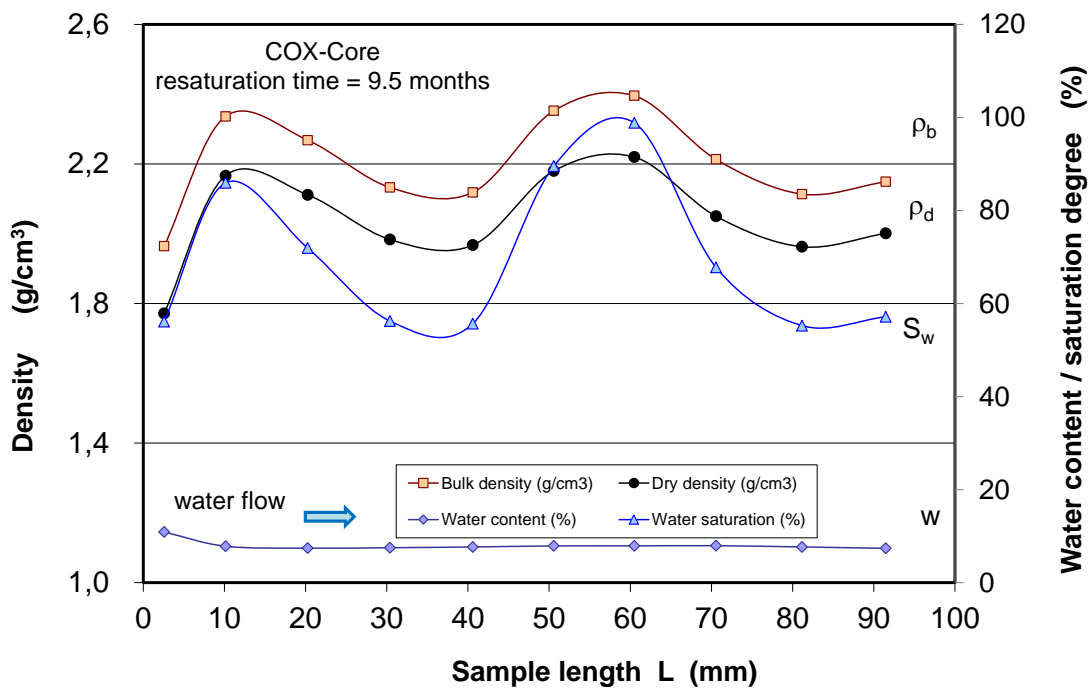


**Fig. B. 9** Distributions of bulk/dry density, water content and saturation of a claystone core after a saturation time period of 9.5 months

**Tab. B. 3** Initial characteristics of the samples tested in group III

Property	60COX+ 40MX80-1	60COX+ 40MX80-2	70MX80+ 30Sand-1	70MX80+ 30Sand-2
Diameter D (mm)	50,0	50,0	50,0	50,0
Height H (mm)	100,0	100,0	102,0	100,0
Grain size d (mm)	< 5.0	< 5.0	< 2.0	< 2.0
Water content w (%)	7,0	7,0	9,0	9,0
Bulk density $\rho_b$ (g/cm <sup>3</sup> )	2,04	2,00	1,91	1,95
Dry density $\rho_d$ (g/cm <sup>3</sup> )	1,91	1,87	1,75	1,79
Grain density $\rho_s$ (g/cm <sup>3</sup> )	2,73	2,73	2,75	2,75
Total porosity $\phi$ (%)	30,0	31,0	36,0	35,0
Water saturation $S_w$ (%)	44,4	41,6	43,6	46,0

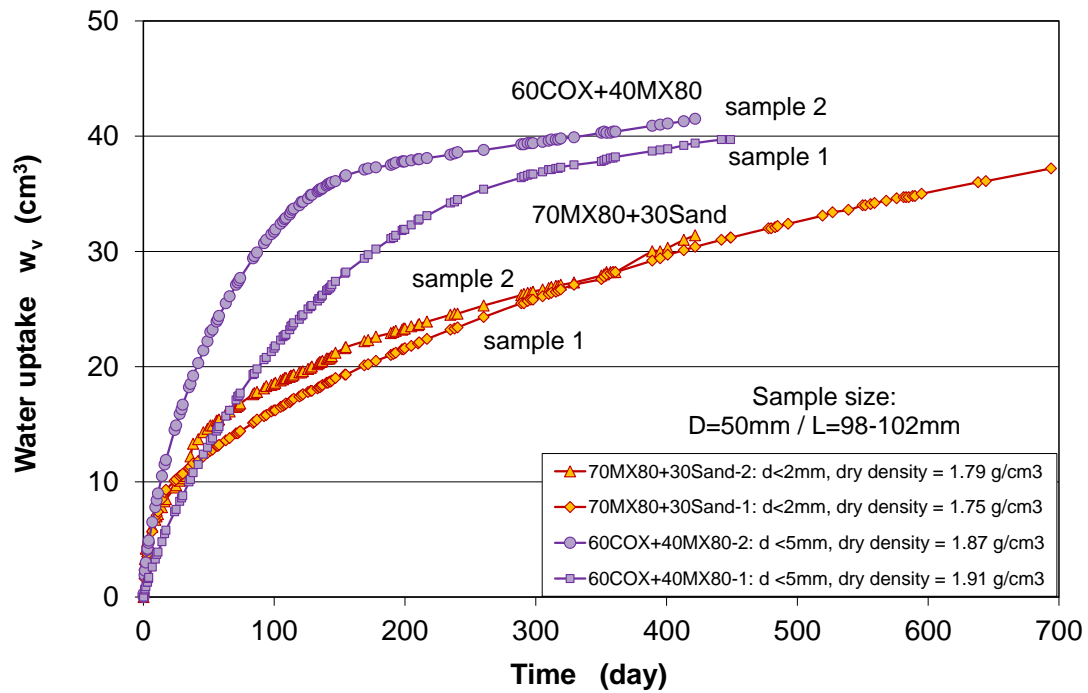


**Fig. B. 10** Evolution of water uptake by the compacted claystone-bentonite and bentonite-sand mixtures

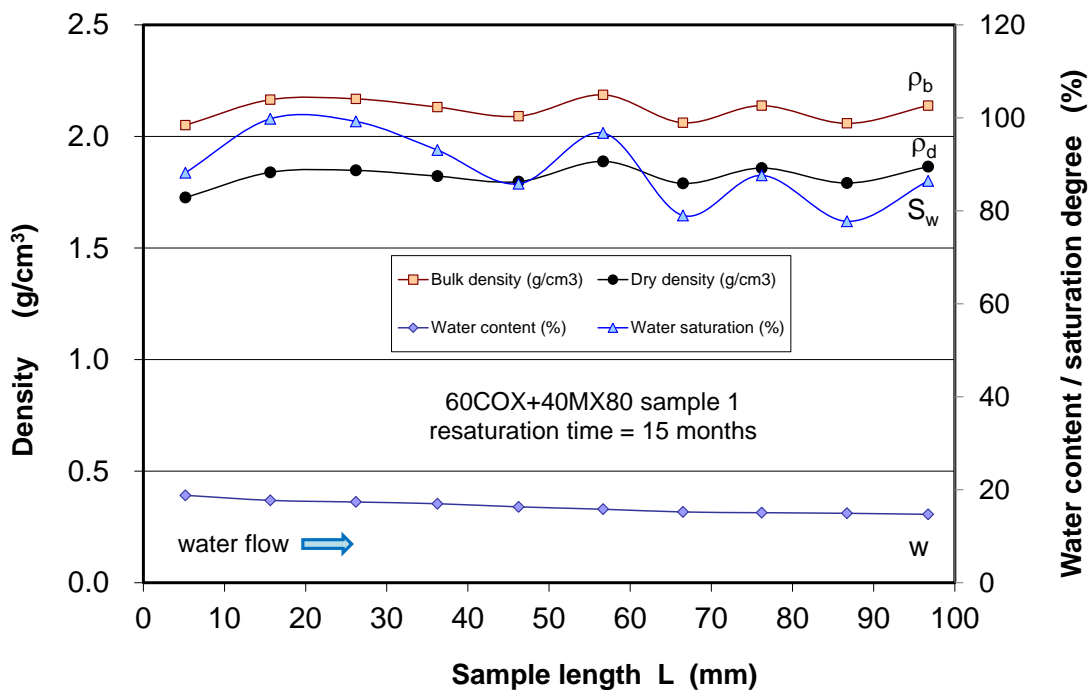


**Fig. B. 11** Distributions of bulk/dry density, water content and saturation of compacted claystone-bentonite mixture (60/40) after a saturation time period of 15 months

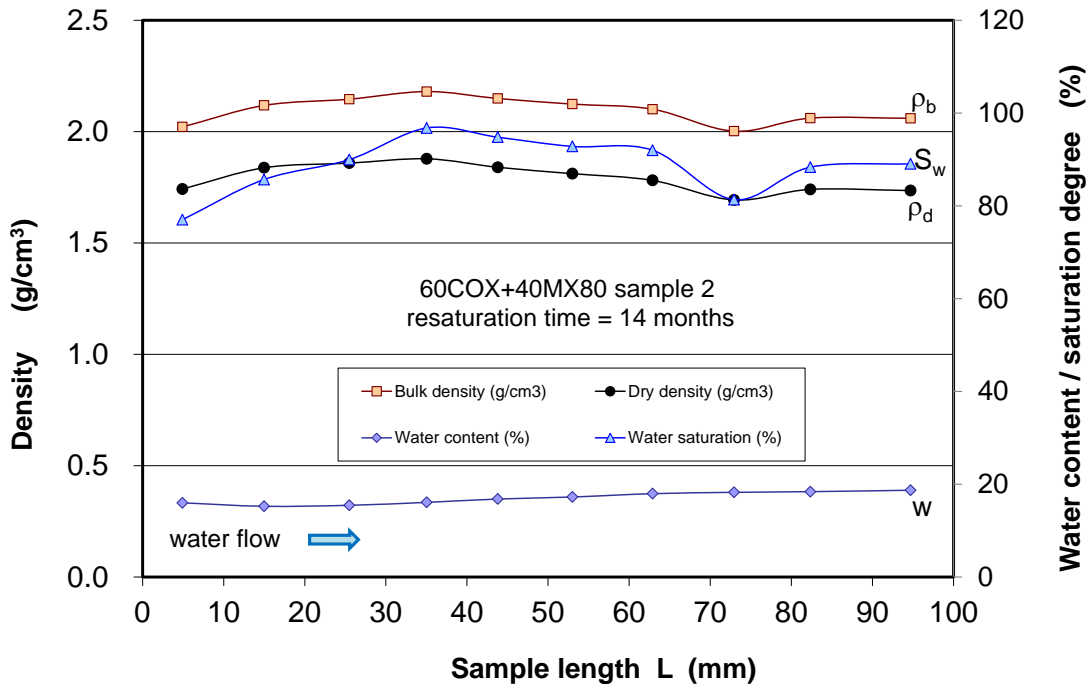


**Fig. B. 12** Distributions of bulk/dry density, water content and saturation of compacted claystone-bentonite mixture (60/40) after a saturation time period of 14 months

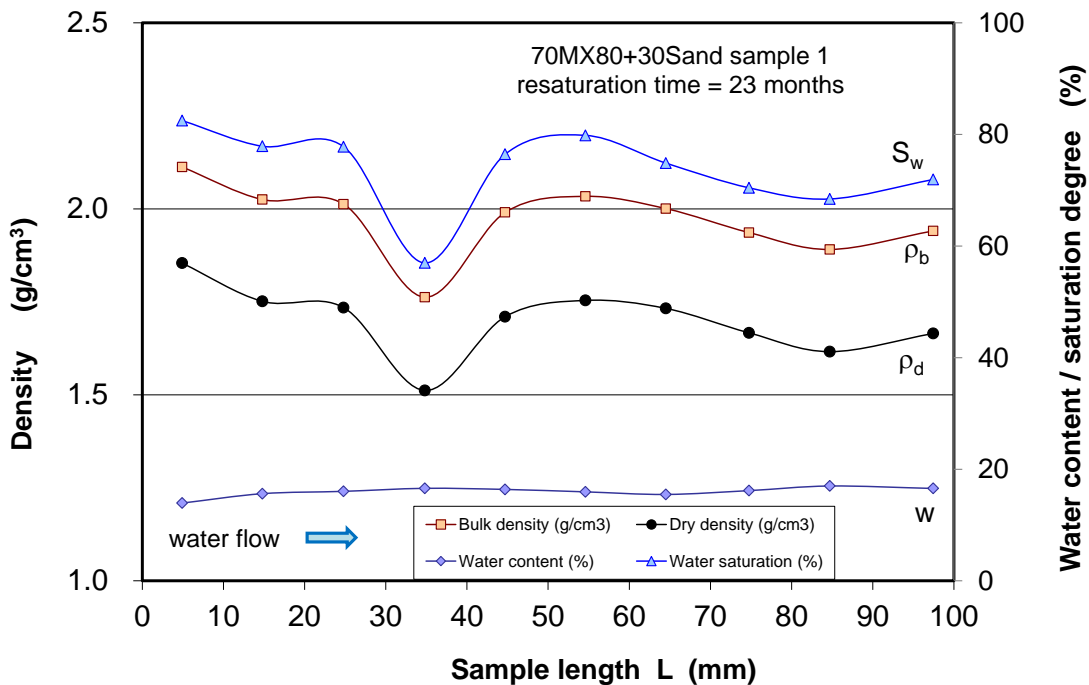


**Fig. B. 13** Distributions of bulk/dry density, water content and saturation of compacted bentonite-sand mixture (70/30) after a saturation time period of 15 months

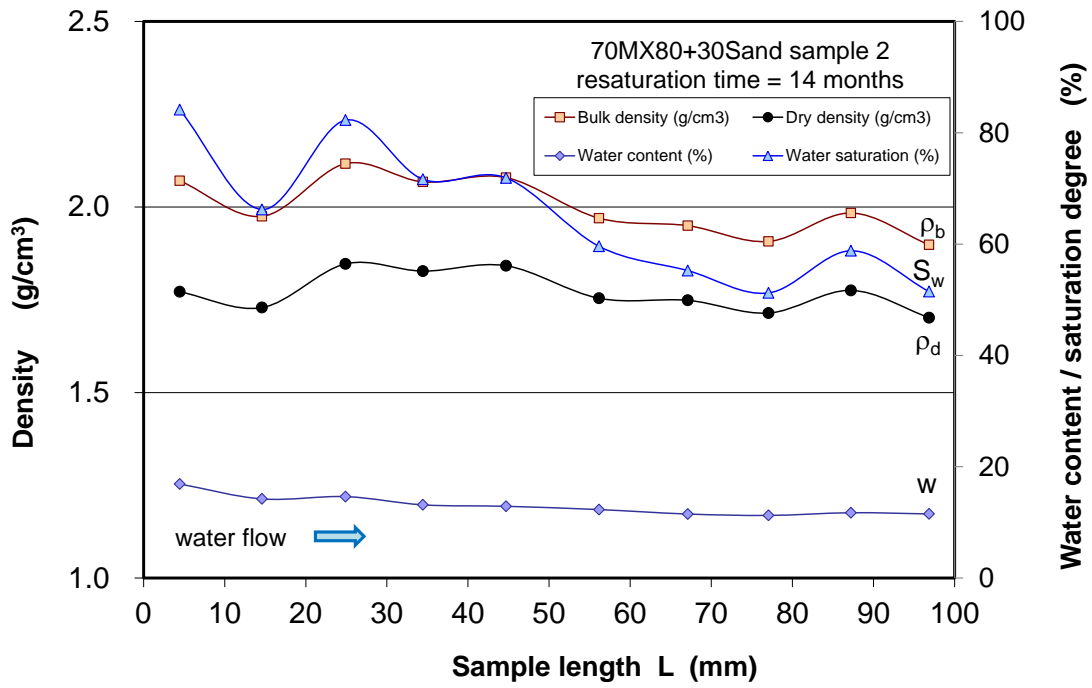


**Fig. B. 14** Distributions of bulk/dry density, water content and saturation of compacted bentonite-sand mixture (70/30) after a saturation time period of 14 months

**Gesellschaft für Anlagen-  
und Reaktorsicherheit  
(GRS) gGmbH**

Schwertnergasse 1  
**50667 Köln**  
Telefon +49 221 2068-0  
Telefax +49 221 2068-888

Boltzmannstraße 14  
**85748 Garching b. München**  
Telefon +49 89 32004-0  
Telefax +49 89 32004-300

Kurfürstendamm 200  
**10719 Berlin**  
Telefon +49 30 88589-0  
Telefax +49 30 88589-111

Theodor-Heuss-Straße 4  
**38122 Braunschweig**  
Telefon +49 531 8012-0  
Telefax +49 531 8012-200

[www.grs.de](http://www.grs.de)